Veröffentlichungen der DGK

Ausschuss Geodäsie der Bayerischen Akademie der Wissenschaften

Reihe C | Dissertationen | Heft Nr. 840

Mahmud Haghshenas Haghighi

Local and Large Scale InSAR Measurement of Ground Surface Deformation

München 2019

Verlag der Bayerischen Akademie der Wissenschaften

ISSN 0065-5325 | ISBN 978-3-7696-5252-9

Diese Arbeit ist gleichzeitig veröffentlicht in:
Wissenschaftliche Arbeiten der Fachrichtung Geodäsie und Geoinformatik der Universität Hannover
ISSN 0174-1454, Nr. 354, Hannover 2019

Veröffentlichungen der DGK

Ausschuss Geodäsie der Bayerischen Akademie der Wissenschaften

Reihe C | Dissertationen | Heft Nr. 840

Local and Large Scale InSAR Measurement of Ground Surface Deformation

Von der Fakultät für Bauingenieurwesen und Geodäsie

der Gottfried Wilhelm Leibniz Universität Hannover

zur Erlangung des Grades

Doktor-Ingenieur (Dr.-Ing.)

genehmigte Dissertation

Vorgelegt von

M.Sc. Mahmud Haghshenas Haghighi

Geboren am 03.03.1986 in Estahban

München 2019

Verlag der Bayerischen Akademie der Wissenschaften

ISSN 0065-5325 ISBN 978-3-7696-5252-9

Diese Arbeit ist gleichzeitig veröffentlicht in:
Wissenschaftliche Arbeiten der Fachrichtung Geodäsie und Geoinformatik der Universität Hannover
ISSN 0174-1454, Nr. 354, Hannover 2019

Adresse der DGK:



Ausschuss Geodäsie der Bayerischen Akademie der Wissenschaften (DGK)

Alfons-Goppel-Straße 11 ● D – 80 539 München

Telefon +49 – 331 – 288 1685 ● Telefax +49 – 331 – 288 1759

E-Mail post@dgk.badw.de ● http://www.dgk.badw.de

Prüfungskommission:

Vorsitzender: Prof. Dr.-Ing. Christian Heipke

Referent: Prof. Dr. Mahdi Motagh

Korreferenten: Prof. Falk Amelung (University of Miami)
Prof. Dr.-Ing. Steffen Schön

Tag der mündlichen Prüfung: 27.06.2019

© 2019 Bayerische Akademie der Wissenschaften, München

Alle Rechte vorbehalten. Ohne Genehmigung der Herausgeber ist es auch nicht gestattet,
die Veröffentlichung oder Teile daraus auf photomechanischem Wege (Photokopie, Mikrokopie) zu vervielfältigen

ISSN 0065-5325 ISBN 978-3-7696-5252-9

Abstract

Interferometric Synthetic Aperture Radar (InSAR) is a remote sensing technique frequently used for measuring Earth's surface deformation. InSAR time series approaches provide detailed information about the evolution of displacement in time and also overcome the limitations of conventional InSAR. Both InSAR and InSAR time series methods have been used for measuring tectonic and non-tectonic surface deformations caused by natural and anthropogenic processes in local to regional scales. In the past, the availability of SAR data suitable for InSAR purpose was a major constraint for InSAR applications in many areas of the world. The launch of the Sentinel-1 mission in 2014 guaranteed a regular long-term acquisition plan of SAR data available all over the globe that enables us to increase the scale of deformation mapping from regional to national. However, there are challenges in large-scale InSAR processing that needs to be addressed. In this thesis, InSAR time series approaches are used to obtain detailed maps of the time-varying surface displacement fields caused by non-tectonic processes at a local to regional scales and find the link between surface displacement and its drivers. Then, a workflow for large-scale InSAR time series analysis is suggested that benefits from extensive collections of data provided by Sentinel-1 to identify and monitor displacement fields over extensive areas.

In the first part of this thesis, InSAR time series approaches are used at local to regional scales in three independent case studies. In the first case study, a localized displacement of as much as 1 cm/yr attributed to slope movement of a landslide in Taihape, New Zealand is observed. Along with the long-term trend of displacement caused by slope movement, the analysis of time series reveals an acceleration in surface displacement due to a rainstorm as well as the seasonal variations of displacement linked to groundwater variations. In the second study area, land subsidence in Tehran, Iran is analyzed at a regional scale. Using an extensive collection of SAR data, land subsidence areas with a peak exceeding 25 cm/yr are detected. After combining time series from different datasets, both long-term subsidence trend due to the constant decline of groundwater level, and seasonal variations of surface displacement linked to the discharge/recharge cycle of groundwater are investigated. In the third case study, localized displacement of a natural gas reservoir in Berlin is analyzed and a long-term uplift of approximately 0.2 cm/yr and 2 cm of seasonal variations linked to the injection of gas in summer and extraction in winter are observed. Furthermore, mining-induced displacements in an area near Leipzig are measured and approximately 4 cm/yr of subsidence coupled with 5 cm/yr of east-west displacement are observed.

To extend the InSAR measurement of non-tectonic displacement fields from local and regional to national scale, a workflow is developed in this thesis that benefits from the vast amount of data col-

lected by Sentinel-1 mission. The proposed workflow notably reduces the broad-scale and topography-dependent components of tropospheric errors in an adaptive approach and provides a quick, but robust displacement field map from large stacks of Sentinel-1 data. The proposed method is applied on two tracks of Sentinel-1 data across Iran and Germany and successfully obtained the displacement fields in large scales. In the first case study, more than 20 displacement areas mostly attributed to land subsidence induced by over-extraction of groundwater are identified. In the second case study, approximately 10 displacement areas mainly related to anthropogenic activities including mining and gas/oil injection/extraction are detected.

Keywords: InSAR, Displacement time series, large-scale mapping, Land subsidence, Landslide, anthropogenic deformation

Zusammenfassung

Radarinterferometrie (InSAR) ist eine Fernerkundungsmethode, die häufig zur Messung von Erdoberflächenverformungen eingesetzt wird. InSAR-Zeitreihen-Ansätze liefern detaillierte Informationen über die Entwicklung der Verformung in der Zeit und überwinden zudem die Grenzen des konventionellen InSAR. Sowohl InSAR als auch InSAR-Zeitreihenmethoden wurden auf lokaler bis regionaler Ebene zur Messung tektonischer und nicht-tektonischer Oberflächenverformungen infolge natürlicher und anthropogener Prozesse eingesetzt. In der Vergangenheit war die Verfügbarkeit von SAR-Daten, die für InSAR-Zwecke geeignet sind, für viele Gebiete in der Welt ein wesentliches Hindernis für InSAR-Anwendungen. Der Start der Mission Sentinel-1 im Jahr 2014 garantierte einen regelmäßigen, langfristigen Akquisitionsplan für SAR-Daten sowie eine weltweiten Verfügbarkeit und ermöglicht es damit den Umfang der Deformationskartierung von regional auf national zu erhöhen. Es gibt jedoch Herausforderungen bei der groß angelegten InSAR-Verarbeitung, die es zu bewältigen gilt. In dieser Arbeit werden InSAR-Zeitreihenansätze verwendet, um detaillierte Karten der zeitvariablen Oberflächenverformungsfelder nicht-tektonischer Prozesse auf lokaler bis regionaler Ebene zu erhalten, welche dazu dienen den Zusammenhang zwischen Oberflächenverlagerungen und ihren Ursachen zu finden. Anschließend wird ein Workflow für die groß angelegte InSAR-Zeitreihenanalyse vorgeschlagen, der von den umfangreichen Datensammlungen von Sentinel-1 zur Identifizierung und Überwachung von Deformationsfeldern über große Gebiete hinweg profitiert.

Im ersten Teil dieser Arbeit werden InSAR-Zeitreihenansätze auf lokaler bis regionaler Ebene in drei unabhängigen Fallstudien verwendet. In der ersten Fallstudie wird eine lokale Verschiebung von bis zu 1 cm/a beobachtet, die auf die Hangbewegung eines Erdrutsches in Taihape, Neuseeland, zurückzuführen ist. Neben dem langfristigen Trend der Verschiebung durch die Hangbewegungen zeigt die Analyse von Zeitreihen eine Beschleunigung der Oberflächenverschiebung durch einen Regensturm sowie saisonale Verschiebungen durch Grundwasserschwankungen. Im zweiten Untersuchungsgebiet, der Landabsenkung in Teheran, wird der Iran auf regionaler Ebene analysiert. Mit einer umfangreichen Sammlung von SAR-Daten werden Landabsenkungsgebiete mit einer Höchstrate von mehr als 25 cm/a detektiert. Mit Hilfe einer Kombination von Zeitreihen aus verschiedenen Datensätzen werden sowohl der langfristige Absenkungstrend aufgrund des konstanten Absinkens des Grundwasserspiegels als auch saisonale Schwankungen der Oberflächendeformation im Zusammenhang mit dem Abfluss-/Zuflusszyklus des Grundwassers untersucht. In der dritten Fallstudie wird die lokale Deformation eines Erdgasspeichers in Berlin analysiert und eine langfristige Hebung von ca. 0,2 cm/a und 2 cm saisonale Schwankungen im Zusammenhang mit der Gaseinleitung im Sommer und der Förderung im Winter beobachtet. Darüber hinaus werden bergbaubedingte Verlagerungen in einem Gebiet bei Leipzig gemessen und ca. 4 cm/a Absenkung bei gleichzeitiger 5 cm/a Ost-West-Verschiebung

beobachtet. Um die InSAR-Messung von nicht-tektonischen Deformationsfeldern von der lokalen und regionalen auf die nationale Ebene zu erweitern, wird in dieser Arbeit ein Workflow entwickelt, der von der großen Menge aufgenommener Sentinel-1-Missionsdaten profitiert. Der vorgeschlagene Workflow reduziert insbesondere die großräumigen und topographieabhängigen Komponenten troposphärischer Fehler in einem adaptiven Ansatz und liefert eine schnelle, aber robuste Oberflächenverformungskarte aus großen Stapeln von Sentinel-1-Daten. Die vorgeschlagene Methode wird auf zwei Tracks von Sentinel-1-Daten im Iran und in Deutschland angewendet und ermittelt erfolgreich die großräumigen Deformationsfelder. In der ersten Fallstudie werden mehr als 20 Verformungsgebiete identifiziert, die meist auf Bodensenkungen, verursacht durch Überbeanspruchung des Grundwassers, zurückzuführen sind. In der zweiten Fallstudie werden etwa 10 Deformationsgebiete erfasst, die hauptsächlich mit anthropogenen Aktivitäten wie Bergbau und Gas/Erdöl Einspeisung/Extraktion zusammenhängen.

Contents

1. Introduction **11**
1.1. Research Objectives . . . 13
1.2. Outline and Structure of the Thesis . . . 14

2. Theoretical Background **17**
2.1. Introduction . . . 18
2.2. SAR Imaging . . . 18
2.2.1. SAR Image Distortions . . . 19
2.2.2. SAR Imaging Modes . . . 20
2.2.3. SAR Missions . . . 20
2.3. SAR Interferometry . . . 21
2.3.1. InSAR Workflow . . . 21
2.3.2. InSAR Decorrelation . . . 24
2.3.3. Errors in InSAR . . . 25
2.3.4. Examples of Interferograms . . . 28
2.3.5. Decomposition of Line-of-Sight Measurements . . . 29
2.4. Multi Temporal InSAR . . . 29
2.4.1. Scattering Mechanisms in SAR Images . . . 30
2.4.2. Interferogram Stacking . . . 30
2.4.3. Persistent Scatterer InSAR . . . 31
2.4.4. Small Baseline InSAR . . . 32
2.5. Analysis of Displacement Time Series . . . 33
2.5.1. Continuous Wavelet Transform . . . 34
2.5.2. Cross Wavelet Transform . . . 34
2.5.3. Application of CWT and XWT to InSAR Time Series . . . 35

3. Methodological Contribution **37**
3.1. Introduction . . . 38
3.2. Challenges in Large-scale InSAR . . . 38
3.3. Proposed Method . . . 39
3.3.1. Interferogram Formation . . . 39
3.3.2. Adaptive Correction of Interferograms . . . 41
3.3.3. Estimating the Displacement Rate . . . 42
3.3.4. Estimating the Time Series of Displacement . . . 42

4. InSAR Monitoring of Localized Landslide in Taihape, New Zealand 43
4.1. Abstract . . . 44
4.2. Introduction . . . 44
4.3. Study Area . . . 45
4.4. Methods . . . 46
4.4.1. InSAR Measurement . . . 46
4.4.2. Ancillary Data . . . 47
4.4.3. Cause-Effect Analysis . . . 48
4.5. Results . . . 48
4.5.1. Small-baseline Interferograms . . . 48
4.5.2. Time-series Results . . . 49
4.6. Discussion . . . 50
4.6.1. Suitability of InSAR Measurements for Monitoring the Taihape Landslide . . . 50
4.6.2. Interpretation of InSAR Results . . . 52
4.6.3. Comparison with Ground Truth . . . 52
4.6.4. Comparison with Rainfall and Groundwater Level . . . 53
4.7. Conclusion . . . 56
4.8. Acknowledgments . . . 57
4.9. Supplementary Materials . . . 58

5. InSAR Measurement of Regional Land Subsidence in Tehran, Iran 61
5.1. Abstract . . . 62
5.2. Introduction . . . 62
5.3. Study Area and Problem Description . . . 63
5.4. Datasets . . . 66
5.4.1. SAR Data . . . 66
5.4.2. Leveling . . . 67
5.4.3. Groundwater Level . . . 67
5.5. Methods . . . 67
5.5.1. Multi-temporal InSAR Analysis . . . 67
5.5.2. Merging InSAR Time Series . . . 71
5.5.3. Cause-Effect Analysis . . . 72
5.6. Results . . . 73
5.6.1. Southwest of Tehran . . . 73
5.6.2. IKA Airport . . . 75
5.6.3. Varamin County . . . 76
5.6.4. Time Series of Displacement . . . 77
5.6.5. Accuracy, Precision and Consistency Assessments . . . 78
5.7. Discussion . . . 81
5.7.1. Structural Control of the Displacement . . . 81
5.7.2. Comparison with Groundwater . . . 82
5.7.3. Elastic vs. Inelastic Compaction . . . 85

5.8. Conclusion . . . 86
5.9. Acknowledgments . . . 87
5.10. Supplementary materials . . . 87
5.10.1. Significance of Tropospheric Delay . . . 87
5.10.2. Decomposition of LOS Measurement . . . 88
5.10.3. Under/Overestimation of Displacement Rates . . . 89

6. Sentinel-1 InSAR Measurement of Anthropogenic Deformation in Germany 91
6.1. Summary . . . 92
6.2. Introduction . . . 92
6.3. Sentinel-1 InSAR Processing . . . 94
6.4. Large-scale Sentinel-1 Processing . . . 98
6.5. Anthropogenic Ground Motion in Berlin . . . 100
6.6. Mining-induced Deformation in Leipzig . . . 104
6.7. Conclusions and Prospect . . . 107
6.8. Acknowledgements . . . 108

7. Subsequent Work: Measurement of Localized Deformations over Extensive Areas 109
7.1. Introduction . . . 110
7.2. SAR Datasets . . . 110
7.3. Sentinel-1 Interferograms . . . 110
7.4. Corrected Interferograms . . . 112
7.5. Displacement Maps and Time Series . . . 114
7.6. Discussion . . . 118
7.7. Conclusion . . . 121

8. Cooperation Works 123
8.1. Quantifying Land Subsidence in the Rafsanjan Plain, Iran Using InSAR Measurements 124
8.1.1. Abstract . . . 124
8.1.2. Author Contribution . . . 124
8.2. Characterizing Post-construction Settlement of Masjed-Soleyman Dam Using TerraSAR-X SpotLight InSAR . . . 125
8.2.1. Abstract . . . 125
8.2.2. Author Contribution . . . 126
8.3. InSAR Observation of the 18 August 2014 Mormori (Iran) Earthquake . . . 126
8.3.1. Author Contribution . . . 126

9. Summary and Future Work 129
9.1. Future works . . . 132

A. Software and Tools 135

Bibliography 137

Chapter 1

Introduction

Geohazards, natural or anthropogenic, substantially influence the life of many people across the globe. They can be catastrophically rapid, like earthquakes or volcanic eruptions, or slowly degrading the living environment like land subsidence or slow-moving landslides. Geohazards are enormous threats to human life, civilian properties, and infrastructure. For example, from 2004 to 2016, approximately 4700 distinct non-seismic landslides were detected to be responsible for a total of 56000 fatalities across the globe. Such landslides are widespread globally and their anthropogenic occurrence is growing in recent years (Froude and Petley, 2018). As another example, land subsidence associated with excessive groundwater pumping is an increasing challenge in many areas. Groundwater is the primary source of freshwater in semi-arid to arid regions of the world. Unsustainable depletion of groundwater is an immense problem endangering the availability of water to approximately 1.7 billion people (Gleeson et al., 2012) and posing a significant hazard due to associated land subsidence.

We need to enhance our understanding of geohazards and develop solutions to reduce their inherent risks. In this regard, detailed geodetic measurements are critical for the detection, study and understanding of earth surface processes and geohazards, yet their field measurements are time-consuming and expensive. In this regard, Interferometric Synthetic Aperture Radar (InSAR) has been widely used in the past three decades as a powerful geodetic method that provides valuable insight into spatial and temporal kinematics of earth processes from space (Rosen et al., 2000; Bürgmann et al., 2000). The main advantage of InSAR is its ability to provide precise displacement measurements over large areas. Decorrelation of interferometric phase, due to temporal variations of earth surface or imaging geometries, is one of the main limitations of InSAR (Zebker and Villasenor, 1992). Moreover, remaining errors, particularly from atmospheric phase delay, may reach several centimeters across the interferogram and obscure the desired signal (Hanssen, 2001).

With the increasing availability of multi-temporal SAR data in the past decades, different time series approaches have been developed to address the limitations of conventional InSAR. They can be classified into two main branches, Persistent Scatterer InSAR (PS) (Ferretti et al., 2001; Hooper et al., 2004) and Small Baseline (SB) (Berardino et al., 2002; Hooper, 2008). Both mentioned approaches search for coherent pixels in a stack of SAR data and connect their interferometric phase in time to obtain the displacement history of each pixel. Furthermore, they either use external information or implement temporal and spatial filters to reduce the errors and extract the displacement signal properly (Hooper et al., 2012).

Several SAR sensors have been launched in the past three decades for both commercial and scientific purposes. As a result, in many areas of the world, a rich collection of SAR data is available that can be used for the historical analysis of displacement. The launch of the Sentinel-1 mission in 2014 has dramatically increased the availability of SAR data. Regular SAR data acquisition by Sentinel-1 gives a unique opportunity for displacement monitoring anywhere in the world (Torres et al., 2012; Salvi et al., 2012). However, new methods are needed to efficiently deal with the massive amount of acquired data and extract relevant information from them.

1.1. Research Objectives

This thesis deals with InSAR geodetic measurements for a better understanding of geohazards at local to regional scales from two major aspects. The first aspect is monitoring, which is the precise measurement of the earth's surface deformation at specific locations in order to understand the past behavior and current status of the processes. The second aspect is detection, which is the large-scale surveys of local to regional deformations to identify specific geohazard hot spots for further precise measurement and monitoring.

The first major aspect, measurement and monitoring of local to regional geohazards, is performed for four different areas prone to different geohazards caused by slope instability, groundwater extraction, open-pit mining, and underground gas injection/extraction. InSAR time series analysis approaches are utilized to obtain the history of displacement from older SAR data and the current status from the recent SAR data. Then, the results of InSAR time series are used to find the link between the surface displacements and their driving mechanisms.

The second major aspect of this thesis is to assess the potentials of the Sentinel-1 mission in large-scale detection of local to regioanl geohazards. In this regards, this thesis suggests a novel method that benefits from massive and regular data acquisition of Sentinel-1 mission for detection of local to regional displacements in a broad area. This approach reduces the tropospheric phase delay, which is a significant error source in large-scale InSAR, and robustly estimates the displacement time series.

This thesis discusses several challenges of InSAR time series analysis and the approaches to tackle them. One of the main challenges is the effect of tropospheric phase delay. The performance of InSAR time series analysis in reducing the tropospheric artifact in local to regional scales are assessed in this thesis. Furthermore, the effectiveness of external atmospheric models in correcting InSAR measurements is investigated. Another challenges of InSAR time series analysis, in particular with older SAR sensors, is their irregular and sporadic data acquisitions. New generations of SAR sensors, particularly Sentinel-1 mission, provide regular data acquisition. The performance of such regular measurements is compared with sporadic measurements of former sensors to identify how they can improve our ability in measurement and monitoring of geohazards.

In summary, the main research questions addressed in this thesis are as follows:

1. What is the performance of InSAR in monitoring local to regional geohazards caused by different earth surface processes and how Sentinel-1 SAR mission with dense and regular temporal resolution can improve it?

2. To what extent atmospheric artifact is important in InSAR analysis at local, regional and national scales? How can it be addressed in order to highlight the displacement signals at different scales?

3. How localized deformations can be efficiently detected and measured over large areas in the scale of hundreds to thousands of kilometers using Sentinel-1 mission which provides temporally dense and regular data with extensive spatial coverage? What are the main challenges and how they can be tackled?

1.2. Outline and Structure of the Thesis

Chapter 2 provides a brief overview of SAR and InSAR. It describes the basics of SAR imaging geometry and InSAR processing flow and includes information on different phase components and errors in InSAR. It describes multi-temporal InSAR approaches that are used in this thesis including stacking, PS and SB. Eventually, it discusses the mathematical tools to interpret the displacement time series and examine the causes of displacement.

Chapter 3 presents the methodological contribution of this thesis in large-scale InSAR processing of Sentinel-1 data. After describing the challenges, a processing workflow is suggested to obtain reliable information on local to regional displacement from regular Sentinel-1 acquisitions over large areas. The main aim is to provide a processing chain that is computationally fast and non-expensive which can be applied unsupervisedly on stacks of SAR data over extensive areas. The proposed approach addresses tropospheric error, as the major limitation of large-scale InSAR, and provides the average rate of displacement and displacement time series as outputs.

In chapter 4, mm-scale displacement of a localized landslide in Taihape, New Zealand is estimated by InSAR time series analysis using different SAR satellite data. The results are validated with ground-truth observation obtained from prism measurement. Then, using Continuous Wavelet Transform and Cross Wavelet Transform, the link between the cause of landslide and the surface displacement is analyzed. This chapter has been published in *New Zealand Journal of Geology and Geophysics* (Haghshenas Haghighi and Motagh, 2016).

In chapter 5, regional land subsidence up to several cm/yr due to groundwater extraction is measured using all available SAR data acquired by several different sensors in Greater Tehran, Iran. The results are validated with leveling measurements. Then, long-term and short-term displacement obtained from InSAR time series analysis are compared against groundwater level measurements to find the link between them. This chapter has been published in *Remote Sensing of Environment* (Haghshenas Haghighi and Motagh, 2019).

In chapter 6, Sentinel-1 data are used to assess their potentials in monitoring localized displacement in the order of mm/yr to cm/yr due to anthropogenic activities, including mining and underground gas storage in Leipzig and Berlin, Germany. Furthermore, the effect of tropospheric artifact in large-scale Sentinel-1 interferogram and potentials of tropospheric delays derived from global weather models or Global Navigation Satellite System (GNSS) in correcting interferograms are discussed. This chapter is published in *zfv – Zeitschrift für Geodäsie, Geoinformation und Landmanagement* (Haghshenas Haghighi and Motagh, 2017).

In chapter 7 the processing workflow proposed in chapter 3 is used to obtain reliable information on local to regional displacement from regular Sentinel-1 acquisitions over large areas. The suggested method is successfully applied to two independent collections of Sentinel-1 data, one track across Iran and another track across Germany and identified several displacement hot spots and their displacement time series in both study areas.

Finally, chapter 9 summarizes the dissertation and suggests the future works that can be done based on the findings of this thesis.

This thesis is presented in a cumulative way. Chapter 4 to 6 compile individual research studies previously published in peer-reviewed scientific journals in their original form after formatting and referencing adjustments. The references are accumulated at the end of the thesis. The results provided in chapter 4 to 7 are based on the original research studies lead by the author of this thesis. In addition, chapter 8 provides a brief overview of the other cooperative works the author was involved in during the completion of this thesis.

Chapter 2

Theoretical Background

2.1. Introduction

This chapter outlines the basics of Synthetic Aperture Radar (SAR) imaging, Interferometric Synthetic Aperture Radar (InSAR) processing, and the mathematical tools to interpret the InSAR data. It starts with a brief introduction of satellite SAR imaging, their different acquisition modes, distortions in SAR images, and an overview of different SAR satellite missions. Then, it explains the workflow of Differential InSAR (DInSAR) to obtain surface displacement and discusses errors in InSAR processing. It also explains different time series approaches developed in the past to overcome the limitations of conventional DInSAR and obtain the history of displacement. Finally, it describes mathematical approaches to find and analyze features in the displacement time series.

2.2. SAR Imaging

Synthetic Aperture Radar (SAR) is an imaging system that employs electromagnetic waves in the microwave range. It transmits microwave signals through its antenna towards the earth surface in an off-nadir direction, called slant range. After interaction with the surface, a portion of the signal returns towards the satellite and is recorded by the sensor. As the satellite moves forward along its flight direction, it illuminates and records the next parts of the earth and forms the SAR image (Figure 2.1).

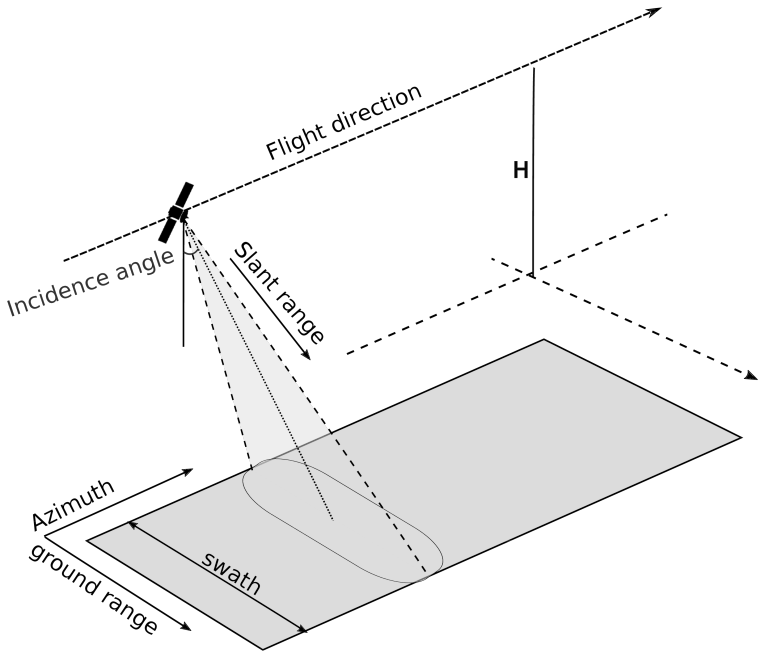


Figure 2.1.: Simplified sketch of SAR imaging geometry.

The SAR sensor records two quantities: the amplitude of the received signal and the phase difference between the transmitted and received signal. The recorded amplitude is a function of the interaction between the signal and the illuminated surface. A high amplitude value indicates a high reflection from the surface towards the sensor while a low amplitude indicates low reflection. The recorded phase

depends on the distance between the sensor and the pixel on the ground and can be used to estimate the topography or displacement of the surface (Bürgmann et al., 2000).

2.2.1. SAR Image Distortions

SAR sensors map ground-range objects to the slant-range direction. This specific type of viewing geometry results in three types of distortions in the SAR image: shadow, foreshortening, and layover (Figure 2.2. Radar shadow occurs when an object is not illuminated because of the higher elevation of other elements closer to the sensor. Foreshortening accrues when a slope is mapped in slant-range shorter than it would be mapped if the surface was flat. Layover occurs in specific slopes where the location of pixels are inverted after being mapped on slant range (Rosen et al., 2000). Figure 2.3 shows an example of SAR amplitude image acquired by TerraSAR-X from the Pyramids of Giza. Three types of SAR distortions are identified on the images.

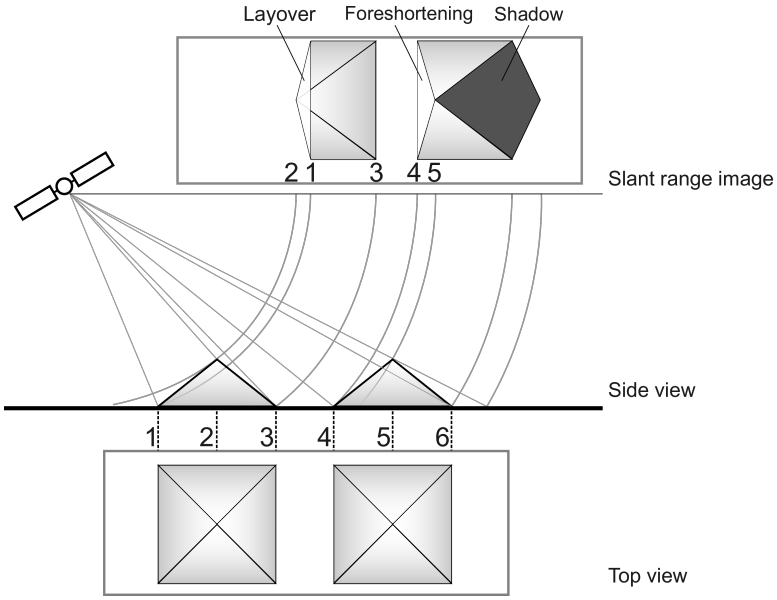


Figure 2.2.: Simplified sketch of distortions in SAR imaging.

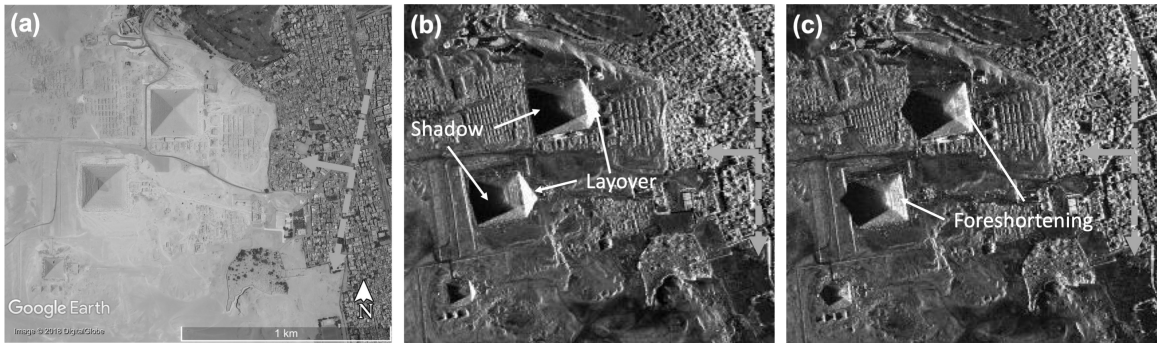


Figure 2.3.: Giza pyramid seen by optical vs SAR sensors. (a) Digital globe image from Google Earth™. (b) and (c) SAR images acquired by TerraSAR-X from the same area. Areas of shadow, Layover and Foreshortening are indicated on the SAR images.

2.2.2. SAR Imaging Modes

There are different acquisition modes developed for satellites SAR sensors (Figure 2.4). StripMap is the standard mode used by many SAR satellites such as ERS, Envisat, ALOS, and TerraSAR-X. In StripMap mode the pointing direction of the sensor is fixed, and as the sensor flies forward along its orbit, following lines of the image are recorded (Lanari et al., 2001). Spotlight is another mode that was designed to achieve high-resolution SAR imaging with the sacrifice of spatial coverage. This mode benefits from steering the antenna in the azimuth direction to increase the illumination time for each element of the image. As a result, a higher spatial resolution can be achieved in this mode, but the scene size is smaller than the Stripmap mode (Eineder et al., 2009).

To increase the coverage of acquired SAR images, Interferometric Wide Swath (IW) or Terrain Observation with Progressive Scan (TOPS) was developed which is the default acquisition mode for Sentinel-1 over land. An IW image is formed from three sub-swaths, and each sub-swath contains several bursts that slightly overlap. The image is not acquired continuously, but after recording a burst from a sub-swath, the antenna is steered to record a burst from the next sub-swath. It results in an image with extensive spatial coverage and a moderate resolution (Torres et al., 2012).

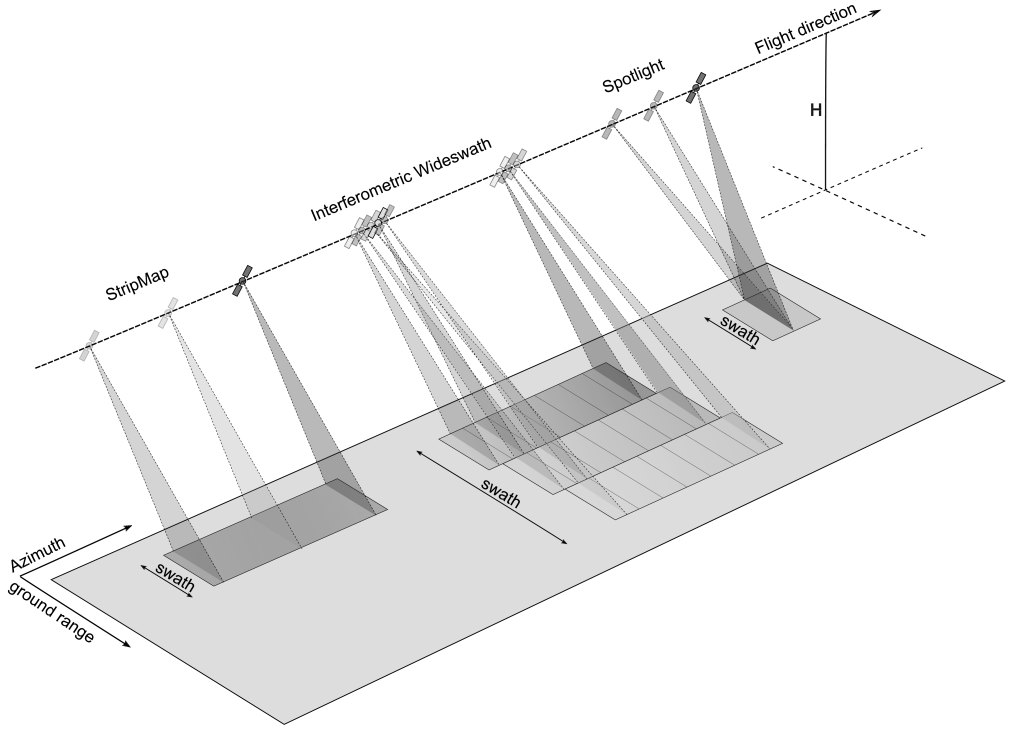


Figure 2.4.: Different image acquisition modes of satellite SAR sensors.

2.2.3. SAR Missions

Figure 2.5 shows an overview of the timeline, frequency band, and repeat cycle of most important SAR satellite missions. A rich archive of SAR data is available since the 1990s that is highly valuable for historical analysis. In particular, SAR data provided by ERS-1, ERS-2, and Envisat, the satellites

launched by European Space Agency, made InSAR widely applicable and boosted the development of InSAR techniques and time series analysis in the past years (Ferretti et al., 2001; Berardino et al., 2002). However, SAR data provided by those satellites were temporally sparse, and their coverage was limited to specific regions.

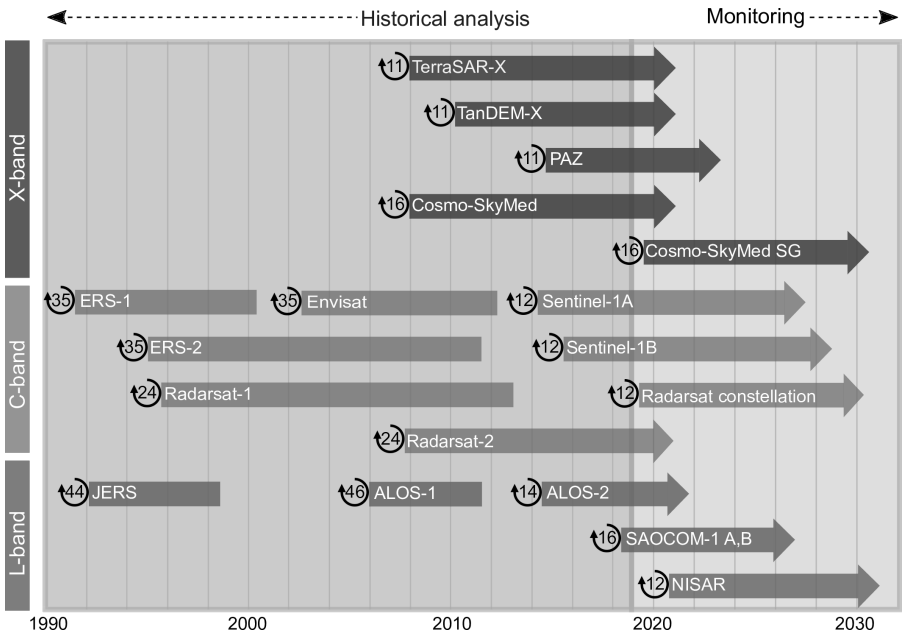


Figure 2.5.: Overview of main SAR satellite missions. The numbers indicate the repeat cycle of the satellites.

High-resolution sensors such as TerraSAR-X and Cosmo-SkyMed broadened the applications of InSAR in detailed displacement mapping particularly in urban and infrastructure monitoring (Perissin et al., 2012; Cigna et al., 2014). These sensors can be tasked to monitor specific areas with high spatial and temporal resolutions. In other areas, however, their background archive is very sporadic.

By the launch of Sentinel-1 in 2014, it has dramatically changed the availability of SAR data. It is the first mission specifically designed to be capable of SAR imaging suitable for InSAR applications. Sentinel-1 mission regularly acquires medium resolution data all over the world and is planned to continue at least for twenty years (Torres et al., 2012).

2.3. SAR Interferometry

2.3.1. InSAR Workflow

Using two SAR images acquired by a sensor from slightly different locations in space (Figure 2.6), it is possible to form an interferogram by subtracting the phases of the two images. The produced interferogram can be used for two major applications: topography mapping (Zebker and Goldstein, 1986; Rufino et al., 1998; Rossi et al., 2012) and displacement measurement (Gabriel et al., 1989; Amelung et al., 1999).

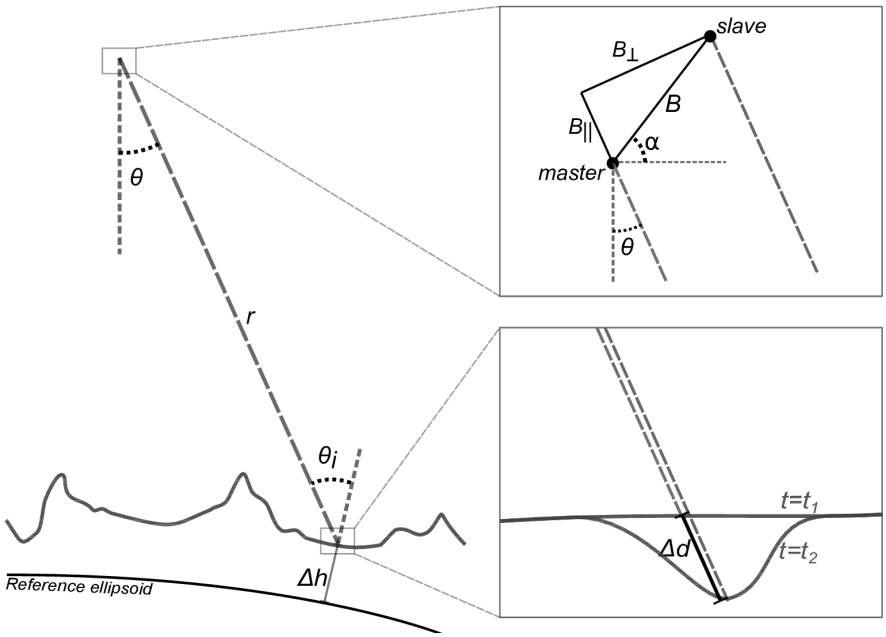


Figure 2.6.: Imaging geometry of InSAR in the plane normal to the flight direction. r is the distance between the sensor and the earth surface. θ and θ_i are the look angle and incidence angle respectively. B is the baseline between the sensor positions at the two times and can be decomposed into $B^{\perp}$ and $B^{||}$. Δd is the surface deformation occurred between the two times t_1 and t_2.

Figure 2.7 outlines the simplified workflow of Differential InSAR (DInSAR) to go from original SAR images to the displacement map. In brief, two SAR images are coregistered and resampled to form the interferogram. Then, flat-earth and topography components are removed from the interferogram, and the so called differential interferogram is generated. After filtering the differential interferogram, its wrapped phase is unwrapped and geocoded (Bürgmann et al., 2000). In the following, different steps of DInSAR workflow are described in more details.

Coregistration defines a mathematical transformation to align the slave image to the master image. Usually, a low order polynomial can accurately define the transformation model. The transformation parameters are calculated through the least-squares fit of the estimated shifts at different locations over the amplitude images. A coregistration assisted by Digital Elevation Model (DEM) can improve the accuracy (Nitti et al., 2011). Resampling applies the transformation model to slave image and aligns it so identical pixels from master and slave images coincide with each other.

Once the master and slave images are aligned, the interferogram can be generated by multiplying the master image with the complex conjugate of the resampled slave image. The interferometric phase ($\Delta\phi$) is the coherent sum of components from surface deformation ($\Delta\phi_{defo}$), flat-earth ($\Delta\phi_{flat-earth}$), topography ($\Delta\phi_{topo}$), atmosphere ($\Delta\phi_{atmo}$), and noise ($\Delta\phi_{noise}$) (Bamler and Hartl, 1998; Rosen et al., 2000; Bürgmann et al., 2000):

$$\Delta\phi = \Delta\phi_{defo} + \Delta\phi_{flat-earth} + \Delta\phi_{topo} + \Delta\phi_{atmo} + \Delta\phi_{noise} \tag{2.1}$$

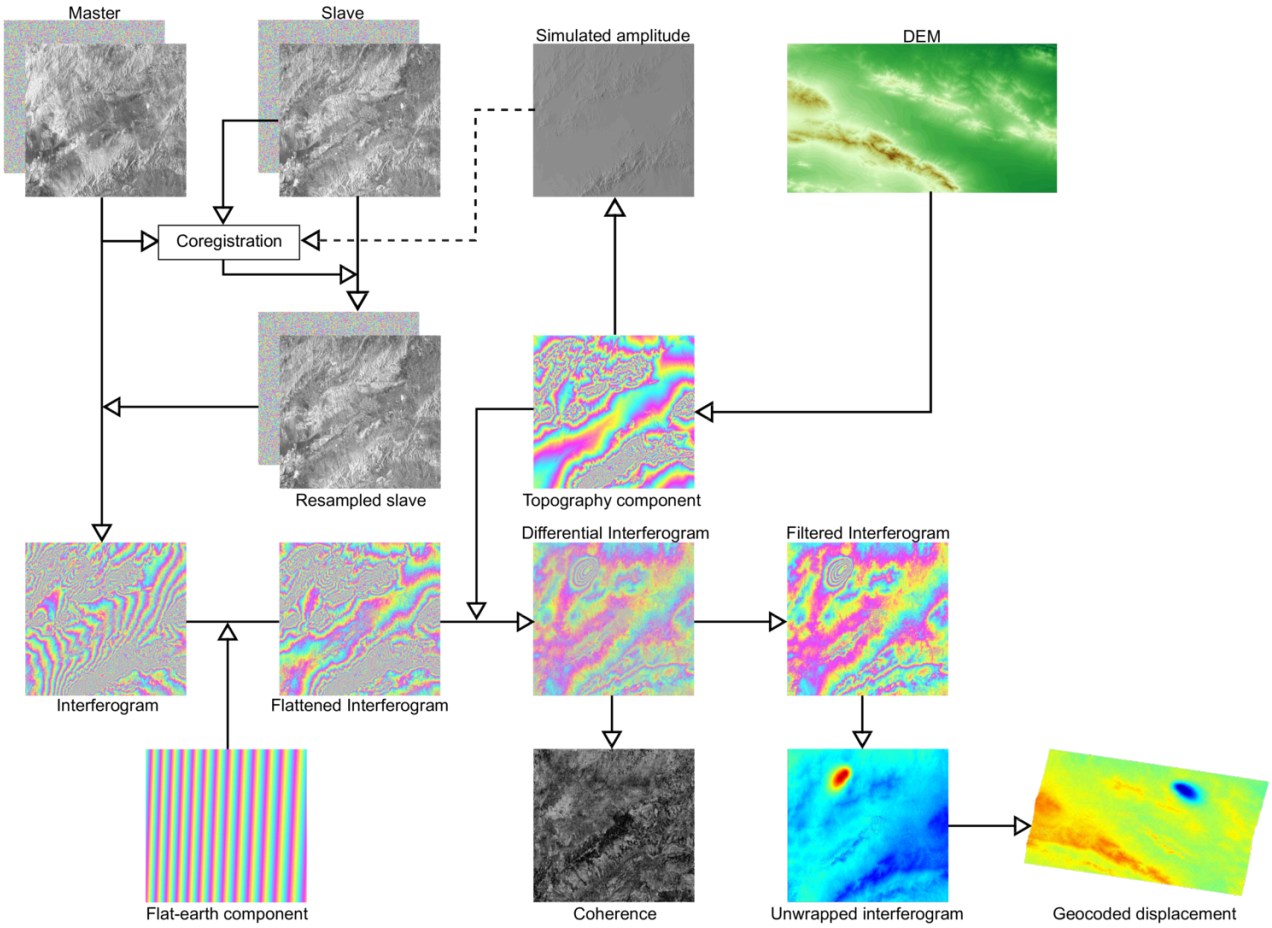


Figure 2.7.: Simplified workflow of DInSAR to go from original SAR images to the displacement map.

When the desired component is deformation, other components should be estimated and removed from the interferogram. The flat-earth and topography components are functions of the geometry of the sensor and earth model and can be estimated rigorously. The tropospheric component is either neglected or estimated using the interferometric phase itself or external atmospheric information. Finally, the remaining noise term is commonly neglected.

The flat-earth component depends on the relative geometry of the sensor at the two acquisition times and the shape of the earth. Therefore, using the precise orbital data and an ellipsoidal model for the earth, usually World Geodetic System 1984 (WGS84), it is possible to estimate and remove this component (Bamler and Hartl, 1998):

$$\Delta\phi_{flat-earth} = -\frac{4\pi}{\lambda} B^{||} \tag{2.2}$$

where λ is the wavelength of the SAR system and $B^{||}$ is the parallel baseline. The interferogram after removing the flat-earth component is so called flattened interferogram.

The topographic component of the interferogram is caused by the elevation of the earth surface from the assumed ellipsoidal model. Using an external DEM, this component is estimated and removed from the interferogram (Bamler and Hartl, 1998):

$$\Delta\phi_{topo} = -\frac{4\pi}{\lambda}\frac{B^{\perp}}{r\sin\theta_i}\Delta h \tag{2.3}$$

where Δh is the surface height from ellipsoid, $B^{\perp}$ is the perpendicular baseline of the interferogram, r is the distance between the sensor and the earth surface, and θ_i is the incidence angle. The interferogram after removing topography component is so called differential interferogram.

In contrast to flat-earth and topography components, phase contributions from the atmosphere cannot be rigorously estimated. Atmospheric phase delay is a function of physical parameters of ionosphere and troposphere layers. Because precise information on such parameters are not available neither in time nor in space, estimating atmospheric phase is challenging (Hanssen, 2001). The atmospheric artifact is discussed in more details later.

To reduce the noise phase, the interferogram is usually multilooked, which is a spatial averaging of neighboring pixels. Multilooking increases the signal to noise ratio by sacrificing the spatial resolution (Hanssen, 2001). Furthermore, the interferometric phase is filtered to reduce the effect of noise and increase the phase measurement accuracy (Goldstein and Werner, 1998).

After the unwanted components are removed from the interferogram, ignoring the remaining noise, it is assumed that the phase change is caused by surface deformation:

$$\Delta\phi_{defo} = -\frac{4\pi}{\lambda}\Delta d \tag{2.4}$$

where Δd is the surface deformation occurred between the two acquisition times. Because of the cyclic nature of the interferometric phase, only a modulo 2π of the phase values are known. Therefore, it is necessary to recover the integer phase-cycle ambiguity to obtain absolute values in a so called unwrapping process (Goldstein et al., 1988). Afterward, the unwrapped interferogram is geocoded to produce the displacement map.

2.3.2. InSAR Decorrelation

Decorrelation is a major source of noise in InSAR. The phase of master and slave images are correlated if the interaction of the radar echoes with elements within a resolution cell is similar for the two images. Assuming the thermal noise of the radar system is negligible, there are two sources of interferometric phase decorrelation. First, Significant change of scattering properties, e.g., because of dense vegetation or snow cover, causes temporal decorrelation. Second, slightly different viewing geometries of master and slave acquisitions cause a so called spatial decorrelation (Zebker and Villasenor, 1992).

The similarity of radar echos of master s_1 and slave s_2 acquisitions is usually estimated by coherence:

$$\gamma = \frac{|E[s_1 s_2^*]|}{\sqrt{E[s_1 s_1^*]E[s_2 s_2^*]}} \tag{2.5}$$

where * denotes the complex conjugate of a SAR image and $E[]$ is the mathematical expectation. In Practice, because we do not have repeated measurement to estimate the mathematical expectations, values inside a window around a pixel are used to estimate the coherence:

$$\hat{\gamma} = \frac{|\sum_{i=1}^{n} s_1^i s_2^{i*}|}{\sqrt{\sum_{i=1}^{n} s_1^i s_1^{i*} \sum_{i=1}^{n} s_2^i s_2^{i*}}} \tag{2.6}$$

It is common to remove the flat-earth and topography components before coherence estimation. An assumption in coherence estimation is that the pixels within the estimation window are statistically stationary (Zebker and Chen, 2005). To satisfy this hypothesis, all pixels within the coherence window should have the same scattering mechanisms.

2.3.3. Errors in InSAR

Atmospheric Error

Atmospheric artifact in InSAR consists of phase delays in ionospheric and tropospheric layers of the atmosphere. Ionospheric phase shift $\Delta\phi_{iono}$ is caused by variations of Total Electron Content (TEC) in the ionospheric layer of the atmosphere and can be approximated by

$$\Delta\phi_{iono} \approx 4\pi \frac{k}{c f_0} \Delta TEC \tag{2.7}$$

where ΔTEC is the TEC variations in slant direction between the two acquisition times, f_0 is the frequency of the traveling signal, c is the vacuum light speed, and $k = 40.3\ m^3/s^2$ is a constant (Fattahi et al., 2017).

Ionospheric phase change can be estimated and reduced based on internal information in the original SAR data (Jung et al., 2013; Gomba et al., 2016). The delay is proportional to the wavelength of the microwave signal and is severe at high latitudes and equatorial regions (Meyer, 2010). Therefore, the ionospheric artifact is usually neglected for shorter wavelength, i.e., C- and X-band, in mid-latitudes.

The interferometric phase delay due to troposphere $\Delta\phi_{tropo}$ is the difference between the two-way tropospheric propagation delays corresponding to the master ϕ^1_{tropo} and slave ϕ^2_{tropo} images:

$$\Delta\phi_{tropo} = \phi^1_{tropo} - \phi^2_{tropo} \tag{2.8}$$

The two-way tropospheric phase delay of a specific pixel is the integral of the refractivity N, which can be divided into wet and hydrostatic parts, between the height of pixel on the ground h_1 and top of troposphere h_{top}:

$$\phi_{tropo} = \frac{-4\pi}{\lambda} \frac{10^{-6}}{\cos\theta_i} \int_{h_1}^{h_{top}} (N_{hydro} + N_{wet}) dh \tag{2.9}$$

$$N_{hydro} = K_1 \frac{P}{T} \tag{2.10}$$

$$N_{wet} = K_2^{'} \frac{e}{T} + K_3 \frac{e}{T^2} \tag{2.11}$$

where P, T, and e are total atmospheric pressure, temperature, and water vapor partial pressure respectively and $k_1 = 77.6\ K\ hPa^{-1}$, $k_2^{'} = 23.3\ K\ hPa^{-1}$, and $k_3 = 3.75 \cdot 10^5\ K^2\ hPa^{-1}$ are empirical constants (Bekaert et al., 2015a). The hydrostatic part of troposphere depends on the temperature and total pressure, while the wet part depends on temperature and water vapor partial pressure (Delacourt et al., 1998).

Tropospheric delays are produced by three types of variations in tropospheric parameters. Figure 2.8 shows some examples of interferograms affected by these three types. The first type comes from the broad-scale lateral variations of troposphere (Figure 2.8-a). This type of tropospheric phase delay increases with relative lateral distance. In small interferograms, this effect is corrected by removing a low-order phase ramp. Alternatively, it is estimated using external tropospheric information like global weather models (Jolivet et al., 2011).

The second type of tropospheric artifact in the interferometric phase is caused by vertical variations of water vapor that produces topography-dependent atmospheric delays (Figure 2.8-b). This kind of atmospheric artifact is usually estimated empirically based on the correlation of the interferometric phase with topography or using global weather models (Jolivet et al., 2011).

Finally, short-wavelength turbulent troposphere causes another type of tropospheric delay which is highly variable both in space and time (Figure 2.8-c). Therefore, it is challenging to estimate this kind of tropospheric phase delay (Bekaert et al., 2015a). Reducing this kind of tropospheric delays needs atmospheric information with a high spatial and temporal resolution, for example from dense Global Navigation Satellite System (GNSS) networks.

Remaining DEM and Orbital Errors

As expressed in equation 2.3, the topographic component is proportional to the perpendicular baseline of the interferogram. Therefore, inaccuracies in the DEM appears as errors correlated with the perpendicular baseline:

$$\delta\phi_{topo} = -\frac{4\pi}{\lambda} \frac{B^{\perp}}{r \sin\theta_i} \delta h \tag{2.12}$$

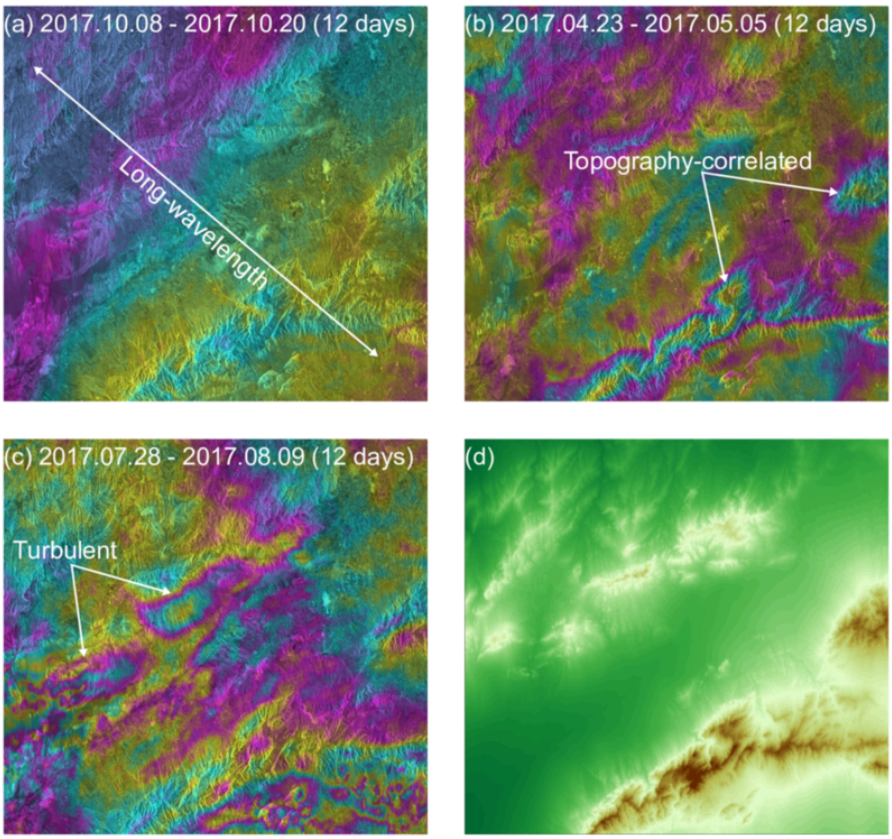


Figure 2.8.: Examples of tropospheric effect in different interferograms over a region in the northeast of Iran. All interferograms have 12-day temporal baselines, so it is expected that the magnitude of displacement is small and the interferograms are mostly affected by tropospheric phase delay. (a) the long-wavelength signal (diagonal from top left to bottom right) is caused by broad-scale lateral variations of the troposphere. (b) the topography-correlated fringes are caused by vertical variations of the troposphere. (c) short-wavelength fringes are caused by turbulent in the troposphere. (d) the topography of the area in the radar coordinate system.

where $\delta\phi_{topo}$ is the phase error caused by topography error $\delta\phi_h$. Significant errors in the DEM combined with large perpendicular baselines causes significant remaining topography errors. In case several images are available, by generating interferograms with different perpendicular baselines, it is possible to estimate the remaining DEM error through least square adjustment and correct the interferograms (Fattahi and Amelung, 2013). Because Sentinel-1 is specifically designed to collect SAR images suitable for DInSAR applications, its orbital tube is designed to be narrow. Therefore, the DEM error is less significant for Sentinel-1 in comparison to other sensors (Salvi et al., 2012).

Inaccuracies in the orbital estimation of the satellite results in errors in the estimation of the flat-earth component. Such errors usually appear as a linear trend across the interferogram and are commonly corrected by fitting a linear ramp to the phase change across the interferogram. For older satellites like ERS and Envisat, the ramps caused by orbital inaccuracies are common, but for modern satellites like TerraSAR-X and Sentinel-1, the orbital accuracy is usually enough for a precise estimation of flat-earth component (Fattahi and Amelung, 2014).

2.3.4. Examples of Interferograms

Figure 2.9 shows four examples of differential interferograms with different temporal intervals over a region in the northeast of Iran. The first example (Figure 2.9-a) is a 12-day interferogram with no significant displacement expected in this period. A long-wavelength trend in this interferogram is most likely occurred due to broad-scale lateral variations of the troposphere.

The second interferogram (Figure 2.9-b) covers a 96-day period. This time interval is enough to make localized displacement due to land subsidence visible. The third example interferogram (Figure 2.9-c), which covers 84 days, also shows the subsidence signal. However, Temporal decorrelation has occurred in some areas of the interferogram because of snow cover during the acquisition of 2017.02.22 image.

The last interferogram (Figure 2.9-d) covers a period of 360 days. During the period covered by this interferogram, the 2017.04.05 Mashhad earthquake (Mw 6.1) had occurred. The earthquake fringes are clearly observed in the interferogram. Because of temporal decorrelation due to vegetation cover, the subsidence fringes are obscured by noise.

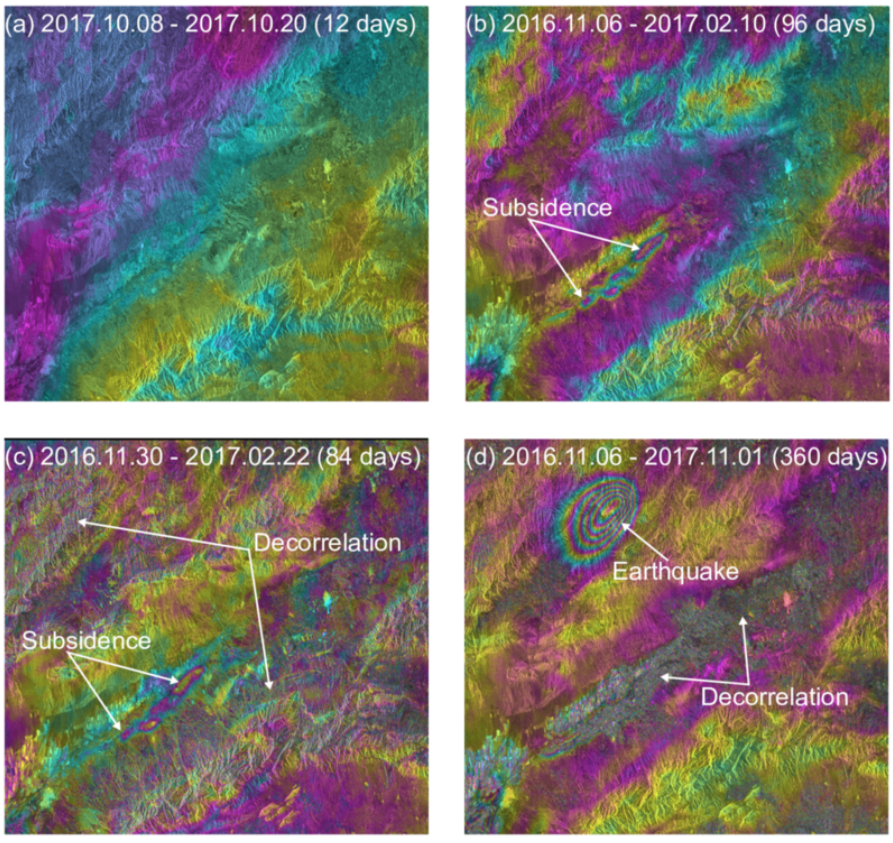


Figure 2.9.: Examples of interferograms with different temporal separations over a region in the northeast of Iran. (a) a 12-day interferogram does not show any specific deformation feature. (b) Land subsidence features are indicated in a 96-day interferogram. (c) 84-day interferogram exhibits subsidence features. Some areas of the interferogram are decorrelated because of snow cover in the 2017.02.22 image. (d) an approximately 1-year interferogram shows deformation caused by the 2017.04.05 Mashhad earthquake. The subsidence fringes are obscured by temporal decorrelation in the agricultural area.

2.3.5. Decomposition of Line-of-Sight Measurements

InSAR measures the projection of 3-D surface displacement vector on the 1-D line of sight (LOS) vector, which is the direction between the sensor and the ground pixel and is controlled by the incidence angle of the sensor and heading of the satellite. For a right looking sensor, which is the case for most current SAR satellite system, LOS measurement can be expressed as:

$$\Delta d = \begin{bmatrix} S_x & S_y & S_z \end{bmatrix} \begin{bmatrix} \Delta d_x & \Delta d_y & \Delta d_z \end{bmatrix}^T, \tag{2.13}$$

$$S_x = -\cos\alpha \sin\theta_i \qquad S_y = \sin\alpha \sin\theta_i \qquad S_z = \cos\theta_i \tag{2.14}$$

where Δd is the displacement of the target pixel in the LOS direction, S_x, S_y, and S_z are components of sensitivity vector which defines the sensitivity of LOS measurement to 3-D components of surface displacement (Δd_x, Δd_y, and Δd_z). α and θ_i are the heading and incidence angle of the satellite (Hanssen, 2001).

InSAR LOS measurement is highly sensitive to vertical displacement and the lower the incidence angle, the higher the sensitivity to vertical displacement. The SAR satellites travel in near-polar orbits and conduct measurements perpendicular to their orbits. As a result, the sensitivity of LOS measurements to surface displacement in the south-north direction is significantly lower than the east-west direction. Therefore, it is common to neglect the south-north component and estimate the other two components of displacement by combining the results from both ascending and descending tracks.

In certain cases, it is possible to assume that the displacement takes place in specific directions, particularly in landslide or land subsidence monitoring. In landslide monitoring, it is commonly assumed that the gravity-driven displacement occurs in the slope direction. Therefore, it is possible to estimate the movement direction from the DEM and convert 1-D LOS displacement to 1-D slope movement. In the case of land subsidence, it is common to neglect the horizontal movement and attribute the LOS measurement to vertical displacement. Then, it is possible to estimate the vertical subsidence from InSAR LOS measurements.

2.4. Multi Temporal InSAR

Conventional DInSAR is a powerful method to study large displacements caused by abrupt events like earthquakes. However, when the displacement is within the range of a few millimeters or centimeters, spanning a relatively long period of time, DInSAR approach faces some difficulties in retrieving the signal mainly because of phase decorrelation and atmospheric artifact. There are different methods developed to analyze the multi-temporal stack of SAR data to overcome the limitations of DInSAR and obtain the history of displacement.

Although they have significant theoretical and practical differences, the common goal of InSAR time series methods is to produce a record of displacement from a collection of SAR data in a few general steps. First, a stack of interferograms is produced. Then, coherent pixels are detected, and their

interferometric phases are connected in time to obtain the time series of displacement. Multi-temporal InSAR analysis approaches are categorized into two general categories: Persistent Scatterer InSAR (PS or PSI) and Small Baseline (SB or SBAS). Each of those categories is optimized for a specific type of scattering mechanisms in SAR images.

2.4.1. Scattering Mechanisms in SAR Images

The phase of a pixel in a SAR image is the coherent sum of wavelets from all scattering elements within the pixel (Figure 2.10). Random movements of those elements result in phase changes in repeated radar measurements. In an ideal case for InSAR, the pixel contains only one strong scattering element, e.g., a corner reflector. The level of phase noise for such pixel is very low, and the pixel's phase is coherent in any combination of SAR images.

In practice, a pixel might contain several scattering elements. If one of the scattering elements within the pixel dominates the other elements, it might preserve enough temporal phase correlation even in interferograms with long temporal and perpendicular baselines. Such a pixel is called a Persistent Scatterer (PS). Persistent scatterers are usually found in urban areas where buildings act as strong scattering elements. Detection of PS points is done at original image resolution, i.e. no multi-looking is applied to the interferograms when analyzing PS points because multi-looking adds more scatterers to a resolution cell (Hooper et al., 2012).

Persistent Scatterers are rare in natural lands where usually a pixel contains several comparable scattering elements. Such pixel is called a Distributed Scatterer (DS). As a result of random movements of the scatterers, the correlation of the pixel's phase decay quickly. Therefore, distributed scatterers only maintain enough correlation in short-baseline interferograms. It is common to enhance the signal to noise ratio of distributed scatterers by multilooking (Parizzi and Brcic, 2011).

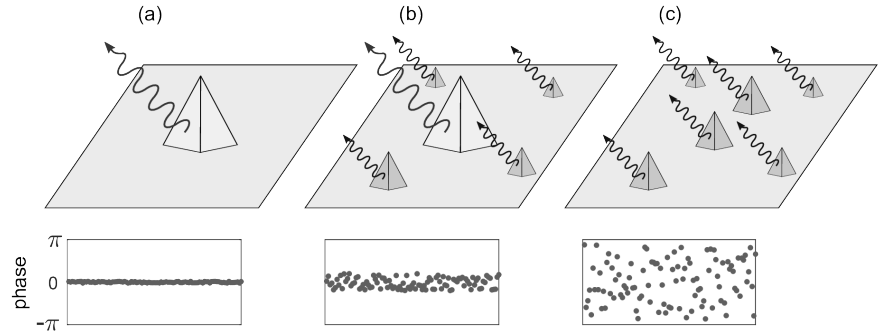


Figure 2.10.: Scattering mechanism for (a) an ideal single scatterer element, (b) a persistent scatterer element, and (c) a distributed scatterer and simulation of temporal phase variations corresponding to each of them.

2.4.2. Interferogram Stacking

Stacking is the simplest approach of multi-temporal InSAR that assumes a linear model for displacement and estimates the average rate of displacement from a collection of interferograms. To preserve

the phase correlation of distributed scatterers, the interferograms are generated using image pairs with short temporal and perpendicular baselines. Furthermore, the interferograms are multilooked to enhance the signal to noise ratio. The interferometric phase of a pixel in differential interferogram i can be expressed as (Hooper et al., 2004):

$$\Delta\phi^i = \Delta\phi^i_{defo} + \delta\phi^i_{orb} + \delta\phi^i_{topo} + \Delta\phi^i_{atmo} + \Delta\phi^i_{noise} \tag{2.15}$$

where $\delta\phi^i_{orb}$ and $\delta\phi^i_{topo}$ are the phase caused by errors in orbital data and remaining topography respectively. For pixel i in m sample interferograms, the linear rate of displacement $\hat{v}$ is:

$$\hat{v} = \frac{1}{m}\sum_{i=1}^{m}\frac{\Delta\phi^i}{B^i_T} \tag{2.16}$$

where B^i_T is temporal baseline of interferogram i (Wright et al., 2001). Stacking works when $\Delta\phi^i$ has a linear trend in time while other terms in equation 2.15 are stationary in time. Hence, averaging cancels out the random errors and preserves the linear trend of displacement. In reality, violation of this assumption can bias the estimated rate of displacement. Mitigating the errors from atmospheric phase delay, orbital inaccuracies, and remaining DEM, before averaging the interferograms increases the reliability of the estimated rate of displacement (Wang et al., 2009).

2.4.3. Persistent Scatterer InSAR

This approach finds persistent scatterers and performs time series analysis on their phases. Because persistent scatterers preserve a stable phase even in interferograms with large temporal and perpendicular baselines, one of the SAR images is selected as the reference. Then, all other images are resampled to the reference image and a star-like network of interferograms is generated (Figure 2.11-a).

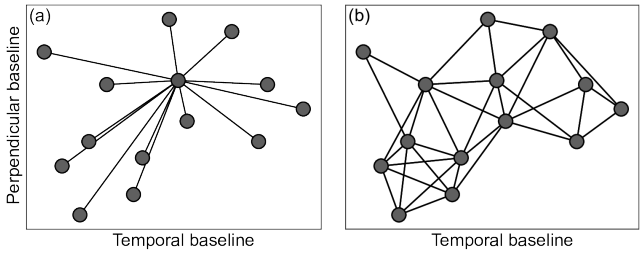


Figure 2.11.: An example of interferogram network in (a) Persistent Scatterer InSAR and (b) Small Baseline approaches. The circles and lines represent SAR images and interferograms respectively.

The key step in Persistent Scatterer InSAR is to find pixels containing persistent scatterers. Assuming that a PS pixel demonstrates a low amplitude variation through time, amplitude dispersion D_A can be used as a first order test to determine if a pixel is a PS:

$$D_A = \frac{\sigma_A}{\mu_A} \tag{2.17}$$

where σ_A and μ_A are standard deviation and average of amplitude values for a specific pixel in a stack of the interferogram (Ferretti et al., 2001). Once the initial set of PS candidates are selected, their temporal phase behavior is analyzed to estimate the noise level of each pixel. The final set of PS pixels is formed from the pixels that exhibit a subtle level of phase noise. To estimate the noise level $\Delta\phi^i_{noise}$, other phase contributions should be estimated and removed from equation 2.15.

There are two main approaches to estimate the noise level of a pixel. The first approach utilizes the double phase difference between neighboring PS candidates (Ferretti et al., 2001; Kampes, 2005). Because atmospheric and orbital errors are spatially correlated, they are removed in the double difference phase. DEM error is estimated from the correlation of phase with perpendicular baselines in the stack of interferogram. Finally, the displacement is estimated by using a predefined model, usually linear or sinusoidal. The remaining noise for double difference phases is adjusted to estimate the noise level of each pixel (Hooper et al., 2012). This method is mostly applicable in urban areas where many buildings act as stable scatterers. The main drawback of this approach is that it needs a predefined displacement model; deviations from the predefined displacement model cause falsely high estimation of noise, and hence less number of PS pixels are selected.

There is another approach to estimate the noise level in a stack of interferograms without any predefined displacement model (Hooper et al., 2004). In this approach, it is assumed that contributions from deformation, atmosphere and orbital error in equation 2.15 have low spatial frequencies and therefore are estimated by spatial filtering. The remaining DEM error which has a high spatial frequency can be estimated from its correlation with perpendicular baseline. After removing all these contributions, the noise phase is the only remaining component in equation 2.15. In comparison to the former methods, this approach provides a higher density of detected persistent scatterers in non-urban areas (Hooper et al., 2012).

Once the persistent scatterer pixels are selected, their phases are unwrapped and connected temporally to obtain the time series of displacement. Then, the unwanted components like tropospheric artifact are estimated and removed from the time series by spatial and temporal filtering. Furthermore, the remaining DEM errors are modeled and removed based on the correlation of unwrapped phases with perpendicular baselines.

2.4.4. Small Baseline InSAR

In Small Baseline approach, a network of interferograms is generated with short perpendicular and temporal baselines to minimize the spatial and temporal decorrelations of distributed scatterers (Figure 2.11-b). In this approach, the pixels are usually selected based on their coherence values. By setting a threshold, pixels with high coherence in a given percentage of interferograms are included in the processing (Berardino et al., 2002).

To increases the signal to noise ratio of phase values in the interferograms and hence the chance of finding reliable DS pixels, the SB interferograms are usually multilooked. However, multi-looking decreases the resolution of the interferograms and smears isolated coherent pixels surrounded by noisy pixels. To overcome this, a statistical phase analysis similar to Persistent Scatterer InSAR can be performed to select pixels at original interferogram resolution (Hooper, 2008).

After the reliable pixels are detected, their phases are unwrapped either in 2 dimensions in each interferogram independently or jointly using time as the third dimension (Berardino et al., 2002; Hooper, 2008). Then, the unwrapped displacement of different interferograms in the network are inverted to solve the displacement at each date. If $\Delta d_i^{t_1,t_2}$ is the displacement in ith interferogram between dates t_1 and t_2, a linear system with m equations corresponding to each inteferogram and n unknowns corresponding to each SAR date is formed for each pixel as follows:

$$A_{m,n}X_{n,1} = L_{m,1} \tag{2.18}$$

Where A is filled with -1 and 1 for elements corresponding to master and slave images respectively and 0 otherwise. L contains the displacement values of a pixel in all SB interferograms. X is the unknown displacement at each SAR date and is solved by minimizing the L_p norm of residuals:

$$\hat{X} = \arg\min \|L - AX\|_p = \arg\min \left(\sum_{i=1}^{m} |L - AX|_i^p \right)^{\frac{1}{p}} \tag{2.19}$$

A $L_2 - norm$ minimization provides the solution:

$$\hat{X} = (A^T A)^{-1} A^T L \tag{2.20}$$

After estimating the time series of displacement, as the final step of Small Baseline processing, DEM error is estimated by considering its correlation with perpendicular baseline and the atmospheric artifact is filtered out from the time series by spatial and temporal filtering.

2.5. Analysis of Displacement Time Series

Displacement time series obtained from Multi Temporal InSAR can be further examined to investigate significant temporal features and their link to their causes. Mathematical tools such as Fourier transform and Wavelet transform provide information about periodicities in the time series. The former method determines frequencies in a stationary time series but does not give information about the time of occurrence. In contrast, wavelet transform yields a time-frequency representation of the signal to detect periodicities and locate them in time.

Wavelet transform has been used extensively for decades in different geophysical applications (Foufoula-Georgiou et al., 1994; Chakraborty and Okaya, 1995; Martelet et al., 2001; Hetland et al., 2012). There are two classes of the wavelet transform. Discrete wavelet transform is mostly used in noise reduction and image compression, while Continuous Wavelet Transform (CWT) is used for feature extraction (Grinsted et al., 2004).

2.5.1. Continuous Wavelet Transform

Convolution of a time series (x_n, $n = 1, ..., N$) with a wavelet function $\psi_0(\eta)$ gives the continuous wavelet transform:

$$W_n^X(s) = \sqrt{\frac{\delta t}{s}} \sum_{n'=1}^{N} x_{n'} \psi_0 \left[(n' - n) \frac{\delta t}{s} \right] \tag{2.21}$$

where s is the scale that defines the width of wavelet and δt is the time step for sliding the wavelet along the time series. Morlet, one of the wavelet functions frequently used in geophysical applications is defined as:

$$\psi_0(\eta) = \pi^{-\frac{1}{4}} e^{i\omega_0 \eta} e^{-\frac{1}{2}\eta^2} \tag{2.22}$$

where ω_0 and η are the dimensionless frequency and time, respectively. The wavelet power spectrum $|W_n^X(s)|^2$ provides information on periodicities at different scales through the time (Torrence and Compo, 1998).

2.5.2. Cross Wavelet Transform

It is possible to jointly analyze time series x_n and y_n in time-frequency space to examine their relationship. Cross Wavelet Transform (XWT) of the two time series, defined as $W^{XY}(s) = W^X(s)W^{Y*}(s)$ where * represents complex conjugate, provides information on the link between the time series. XWT can be decomposed into amplitude and phase as:

$$W^{XY}(s) = \left| W^{XY}(s) \right| e^{i\Phi_j(s)} \tag{2.23}$$

where the amplitude $\left| W^{XY}(s) \right|$ represents the cross-wavelet power and the phase $\Phi_j(s)$ represents the time lag between two time series at different scales through time (Torrence and Compo, 1998; Maraun and Kurths, 2004).

2.5.3. Application of CWT and XWT to InSAR Time Series

The CWT and XWT can be applied to any time series that is evenly distributed in time; InSAR time series do not usually satisfy this rule, however. Therefore, before performing the time-frequency analysis, the displacement time series should be interpolated to uniformly-spaced intervals. Time series of other geophysical measurements such as rainfall and groundwater level should be interpolated to similar intervals. Applying CWT on the interpolated time series reveals periodicities at specific scale and specific time. Then, common frequencies and the time lag between the time series can be identified by XWT.

Chapter 3

Methodological Contribution

3.1. Introduction

Sentinel-1, launched in 2014, is the first SAR satellite mission to provide regular SAR acquisitions all over the globe. This mission is specifically designed to provide SAR data suitable for InSAR applications. Its moderate resolution and extensive coverage make it a great candidate for InSAR observation for many applications. Although Sentinel-1 offers a new opportunity for monitoring displacement regularly over broad areas, it brings new challenges that have to be addressed to be able to extract relevant information from the data.

There have been successful attempts in the past few years in order to adapt the already established InSAR processing methods, split the data into several chunks and process them in parallel. Such approaches can be implemented in cloud computing platforms to provide reliable results over extensive areas (Luca et al., 2017; Zinno et al., 2018). The main aim of this chapter is, however, to give a new undemanding workflow that benefits from the massive stream of Sentinel-1 data to effectively reduce the errors and provide reliable time series of displacement.

3.2. Challenges in Large-scale InSAR

There are several challenges in large scale InSAR analysis that need to be addressed. The first challenge is the large amount of data and the need for efficient workflows that are computationally affordable. Furthermore, the workflow should work with minimal operator interactions. It is not the case in many sophisticated approaches that need the operator to observe and control the processing chain carefully.

The second challenge of large-scale InSAR processing is to specify the appropriate reference area. InSAR measures displacement with respect to an arbitrary reference area. The reference is usually selected as close as possible to the region of interest, so the spatially correlated nuisance phases in the reference area are approximately similar to the region of interest. Therefore, subtraction of the reference area's phase removes parts of spatially correlated noises. As the distance between the reference point and the region of interest increases, the error propagated between them increases (Fattahi and Amelung, 2015).

External information from independent geodetic measurements can help a reliable selection of reference areas. In many cases, InSAR measurements are constrained by external measurements, e.g. from GNSS, but such information is not available in many areas. When such data are not available, it is common that the operator visually inspects the results and selects the reference point in an area close to the study area that is assumed to be free of displacement. However, visual inspection is time-consuming and inefficient as the scale of data grows. Therefore, an automatic selection of the reference area is needed in order to obtain homogeneous and reliable information.

Finally, the spatially propagated errors cause significant phase biases in the regions far from the reference area. The errors should be reduced as much as possible in order to obtain reliable displacements. Tropospheric artifact is the major source of error that biases the phase difference over the large distances. The relationship between phase and topography or external information such as

global atmospheric models have been widely used to correct the tropospheric artifact (Bekaert et al., 2015a; Cavalié et al., 2007; Elliott et al., 2008). Although they are proven to improve the results in many cases, the effectiveness of these approaches should be carefully investigated by the operator.

In the next section, a new method is proposed that filters out the tropospheric errors from large stacks of interferograms and highlights the local displacements over large areas. It works with minimal operator interaction and relaxes the need for specifying the reference area.

3.3. Proposed Method

In this section, a fast yet effective method is proposed for the detection and monitoring of local displacements over extensive areas. The proposed processing approach, which is described in the next section, takes advantage of the high temporal resolution of Sentinel-1 and forms a network of interferograms slightly different than the conventional Small Baseline approach. The workflow includes an adaptive tropospheric correction that also accounts for reference area selection. It rapidly calculates the linear rate of displacement from a large stack of interferograms and provides the time series of displacement for individual pixels.

Figure 3.1 outlines the main steps of the workflow proposed here for large-scale Sentinel-1 InSAR analysis in order to identify localized displacements and analyze their time series. The processing approach consists of two major steps. In the first step, a stack of interferograms is generated and unwrapped. In the second step, the interferograms are corrected and the displacement rate and time series of displacement are generated.

3.3.1. Interferogram Formation

In the first major step of the workflow, the stack of interferograms is generated. First, all frames of SAR images along a track of Sentinel-1 are concatenated to form long SLC images over the study area. Then, after selecting one of the acquisition dates as the reference, all images are coregistered to the reference image. The coregistration is performed using the spectral diversity methods (Scheiber and Moreira, 2000) to achieve an accuracy in the order of 1/1000 of the pixel size in the azimuth direction. All images are then resampled to the same reference image.

In the next step of the workflow, the interferometric pairs are selected, slightly different than in conventional Small Baseline network. In conventional Small Baseline InSAR, the network is formed based on constraints imposed on maximum spatial and temporal baselines (Berardino et al., 2002). Because the orbital tube of Sentinel-1 is designed to be narrow (Torres et al., 2012), it is possible to relax the constraint on the spatial baseline. Furthermore, in most parts of the world, Sentinel-1 mission acquires data in each track every 6 or 12 days that allows generating highly coherent interferograms. Hence, it provides the possibility to form flexible interferogram networks considering the characteristics of the study area and its displacement nature.

Here, two thresholds are set on the temporal baseline: The upper threshold, similar to conventional Small Baseline, is chosen to keep the level of temporal decorrelation low. The lower threshold is chosen

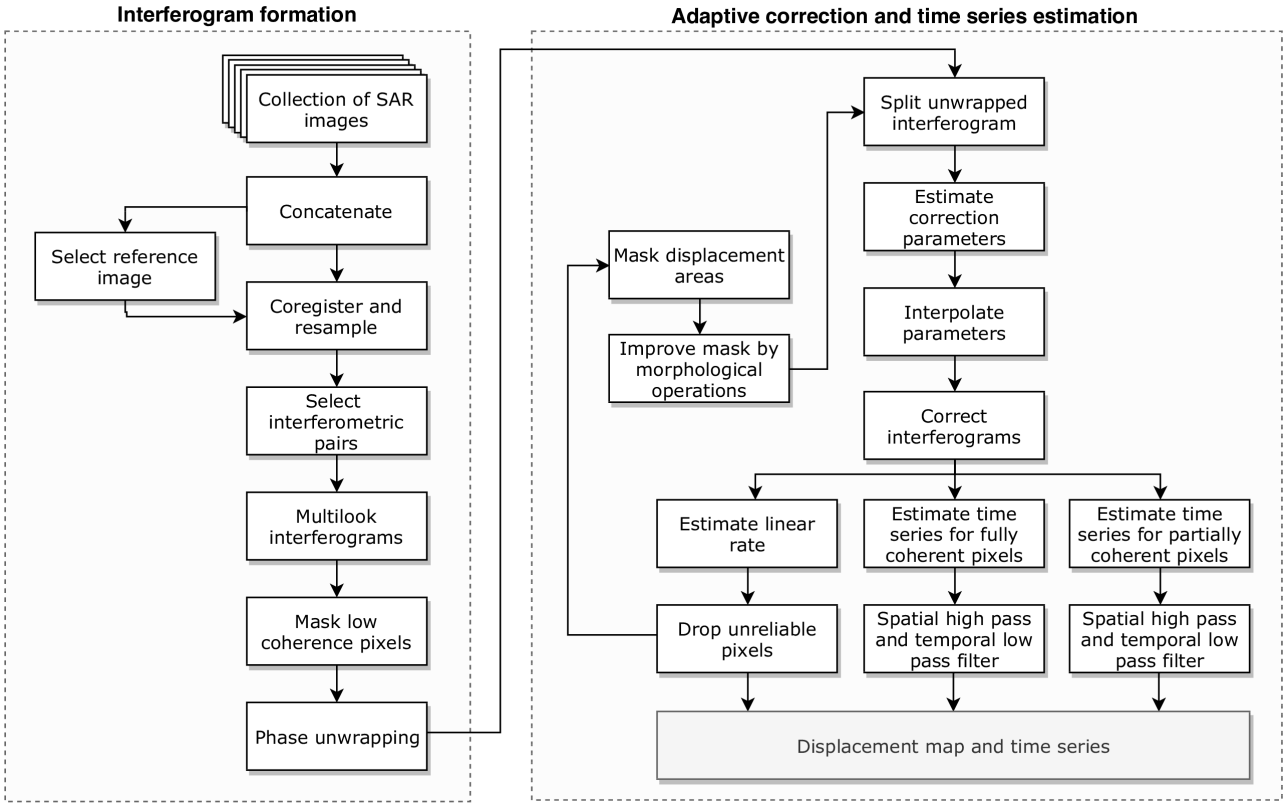


Figure 3.1.: Workflow of large-scale Sentinel-1 data processing to identify and analyze localized displacements.

to decrease the chance of displacement signals being obscured by errors. Although atmospheric artifact changes dramatically in different interferograms, its magnitude appears to be approximately similar at different temporal baselines. As a result, temporally correlated displacement is better visible in the long temporal-baseline interferogram.

After selecting the interferometric pairs, the interferograms are generated. Similar to conventional Small Baseline (Berardino et al., 2002), multilooking is applied to the interferograms. On the one hand, multilooking increases the signal to noise ratio and facilitates reliable 2-D unwrapping of the interferogram. On the other hand, it dramatically reduces the processing load. InSAR time series analysis and pixel selection at original resolution tend to be time-consuming and computationally expensive as the size of study areas and temporal resolution of the data increases. In contrast, for example, a multilook factor of 10x2 scales down the data by a factor of 20. When processing a large amount of data, it dramatically speeds up the processing.

The main drawback of multilooking is that it obscures the displacements that span spatial extent smaller than the multilooking window. Therefore, the size of multilook window should not be larger than the spatial wavelength of the desired displacement. In many applications, such as monitoring gradual land subsidence or large landslides bodies where the displacement changes smoothly over hundreds of meters, the signal is preserved in the multilooked interferogram.

The low coherence areas of the interferograms are masked to facilitate the unwrapping process and obtain reliable unwrapped interferograms. In conventional Small Baseline, the masked areas are

filled after unwrapping by interpolation (Berardino et al., 2002). However, in the natural terrain where large areas of interferogram exhibit poor coherence, filling the masked areas might introduce significant errors. To prevent the propagation of errors, in the proposed workflow, the masked areas are not filled.

3.3.2. Adaptive Correction of Interferograms

The second major step of the proposed workflow applies phase corrections to the interferograms and estimates the displacement rate and time series. Errors caused by stratified troposphere are commonly estimated by fitting a linear phase-topography model to the unwrapped phase (Cavalié et al., 2007; Elliott et al., 2008). However, this approach fails for large areas because the phase-topography correlation is spatially variable over large distances (Bekaert et al., 2015b). To resolve this issue, here, the interferograms are divided into several small windows, and the coefficient k is estimated for each window individually. A reference phase shift $k^{'}$ is also estimated for the unwrapped phase $\Delta\phi_{uw^i}$ at average altitude $\bar{h}$ of the window. Assuming there is no deformation component in the unwrapped interferogram:

$$\Delta\phi^i_{uw} = k(h^i - \bar{h}) + k^{'} \tag{3.1}$$

where h^i is the elevation of pixel i. Once the coefficients are estimated for every window, $\bar{h}$ and the estimated values of k and $k^{'}$ are assigned to the center of the windows and then interpolated to every pixel in the interferogram. A bicubic interpolation (Keys, 1981) is used to ensure the estimated parameters vary smoothly in space. The interpolated values are then used to correct the interferogram. The coefficient k accounts for the linear correlation of stratified troposphere and topography. The coefficient $k^{'}$ accounts for the broad-scale signals in the interferogram and is analogous to subtracting a high-order ramp from the interferogram.

The window size should be chosen carefully in order to have an unbiased estimation of the tropospheric phase and preserve the displacement signal. It should be small enough to sample the broad-scale tropospheric artifact and the spatial variations of the topography-correlated troposphere. However, too small windows would over-fit the phase and filter out displacements. A window size corresponding to approximately 25 km is used here.

Large-magnitudes displacements in the unwrapped interferograms biases the estimated coefficients of empirical atmospheric correction. Therefore, it is crucial to mask the areas of significant displacement before estimating the coefficients. An iterative approach is used to mask the displacement areas and improve the estimation of coefficients. In the first iteration, all pixels are used in the estimation. After correcting the interferograms and estimating the average velocities, an image thresholding filter is applied on the average velocity to classify the pixels into deforming and non-deforming. The threshold value should be chosen high enough, e.g., $2cm/yr$, to reliably separate displacement from background errors in the average velocity. Then, a morphological closing operator with a large kernel (e.g., 50 pixels) is applied to enhance the mask image and expand the identified areas to include

their neighboring pixels which have displacement smaller than the threshold. After masking out the displacement areas from the interferograms, the coefficients are estimated again, and the procedure is repeated.

After a few iterations, the unwrapped interferograms are reliably corrected for broad-scale and stratified troposphere. Turbulent part of the troposphere that has a smaller magnitude than the selected windows remain uncorrected. Assuming the remaining errors are stationary in time, averaging n interferograms decrease the error by a factor of $\sqrt{n}$.

3.3.3. Estimating the Displacement Rate

The rate of displacement is estimated by averaging the corrected interferograms weighted by their temporal intervals (Equation 2.16). In the conventional Small Baseline InSAR, areas with coherence higher than a threshold in a certain percentage, typically 30%, of interferograms are involved in time series analysis (Berardino et al., 2002). Here, pixels exhibiting a coherence lower than a threshold of 0.2 are masked out before unwrapping, and unlike the conventional Small Baseline, the masked pixels are not filled in. Therefore, in the estimation of average velocity, only pixels that exhibit valid unwrapped values in a specific percentage of interferograms are used.

Assuming a linear rate of displacement, averaging the interferograms allows dropping noisy interferograms on a pixel-wise basis and estimate the rates even for pixels that are incoherent in a subset of interferograms. Because of the high coherence of Sentinel-1 interferograms due to short temporal and perpendicular baselines, a threshold of 90-95% was found to result in a reasonable spatial distribution of pixels.

3.3.4. Estimating the Time Series of Displacement

Two sets of time series are estimated for pixels with different temporal coherence behavior. For pixels that exhibit high coherence in all interferograms, through a least-squares adjustment of the full interferogram network, the time series of displacement is estimated. For pixels that preserve coherence only in a partial set of interferograms, an individual network of interferograms is formed based on the partial set of coherent interferograms, analogous to the Intermittent SBAS (ISBAS) developed by Sowter et al. (2013). Then, the time series is estimated based on the partial network. For the calculated time series, the remaining tropospheric effect, particularly from turbulence part of the troposphere, is estimated by a low pass spatial filter followed by a high pass temporal filter and removed from the time series (Berardino et al., 2002).

Chapter 4

InSAR Monitoring of Localized Landslide in Taihape, New Zealand

This chapter was published as:
Haghshenas Haghighi, M., Motagh, M., 2016. Assessment of ground surface displacement in Taihape landslide, New Zealand, with C- and X-band SAR interferometry. New Zealand Journal of Geology and Geophysics 59, 136–146.

4.1. Abstract

In this study, we assess the capability of C-band advanced synthetic aperture radar (ASAR) data from Envisat and X-band Stripmap SAR from TerraSAR-X to analyse the extremely slow displacement rate of Taihape landslide in the central North Island of New Zealand. The small-baseline subset (SBAS) technique is applied to obtain displacement time series from SAR images between 2003 and 2011. Time-series results suggest that the landslide is active near its toe with maximum line-of-sight (LOS) surface velocity of 6 mm/yr between 2003 and 2010, derived from Envisat, and 8 mm/yr in the year 2010 to 2011, derived from TerraSAR-X. Comparing TerraSAR-X and Envisat results, the former detects approximately 15 times more coherent pixels for deformation analysis. Interferometric SAR (InSAR) displacement time series show a good agreement with field measurement from prisms installed on the surface of the landslide (maximum root-mean-square error or RMSE $<$8 mm). In addition to the long-term gravitational slope motion we also observe seasonal uplift and subsidence at the toe, which is attributed to surficial swelling and shrinkage of ground surface in response to cyclic variations in groundwater level.

4.2. Introduction

As a specific form of gravitational mass movement, landslides represent the geological phenomenon which refers to the downwards sliding of a mass of soil and rock material, mostly occurring on hillslopes in the forelands of mountainous regions dominated by weakly consolidated sediments. These events lead to large human and economic losses in the world every year (Petley, 2012).

Slow-moving landslides are widespread around the world in different geological and climate settings (Handwerger et al., 2013). Topographic setting, soil properties and groundwater condition are the key factors in the occurrence of slow-moving landslides (Ellen et al., 1995). Their kinematics seem to follow three different patterns: (1) fast displacement over periods of a few days to a few weeks; (2) constant slow displacement over periods of months to years; and (3) seasonal cyclic motion (Massey et al., 2013).

Monitoring of surface displacement in slow-moving landslides is a key in assessing their kinematic behaviour and mitigating hazards and damages associated with them (Rott et al., 1999; Froese CR, 2004). Traditionally, landslide monitoring has focused on using classical ground- and satellite-based surveying methods such as Global Positioning System (GPS), tacheometry and aerial photogrammetry (Gili et al., 2000; Delacourt et al., 2004; Chadwick et al., 2005; Baldi et al., 2008). However, technological improvements in the field of radar remote sensing over the last two decades have brought the addition of the relatively sophisticated geodesy and remote-sensing technique known as interferometric synthetic aperture radar (InSAR) to landslide monitoring (Kimura et al., 2000; Strozzi et al., 2005; Colesanti and Wasowski, 2006; Rott and Nagler, 2006).

InSAR involves the processing of radar images of the same area of Earth's surface acquired by the same antenna in space but from slightly different orbital positions at different times. The radar images are superimposed on each other and differenced in phase, allowing centimetre- to millimetre-scale changes in Earth's topography to be measured over time spans of days to years (Hanssen,

2001). The availability of sufficiently long time series of radar images, acquired as a result of missions such as European Remote Sensing (ERS) and Envisat, and the development of the multi-temporal interferometry methods such as persistent scatterer interferometry (PSI) and small-baseline subset (SBAS) further enhanced the capability of the InSAR technique in landslide investigation (Greif and Vlcko, 2012; Akbarimehr et al., 2013; Motagh et al., 2013; Wasowski and Bovenga, 2014).

In this work, we investigate the capability of C-band (wavelength ∼5.6 cm) and X-band (wavelength ∼3.1 cm) InSAR for monitoring surface deformation on Taihape landslide on the North Island, New Zealand. This landslide has been monitored since 1985 using classical geodetic measurements. Recent geodetic results suggest that the landslide displacement rate over the last two decades does not exceed 15 mm/yr (Massey, 2010). Based on (Cruden and Varnes, 1996), this landslide is classified as an extremely slow landslide.

We use C-band and X-band SAR data acquired by the European Space Agency (ESA) Envisat and the German TerraSAR-X satellites, respectively, and present the performance of these data for displacement monitoring at Taihape. We show that InSAR observations provide a clear presentation of the extremely slow motion at Taihape comparable to that depicted from available ground-based geodetic measurements. Finally, to better understand the dynamics of the landslide we perform a correlation analysis using a wavelet transform (Grinsted et al., 2004) to investigate the relation between changes in rainfall and groundwater levels, as the likely triggering factors, and landslide kinematics as derived from InSAR observations.

4.3. Study Area

Taihape landslide, located in the town of Taihape in the North Island, New Zealand, is a deep-seated translational landslide that was formed in Tertiary sediments of the Wanganui Basin. The top layer, formed from sandy Taihape mudstone, is superimposed on a layer of Tarare sandstone. Both top and underlying layers are early Pliocene marine sediments and classified in the *Field Description of Soil and Rock* (NZGS, 2005) as extremely weak to weak (Massey, 2010). The first activation of the landslide is suggested to have occurred ∼1.8–11 ka ago (Thompson, 1982).

The west side of Taihape town including 200 houses is built on the sliding slope, emphasising the importance of monitoring the dynamics of this landslide. Surface movement of the landslide has been monitored since 1984 using inclinometers. Since 2006, comprehensive geodetic measurements have been performed by GNS Science using a network of prisms measured by a robotic total station. Rainfall, ground-shaking intensity and groundwater levels have also been measured in the area (Massey, 2010).

The study area and its different sliding zones, slope and aspect maps are shown in Figure 4.1. Previous studies suggest that the lower and central parts of the slide are currently more active than the surrounding area. The toe zone is the most active area, with reported evidence of deformation such as tilted trees and hummocky ground and damage to manmade structures. The central zone is less active than the toe. Activity signs decrease from south to north. The marginal areas of the landslide are currently stable without obvious evidence of recent deformation (Massey, 2010).

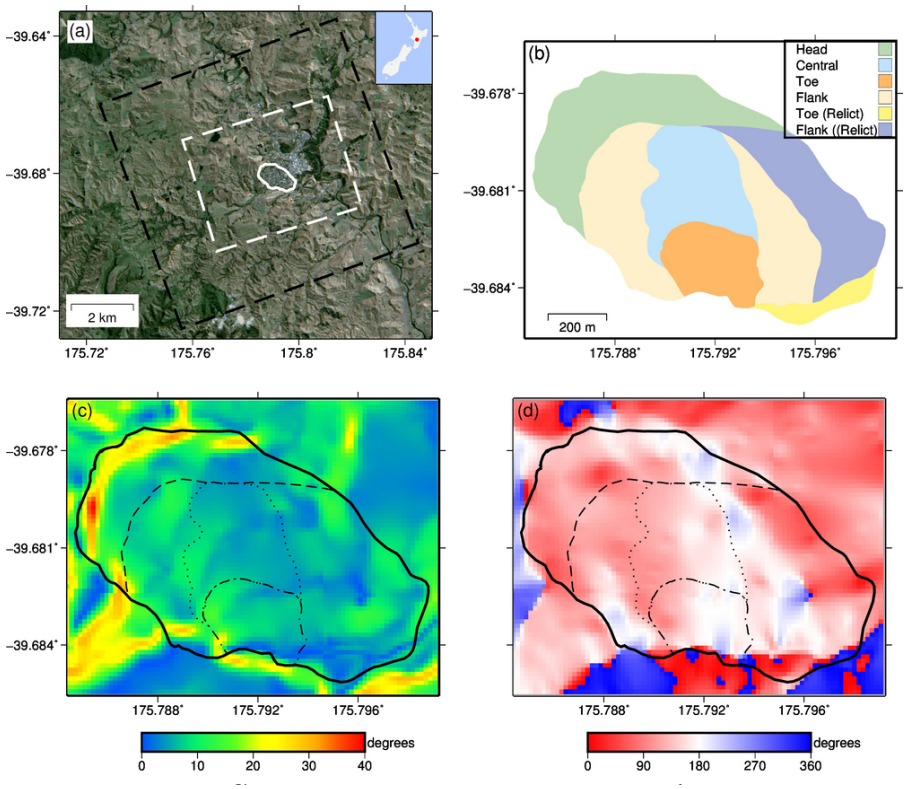


Figure 4.1.: (a) Study area with SAR frames. Black and white dashed boxes show the cropped area of Envisat and TerraSAR-X, respectively, used in InSAR processing. The white polygon is the Taihape landslide boundary, digitised from Massey (2010). Background image is a true colour composite of a Landsat 8 image acquired on 6 March 2014. The inset map shows the location of study area in New Zealand. (b) Different zones of Taihape landslide after Massey (2010). (c) Slope map. (d) Aspect map.

4.4. Methods

4.4.1. InSAR Measurement

The SAR data used for monitoring the Taihape landslide were acquired by Envisat and TerraSAR-X satellites. The C-band Envisat data consist of 31 ASAR images covering the period between August 2003 and May 2010, while the X-band TerraSAR-X data consist of 30 images in Stripmap mode (resolution ∼3 m) covering the September 2010–2011 time period. Figure 4.1 shows the location of study area as well as the cropped parts of Envisat and TerraSAR-X used for processing. The Landsat true-colour image in this figure shows that the area is vegetated, making the use of classical InSAR challenging (Rott and Nagler, 2006). However, the existence of manmade structures such as houses on the sliding slope has encouraged us to evaluate the performance of advanced InSAR time-series techniques.

The Envisat and TerraSAR-X images are both acquired in ascending geometries. The selection of ascending orbit is determined by analysing the sensitivity of InSAR line-of-sight (LOS) measurement to slope movement, which in the case of Taihape slope is higher for ascending orbits. The sensitivity analysis is discussed in more detail in the discussion section.

For the InSAR time-series analysis we used the SBAS method that utilises all possible interferograms with short spatio-temporal baselines to create a network of connected interferograms. The interferometric processing of SAR data was performed using Doris software (Kampes et al., 2003) with a 3 arc-second Shuttle Radar Topography Mission (SRTM) digital elevation model (DEM) (Farr and Kobrick, 2000) used to compensating for DEM contribution from the interferograms. For the Envisat imagery, precise orbital data provided by ESA were used for the processing.

Having created a network of connected interferograms with proper temporal and perpendicular baselines, SBAS time-series analysis was performed using Stanford method for persistent scatterers (StaMPS) software (Hooper et al., 2012). The important parameters tuned in the software are listed in Table 4.1. The StaMPS algorithm identifies coherent pixels for the time-series analysis in two steps: (1) an initial set of coherent pixels is detected by analysing the amplitude dispersion of each pixel in all interferograms (Ferretti et al., 2001); and (2) in a more sophisticated approach, the interferometric phase of the pixels is analysed, signal-to-noise ratio (SNR) estimated and pixels with high SNR are detected (Hooper, 2008). After detecting coherent pixels, the interferograms are unwrapped in space and time using a three-dimensional unwrapping approach described by (Hooper and Zebker, 2007). Finally, using a least-squares estimation, the time series of displacement is estimated from the network of unwrapped interferograms (Akbari and Motagh, 2012).

Figure 4.2 shows the final plot of temporal baselines versus perpendicular baselines for the two SBAS networks used for the time-series analysis in this study. Lists of produced interferograms are provided in the Tables 4.2, 4.3. The maximum perpendicular baseline of produced interferograms from the Envisat and TerraSAR-X dataset are 530 m and 200 m, respectively. The maximum time interval of the interferograms is 735 days for Envisat and 143 days for TerraSAR-X.

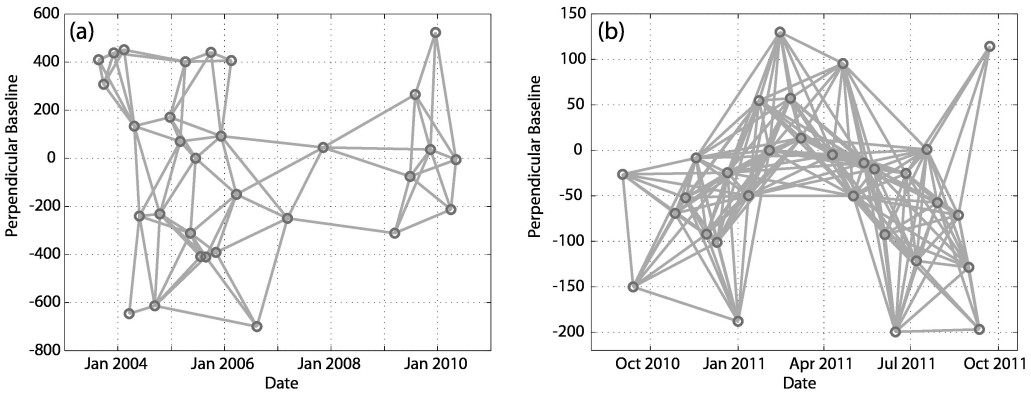


Figure 4.2.: Temporal baselines versus perpendicular baselines (in meters) for (a), Envisat and (b), TerraSAR-X SBAS networks.

4.4.2. Ancillary Data

In order to assess the quality of the InSAR analysis and interpret the results we use some ancillary data that were acquired in the region. Between 2006 and 2011, a comprehensive analysis of surface displacement was performed by GNS Science using a network of 35 prisms on Taihape slope. The 3D movement of the prisms was measured by an automated total station instrument. In addition, data on

rainfall, ground-shaking intensity and groundwater levels were also recorded in the area. Groundwater levels were measured over the same time period as the prism measurements; five piezometric wells on the landslide body recorded the groundwater level on an hourly basis. Daily precipitation was measured at the location of two of the piezometric wells on the slope. However, the rainfall record was not complete; there were some missing data with a maximum gap of 24 days. We therefore used the continuous rainfall record of Taihape Rec station (from www.niwa.co.nz) that had no missing values for the time period covered by the Envisat data. This station is located next to the landslide and its rainfall measurement is not significantly different from the data recorded by GNS Science.

4.4.3. Cause-Effect Analysis

To better interpret InSAR results and find the relationship between the derived displacement and the likely triggering factors (i.e. rainfall/groundwater levels), we used continuous wavelet transform (CWT) analysis (Torrence and Compo, 1998). Wavelet transform has been used extensively for decades for different applications of geophysical data (Foufoula-Georgiou et al., 1994; Chakraborty and Okaya, 1995; Martelet et al., 2001; Hetland et al., 2012). It provides a time-frequency representation of the signal to detect periodicities in the data as well as their time of occurrence. Grinsted et al. (2004) developed a method called cross wavelet transform (XWT) that addresses the correlation between two time series by analysing their corresponding CWTs. XWT detects areas with high common power in both CWTs and also provides information about their phase relationship.

The CWT and XWT tools can be applied to any time series that is evenly distributed in time; InSAR time series do not usually satisfy this rule, however. In this study we took the lead from Tomás et al. (2015) and performed a linear interpolation of InSAR results to uniformly spaced time intervals, allowing us to use wavelet transform tools and analyse the time series of surface displacement against the time series of rainfall and groundwater level.

4.5. Results

4.5.1. Small-baseline Interferograms

Some examples of C-band and X-band interferograms used in our analysis are shown in Figure 4.3. The figure shows that interferograms of both datasets generally have fair qualities in the urban area of Taihape town. In other regions, however, the coherence of interferograms is low because of temporal decorrelation, mainly caused by high vegetation. The coherence loss in vegetated areas is severe in interferograms with large temporal baselines.

A visual inspection of interferograms shows that TerraSAR-X interferograms have better qualities than Envisat interferograms, mainly because of their shorter time intervals and higher spatial resolution. Due to the slow rate of deformation, no clear pattern of displacement is observable in interferograms with short temporal baselines. Some long-wavelength patterns can be observed in some of the interferograms, which are most likely related to atmospheric artefacts (Li et al., 2006).

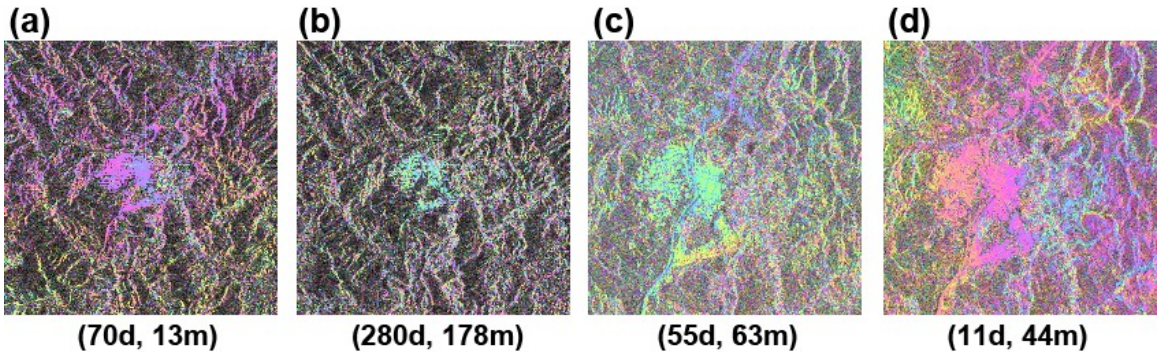


Figure 4.3.: Examples of C-band (a, b) and X-band (c, d) interferograms over Taihape. Time interval and perpendicular baseline of the interferograms are also shown in the figure. It should be noted that the areas covered by Envisat and TerraSAR-X interferograms are different (see Figure 4.1).

4.5.2. Time-series Results

Figure 4.4 shows the average velocities estimated from the SBAS time-series analysis of Envisat and TerraSAR-X datasets. An area with a radius of 150 m outside of the landslide boundary is defined as the reference area for InSAR analysis. Approximately 450 coherent pixels were detected by Envisat within the landslide boundary. TerraSAR-X data resulted in a much denser picture of the displacement field, with about 6500 coherent pixels in the landslide area. The main reason for this is that the TerraSAR-X images have higher spatial resolution and a shorter acquisition interval between consecutive images, resulting in higher interferometric coherence and a better quality of interferograms (Shamshiri et al., 2014; Singleton et al., 2014). Most of the detected pixels in both datasets are in the urban area, where buildings act like persistent/permanent scatterers. Other regions are highly vegetated and neither Envisat or TerraSAR-X were successful in detecting coherent pixels there.

The magnitude of average velocities derived from both TerraSAR-X and Envisat are less than 10 mm/yr in the LOS direction. The standard deviations of all pixels outside of the sliding area, calculated as a measure of precision of InSAR velocities, are 0.7 mm/yr and 1.7 mm/yr for Envisat and TerraSAR-X, respectively.

Displacement time series for some specific points are also shown in Figure 4.4. The plots in Figure 4.4c, d show the displacement time series of a point near the toe area, where the landslide is active. From examination of the trend line (red dashed line), the Envisat time series implies a long-term displacement of about 30±3 mm over a time period of 7 years between 2003 and 2010 and the TerraSAR-X time series show a displacement of about 8±1.5 mm in the year 2010–2011.

The plots in Figure 4.4e, f correspond to a point in the central part of the landslide where the landslide is not active. Both Envisat and TerraSAR-X displacement time series at this point show no significant displacement.

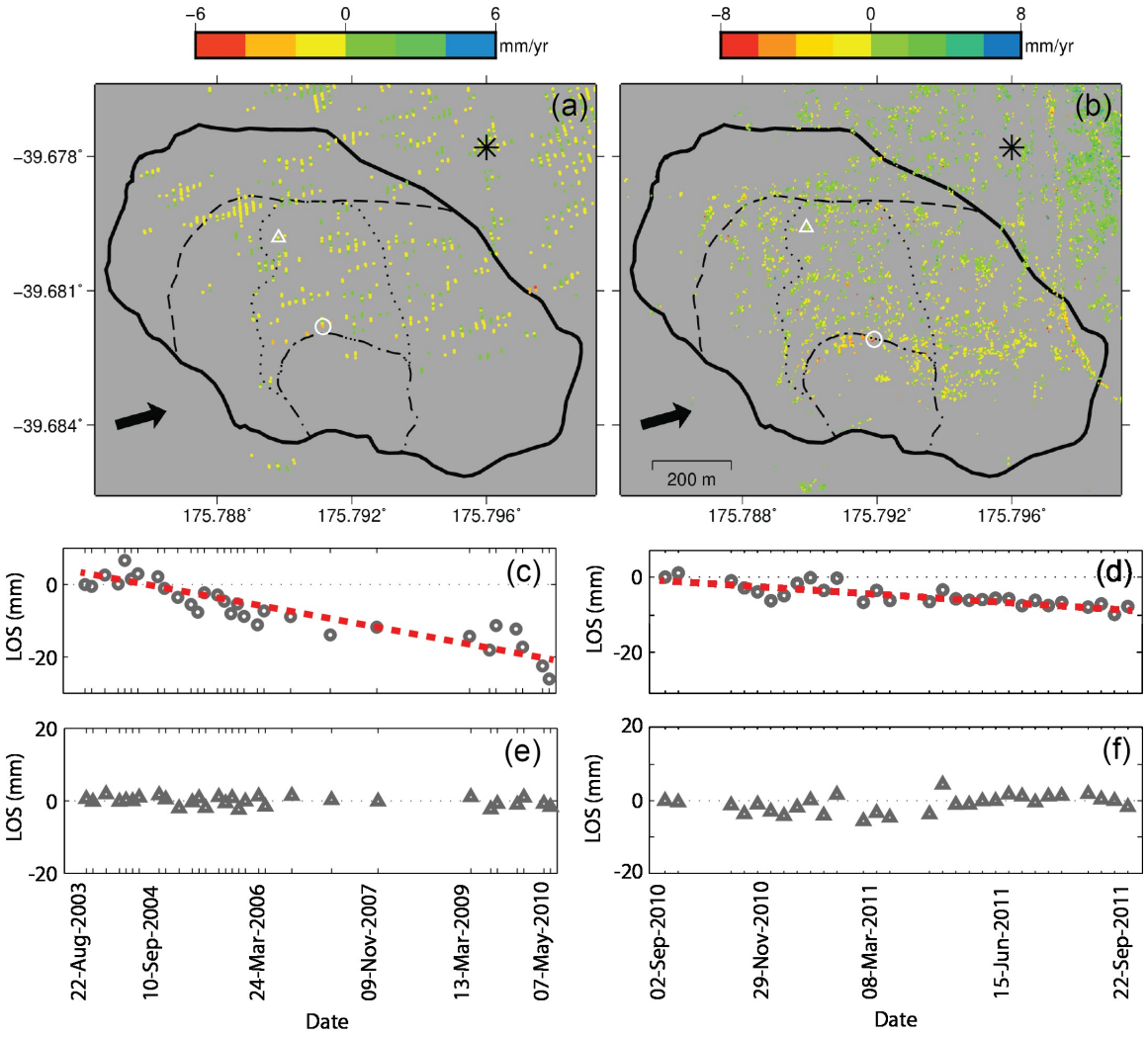


Figure 4.4.: Average annual rate of displacement derived from SBAS analysis of (a), Envisat and (b), TerraSAR-X. Values are in satellite LOS direction. Black polygon shows the landslide boundary. Dashed, dotted and dash-dotted lines indicate the boundaries of head, central part and toe of the landslide, respectively (digitised from Massey (2010)). Black arrow represents the LOS directions. InSAR reference point is shown by the star. (c), Envisat and (d), TerraSAR-X time series for a point near the toe. Dashed red line delineates the trend of displacement derived from InSAR. (e), Envisat and (f), TerraSAR-X time series for a point in the central part of the landslide.

4.6. Discussion

4.6.1. Suitability of InSAR Measurements for Monitoring the Taihape Landslide

InSAR provides a 1D measurement in the LOS direction from the satellite to the ground, defined by incidence and heading angles for Envisat and TerraSAR-X SAR images. It is therefore not possible to directly measure 3D displacement from InSAR measurements that have been made from a single geometry. On the other hand, landslide movement is gravity-driven. It is therefore controlled by the geometry of the slope and assumed to be mainly in the slope direction. To assess the suitability of InSAR for monitoring slope movement in Taihape, we estimate the sensitivity of InSAR LOS

measurement to slope movement. For a sensor with an incidence angle of θ and heading of α, sensitivity s can be derived from Equation (4.1) for every point on the ground (Cascini et al., 2010).

$$s = \begin{bmatrix} \sin(u) & -\cos(u)cos(v) & -\cos(u)sin(v) \end{bmatrix} \begin{bmatrix} \cos(\theta) \\ \sin(\alpha)\sin(\theta) \\ -\cos(\alpha)\sin(\theta) \end{bmatrix} \tag{4.1}$$

where s is sensitivity of LOS measurement to slope movement for a certain point with slope and aspect values equal to u and v. The greater the absolute value of s, the greater the sensitivity of LOS measurement to slope movement and therefore the ability to monitor the slope movement using InSAR.

In order to perform the sensitivity analysis, a 15 m DEM (Columbus et al., 2011) is used to calculate slope and aspect parameters for every pixel on the ground. Using the values of incidence and heading angle of the satellites, sensitivity of LOS measurement to slope movement is calculated for each pixel of the DEM. Satellite imaging geometry of both datasets are slightly different with heading and incidence angle of about 345°and 21°, respectively.

Estimated sensitivity and its histogram are shown in Figure 4.5. Values near zero show low sensitivity, indicating that the SAR data used in this study are not suitable for monitoring slope movement at those locations. Values close to 1 or –1 have a high sensitivity of LOS to slope movement, implying that slope movement at these locations can be measured perfectly by InSAR. The histogram of sensitivity indicates that the geometry of the SAR imagery is suitable for the measurement of slope movement for a large portion of the slope. In particular, most parts of the head area have high values of sensitivity. However, few pixels were detected by InSAR in this region because of dense vegetation cover. Sensitivity value in some parts of the toe and central zone (the eastern part of them) is very low, so it is difficult to estimate the slope movement by InSAR in these areas even if InSAR detects coherent pixels in such regions.

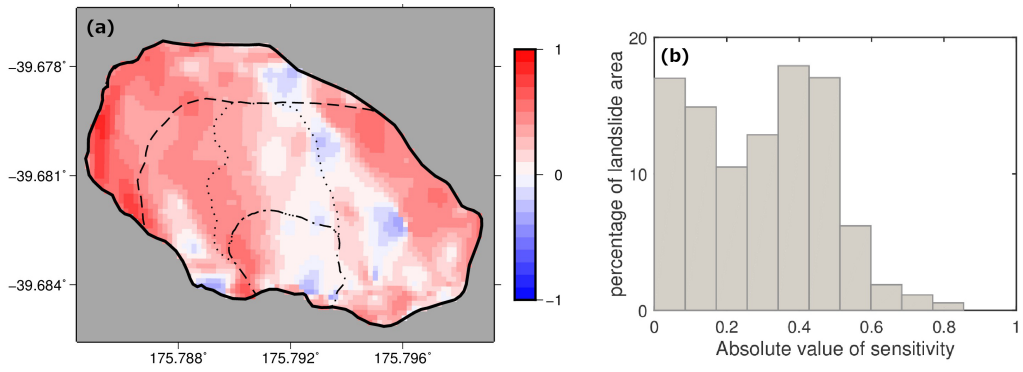


Figure 4.5.: (a), Sensitivity of LOS measurement of Envisat and TerraSAR-X satellites with $\theta = 21°$ and $\alpha = 345°$ to slope movement in Taihape landslide. Dashed, dotted and dash-dotted lines indicate the boundaries of head, central part and toe of the landslide, respectively (digitised from Massey (2010). (b), Histogram of sensitivity in landslide area.

4.6.2. Interpretation of InSAR Results

Envisat time-series results cover a longer period of time as compared to TerraSAR-X results; the former can therefore monitor the long-term gravitational motion better than the latter. TerraSAR-X images cover a time period of only 1 year but with a higher temporal sampling in time. As a result, they can better illustrate short-term temporal fluctuations in surface deformation.

As seen in Figure 4.4, InSAR measurements are not evenly distributed over the sliding slope. The head of the landslide is highly vegetated and only a few pixels have been detected in this area. The central part of the landslide is well covered by InSAR points, especially in TerraSAR-X results, because of artificial structures such as buildings which act as persistent scatterers. However, the results do not show any significant displacement in these areas (Figure 4.4).

It has been discussed in the literature how the toe of the landslide is the most active part the slope (Massey, 2010). Because of vegetation coverage in this area and a lack of manmade structures, InSAR failed to detect a good distribution of coherent pixels there. However, some pixels are detected in the northern parts of the toe by TerraSAR-X which show a small but clear anomaly (about 8 mm/yr displacement away from the satellite). Envisat data analysis detected only a few pixels around the top of the toe. However, they show the same anomaly as TerraSAR-X results (about 4 mm/yr, displacement away from the satellite). InSAR time-series results confirm the meaningful trend of displacement at the top of the toe and the stability of other regions.

4.6.3. Comparison with Ground Truth

The analysis of the surface movement of prisms between 2006 and 2009 by Massey (2010) shows that of 35 prisms, 8 are located in the toe of the landslide and show meaningful landslide-related movements (the location of prisms is shown in Figure 4.6; those with significant motion are indicated by black solid circles). As shown in Figure 4.4, average velocities derived from TerraSAR-X and Envisat also show an anomaly near the location of prisms with meaningful displacement.

To assess the reliability of the InSAR results, the time series of displacement derived from Envisat and TerraSAR-X are compared to prism measurements (Figure 4.7). For each prism location, the time series of all pixels derived from InSAR within a radius of 20 m is averaged. We should stress that the analysis is only performed for those prisms in which both Envisat and TerraSAR-X detected at least one coherent pixel in their vicinity (20 m).

InSAR results are in the LOS direction, but prism measurements are three-dimensional. To be able to compare the results, prism measurements are converted to LOS direction and then compared with the InSAR time series. Because of a high fluctuation of daily prism measurements, a moving average filter with a 21-day kernel is applied to the time series. Moreover, there is a gap in prism measurements between 7 December 2009 and 9 March 2010. Between these two dates a large jump, probably caused by a systematic measurement error, was observed in all the prism time series; this was corrected before comparison with InSAR. Furthermore, for each time series the shift between prism measurement and

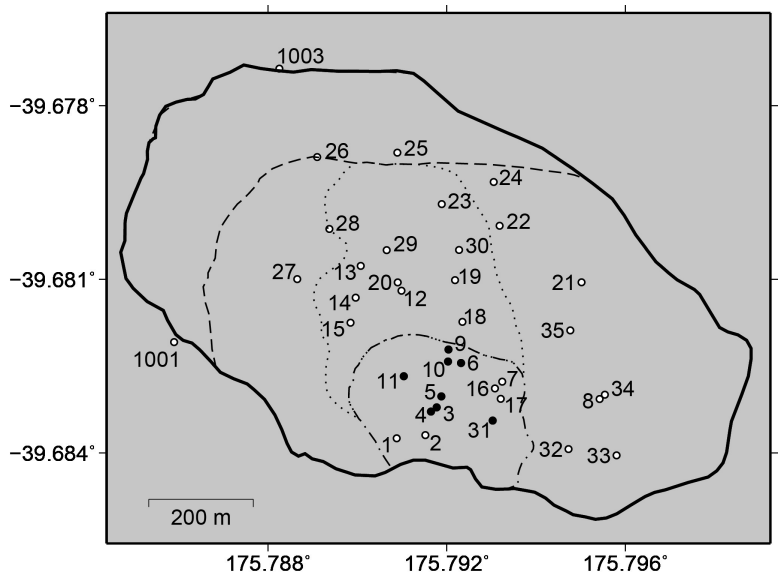


Figure 4.6.: Location of prisms for movement analysis. Prisms that are suggested to have meaningful displacement by Massey (2010) are filled with black colour. Dashed, dotted, and dash-dotted lines indicate the boundaries of head, central part and toe of the landslide, respectively (digitised from Massey (2010).

InSAR time series is removed by calculating the average of differences for the dates in which field measurement and InSAR result are both available.

The root-mean-square error (RMSE) of difference between field measurements and InSAR time series is calculated for each time series. Maximum RMSE of the time series is 8 mm for Envisat and 4 mm for TerraSAR-X. These RMSE values demonstrate the capability of the C-band and X-band InSAR time-series analysis to provide information on surface displacement at Taihape with a sub-centimetre accuracy.

4.6.4. Comparison with Rainfall and Groundwater Level

To analyse temporal variations of slope motion, CWT is applied to Envisat time-series results. We selected a point near the toe of the landslide (the time series of this point is indicated by a circle in Figure 4.4) and first removed a linear trend from the time series. Interpolation to an evenly distributed grid (35 days) is then applied, followed by the CWT analysis (Tomás et al., 2015). The result is shown in Figure 4.8. Two different frequencies are evident in the wavelet spectrum of InSAR time series: a 1-year cycle for the entire time interval and a period of less than 1 year varying roughly between 2004 and 2007. To better understand the reasons for these main frequencies, we also applied CWT to rainfall- and groundwater-level time series.

The CWT result on rainfall data (Figure 4.9a) for the same time interval as covered by the InSAR time series is presented in Figure 4.9b. The result shows a period of $<$200 days in rainfall wavelet spectrum in 2004. We interpret this frequency as being related to the Manawatu rainstorm (Hancox and Wright, 2005). During this storm the highest daily rainfall in Taihape was recorded on 16 February 2004 and a large part of the toe of Taihape landslide was removed by flooding caused by the storm

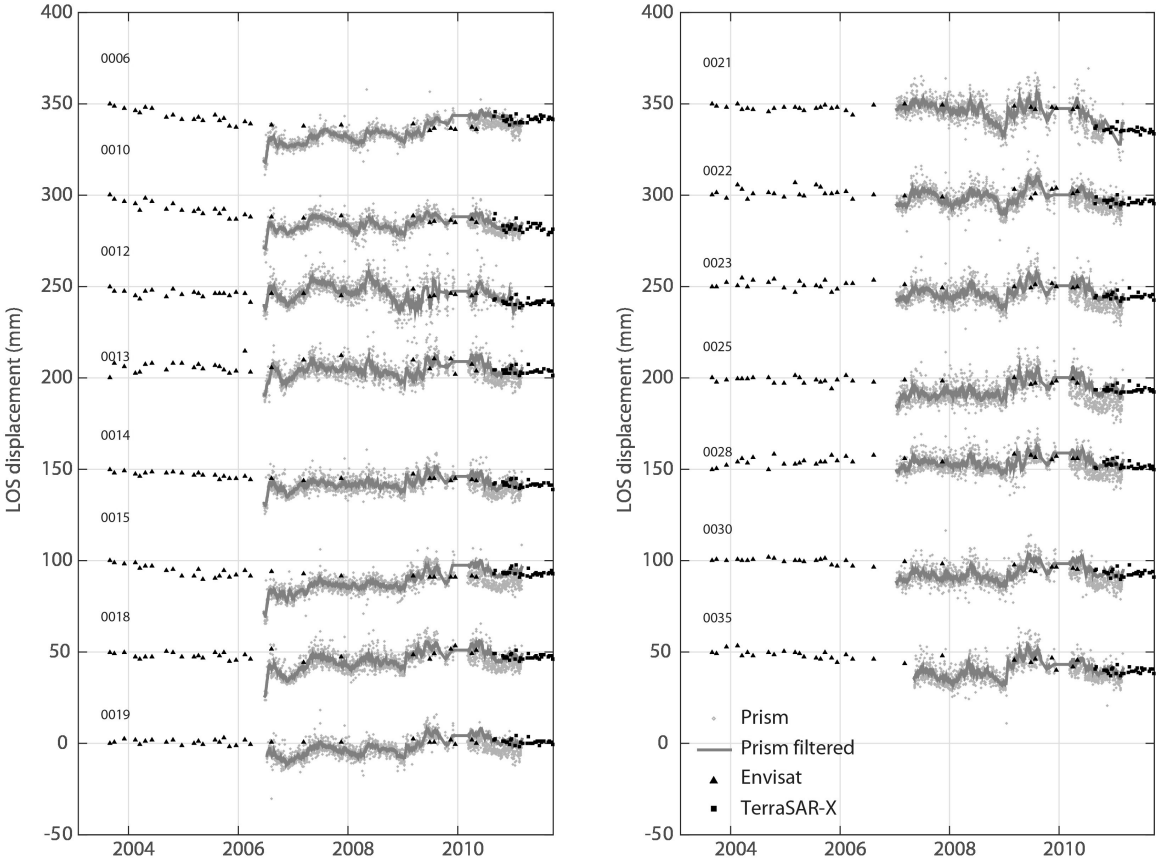


Figure 4.7.: Comparison between prism measurements and InSAR time series derived from Envisat and TerraSAR-X datasets. All values are in satellite line-of-sight direction.

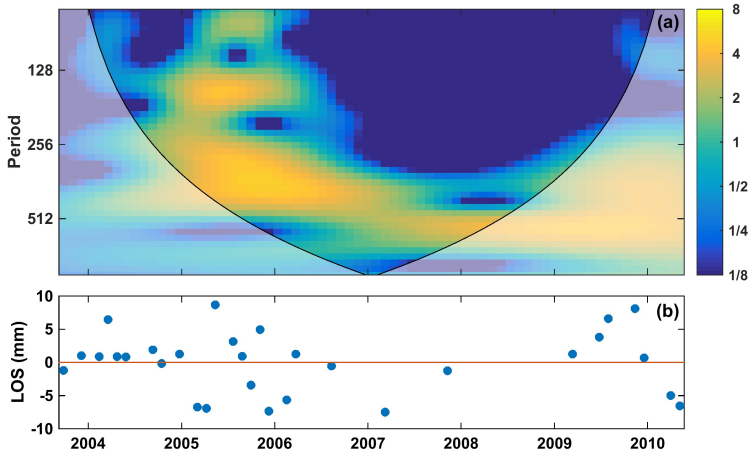


Figure 4.8.: (a), Continuous wavelet power spectrum of Envisat InSAR time series for a point near the toe of the landslide (shown in Figure 4.4a by the white circle). The cone of influence where edge effects might distort the signal is displayed as a lighter shade. (b), InSAR time series after removing the trend (red dashed line in Figure 4.4c).

(Massey, 2010). As mentioned before, the same period (less than 1 year) covering the time frame between 2004 and 2007 is also observable in the InSAR wavelet results; we interpret this as repre-

senting the immediate response of the landslide to the 2004 Manawatu rainstorm and the accelerated deformation that follows this event between 2004 and 2007.

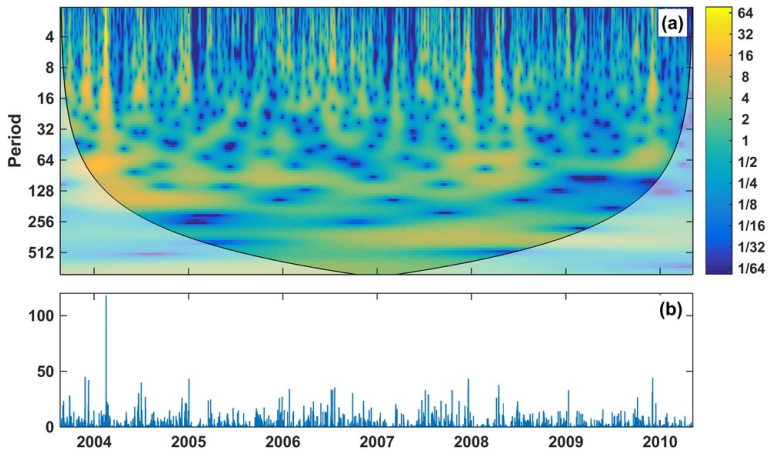


Figure 4.9.: (a), Continuous wavelet spectrum of rainfall. The cone of influence where edge effects might distort the signal is displayed as a lighter shade. (b), Rainfall time series (rainfall values in mm).

The 1-year frequency seen in the wavelet result of the InSAR time series is generally absent from the rainfall wavelet spectrum, except for a short time interval between 2007 and 2009. It therefore cannot be strongly linked to the pattern of the rainfall variation.

In contrast to the rainfall data, groundwater time series in Taihape (Figure 4.10) shows a clear cyclic pattern with a higher level of water in winter and a lower level of water in summer. Applying CWT to groundwater-level time series confirms the existence of an annual frequency for the whole observation period, which is comparable to the annual cyclic pattern seen in InSAR time series. As the groundwater level measurements do not cover the entire time interval of InSAR observations, we applied XWT to both datasets for the same time period covered by the data to better analyse their relationship.

The result is shown in Figure 4.11a with the relative phase between the two datasets indicated by arrows. As seen in this figure, both InSAR and groundwater time series have significant common power of 1 year and the datasets are in phase. This means that rising groundwater level leads to movement towards the satellite and vice versa. This pattern can also be seen directly by comparing InSAR and groundwater-level time series. For example, we observe about 8 mm of LOS subsidence in response to 1 m decline in groundwater in summer 2007 (Figure 4.11b, c). The displacement signal recovers as the groundwater level increases during the following winter. The same pattern is observable in the period between summer 2009 and summer 2010.

As the incidence angle of Envisat sensor in this area is steep ($\sim$21°) we interpret most of these ups and downs in the LOS signal to be related to vertical motion. Such annual cyclic displacement, in phase with groundwater, is unlikely to be related to the downslope movement triggered by groundwater level. Instead, we interpret this as representing cyclic swelling and shrinkage of soil that is superimposed on the long-term downslope motion in response to variations in water content of the soil.

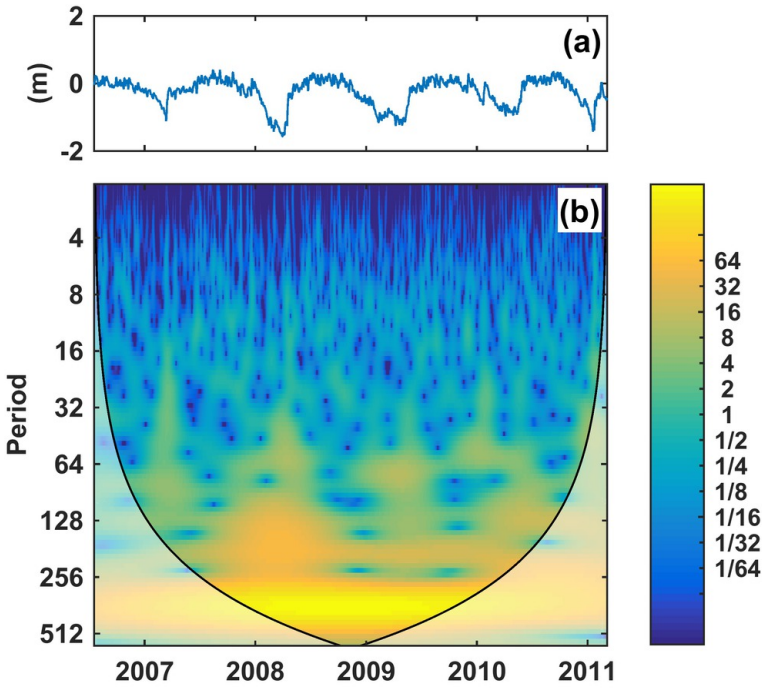


Figure 4.10.: (a), Groundwater-level time series and (b), its continuous wavelet spectrum. The cone of influence where edge effects might distort the signal is displayed as a lighter shade.

4.7. Conclusion

The ability of multitemporal InSAR analysis to monitor the extremely slow movement rate of Taihape landslide was investigated in this study. Using C-band and X-band InSAR time-series analysis, many coherent pixels were detected in the study area. However, detected pixels are not distributed evenly. In the head and toe of the landslide the number of detected pixels is low because of high vegetation coverage. The number of detected pixels in the central part is high because of the existence of manmade structures.

Both Envisat and TerraSAR-X InSAR results show that the area near the toe of the landslide is active with a maximum displacement of <10 mm/yr between 2003 and 2011. Because of its higher resolution and regular data acquisitions, TerraSAR-X Stripmap data were able to detect approximately 15 times more pixels for deformation analysis than Envisat ASAR data. The results are in agreement with ground-based prism measurements at sub-centimetre accuracy. Performing spectral analysis on InSAR-derived displacement suggests a correlation between the 2004 Manawatu rainstorm and the accelerated displacement on the landslide after this event.

We also observe a strong correlation between ground surface displacement and groundwater level, which we relate to surficial shrinkage/swelling of the soil in response to groundwater fluctuations. It is expected that, with a proper and regular data acquisition plan, SAR data on board the recently launched missions such as Sentinel-1 and the use of finer beams such as SpotLight (up to 1 m resolution) and Staring SpotLight (up to 25 cm resolution) from TerraSAR-X further improve our capability to use multitemporal InSAR analysis for landslide investigations.

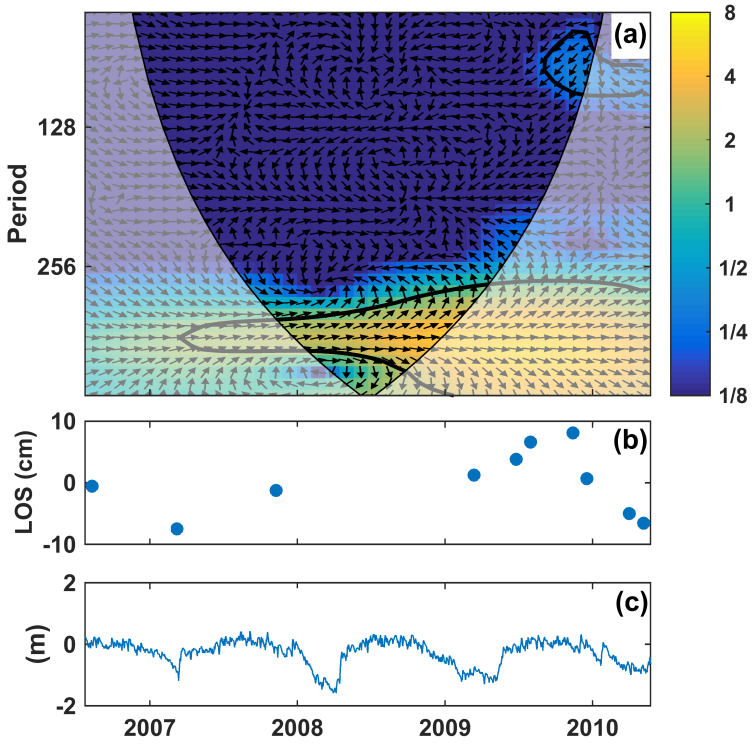


Figure 4.11.: (a), Cross wavelet transform (XWT) applied to the time series of Envisat InSAR and groundwater. The cone of influence where edge effects might distort the signal is displayed as a lighter shade. The thick contour identifies the 5% significance level against red noise. (b), 2007–2010 Envisat time series of a point near the toe after removing the linear trend. (c), Time series of groundwater level.

The same approach applied here can be extended for other areas to analyse extremely slow to very slow motion rates at other landslide-prone slopes to study landslide susceptibility of the areas and update inventory maps. A short revisit cycle and the reduced pixel size in sensors such as TerraSAR-X are helpful to overcome some of the temporal decorrelation problem in analysing long time series of SAR data for vegetated slopes. The interpretation of the results, however, should be performed with care due to limitation in viewing geometry of SAR data to fully characterise the kinematics of landslides. Investigation of the proper orientation of the slope with respect to SAR geometry and analysis of the sensitivity of LOS to slope movement would help to reduce false interpretation of the results.

4.8. Acknowledgments

The authors would like to thank three anonymous reviewers and the guest editor for their helpful comments that significantly improved the manuscript. This work was supported by Initiative and Networking Fund of the Helmholtz Association in the frame of Helmholtz Alliance 'Remote Sensing and Earth System Dynamics'. TerraSAR-X data are provided by DLR under proposal number GEO0714 and Envisat data are provided by ESA under proposal numbers AOALO3740 and 31014.

4.9. Supplementary Materials

Table 4.1.: Parameters used in StaMPS software.

Parameter	Default value	Envisat	TerraSAR-X
filter_grid_size	50	50	10
merge_resample_size	100	0	0
unwrap_grid_size	200	50	20

Table 4.2.: List of Envisat interferograms. B_p and B_t stand for Perpendicular baseline and time interval of a pair, respectively.

No.	Date of Master	Date of Slave	B_p (m)	B_t (days)	No.	Date of Master	Date of Slave	B_p (m)	B_t (days)
1	08/22/03	09/26/03	-102	35	44	05/13/05	07/22/05	-97	70
2	08/22/03	12/05/03	28	105	45	05/13/05	08/26/05	-99	105
3	08/22/03	02/13/04	42	175	46	05/13/05	11/04/05	-80	175
4	08/22/03	04/23/04	-276	245	47	05/13/05	03/24/06	161	315
5	09/26/03	12/05/03	130	70	48	06/17/05	12/09/05	92	175
6	09/26/03	02/13/04	144	140	49	06/17/05	03/24/06	-150	280
7	09/26/03	04/23/04	-174	210	50	07/22/05	08/26/05	-1	35
8	12/05/03	02/13/04	13	70	51	07/22/05	11/04/05	17	105
9	12/05/03	04/23/04	-305	140	52	08/26/05	11/04/05	18	70
10	12/05/03	04/08/05	-37	490	53	08/26/05	03/24/06	260	210
11	02/13/04	04/23/04	-318	70	54	08/26/05	08/11/06	-290	350
12	02/13/04	04/08/05	-50	420	55	09/30/05	12/09/05	-348	70
13	03/19/04	05/28/04	406	70	56	09/30/05	02/17/06	-34	140
14	03/19/04	09/10/04	33	175	57	11/04/05	03/24/06	242	140
15	04/23/04	05/28/04	-374	35	58	11/04/05	08/11/06	-308	280
16	04/23/04	10/15/04	-365	175	59	11/04/05	03/09/07	142	490
17	04/23/04	12/24/04	37	245	60	12/09/05	02/17/06	314	70
18	04/23/04	03/04/05	-63	315	61	12/09/05	03/24/06	-242	105
19	05/28/04	09/10/04	-373	105	62	12/09/05	03/09/07	-342	455
20	05/28/04	10/15/04	9	140	63	12/09/05	11/09/07	-48	700
21	05/28/04	03/04/05	311	280	64	03/24/06	03/09/07	-100	350
22	05/28/04	05/13/05	-71	350	65	03/24/06	11/09/07	195	595
23	09/10/04	10/15/04	382	35	66	08/11/06	03/09/07	450	210
24	09/10/04	05/13/05	302	245	67	03/09/07	11/09/07	295	245
25	09/10/04	07/22/05	205	315	68	03/09/07	03/13/09	-62	735
26	09/10/04	08/26/05	203	350	69	11/09/07	06/26/09	-121	595
27	09/10/04	08/11/06	-86	700	70	11/09/07	07/31/09	220	630
28	10/15/04	03/04/05	302	140	71	11/09/07	11/13/09	-9	735
29	10/15/04	05/13/05	-80	210	72	03/13/09	06/26/09	236	105
30	10/15/04	06/17/05	231	245	73	03/13/09	11/13/09	348	245
31	10/15/04	07/22/05	-178	280	74	03/13/09	04/02/10	98	385
32	10/15/04	08/26/05	-179	315	75	06/26/09	07/31/09	341	35
33	12/24/04	03/04/05	-101	70	76	06/26/09	11/13/09	112	140
34	12/24/04	04/08/05	230	105	77	06/26/09	04/02/10	-138	280
35	12/24/04	06/17/05	-171	175	78	06/26/09	05/07/10	70	315
36	12/24/04	09/30/05	270	280	79	07/31/09	11/13/09	-229	105
37	12/24/04	12/09/05	-79	350	80	07/31/09	12/18/09	258	140
38	03/04/05	04/08/05	331	35	81	07/31/09	05/07/10	-271	280
39	03/04/05	06/17/05	-70	105	82	11/13/09	12/18/09	487	35
40	03/04/05	12/09/05	22	280	83	11/13/09	04/02/10	-250	140
41	04/08/05	09/30/05	39	175	84	11/13/09	05/07/10	-42	175
42	04/08/05	02/17/06	5	315	85	12/18/09	05/07/10	-529	140
43	05/13/05	06/17/05	312	35	86	04/02/10	05/07/10	208	35

Table 4.3.: List of TerraSAR-X interferograms. M. and S. stand for master and slave image. B_p and B_t stand for Perpendicular baseline and time interval between two images of a pair.

No.	Date of Master	Date of Slave	B_p (m)	B_t (days)	No.	Date of Master	Date of Slave	B_p (m)	B_t (days)
1	09/02/10	09/13/10	-124	11	51	11/29/10	03/08/11	106	99
1	09/02/10	09/13/10	-124	11	50	11/29/10	02/03/11	92	66
2	09/02/10	10/27/10	-43	55	51	11/29/10	03/08/11	106	99
3	09/02/10	11/07/10	-26	66	52	12/10/10	12/21/10	76	11
4	09/02/10	11/18/10	18	77	53	12/10/10	01/01/11	-87	22
5	09/02/10	11/29/10	-66	88	54	12/10/10	01/12/11	51	33
6	09/02/10	12/10/10	-75	99	55	12/10/10	01/23/11	156	44
7	09/02/10	12/21/10	2	110	56	12/10/10	02/03/11	101	55
8	09/02/10	01/12/11	-23	132	57	12/10/10	02/25/11	158	77
9	09/13/10	10/27/10	81	44	58	12/10/10	03/08/11	115	88
10	09/13/10	11/07/10	98	55	59	12/21/10	01/01/11	-163	11
11	09/13/10	11/18/10	142	66	60	12/21/10	01/12/11	-25	22
12	09/13/10	11/29/10	58	77	61	12/21/10	01/23/11	79	33
13	09/13/10	12/10/10	49	88	62	12/21/10	02/03/11	25	44
14	09/13/10	12/21/10	125	99	63	12/21/10	02/14/11	155	55
15	09/13/10	01/01/11	-38	110	64	12/21/10	02/25/11	82	66
16	10/27/10	11/07/10	17	11	65	12/21/10	03/08/11	38	77
17	10/27/10	11/18/10	61	22	66	12/21/10	04/10/11	20	110
18	10/27/10	11/29/10	-23	33	67	12/21/10	05/02/11	-26	132
19	10/27/10	12/10/10	-32	44	68	12/21/10	05/13/11	11	143
20	10/27/10	12/21/10	45	55	69	01/01/11	01/12/11	138	11
21	10/27/10	01/01/11	-119	66	70	01/01/11	02/03/11	188	33
22	10/27/10	01/12/11	19	77	71	01/12/11	01/23/11	104	11
23	10/27/10	01/23/11	124	88	72	01/12/11	02/03/11	50	22
24	10/27/10	02/03/11	69	99	73	01/12/11	02/14/11	180	33
25	11/07/10	11/18/10	44	11	74	01/12/11	02/25/11	107	44
26	11/07/10	11/29/10	-40	22	75	01/12/11	03/08/11	63	55
27	11/07/10	12/10/10	-49	33	76	01/12/11	04/10/11	45	88
28	11/07/10	12/21/10	28	44	77	01/12/11	05/02/11	0	110
29	11/07/10	01/01/11	-136	55	78	01/12/11	05/13/11	36	121
30	11/07/10	01/12/11	2	66	79	01/12/11	05/24/11	29	132
31	11/07/10	01/23/11	107	77	80	01/23/11	02/03/11	-55	11
32	11/07/10	02/03/11	52	88	81	01/23/11	02/14/11	75	22
33	11/07/10	03/08/11	66	121	82	01/23/11	02/25/11	3	33
34	11/18/10	11/29/10	-84	11	83	01/23/11	03/08/11	-41	44
35	11/18/10	12/10/10	-93	22	84	01/23/11	04/10/11	-59	77
36	11/18/10	12/21/10	-16	33	85	01/23/11	04/21/11	41	88
37	11/18/10	01/01/11	-180	44	86	01/23/11	05/02/11	-105	99
38	11/18/10	01/12/11	-42	55	87	01/23/11	05/13/11	-69	110
39	11/18/10	01/23/11	63	66	88	01/23/11	05/24/11	-75	121
40	11/18/10	02/03/11	8	77	89	02/03/11	02/14/11	130	11
41	11/18/10	02/14/11	138	88	90	02/03/11	02/25/11	57	22
42	11/18/10	02/25/11	66	99	91	02/03/11	03/08/11	13	33
43	11/18/10	03/08/11	22	110	92	02/03/11	04/10/11	-5	66
44	11/18/10	04/10/11	4	143	93	02/03/11	04/21/11	95	77
45	11/29/10	12/10/10	-9	11	94	02/03/11	05/02/11	-50	88
46	11/29/10	12/21/10	68	22	95	02/03/11	05/13/11	-14	99
47	11/29/10	01/01/11	-96	33	96	02/03/11	05/24/11	-20	110
48	11/29/10	01/12/11	42	44	97	02/14/11	02/25/11	-73	11
49	11/29/10	01/23/11	147	55	98	02/14/11	03/08/11	-116	22

Table 1.3 - continued from previous page

No.	Date of Master	Date of Slave	B_p (m)	B_t (days)	No.	Date of Master	Date of Slave	B_p (m)	B_t (days)
1	09/02/10	09/13/10	-124	11	51	11/29/10	03/08/11	106	99
99	02/14/11	04/10/11	-135	55	147	05/13/11	07/29/11	-44	77
100	02/14/11	04/21/11	-34	66	148	05/13/11	08/20/11	-57	99
101	02/14/11	05/13/11	-144	88	149	05/24/11	06/04/11	-72	11
102	02/25/11	03/08/11	-44	11	150	05/24/11	06/15/11	-179	22
103	02/25/11	04/10/11	-62	44	151	05/24/11	06/26/11	-5	33
104	02/25/11	04/21/11	38	55	152	05/24/11	07/07/11	-101	44
105	02/25/11	05/02/11	-107	66	153	05/24/11	07/18/11	21	55
106	02/25/11	05/13/11	-71	77	154	05/24/11	07/29/11	-37	66
107	02/25/11	05/24/11	-78	88	155	05/24/11	08/20/11	-51	88
108	03/08/11	04/10/11	-18	33	156	05/24/11	08/31/11	-108	99
109	03/08/11	04/21/11	82	44	157	06/04/11	06/15/11	-107	11
110	03/08/11	05/02/11	-64	55	158	06/04/11	06/26/11	67	22
111	03/08/11	05/13/11	-27	66	159	06/04/11	07/07/11	-29	33
112	03/08/11	05/24/11	-34	77	160	06/04/11	07/18/11	94	44
113	03/08/11	06/04/11	-106	88	161	06/04/11	07/29/11	35	55
114	03/08/11	06/26/11	-39	110	162	06/04/11	08/20/11	21	77
115	03/08/11	07/18/11	-12	132	163	06/04/11	08/31/11	-36	88
116	04/10/11	04/21/11	100	11	164	06/04/11	09/11/11	-104	99
117	04/10/11	05/02/11	-45	22	165	06/15/11	06/26/11	174	11
118	04/10/11	05/13/11	-9	33	166	06/15/11	07/07/11	78	22
119	04/10/11	05/24/11	-16	44	167	06/15/11	07/18/11	200	33
120	04/10/11	06/04/11	-88	55	168	06/15/11	07/29/11	142	44
121	04/10/11	06/26/11	-21	77	169	06/15/11	08/20/11	128	66
122	04/10/11	07/07/11	-117	88	170	06/15/11	08/31/11	71	77
123	04/10/11	07/18/11	6	99	171	06/15/11	09/11/11	3	88
124	04/10/11	07/29/11	-53	110	172	06/26/11	07/07/11	-96	11
125	04/21/11	05/02/11	-146	11	173	06/26/11	07/18/11	26	22
126	04/21/11	05/13/11	-109	22	174	06/26/11	07/29/11	-32	33
127	04/21/11	05/24/11	-116	33	175	06/26/11	08/20/11	-46	55
128	04/21/11	06/04/11	-188	44	176	06/26/11	08/31/11	-103	66
129	04/21/11	06/26/11	-121	66	177	06/26/11	09/22/11	140	88
130	04/21/11	07/18/11	-94	88	178	07/07/11	07/18/11	122	11
131	05/02/11	05/13/11	36	11	179	07/07/11	07/29/11	64	22
132	05/02/11	05/24/11	30	22	180	07/07/11	08/20/11	50	44
133	05/02/11	06/04/11	-42	33	181	07/07/11	08/31/11	-7	55
134	05/02/11	06/15/11	-149	44	182	07/07/11	09/11/11	-75	66
135	05/02/11	06/26/11	25	55	183	07/18/11	07/29/11	-58	11
136	05/02/11	07/07/11	-71	66	184	07/18/11	08/20/11	-72	33
137	05/02/11	07/18/11	51	77	185	07/18/11	08/31/11	-130	44
138	05/02/11	07/29/11	-7	88	186	07/18/11	09/22/11	113	66
139	05/02/11	08/20/11	-21	110	187	07/29/11	08/20/11	-14	22
140	05/02/11	08/31/11	-78	121	188	07/29/11	08/31/11	-71	33
141	05/13/11	05/24/11	-6	11	189	07/29/11	09/11/11	-139	44
142	05/13/11	06/04/11	-79	22	190	07/29/11	09/22/11	172	55
143	05/13/11	06/15/11	-186	33	191	08/20/11	08/31/11	-57	11
144	05/13/11	06/26/11	-11	44	192	08/20/11	09/11/11	-126	22
145	05/13/11	07/07/11	-108	55	193	08/20/11	09/22/11	186	33
146	05/13/11	07/18/11	15	66	194	08/31/11	09/11/11	-68	11

Chapter 5

InSAR Measurement of Regional Land Subsidence in Tehran, Iran

This chapter was published as:
Haghshenas Haghighi, M., Motagh, M., 2019. Ground surface response to continuous compaction of aquifer system in tehran, iran: Results from a long-term multi-sensor insar analysis. Remote Sensing of Environment 221, 534 – 550.

5.1. Abstract

Most of the developed groundwater basins in Iran are subject to land subsidence hazards resulting from the over-extraction of groundwater. Several areas in Tehran, the capital city and a provincial center in north-central Iran, have been reported to be subsiding at different rates. In this study, we present the results of an Interferometric Synthetic Aperture Radar (InSAR) time series analysis of Tehran using different SAR data between 2003 and 2017. By constructing more than 400 interferograms derived from 39 Envisat ASAR (C-band), 10 ALOS PALSAR (L-band), 48 TerraSAR-X (X-band), and 64 Sentinel-1 (C-band) SAR datasets, we compile displacement time series from interferometric observations using the Small Baseline (SB) technique. Our analysis identifies 3 distinct subsidence features in Tehran with rates exceeding 25 cm/yr in the western Tehran Plain, approximately 5 cm/yr in the immediate vicinity of Tehran international airport, and 22 cm/yr in the Varamin Plain to the southeast of Tehran city. The temporal pattern of land subsidence, which is dominated by a decreasing trend, generally follows the regional decline in groundwater level, which suggests that anthropogenic processes caused by excessive groundwater extraction are the primary cause of land subsidence. Integrating a decadal time series of subsidence constructed from multi-sensor InSAR with in-situ observations suggests that inelastic and permanent compaction dominates the main deformation regime of the Tehran aquifer, and the ratio between elastic and inelastic deformation is approximately 0.4. A geological analysis indicates that the shape of the subsidence bowl in the western Tehran Plain does not follow the trend of major mapped faults in the region. In contrast, the subsidence bowl in Varamin is controlled by the Pishva Fault, which suggests that either this fault acts as a hydrologic barrier to the groundwater flow in this region or that the differences in sediment thickness causes the discontinuity in land subsidence.

5.2. Introduction

Land surface deformation induced by the over-extraction of groundwater from aquifer systems has been documented in several areas in the world (Schumann and Poland, 1969; Sun et al., 1999; Chen et al., 2003; Phien-wej et al., 2006; Teatini et al., 2006; Galloway and Burbey, 2011). In confined aquifer systems where the excess groundwater discharge surpasses the natural recharge and the stress exceeds the pre-consolidation stress, land surface subsidence occurs as a result of the compaction of fine-grained interbeds (Helm, 1975, 1976; Poland, 1984). Unconfined aquifers are also prone to compaction (Castellazzi et al., 2016); however, they undergo less compaction for a similar amount of discharge (Corapcioglu and Bear, 1983). Knowledge of the spatial and temporal extents of land subsidence for vulnerable groundwater basins can help to develop water management programs and establish measures to mitigate hazards associated with anthropogenic land settlement (Baum et al., 2008).

Interferometric Synthetic Aperture Radar (InSAR) is a powerful technique for measuring the topography of a surface and its changes over time (Bürgmann et al., 2000). Due to its broad spatial coverage and high accuracy, InSAR has become a preferred geodetic method for the study of land deformation in developed groundwater basins and provides insight into the geological and hydrological

parameters that characterize the underlying aquifer systems (Galloway et al., 1998; Amelung et al., 1999; Hoffmann et al., 2001; Schmidt and Bürgmann, 2003; Motagh et al., 2007, 2008a; Bell et al., 2008; Cigna et al., 2012; Akbari and Motagh, 2012; Chaussard et al., 2014; Qu et al., 2015; Motagh et al., 2017). InSAR also provides valuable information about the consequences of rapid subsidence on infrastructure, facilities and urban areas (Emadali et al., 2017; Notti et al., 2016; Samsonov et al., 2014, 2016; Scifoni et al., 2016; Shamshiri et al., 2014).

In recent decades, rapid population growth combined with urban and industrial development have increased the need for water supplies in the Tehran Plain. As a result of extensive groundwater depletion, the plain has been undergoing rapid land subsidence. Leveling measurements along several profiles to the southwest of Tehran confirm the occurrence of land subsidence near Tehran (Arabi et al., 2008). Using the analysis of an Envisat (C-band) interferogram, Motagh et al. (2008a) detected the main features of surface deformation in the Tehran Plain. Dehghani et al. (2013) and Alipour et al. (2008) performed an InSAR time series analysis of Envisat data between 2003 and 2009 and detected land subsidence to the southwest of Tehran and Varamin. Haghshenas Haghighi et al. (2013) evaluated the performance of TerraSAR-X data to analyze land subsidence to the southwest of Tehran. Esmaeili and Motagh (2016) and Esmaeili et al. (2017) demonstrated the effectiveness of dual polarimetry TerraSAR-X data in investigating land subsidence in the Tehran region.

The objective of this investigation is to extend these studies by applying the SAR interferometry remote sensing technique to a more extensive SAR database to better characterize the spatiotemporal evolution of land subsidence in the Tehran Plain. We applied the Small Baseline (SB) InSAR time series technique (Berardino et al., 2002; Hooper, 2008) to nine independent datasets acquired between 2003 and 2017 by SAR sensors onboard the Envisat, ALOS, TerraSAR-X, and Sentinel-1 satellites to derive the time-dependent displacements in Tehran. We combine the results from the different datasets to investigate the short- and long-term responses of the surface elevation changes to groundwater variations and study the elastic/inelastic nature of the deformation. The results have significant implications for developing efficient subsidence hazard and water management strategies in Tehran.

5.3. Study Area and Problem Description

The study area is the Tehran Plain in Iran, which refers to the alluvial pediment area south of the Alborz Range (Figure 5.1). The city of Tehran, which extends roughly east-west along the southern foot of the Alborz mountain range, is located in the northern part of the plain at an average elevation of 1300 m above mean sea level. As the capital city of Iran, Tehran has experienced enormous population growth over the last 40years. Large-scale immigration is the main reason for the unprecedented population boom in Tehran Province, which now hosts approximately 13 million people compared to less than 6 million in 1979. During the last several decades, the urban area of Tehran has increased dramatically, particularly toward the west and southwest. As a result, Tehran has been experiencing an increasing demand for water to meet the needs of its growing population and booming economy (Knill and Jones, 1968).

Several dams were constructed in the 1960s along the main watercourses in the area to channel surface water for farming, municipal and industrial uses. However, these supplies do not meet the

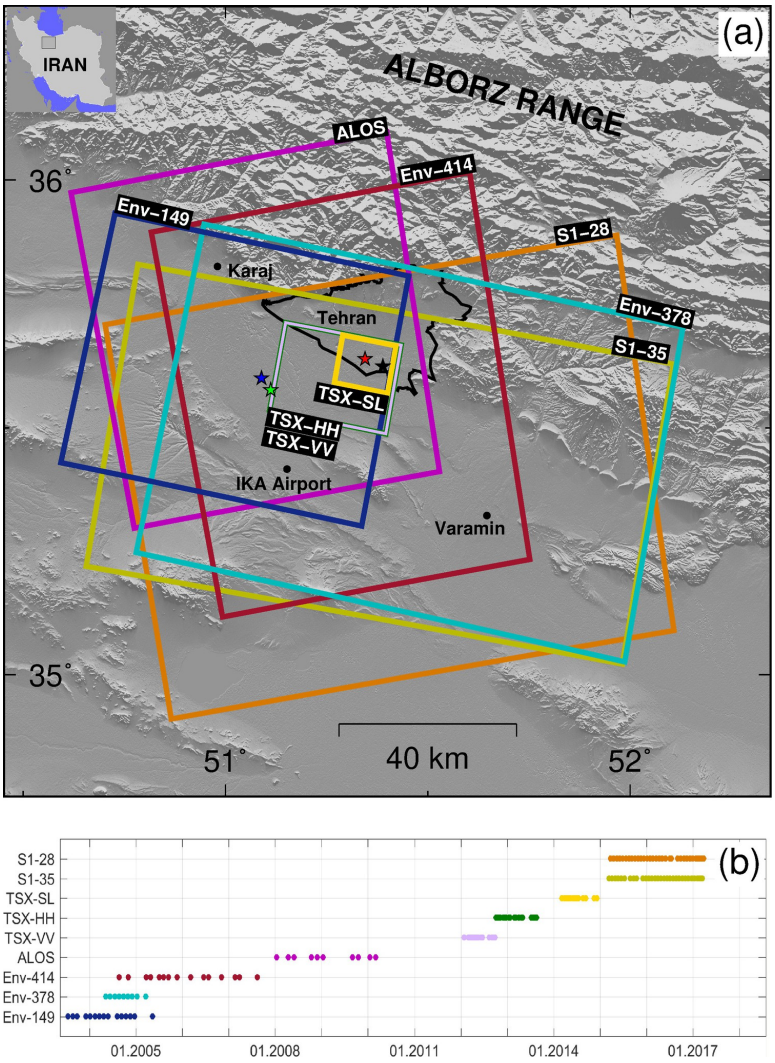


Figure 5.1.: Study area and SAR images used to investigate land subsidence in Tehran. (a) Study area and outline of SAR images superimposed on a shaded relief map. The boundary of Tehran is shown by the black polygon. The blue, green, red and black stars show the locations of the field evidence shown in Figure 5.2 . The inset shows the location of the study area in Iran. (b) Temporal distribution of the SAR data.

water needs of the region, and groundwater is currently the primary source of water for agriculture irrigation and industry in Greater Tehran.

Groundwater table generally follows the topographic gradient in the region and slopes from north to south. The depth of the free groundwater decreases from 100 m in the north at the foot of the Alborz mountain range to 20 m to the south of Tehran. Boreholes studies to a depth of 100 m southwest of Tehran identified three confined aquifers that were mainly composed of silty and clayey sand. Of these three aquifers, the third (from depth of 60 m) is the thickest (2–20 m) and appears to be the major exploited aquifer for groundwater in the region. The aquifers are confined by layers of silty clay and clayey soil. The confining layer of aquifer 3 is the thickest aquitard (9–41 m) and is expected to play the major role in the compression of the aquifer system. Additional details abouth the geological and hydrological properties of the aquifer in Tehran can be found in Mahmoudpour et al. (2016).

The number of exploitation wells in the area has increased from 3906 in 1968 to 26,076 in 2003 and 32,518 in 2012. Tehran's aquifers have been depleted over the last four decades, partly due to increased over-exploitation and partly due to the indirect effects of dams, which have decreased the flow of surface water into the aquifers. The average groundwater level in Tehran decreased by approximately 12 m from 1984 to 2011. Water shortages have also been exacerbated in recent years due to periods of sustained drought in the area, which has in turn put more pressure on existing groundwater resources. Most of the Qanat galleries in the region, which are man made underground water channels built centuries ago to transfer water from the mountains to the plains, have dried out. In 2012, only 167 branches of the 522 in 1970 remained effective as reliable means of water transportation (Mahmoudpour et al., 2016; Shemshaki et al., 2005).

The decrease in the hydraulic head in the Tehran Plain is associated with local and regional land subsidence. Earth fissures, damage to buildings, shifts on the ground, and cracks in walls are evidence of groundwater-induced compaction that have been observed in the Tehran Plain. Figure 5.2 illustrates several examples southwest of Tehran.

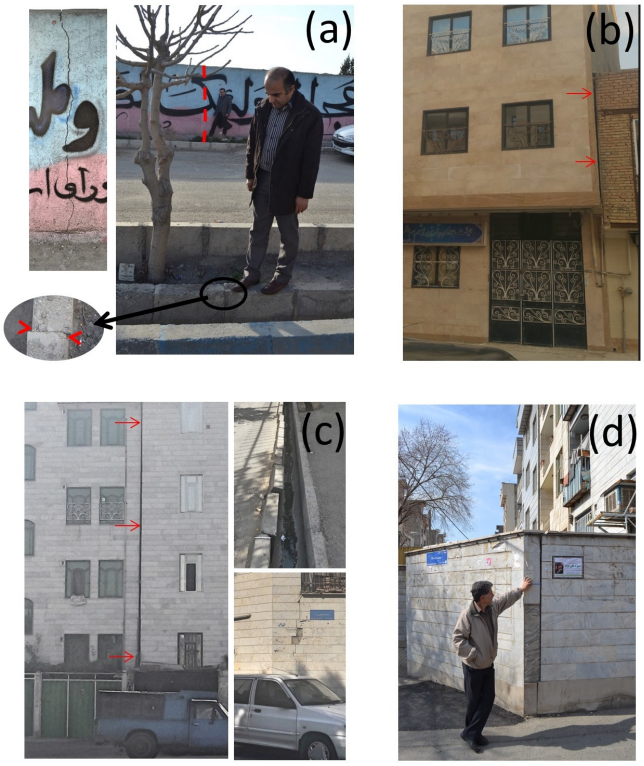


Figure 5.2.: Examples of damage caused by groundwater-induced compaction to the southwest of Tehran. Pictures (a)–(d) are associated with the locations in Figure 5.1 indicated by the blue, green, black, and red stars, respectively. We observed cracks in walls and the ground, shifts in curbstones, and tilted buildings at different locations. The pictures were taken in 2015 and 2017.

Table 5.1.: Details of the SAR datasets used for the InSAR time series analysis: time span, orbit of the satellite (A and D indicate ascending and descending, respectively), heading of the satellite α, incidence angle of the sensor θ, number of SAR images N, wavelength band λ and acquisition mode (SM for StripMap, SL for SpotLight, and IW for Interferometric Wideswath modes). For simplicity, each dataset is denoted by an abbreviation. Envisat, TerraSAR-X, and Sentinel-1 are abbreviated as Env, TSX, and S1, respectively, and the numbers indicate the satellite track number. VV, HH, and SL represent VV polarized, HH polarized and SpotLight mode, respectively.

Dataset	Time span	Orbit	α (°)	θ (°)	N	λ	Mode
Env-149	Jul 2003 - May 2005	D	194	21	15	C	SM
Env-378	May 2004 - Mar 2005	D	194	23	9	C	SM
Env-414	Aug 2004 - Aug 2007	A	346	41	15	C	SM
ALOS	Jan 2008 - Mar 2010	A	347	39	10	L	SM
TSX-VV	Jan 2012 - Sept 2012	D	191	26	15	X	SM
TSX-HH	Oct 2012 - Aug 2013	D	191	26	19	X	SM
TSX-SL	Mar 2014 - Dec 2014	D	191	26	14	X	SL
S1-28	Mar 2015 - Mar 2017	A	350	41	33	C	IW
S1-35	Mar 2015 - Mar 2017	D	190	38	31	C	IW

5.4. Datasets

5.4.1. SAR Data

To survey the land subsidence in Tehran, we used a large collection of SAR images from different sensors onboard the Envisat, ALOS, TerraSAR-X, and Sentinel-1 satellites. Three Envisat datasets and one ALOS dataset cover the study area between 2003 and 2010. The Envisat data were collected in both ascending and descending orbits, but the ALOS data were only collected in an ascending orbit. After a two-year gap, three ascending TerraSAR-X datasets span 2012 to 2014. Finally, Sentinel-1 data in both ascending and descending paths cover a two-year period between 2015 and 2017. The details of the SAR datasets are summarized in Table 5.1. For simplicity, each dataset is denoted by a short name and will be referred to by that name in the paper.

Three Envisat, one ALOS and two TerraSAR-X datasets were acquired in the conventional StripMap mode, which is the default mode for these sensors (Lanari et al., 2001). The TSX-VV and TSX-HH datasets are VV and HH polarized, respectively. Dataset TSX-SL were collected in SpotLight mode, which provides a higher spatial resolution but a smaller scene size than the StripMap mode (Eineder et al., 2009). Two Sentinel-1 datasets were acquired in Interferometric Wideswath (IW) mode, which is the default acquisition mode for Sentinel-1 over land and takes images with an extensive spatial coverage and moderate resolution (Torres et al., 2012).

Figure 5.1 illustrates the spatial extent and temporal distribution of the SAR data in the study area. The spatial coverage of the SAR datasets used in this study is not uniform. Due to the extensive scene size of Sentinel-1, it covers all of the agricultural areas in the Tehran Plain. In contrast, the Envisat and ALOS datasets are mostly limited to the subsidence basin to the southwest of Tehran. The TerraSAR-X datasets only cover a small area near Tehran. Sentinel-1 and TerraSAR-X provide semi-regular acquisitions of SAR data. In contrast, the temporal distributions of the Envisat and ALOS datasets are irregular, and many of the acquisitions are missing.

5.4.2. Leveling

The National Cartographic Center of Iran (NCC) has conducted leveling measurements along several lines to the southwest of Tehran. Figure 5.5-b shows the locations of the leveling profiles that were measured in the study area during two campaigns in 2004 and 2005. However, the temporal interval of the measurements was not exactly one year. Assuming that the surface displacement is linear through time, the one-year rate of displacement for each measurement profile is estimated. For each leveling point, the standard deviation of the height difference is $8\sqrt{k}$ mm, where k is the distance from the starting point of the profile in km. Although the leveling data are only available for a short time window, they coincide with two Envisat datasets (tracks 378 and 414). Therefore, we can compare the InSAR results from these two datasets with the leveling data to assess their reliability.

5.4.3. Groundwater Level

Tehran's regional water authority has conducted groundwater measurements since 1984 at different locations around Tehran. The level of the piezometric head has been measured in several wells on a monthly basis, but there are many sporadic gaps in the data record. The groundwater level data are used later to investigate the long-term and short-term effects of groundwater changes on the surface displacements measured by InSAR. The period between 2003 and 2010, which coincides with the Envisat and ALOS data, is used to analyze the effect of changes in groundwater level on the surface displacement. We will assess the surface response to long-term variations as well as seasonal fluctuations of groundwater.

5.5. Methods

5.5.1. Multi-temporal InSAR Analysis

Interferogram Formation

SAR interferometry is performed using Single Look Complex (SLC) images. However, the Envisat and ALOS data were provided in an unprocessed raw signal format. As a pre-processing step, we focus them and generate SLC data using the ROI_PAC (Repeat orbit interferometry package) software (Rosen et al., 2004).

The standard repeat pass interferometry approach using the DORIS software (Kampes et al., 2003) is used to produce the interferograms for the StripMap and Spotlight datasets. Sentinel-1 interferograms were generated using the GAMMA software (Werner et al., 2000). The spectral diversity method was used to reach a coregistration accuracy on the order of 0.001 of the azimuth resolution to correct the phase jumps between consecutive bursts of Sentinel-1 images (Yagüe-Martínez et al., 2016).

The flat-earth phase is removed using the precise orbit data of the satellite. For ALOS, TerraSAR-X and Sentinel-1, the orbital state vectors attached to the data are sufficiently accurate, but for Envisat, the DORIS Precise Orbit State Vectors (Doornbos and Scharroo, 2004) are used to correct the flat-

earth phase. Any inaccuracies in the orbital data generate a long-wavelength phase ramp in the interferograms that can be removed by trend removal in a post-processing step (Fattahi and Amelung, 2014).

The topographic phase is calculated using the 3-arcsecond SRTM DEM (Farr and Kobrick, 2000) and removed from the interferograms. Inaccuracies in the DEM appear as an error correlated with the perpendicular baseline of the satellite. In the case that several interferograms with different perpendicular baselines are generated, it is possible to estimate and correct the remaining DEM error from the interferograms. However, the topography in the study area is relatively smooth; hence, we expect that the topographic phase can be removed accurately using the 3-arcsecond SRTM DEM.

After removing the flat-earth and topography phases, the remaining phase mainly contains the displacement, atmospheric artifact, and noise. The atmospheric artifact in InSAR consists of phase delays in the ionosphere and troposphere. The ionospheric delay is usually low at mid-latitudes for X- and C-band data. In the study area, visual inspection of the interferograms shows no clear evidence of ionospheric delays even for L-band data except for some long-wavelength phase ramps across some of the interferograms, which might be caused by the ionospheric delay. These ramps are mixed with the previously mentioned orbital ramps and can be corrected by the trend removal.

Tropospheric delays are produced by vertical variations, long-wavelength lateral variations, or short-wavelength turbulence in the atmosphere (Bekaert et al., 2015a). The atmospheric delay caused by vertical variations is highly correlated with the topography. However, the topography in the study area is very smooth with a slight north-south slope; Therefore, this effect is negligible. The other two sources of tropospheric artifacts can produce cm-scale errors in the interferograms. We estimate and remove the part that is not temporally correlated during the time series analysis. We also assess the magnitude of the temporally correlated part to evaluate its significance in our analysis.

Small Baseline Analysis

Several algorithms have been developed in recent years for InSAR time series analysis, which can be roughly categorized into two groups: Persistent Scatterer (PS) InSAR (Ferretti et al., 2001; Hooper et al., 2004) and Small Baseline (SB) (Berardino et al., 2002). The former is mainly used in urban areas where strong scattering elements such as buildings dominate the pixel's phase, whereas the latter works in non-urban areas, where strong scatterers are rare. Because most of our study area is in farmland, we chose SB approach for the time series analysis.

To produce the stack of SB interferograms for each dataset, all of the SLC SAR images are coregistered and resampled to a reference SAR frame. Then, using the SAR images in a common geometry, SB inteferograms are generated. To preserve the phase quality of the interferograms, the SB approach only utilizes interferometric pairs with short temporal and spatial baselines. Maximum temporal and perpendicular baselines are defined independently for each dataset based on the availability of the data and the distribution of the data in time and space (see Table 5.2). Furthermore, to reduce the impact of noise in the time series processing, the SB interferograms are inspected, and noisy interferograms are excluded from the networks. To detect unwrapping errors through measurement redundancies, the

Table 5.2.: Information about the small baseline networks of the interferograms: maximum perpendicular (B_p) and temporal (B_t) baselines, number of possible interferometric pairs (M), and number of produced small baseline interferograms (N) for different datasets used in the SB analysis.

Dataset	Max B_p	Max B_t	M	N
Env-149	600	250	105	31
Env-378	600	250	36	17
Env-414	860	600	105	29
ALOS	4200	700	45	27
TSX-VV	150	110	105	40
TSX-HH	320	121	171	48
TSX-SL	375	210	91	37
S1-28	100	150	528	88
S1-35	100	150	465	86

network of interferograms is constructed in such a way that each image in the network is connected to at least two other images. Figure 5.3 illustrates the final SB network for each dataset.

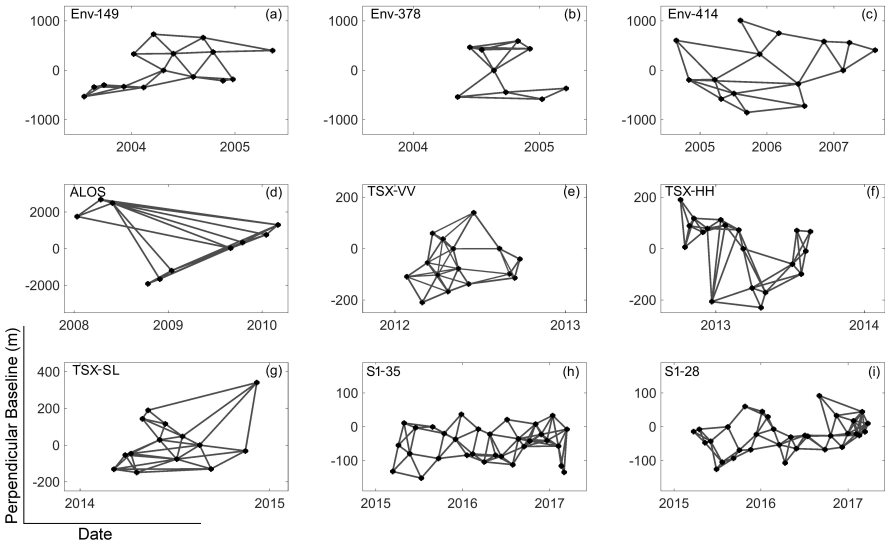


Figure 5.3.: Small baseline network of interferograms for different datasets. Circles and lines represent the image dates and interferograms, respectively.

Pixel Selection

Because of the high rates of subsidence in the study area, it is critical to have a fair spatial distribution of detected pixels to avoid phase aliasing. Several approaches can be used to detect pixels with stable phases in a set of interferograms based on the amplitude or interferometric phase.

Coherence can be used as the first estimation in pixel selection (Berardino et al., 2002). A high value of coherence for a pixel in a series of interferograms indicates a high phase stability over time. The main limitation of coherence approach is that it reduces the resolution of the interferograms due to multi-looking. Multi-looking is applied to the interferograms to increase the signal-to-noise ratio, which lowers the spatial resolution of the interferograms. Furthermore, the coherence is estimated by spatial averaging of the interferometric data inside a window around each pixel. Therefore, single stable pixels surrounded by noisy pixels are not likely to be detected by this approach.

The qualities of the TerraSAR-X and Sentinel-1 interferograms that were produced for the SB network is generally high due to the regular data acquisition and relatively short perpendicular baselines. Therefore, we could detect a sufficient number of pixels for those datasets using the coherence approach. To do so, the interferograms are first multilooked by factors of 5×5 for TerraSAR-X and 1×5 (1 in the azimuth and 5 in the range direction) for Sentinel-1. Then, using a 5×5 coherence window, we selected a pixel if the coherence value was higher than 0.6 in at least 30% of the interferograms.

For Envisat and ALOS, coherence approach fails to select enough pixels in the agricultural areas, where the main part of the subsidence in Tehran takes place. This is mainly due to the temporal decorrelation of the interferograms caused by the haphazard acquisition plans of Envisat and ALOS in this area. Therefore, we used a more sophisticated technique to detect high quality pixels as described in detail by Hooper et al. (2004) and Hooper (2008).

In this approach, the phase stability of pixels in a stack of single look interferograms is analyzed to find pixels with stable phases. The variations of the noise level of a pixel over time are the indicator of its phase stability. To estimate the level of noise, other contributions to the interferometric phase of a candidate pixel are separated. Then, through statistical analysis, the variations of the noise level in the set of interferograms are analyzed, and pixels with low variations are considered to be pixels with stably distributed scatterers. The analysis is performed at the highest possible resolution of the SAR images, which increases the chance of finding stable pixels surrounded by noisy pixels.

Unwrapping and Time Series Analysis

After generating the network of SB interferograms and detecting high-quality pixels, the modulo 2π interferometric phases of the identified pixels are unwrapped to estimate their unambiguous phase values. In the standard SB approach, the individual interferograms are unwrapped in space and then connected in time to estimate the displacement time series (Berardino et al., 2002). This approach requires a high-quality interferometric phase and a proper distribution of detected pixels over the study area that provides sufficient spatial sampling of the displacement field, which is not the case in the study area. Using the data of the time dimension can increase the chance of reliable unwrapping. We use the approach described in Hooper (2009) to unwrap the interferograms in 3D. Prior to the unwrapping, an adaptive filter is applied to the interferograms to make them spatially smooth. A Delaunay triangulation connects neighboring pixels, and their phase differences are unwrapped in time. After the temporal unwrapping, each interferogram is unwrapped spatially.

The unwrapped interferograms of the SB network are inverted in a least-squares adjustment to retrieve the displacement time series and the average rate of displacement. The redundancies in the SB network help detect any inconsistencies in the unwrapped interferograms. The estimated time series is the sum of the displacement, noise, and several errors that might bias the results. To obtain a reliable estimation of the displacement, the errors should be filtered as much as possible. First, a linear 2D ramp is estimated and subtracted from each unwrapped interferogram. The estimated ramp contains phase ramps from orbital inaccuracies and the long-wavelength troposphere/ionosphere. Then, assuming that the displacements are correlated in space and time, the time series are filtered

in time and space to remove spatially correlated errors that are not temporally correlated. This error mainly includes temporally uncorrelated tropospheric artifact (Hooper et al., 2012). It is important to note that the temporally correlated part of the tropospheric effect is mixed with the displacement; therefore, it is not possible to filter it out. Our analysis using ERA-I reanalysis data from ECMWF shows that the magnitude of this artifact is less than 0.4 cm in the study area. Additional information can be found in the supplementary materials. Any other errors in the time series that are correlated neither spatially nor temporally can be treated as noise.

5.5.2. Merging InSAR Time Series

The time span of each individual SAR dataset used in this study is limited to a few years. Furthermore, the period between 2003 and 2010 is only covered by haphazard data acquisitions of Envisat and ALOS. This prevents us from obtaining homogeneous and long-term information about the dynamics of land subsidence in the study area. Joining the InSAR time series derived from different datasets enables us to obtain a long time series with a higher temporal resolution (Castellazzi et al., 2017). However, three points should be taken into account.

First, the locations of the detected pixels in each dataset are different. Therefore, the results from different datasets should be transformed to a common spatial grid. We resampled the data into a common 200-m grid.

Second, the imaging geometry of each dataset is different; i.e., each dataset is measured in a unique line-of-sight. Therefore, before joining time series derived from different viewing angles, they should be transformed to a common geometry. We neglect the horizontal displacement and convert line-of-sight time series of the dataset m to vertical by

$$v_{zi}^{m} = \frac{\Delta r_i^m}{\cos\theta_i^m} \tag{5.1}$$

where Δr_i^m and v_{zi}^m are the line-of-sight and estimated vertical values for the dataset m at time t_i, respectively and θ is the incidence angle of the sensor. Before converting the line-of-sight measurements to vertical, it is crucial to test if the horizontal displacement is negligible.

The third point that should be considered in merging the time series is that InSAR provides relative time series with respect to an arbitrary reference date (here, the first date of the dataset). Therefore, to have all of the time series in a common time reference, a shift needs to be estimated and applied to each dataset. To do so, we assume that the rate of subsidence remains constant during the observation period; in other words, for a specific point on the ground, time series from different datasets follow the same trend line. Consequently, for a vertical measurement at time ti in dataset m, we have

$$v_{zi}^{m} = a(t_i - t_0) + b^m \tag{5.2}$$

where t_0 is an arbitrary date, b^m is the shift of dataset m, and a is the constant rate of displacement. The linear rate and shifts can then be estimated separately for each pixel by a linear least-squares adjustment. The individual time series are then merged, and a long and dense time series of displacement is generated.

5.5.3. Cause-Effect Analysis

To understand the relationship between the groundwater level and the change in surface elevation, we analyze both long-term and seasonal variations of the surface displacement against the groundwater level. We expect two different mechanisms to drive the surface displacement. First, the long-term decline of groundwater causes the consolidation of fine-grained soils and thus a long-term deformation that is mainly inelastic. This part can be observed as a long-term trend of displacement. Second, the seasonal variations of the groundwater level caused by alternating charging and discharging of the reservoir in the winter and summer, respectively, might cause an elastic response of the aquifer that can be measured as seasonal variations of the surface elevation change.

To investigate the elastic response to seasonal variations in groundwater, the variations are segregated from the long-term displacement trend. Then, a Continuous Wavelet Transform (CWT) is applied to the seasonal variations to investigate the periodic signals. The CWT transforms the data to a time-frequency domain and provides a better visualization of the cyclic patterns in the data as well as the time of occurrence of these patterns (Torrence and Compo, 1998).

An advanced method called Cross Wavelet Transform (XWT) (Grinsted et al., 2004) is used to investigate the correlation between the time series of the groundwater level and surface displacement. XWT extracts the common powers in the wavelet spectrum of the groundwater level and surface displacement and derives the correlation and phase relationship between them. Therefore, it is possible to find the correlations and the time-lag between seasonal variations in the groundwater level and surface elevation.

CWT and XWT are usually applied to time series that are equally sampled in time. However, InSAR time series are unevenly distributed in time. To overcome this problem, a linear interpolation of InSAR time series was suggested by Tomás et al. (2015). We applied the same interpolation method and resampled the InSAR displacements to a regular 1-month grid (the same resolution as the groundwater level data). After removing the trend from the time series, CWT and XWT were applied to the data (Haghshenas Haghighi and Motagh, 2016).

To compare the elastic and inelastic responses of the aquifer to the variations in groundwater, we estimate the elastic/inelastic deformation ratio ($R_{ed/id}$) as suggested by Ezquerro et al. (2014). The ratio is calculated considering the long-term displacement trend as the inelastic part of the deformation and the maximum short-term variations of the displacement as the elastic part. A value higher than 1 indicates that the deformation is dominated by the elastic response, whereas a value lower than 1 indicates that the dominant part is inelastic.

5.6. Results

Figure 5.4 shows an example interferogram of the Tehran Plain. The interferogram spans approximately 7 months between 15 August 2015 and 18 March 2016. Three dominant subsidence features are identified in this interferogram: (1) the southwest of Tehran, (2) near IKA international airport and (3) near Varamin. The subsidence mainly occurs in agricultural areas but affects urban areas and infrastructure as well. Each area is investigated in detail in the following sections. All of the results hereafter are converted from line-of-sight to vertical.

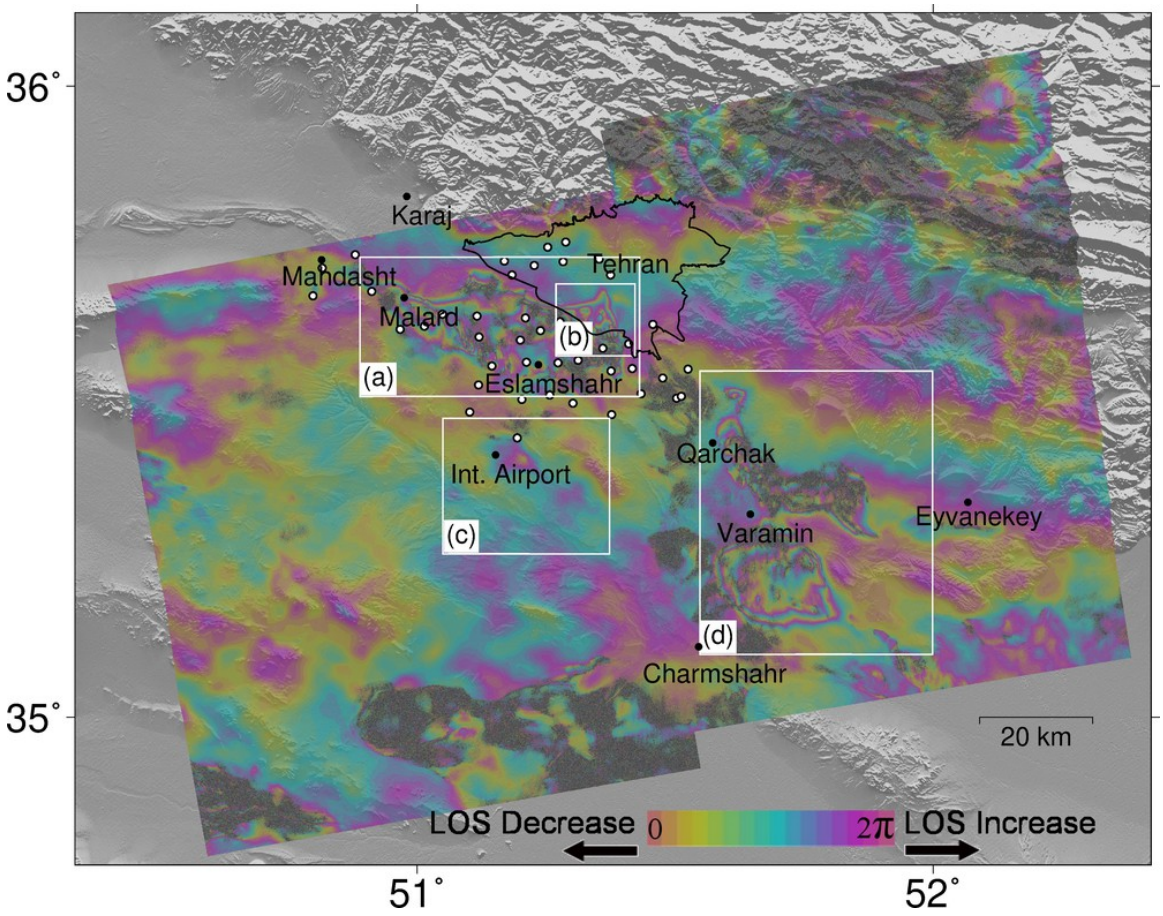


Figure 5.4.: Example of an interferogram produced from Sentinel-1 SAR images acquired in ascending orbit on 2015.08.15 and 2016.03.18. The white boxes (indicated by a–d) delineate the main displacement features in the area discussed in detail in Figs. 5–8. White circles show the locations where groundwater measurements were available. Each color cycle represents approximately 2.8 cm of displacement in the satellite's line of sight.

5.6.1. Southwest of Tehran

The largest deformation feature is an elongated east-west zone of subsidence to the southwest of Tehran, east of Malard and north of Eslamshahr. It covers an area of approximately 600 km^2 (Figure 5.5). This area is completely covered by the Envisat, ALOS, and Sentinel-1 datasets and partially covered by the TerraSAR-X data. The overall shape and boundary of the subsidence area is similar over the

15 years of InSAR observations. However, the rates and locations of local peaks of displacement vary slightly.

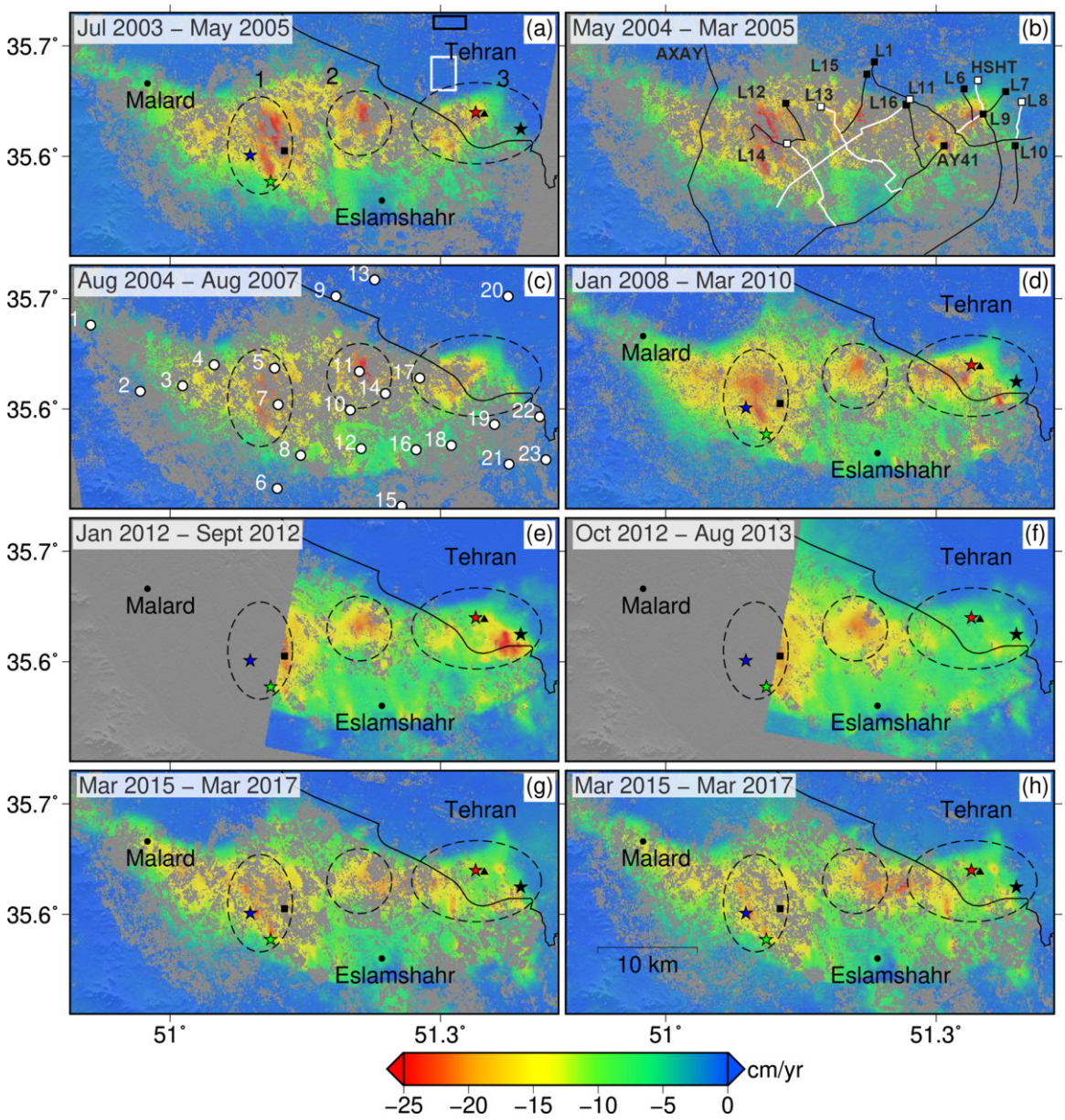


Figure 5.5.: Average subsidence rates in the southwest of Tehran. The rates shown in (a)–(h) correspond to the results from Envisat tracks 149, 378, and 414, ALOS, TerraSAR-X VV and HH polarized and Sentinel-1 orbits 35 and 28, respectively. The boundary of Tehran's urban area is shown by the solid black line. Three dashed polygons (1, 2, and 3) show major subzones of subsidence in the region. The stars indicate the locations of the field evidence shown in Figure 5.2. The black triangle and square show the locations of the time series plotted in Figure 5.9-a and b, respectively. A region in the urban area in which we do not expect any displacement is selected as the reference area and is shown by the black box in (a). The white box shows the area where the precision of the velocities is estimated. In (b), leveling profiles to the southwest of Tehran are superimposed on the subsidence map. The squares represent the starting points of each leveling line. To distinguish different profiles, they are shown in black and white. In (c), groundwater measurement wells are indicated by white circles.

The average velocities derived from the different datasets are generally consistent, except for TSX-VV and TSX-HH results. The main reason is that the TSX-VV and TSX-HH datasets cover time periods shorter than one year. The displacement during the cold season is expected to be less than that in the warm season. The TSX-VV data cover part of the cold season and most of the warm season. Therefore, we assume that the rate of displacement is overestimated by TSX-VV. In contrast, the TSX-HH dataset covers the cold season and part of the warm season. Consequently, it underestimates the displacement rate. To test this, we estimated the rate of displacement using Sentinel-1 data for periods shorter than one year. The data are from 2015 and 2016 but cover similar periods of the year as TSX-VV (January to September) and TSX-HH (October to August). The results, which are presented in the supplementary materials, confirm our hypothesis that the displacement rate is underestimated and overestimated by TSX-VV and TSX-HH, respectively.

The peak of the subsidence in the southwest of Tehran exceeds 25 cm/yr in the Envisat results from 2003 to 2005. However, in the Sentinel-1 results, it decreased to approximately 20 cm/yr. The slightly lower rate of subsidence in the recent years might be the result of groundwater management and decreased extraction in the recent years.

The main subsidence bowl in this area includes a few smaller sub-zones of subsidence. Three main sub-zones of higher subsidence are indicated by dashed lines 1–3 in Figure 5.5. The pattern of subsidence changes slightly in sub-zones 1 and 2 over 15 years. In contrast, the subsidence in sub-zone 3 is more dynamic and has been spreading eastward, threatening the urban area of Tehran. The increase in demand for groundwater in the urban area in the southwest of Tehran is probably the main reason for this eastward expansion of the subsidence area.

The InSAR results from the TSX-SL data reveal the subsidence in this area in more detail (Figure 5.6). We expect this dataset to slightly overestimate the subsidence rate for the same reason that we described previously for TSX-VV. Nevertheless, it helps to identify a large urban area approximately 40 km2 north of the Azadegan Expressway that is affected by land subsidence. Many buildings in the area have been damaged as a result of land subsidence. Some infrastructure, including two railways (Tehran-Qom and Tehran-Tabriz), The Tehran Metro line 3 and several highways have been affected by the subsidence. Some of the damage caused by land subsidence in this area is shown in Figure 5.2-c and Figure 5.2-d.

5.6.2. IKA Airport

The second remarkable subsidence feature in the study area is a localized area of ground deformation near the IKA international airport in Tehran. IKA is the busiest airport in Iran; it opened in 2005 and serves Tehran with international flights. InSAR displacement maps (Figure 5.7) identify a northwest-southeast-oriented subsidence feature in the immediate vicinity of the airport with a maximum subsidence rate of approximately 5 cm/yr. A Comparison of the results from the Envisat and Sentinel-1 datasets shows that the peak of the subsidence is moving toward the airport. Parts of the airport's terminal and runway are affected by approximately 2 cm/yr of subsidence. Therefore, it is

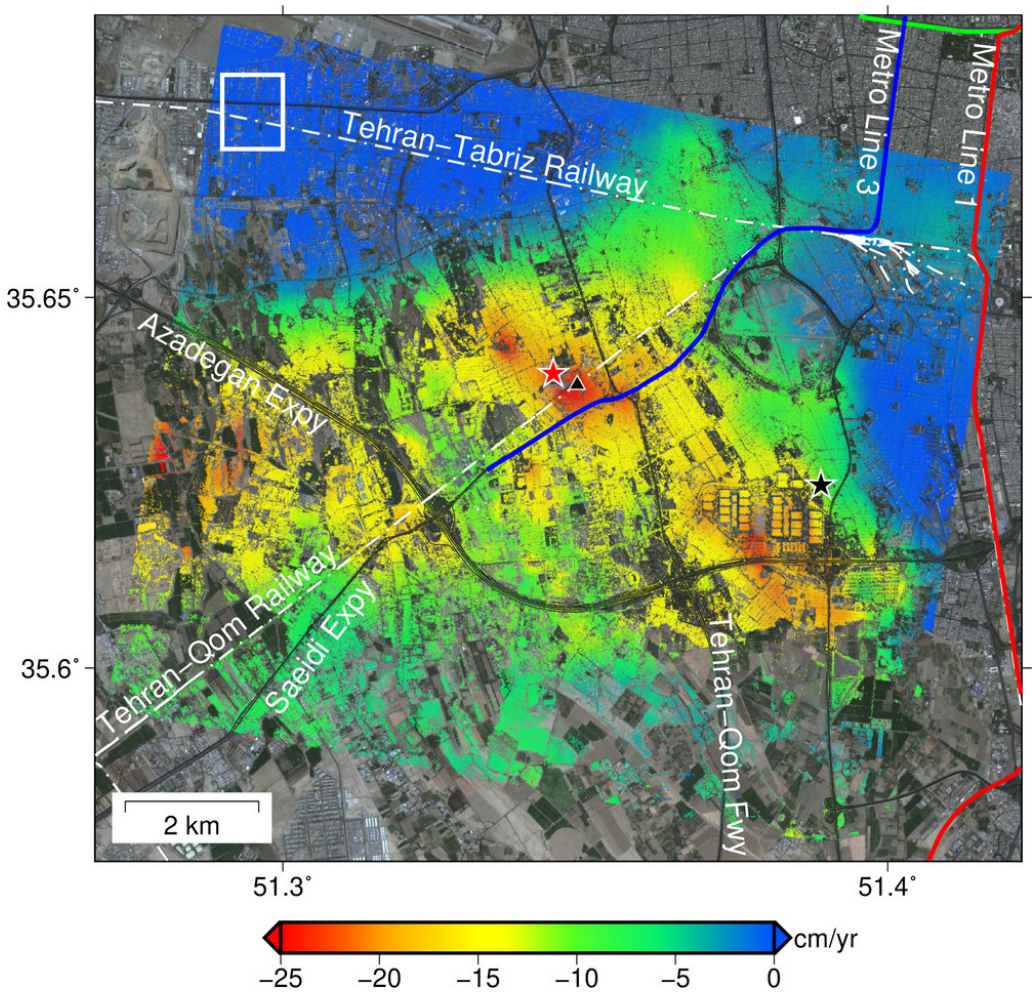


Figure 5.6.: Average rates of subsidence in the urban area of Tehran derived from the TerraSAR-X spotlight dataset. Metro lines 1, 3, and 7 in Tehran are represented by the blue, red, and green lines, respectively. The white dot-dashed line shows the railways, and the black solid lines show major highways and roads in the area (railway, highway and metro line data © OpenStreetMap). The red and black stars show the locations of the field evidence in Figure 5.2-c and Figure 5.2-d, respectively. The black triangle shows the location of the time series plotted in Figure 5.9. The white box represents the reference area in the time series analysis of TSX-Spot. The background image is a true color image (band combination 432) from Sentinel-2.

important to continue monitoring the land subsidence in the region and implement necessary measures to prevent potential damage to the airport.

5.6.3. Varamin County

The last interesting deformation feature in greater Tehran occurs in Varamin County, 50 km to the southeast of Tehran. This area is only covered by Envisat track 378 and two Sentinel-1 datasets. Figure 5.8 shows the average velocities in this area. A comparison of the Envisat data from 2004 to 2005 with the Sentinel-1 data from 2015 to 2017 shows that the overall shape of deformation is similar with a maximum displacement rate of 22 cm/yr. The results also indicate that the subsidence

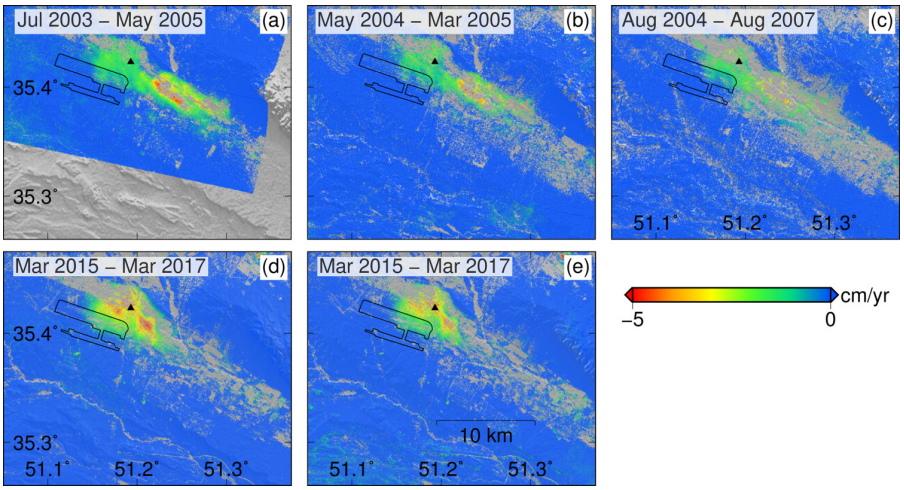


Figure 5.7.: Average subsidence rates near IKA airport. The rates in (a)–(e) correspond to the results from Envisat tracks 149, 378, and 414 and Sentinel-1 orbits 35 and 28, respectively. The black polygon shows the location of the international airport, and the triangle shows the location of the time series plotted in Figure 5.9-c.

area in Varamin County consists of two separate subsidence zones: a 300 km^2 round lobe of ground deformation south of Varamin and a 350 km^2 curved trough-like subsidence area north of Varamin.

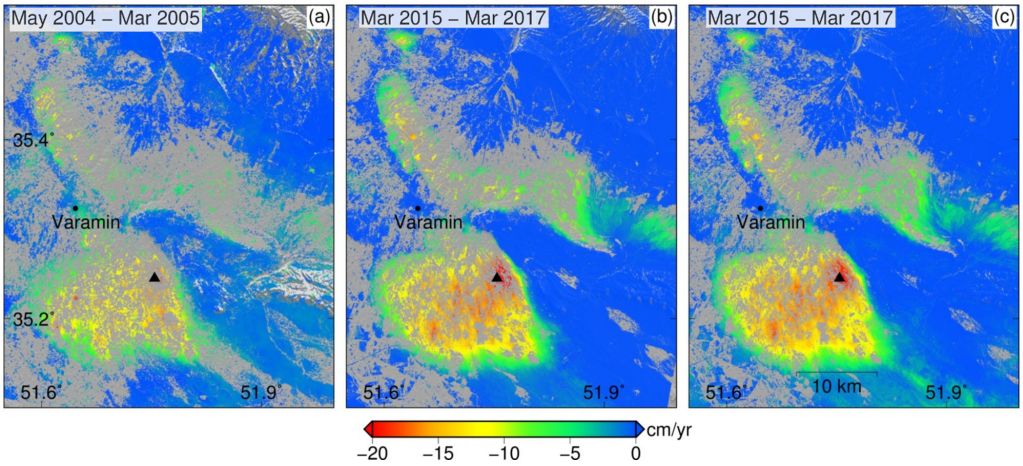


Figure 5.8.: Average subsidence rates in Varamin. The rates in (a)–(c) correspond to the results from Envisat tracks 378 and Sentinel-1 orbits 35 and 28, respectively. The triangle shows the location of the time series plotted in Figure 5.9-d.

5.6.4. Time Series of Displacement

Example time series of the vertical displacements from different datasets are shown in Figure 5.9 (see figures 5.5-5.8 for the locations). All of the time series are dominated by a permanent declining trend and minor seasonal variations. The first time series (a) is plotted for a point in the urban area of Tehran that is indicated by the triangle in Figure 5.5. An example of field evidence from this area was shown in Figure 5.2-c. This area is covered by all of the datasets used in this study; therefore, the temporal variations of land subsidence in this region can be investigated in detail. The seasonal

variations can be better observed in the Sentinel-1 time series due to its regular acquisitions with a short temporal resolution.

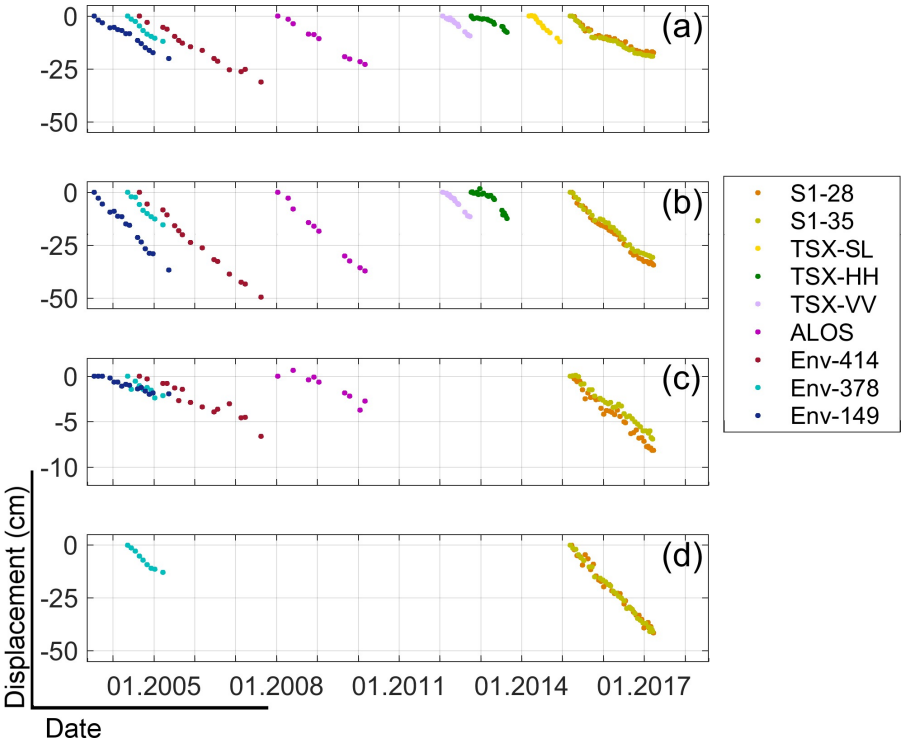


Figure 5.9.: Examples of time series of vertical displacements derived from different datasets. For the locations of the time series, see Figs. 5–8. For each dataset, the first date is assumed as the reference date for the time series, and the values for the other time epochs are calculated with respect to that date.

The second row (b) in Figure 5.9 shows time series for a subsiding point in an agricultural area near Tehran that is indicated by the square in Figure 5.5. All of the datasets except for TSX-SL cover this area and delineate rapid subsidence in the area. Another time series (c) is plotted for a point near the IKA airport. A comparison of the time series from 2003–2010 with those from 2015–2017 shows that the rate of subsidence at this location has accelerated in recent years. The last time series (d) is plotted for a point in the Varamin subsidence area. This area is only covered by Envisat track 378 and the Sentinel-1 datasets. Therefore, there is a 10-year gap in the time series from 2005 to 2015 that makes it impossible to study the variations of the subsidence over time.

5.6.5. Accuracy, Precision and Consistency Assessments

In this section, we assess the accuracy, precision and consistency of the subsidence rates derived from the individual SAR datasets. To evaluate the accuracy of the results, the vertical displacement rates derived from InSAR (neglecting horizontal movements) are compared to independent results obtained from leveling measurements. Along each leveling profile, the vertical movement is extracted from the InSAR results from two Envisat datasets (tracks 378 and 414), which cover the period in which the leveling measurements were performed. A shift between each leveling profile and the vertical component derived from InSAR is calculated and subtracted from the leveling measurements

to bring the results into the same datum. The results (Figure 5.10) show that the InSAR and leveling measurements are generally in very good agreement and show similar patterns of ground deformation. However, at some locations, there are differences of a few centimeters per year, and the InSAR results fall outside the error bars of the leveling data. To investigate the differences, the RMS of the difference between the InSAR and leveling measurements is calculated for each profile. The maximum RMSE value of the individual profiles are 4.3 and 3.7 cm/yr for Envisat tracks 414 and 378, respectively. An overall RMSE is also calculated from the differences between all of the leveling profiles and the InSAR vertical displacement rates. The overall RMSEs are 2.9 cm/yr and 2.8 cm/yr for tracks 414 and 378, respectively. The RMSEs are within a few centimeters per year, which shows the small inconsistency between the vertical displacements calculated by independent measurements.

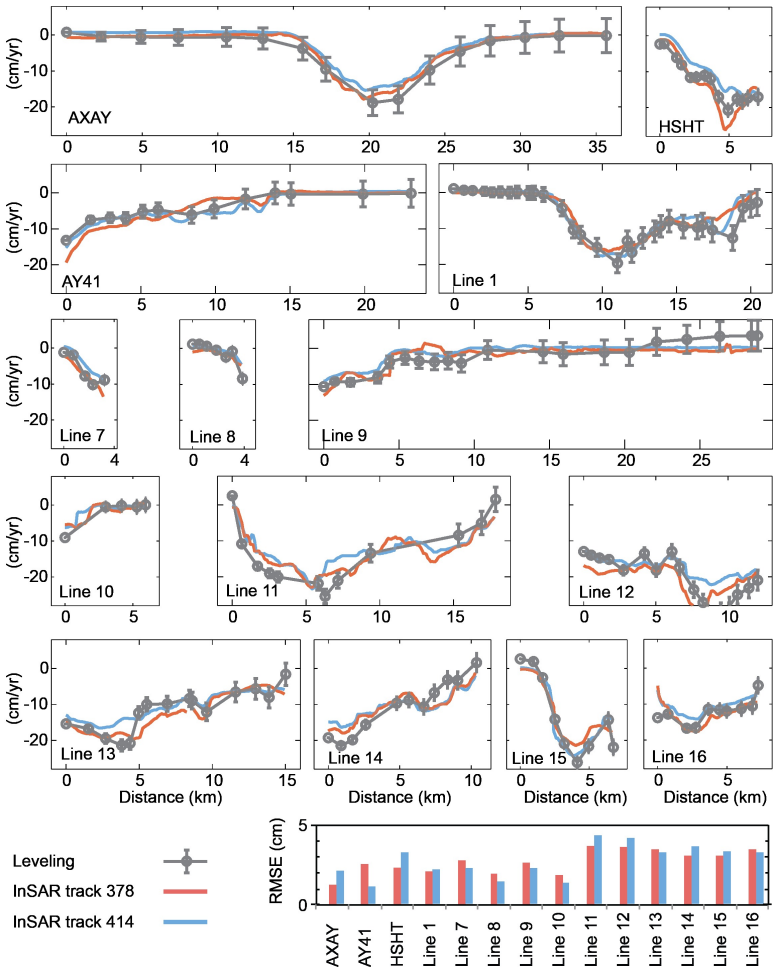


Figure 5.10.: Comparisons of vertical displacements estimated from Envisat tracks 378 and 414 to leveling measurements. The error bars represent the precision of the levelling measurements. The red and blue lines show vertical displacements derived independently from Envisat tracks 378 and 414, respectively, by converting LOS to vertical. The chart shows the RMSEs of the vertical estimations with respect to the leveling measurements.

The cm-scale difference between the InSAR and leveling measure- ments is partially generated because we neglected the horizontal component in the InSAR estimation of the vertical displacement. However, two other factors might also have had minor effects. First, the time spans of the leveling

and InSAR observations are not exactly the same. Second, the leveling intervals are not exactly one year; therefore, the annual rate of the height differences might be over- or under-estimated.

Variations of the estimated subsidence rates in areas where we do not expect displacements to occur can provide an estimate of the precision of the measurements. To assess the precision of the estimated average rates of displacement, we calculated the standard deviations of the results in an 8-km^2 area outside the subsidence zone (white box in Figure 5.5). The estimated standard deviations vary from 0.13 cm/yr to 0.50 cm/yr for the different datasets. Therefore, we can conclude that the precision of the displacement rates is better than 0.5 cm/yr.

To assess the consistency, the results from different datasets are compared. The area covered by the TSX-SL dataset is chosen as the reference area because it is covered by all of the datasets. The results from different datasets are resampled to a common 50-m grid and converted from LOS to vertical by assuming that the horizontal components of the displacement are negligible. The vertical displacements are then compared with the results from S1-35 (Figure 5.11). The results are in general agreement with some minor inconsistencies.

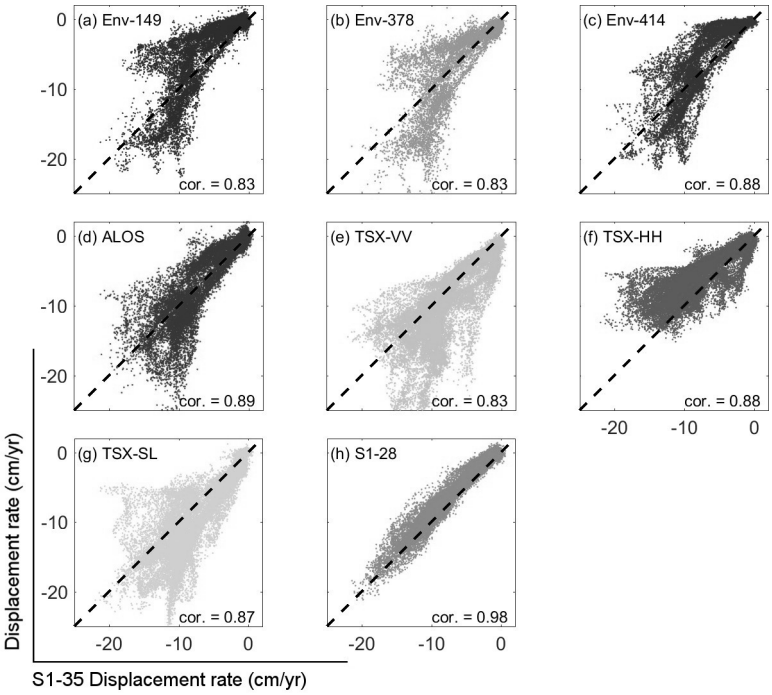


Figure 5.11.: Inter-consistency of the vertical displacement rates derived from different datasets. The vertical displacement rate from dataset S1-35 is chosen as a reference. The dashed lines represent identical vertical displacement rates.

The correlation between the displacement rates of S1-35 and those from the other datasets varies between 0.83 and 0.98, which confirms the general consistency of the results. The results from the two Sentinel-1 datasets are in very good agreement with a 0.98 correlation. However, the results from the other datasets show lower correlations with S1-35. Among them, Env-149 and Env-378, which cover the oldest time windows, show the lowest correlations with S1-35 (0.83).

We assume that the inconsistencies are mainly because of the temporal variations of the land subsidence. To confirm this, we chose the Env-414 dataset as a reference; the correlation with the other Envisat datasets increased to 0.97 and 0.95 for Env-149 and Env-378, respectively. Because the Envisat datasets generally cover similar time spans, the correlations between them are high.

The high consistency between the ascending and descending results of Sentinel-1 confirms our assumption that the vertical displacement has the major contribution to the displacement. Our analysis of the three study areas shows that the east-west displacements reach to up to 3, 1.5, and 3 cm/yr to the southwest of Tehran, at IKA airport and in Varamin, respectively. Additional information about the horizontal vs. vertical displacements is provided in the supplementary materials.

5.7. Discussion

5.7.1. Structural Control of the Displacement

Close inspections of the area of subsidence southwest of Tehran and the location of the main faults in the region indicate that the observed subsidence in this region does not have a tectonic origin. As shown in Figure 5.12, the main geologic structure in the Tehran Plain is the North Tehran Fault (NTF), which is a north-dipping thrust fault that passes just to the north of Tehran (Abbassi and Farbod, 2009). However, the extent of the ground deformation that we identified in western Tehran is very localized and does not extend across all of the NTF's footwall, as would be expected if tectonic motion was the source of deformation. Moreover, the high rate of surface deformation, which exceeds 25 cm/ yr at some locations, is not consistent with the long-term horizontal shortening rate of the North Tehran Fault, which is estimated to be <0.5 cm/yr (Bachmanov et al., 2004).

Similar arguments can be made about the source of deformation in the Varamin area. The nearest fault zone to the Varamin area is the Pishva Fault, which is a 30-km-long thrust structure with an overall NW-SE orientation that accommodes < 0.3 cm/yr of north-south shortening across the Alborz Range (Vernant et al., 2004). However, the deformation field resulting from this thrust motion is compatible neither with the shape nor with the amount of ground displacements we derive for the Varamin area. Therefore, we rule out a tectonic origin as the source of the surface deformation revealed by the InSAR results. Instead, considering the decreasing hydraulic heads illustrated in Figure 5.14 coupled with the geologic structure of the underlying sediments in Tehran, which are composed of unconsolidated, fine-grained elements, we associate the ongoing deformation to land subsidence caused by extensive aquifer depletion.

Geologic structures and Quaternary faults can influence the shape and spatial extent of the subsidence areas in groundwater basins, as has been observed in Las Vegas, Nevada (Bell et al., 2008) and Mashhad, Iran (Motagh et al., 2007) and Rafsanjan (Motagh et al., 2017), Iran. In the Tehran region, the shape of the western subsidence bowl does not appear to follow the trends of major mapped faults in the region. By contrast, the round lobe of subsidence in Varamin appears to be influenced on its northeastern border by the Pishva Fault, as shown in Figure 5.12. This fault zone might act as a hydrological barrier in the area, separating sediments of differing compressibilities between the Varamin Plain to the west and other Quaternary units to the east, which in turn impedes the eastward

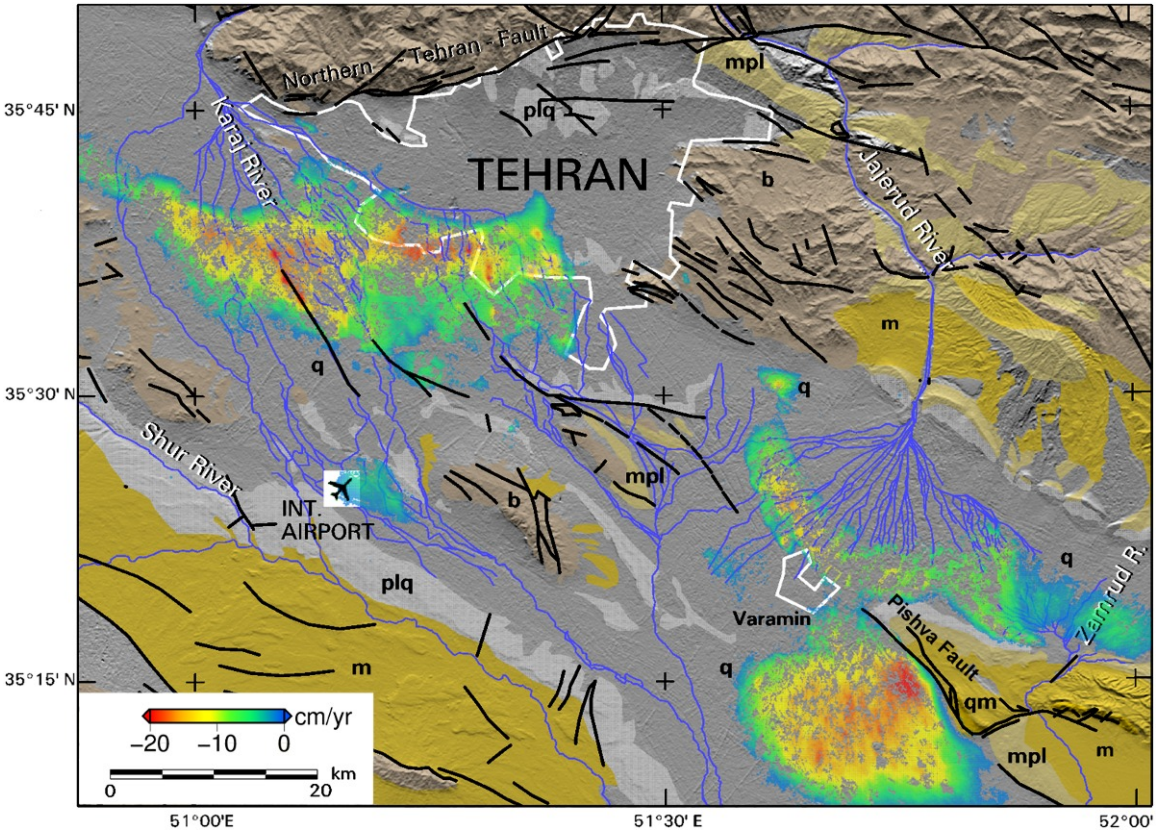


Figure 5.12.: Displacement map showing vertical displacement rates for the period between March 2015 and March 2017 derived from the decomposition of Sentinel-1 line-of-sight measurements. Assuming that the precision of the observations is 0.5 cm/yr, the displacement rates higher than −1 cm/yr (2σ) are masked out, and values lower than −1 cm/yr are taken as reliably measured subsidence. The velocity map is overlaid on a shaded-relief map generated from the SRTM digital elevation model. The black lines indicate the main faults and fracture zones in the Tehran region. The small letters indicate geological units in the Tehran Plain; q: Quaternary, including Tehran Alluvium; plq: Kahrizak Formation, Plio-Pleistocene conglomerates; mpl: Hezardareh Formation, Mio-Pliocene conglomerates; m: Upper Red Formation, Miocene sandstones, mudstones, shales and evaporates; qm: Qum Formation, Oligocene-Miocene limestones and marls; b: Basement undifferentiated, mainly Mesozoic-Eocene volcanic and sedimentary units. The geological units and faults were simplified from the reference maps in Amidi et al. (1984) and Haghipour et al. (1987) and the 1:100,000 geological map of Tehran from the National Geoscience Database of Iran.

propagation of subsidence. Moreover, the difference in sediment thickness across this fault may have contributed to this discontinuity.

5.7.2. Comparison with Groundwater

In Figure 5.13, displacement time series from the Envisat and ALOS datasets are merged and compared with groundwater data at several locations southwest of Tehran at which groundwater measurements were available. Because we only have access to groundwater data collected before 2010, only time series from Envisat and ALOS are used in this analysis.

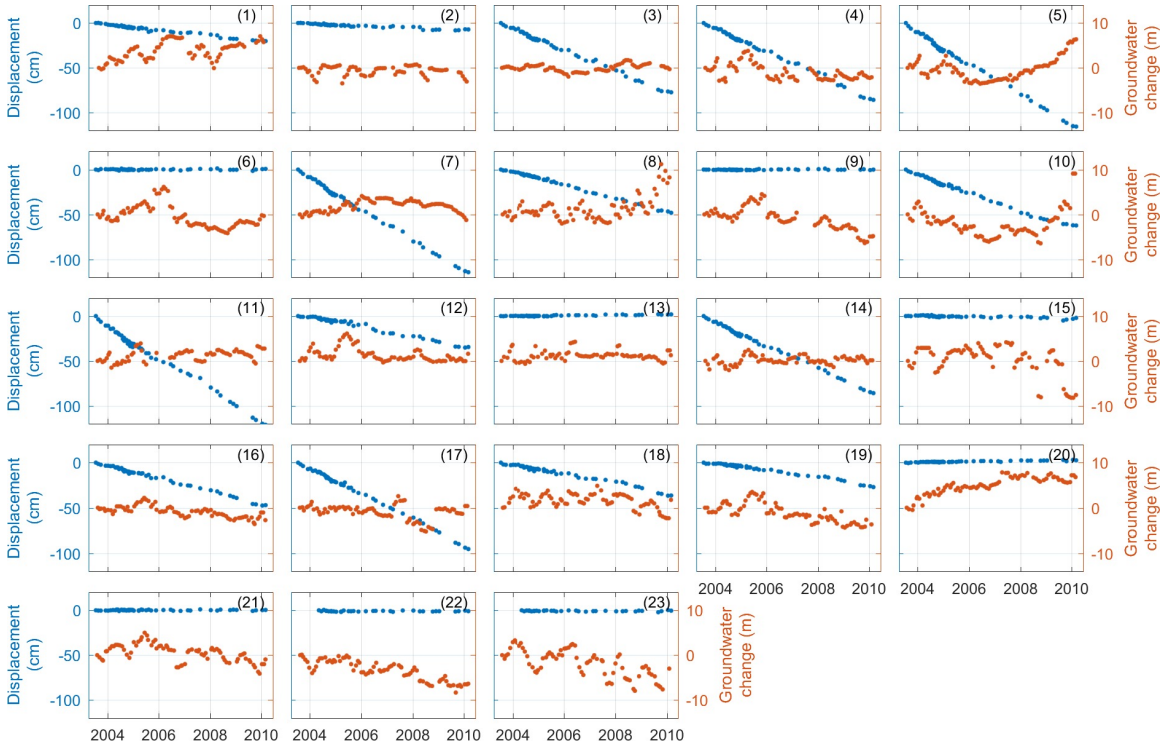


Figure 5.13.: Comparison of time series of vertical displacements and groundwater level changes at different locations. The numbers represent the measurement wells indicated in Figure 5.5-c. July 2003 is the reference date to estimate the groundwater variations.

The behavior of the groundwater differs significantly at different locations. In some wells, we observe a clear drop in the groundwater level, whereas at other locations, it is stable or even rising. Some of the rise in groundwater might be caused by groundwater management and the resulting decrease in water extraction. However, at some wells in urban areas, such as well 20, the increase is likely related to the direct disposal of sewage water into the ground due to the poor development of sewage treatment in the past. It is also important to note that at some locations, the measurement wells might not be deep enough to accurately measure the groundwater level.

A comparison of the groundwater levels with the InSAR displacement time series shows several discrepancies in the link between groundwater and surface displacements. At some locations, such as wells 10 and 16 to 19, ground subsidence coincides with decrease in the groundwater level. However, at other locations, the long-term trend of ground displacement does not follow the groundwater variations. For example, at wells 11 and 14, the groundwater is stable, but the land subsidence is significant. Interestingly, at wells 1 and 20, the groundwater level rises, whereas we observe land subsidence at well 1 and stable ground at well 20. This inconsistency between the groundwater and surface displacement indicates that the long-term trend of subsidence is driven mainly by the long-term decline of groundwater in the past decades.

To investigate the long-term variations of groundwater southwest of Tehran (box (a) in Figure 5.4), the average of the data from different wells is presented in Figure 5.14-a. The average groundwater head decreased by nearly 10 m from 1984 to 2010. However, its rate was not constant over time. Two periods of rapid decline in groundwater occurred from 1985 to 1992 and from 1995 to 2003, and the

groundwater level recovered slightly between them. After those periods, there was a slight increase in the groundwater level between 2003 and 2008 followed by a gentle decline until 2010. There was also a seasonal fluctuation in the groundwater level of approximately 1m in response to annual pumping and recharge, which was caused by the high demand for water in the summer and the relatively wetter winters.

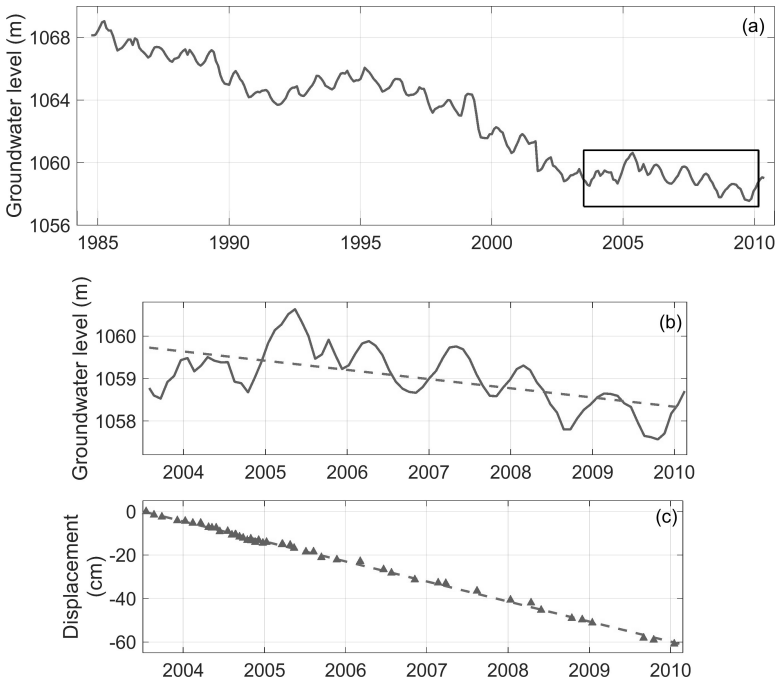


Figure 5.14.: (a) Average groundwater level for the Tehran Plain between 1984 and 2010. The groundwater level decreased by approximately 10 m during this period. Periods of rapid and gentle declines, slight recoveries and seasonal fluctuations are observable in the graph. The black box represents the time window for which the groundwater measurements coincide with the InSAR measurements. (b) Close-up view of groundwater changes and the trend line (indicated by the dashed line) for the time period of the InSAR measurements. (c) Average vertical displacement derived by combining the Envisat and ALOS time series of all points with subsidence rates greater than 2 cm/yr to the southwest of Tehran. The trend is shown by the dashed line.

Furthermore, the average time series of all points with subsidence rates higher than 2 cm/yr is used as an average representation of the subsidence southwest of Tehran (the estimated parameters in Eq. 5.2 are $a = -9$ cm/yr and $b^m = -1$, –30, –35, and –42 cm for the Env-149, Env-378, Env-414, and ALOS datasets, respectively). The combined time series is then compared with the average groundwater data for the same time period.

Figure 5.14-b shows the water level decline (approximately 1.4 m) in the time period covered by the InSAR time series (6 years and 8 months). Over the same time period, a constant trend of subsidence (60 cm) is observed in the displacement time series shown in Figure 5.14-c.

Although the displacement time series is dominated by a strong declining trend, removing the trend from the time series reveals the fluctuation of approximately ±2 cm between 2003 and 2010 (Figure 5.15- b). During the same time period, the groundwater level deviates from its trend line by a maximum of ±1.3 m (15-a).

To investigate the correlation between the seasonal variations in groundwater and surface displacement, XWT is applied to the data. The results are shown in Figure 5.15-c and indicate a strong in-phase correlation with a 1-year period between the variations in groundwater and displacement. This suggests that the displacement variations occur in response to the seasonal changes in the groundwater level due to natural recharge/discharge by rain and snowfall. There is a time lag of approximately 45 days between the seasonal variations in the groundwater and the surface displacement.

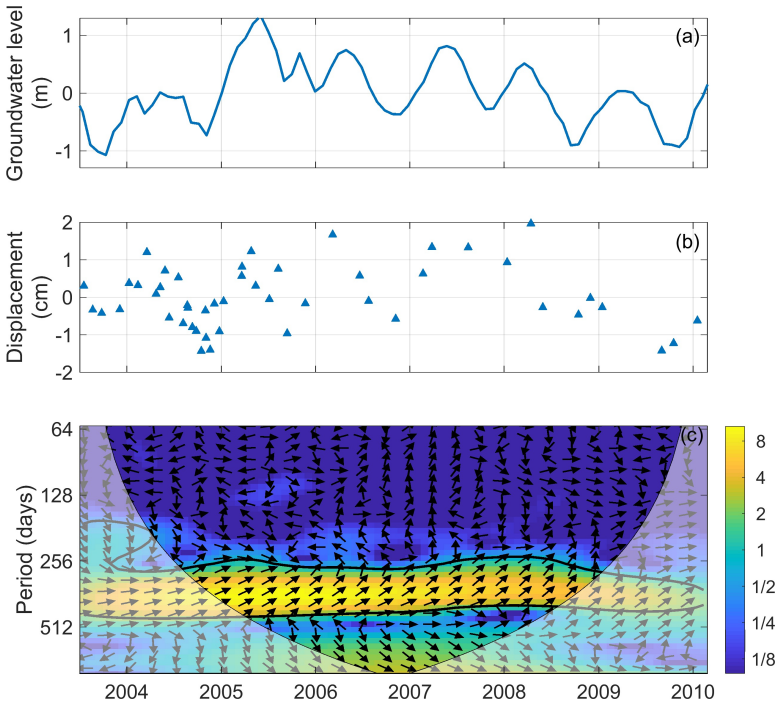


Figure 5.15.: Short-term variations of groundwater and displacement and their correlation. (a) Deviations of groundwater from its trend line. (b) Deviations of displacement from its trend line. (c) Cross-wavelet power between the groundwater and displacement. The color bar represents the common wavelet power of both time series. The 5% significance level against red noise is shown by the black contour. The only significant component in this plot occurs at approximately the 365-day period, which corresponds to the seasonal variations in both time series. The vectors indicate the phase difference between the two time series. The vectors pointing to the right and left correspond to in-phase and anti-phase correlations, respectively. The vectors in the peak band at approximately 365 days mostly point to the upper right, which corresponds to the groundwater leading the surface displacement by approximately 45 days. The lighter shade indicates the cone of influence (COI), where the edge effects might disturb the wavelet analysis results.

5.7.3. Elastic vs. Inelastic Compaction

A key question raised by the results of this study is whether the subsidence observed in Tehran is recoverable (elastic) or irrecoverable (inelastic). The redistribution of groundwater in an aquifer system and the resulting changes in the pore pressure lead to surface deformation in groundwater basins (Galloway et al., 1998). A decrease in hydraulic head results in a higher effective stress, causing the soil skeleton to compact. Conversely, a rise in the groundwater level decreases the effective stress by increasing the pore fluid pressure, resulting in an expansion of the soil skeleton. This elastic

(recoverable) deformation can occur in both aquifers and aquitards. However, if the stresses caused by groundwater decline exceed the maximum previous stress (preconsolidation stress), then the aquifer system experiences permanent (inelastic) compaction due to the consolidation of aquitards (Galloway et al., 1998; Helm, 1975, 1976; Hoffmann et al., 2003; Lu and Danskin, 2001).

If the subsidence turns into uplift as a result of a major recovery in the groundwater level, the deformation of the aquifer system would be dominated by its elastic regime. Conversely, if subsidence continues or there is little sign of rebound in spite of a major recovery in groundwater levels, the irreversible compaction of aquitards would be the main cause of land subsidence. A comparison with groundwater measurements in the region provides valuable insight into the elastic/inelastic regime of deformation.

In the study area, the long-term trend in the time series of displacement occurs due to the intensive pumping and subsequent compaction of the reservoir over the last 3 decades, and it has likely resulted in inelastic deformation of the aquifer system, which is manifested in form of earth fissures and cracks. The inconsistency between the groundwater variations and surface displacements at individual wells supports the hypothesis that a large part of the displacement in the southwest of Tehran is inelastic. In contrast, the rapid response of the surface displacements to short-term variations in the groundwater is the only clear elastic deformation we observe in the region.

The trend of the average displacement time series (for all points with subsidence rates higher than 2 cm/yr) between 2003 and 2010 southwest of Tehran shows that the surface subsides by approximately 9 cm each year and fluctuates by approximately ± 1.5 cm. The Sentinel-1 time series of the displacement show the same order of magnitude of seasonal variations. However, the average subsidence rate decreased to 7 cm/yr in the Sentinel-1 results. Assuming that the long-term subsidence is inelastic and the short-term variations are the only elastic component that we observe, the elastic/inelastic ratios for each year are approximately 0.3 for the period between 2003 and 2010 and 0.4 between 2015 and 2017. This ratio confirms predominantly inelastic deformation.

For overexploited aquifer systems subjected to large overdrafts, the elastic/inelastic ratio tends to be close to zero, as is the case for Tehran. A large portion of the deformation in such aquifers is often inelastic, which results in irreversible compression of aquitards due to the rearrangement of the granular structure (Galloway and Burbey, 2011; Hoffmann et al., 2001). Because the inelastic compressibility of aquitards is generally 1–3 orders of magnitude greater than the elastic compressibilities of both aquitards and aquifers (Pavelko, 2004), any recharge and groundwater management in this aquifer system can only recover a portion of the compaction (Schmidt and Bürgmann, 2003).

5.8. Conclusion

This study presents an InSAR time series investigation of surface displacements for the period of 2003–2017 in the Tehran Plain, Iran. A total area of approximately 1300 km^2 is affected by land subsidence in this region, including the southwestern part of Tehran, IKA international airport and Varamin County. Multi-sensor InSAR time series analysis over 14 years reveals a consistent pattern

of subsidence in the study area. The maximum rates of subsidence exceed 25 cm/yr to the southwest of Tehran, 5 cm/yr near IKA airport, and 22 cm/yr in Varamin County.

The analysis of the observed displacements coupled with information obtained from geological mapping and groundwater levels in the region suggests that excessive groundwater withdrawal is the main cause of the surface deformation. The subsidence has two main patterns: a long-term displacement as a result of declines in the groundwater level in recent decades and short-term variations related to seasonal groundwater discharge and recharge. Our analysis of the area southwest of Tehran shows that the non-recoverable portion of the deformation is likely to be dominant with an average elastic/inelastic ratio of approximately 0.4. Unless effective groundwater management is implemented, ongoing subsidence in Tehran is expected to cause further damage to infrastructure, particularly in the regions of high displacement gradients in the urban areas of Tehran and near IKA airport.

A comparison of the different sensors reveals that regular data acquisition and high spatial and temporal resolutions helped TerraSAR-X and Sentinel-1 to provide better results for investigations of land subsidence. In general, Sentinel-1 provides a more complete spatial picture of land subsidence due to its large spatial coverage. Therefore, it has great potential to extend the monitoring to other subsidence basins and perform analyses at regional to country scales. Sentinel-1 also provides temporally dense time series of elevation changes with different geometries. The data are freely available shortly after each acquisition. Therefore, semi-real-time InSAR time series analyses are possible.

5.9. Acknowledgments

This work was supported by the Initiative and Networking Fund of the Helmholtz Association in the framework of the Helmholtz Alliance 'Remote Sensing and Earth System Dynamics'. The TerraSAR-X data were provided by DLR under proposal number GEO1916, and the Envisat data were provided by the European Space Agency (ESA) under CAT-1 project ID 31014. The original ALOS data are copyright Japanese Aerospace Exploration Agency and were provided under proposal 1162. The Copernicus Sentinel data were provided by ESA. Some of the figures were generated using Generic Mapping Tools (Wessel et al., 2013). We would like to thank Siavash Arabi from the National Cartographic Center of Iran (NCC) for providing leveling data, Leila Karimi from University of Tehran for sharing groundwater level measurements from Tehran Regional Water Authority, and Hans-Ulrich Wetzel from GFZ for preparing geological map of Tehran. We are grateful to Bahman Akbari from Forest, Range and Watershed Management (FRWM) organization of Iran for supporting us during the field work. We acknowledge constructive reviews by Pascal Castellazzi and three anonymous reviewers, whose comments greatly improved the quality of the original manuscript.

5.10. Supplementary materials

5.10.1. Significance of Tropospheric Delay

We processed daily ERA-I data at 12:00 from 2000 to 2018 to estimate the tropospheric delay in the study area. The delays were estimated in the range direction of 40°off-nadir. The same reference

area was used as for the InSAR time series analysis. In the time series analysis, a linear ramp is removed from the unwrapped interferograms to correct for the orbital ramp and the long-wavelength spatial trend of the troposphere. Therefore, we also estimate and remove a linear ramp from each ERA-I estimation of the tropospheric delay. The remaining signal shows the seasonal variations in the tropospheric delay. However, its amplitude is less than 0.4 cm to the southwest of Tehran (figure 5.16). Therefore, seasonal variations of the displacement with magnitudes larger than 0.5 cm are not likely to be generated by tropospheric delays.

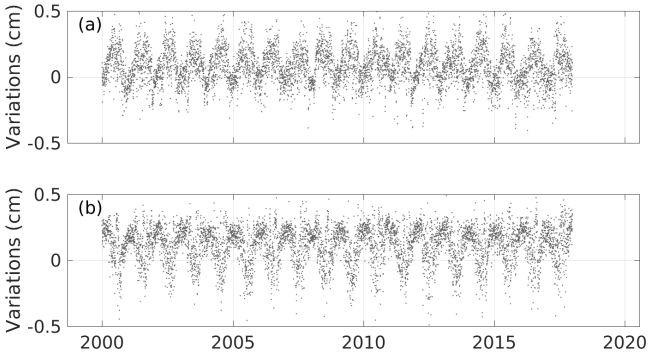


Figure 5.16.: Temporal variations of troposphere at locations indicated by black square and triangle in in figure 5.5. Time series of displacement for these locations are illustrated in figure 5.9.

5.10.2. Decomposition of LOS Measurement

We use coinciding InSAR measurements provided by Sentinel-1 with different geometries to estimate the vertical and east-west components of displacement. The results are shown in figure 5.17. The results confirm that the subsidence is the main component of the displacement and that the east-west component is relatively small. Most of the east-west movement occurs around the subsidence areas and point toward the local peak of the subsidence zones.

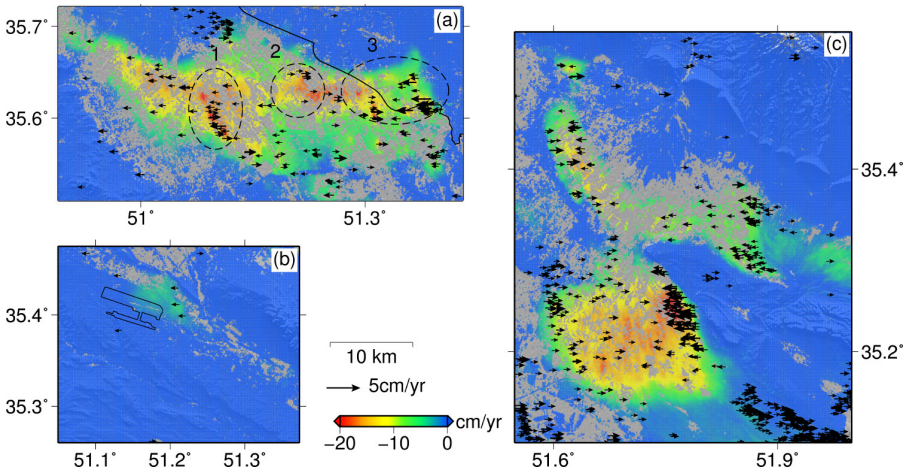


Figure 5.17.: Vertical and east-west displacement rates derived from the decomposition of Sentinel-1 ascending and descending tracks (a) southwest of Tehran, (b) near IKA airport, and (c) in Varamin County. Colors show the vertical displacement and the vectors represent the horizontal displacements.

5.10.3. Under/Overestimation of Displacement Rates

To investigate whether the displacement rates are over/underestimated by the TerraSAR-X datasets that cover periods shorter than one year, we analyzed the Sentinel-1 data in descending orbit for different periods of time. The results in figure 5.18 confirms that a dataset covering October to August underestimates the displacement rate because it mostly covers the cold season. In contrast, a dataset covering January to September overestimates the displacement rate because it mostly covers the hot season.

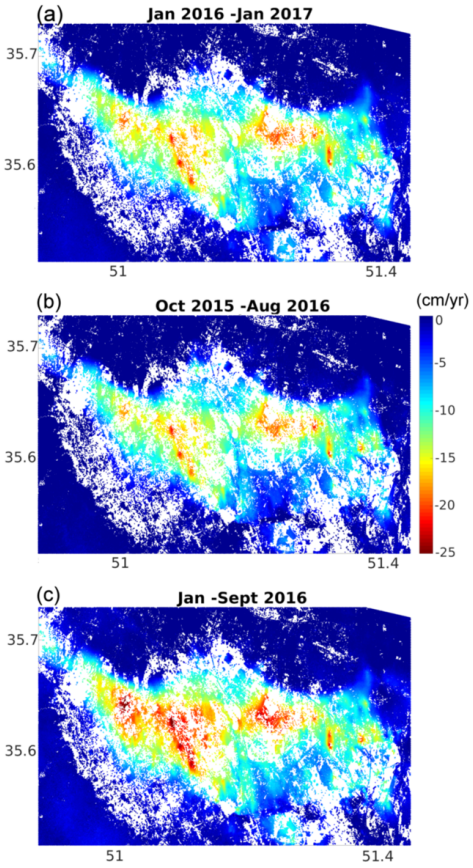


Figure 5.18.: Displacement rates derived from analysis of S1-35 dataset for different periods of time. (a) a one year period dataset correctly estimates the displacement rate. (b) a dataset covering October 2015 to August 2016 (similar to TSX-HH dataset) underestimates the displacement rate. (c) a dataset covering January to September 2016 (similar to TSX-VV dataset) overestimates the displacement rate.

Chapter 6

Sentinel-1 InSAR Measurement of Anthropogenic Deformation in Germany

This chapter was published as:
Haghshenas Haghighi, M., Motagh, M., 2017. Sentinel-1 insar over germany: Large-scale interferometry, atmospheric effects, and ground deformation mapping. zfv – Zeitschrift für Geodäsie, Geoinformation und Landmanagement 4, 245 – 256.

6.1. Summary

In this study, three highlights of Sentinel-1 (S-1) Interferometric Synthetic Aperture Radar (InSAR) over Germany are presented to evaluate the potential and opportunities provided by this European SAR mission. Firstly, large-scale interferometry across the country is presented and analyzed against atmospheric models from ERA-Interim and GNSS (Global Navigation Satellite System) to assess the perspective provided by S-1 for atmospheric modeling and large-scale displacement analysis. We then analyzed localized deformations related to anthropogenic activities at two different regions using S-1 InSAR time-series analysis. In the first case study, small-magnitude (mm/yr) displacement related to underground gas storage and landfill compaction in Berlin is investigated. Despite low rates of displacement, Persistent Scatterer InSAR (PSI) using an extensive collection of S-1 data reflects both the long-term trend and seasonal variations related to dynamics of gas storage in the reservoir. We estimate long-term surface uplift of up to 2 mm/yr between October 2014 and January 2017 and seasonal variations of up to 2 cm due to charge and discharge of the reservoir during summer and winter periods. An old demolishing landfill NW of Berlin was also found to be subsiding with rates as much as 8 mm/yr. The other case study is a brown coal mining area south of Leipzig. Time-series of S-1 data using the Small BAseline Subset (SBAS) approach provides new insights into mining-induced deformations in this region. Our results show rapid subsidence of up to 4 cm/yr between October 2014 and April 2017 in two active open-pit mining areas in the region.

6.2. Introduction

Since 1991, when the ERS-1 satellite was launched and then followed by ERS-2 and Envisat, European Space Agency (ESA) has been providing repeated SAR data for over two decades. Although ERS and Envisat missions were originally designed to be used mainly for oceanic applications, they also provided spectacular opportunities for scientists to use the interferometric capability of the system for a broad range of geophysical (Hole et al., 2007; Kumar et al., 2008; Motagh et al., 2008a; Pritchard and Fielding, 2008; Samsonov et al., 2014) and environmental (Castel et al., 2000; Santoro et al., 2007; Lu and Kwoun, 2008; Xiuming et al., 2008; Millin-Chalabi et al., 2014) applications. Using SAR acquisitions, repeated approximately from the same point in space at different times, InSAR provides the capability to derive the path-length differences in the scale of the carrier wavelength and below due to changes in topography (Massonnet and Feigl, 1998; Bürgmann et al., 2000)). However, conventional InSAR suffers from some severe limitations when unwanted signals in the interferograms, caused by various sources such as variations of scattering properties of earth's surface or atmospheric conditions through time, surpass the displacement signal (Hooper et al., 2012). Multi-temporal interferometric methods (MTI) including Persistent Scatter InSAR (PSI) (Ferretti et al., 2001; Hooper et al., 2004) and Small Baseline Subset (SBAS) (Berardino et al., 2002) present a specific class of processing that exploits multiple SAR images acquired over an area in order to overcome these limitations and separate the displacement signal from other unwanted sources. The techniques are widely used by scientific communities to investigate surface deformations related to a broad range of geophysical (Hooper and Zebker, 2007; Gourmelen et al., 2010; Haghshenas Haghighi and Motagh, 2016; Motagh et al., 2017) and engineering (Fornaro et al., 2013; Milillo et al., 2016; Emadali et al., 2017) applications.

The idea of displacement monitoring in wide areas using standard InSAR or advanced InSAR time-series analysis has been an interesting topic in the last years (Motagh et al., 2008b, 2010; Adam et al., 2013; Francesca et al., 2013; F. Raspini, 2015). A major limiting factor to this purpose was the non-availability of both spatially and temporally homogeneous SAR dataset in a nationwide or continental scale. The launch of Sentinel-1A in 2014, followed by Sentinel-1B in 2016, revolutionized the availability of SAR data by regular acquisition from every part of the world. S-1 obtains several frames of SAR data (250 × 250 km2) along each observation track. Mosaicking the SAR frames provides then the possibility to monitor even larger areas along a specific track.

Sentinel-1 constellation is the follow-on to the former ESA SAR missions but is specifically designed to be suitable for InSAR applications and displacement monitoring. Therefore, its imaging parameters, revisit time, spatial resolution, scene coverage, and orbital status are optimized for InSAR applications (Salvi et al., 2012).

The operational lifetime of S-1 is expected to be 20 years. With both Sentinel-1A and Sentinel-1B in orbit this mission currently provides more than 10 TB of products every day. Based on its acquisition plans, SAR images from the same orbit are acquired every 6 days over Europe as well as some hotspots with very rapid changes like Greenland. In other parts of the world SAR data are acquired every 12 or 24 days.

In this study, three highlights of using S-1 InSAR over Germany are presented. In Germany, InSAR has been widely used in the past decades to address a variety of geological, geophysical, and engineering applications at local and/or regional scale, e.g. urban uplift due to geothermal energy production (Lubitz et al., 2013; Heimlich et al., 2015), monitoring tunneling processes (Liu et al., 2014), post-mining activities (Kircher et al., 2003; Wegmuller et al., 2004; Samsonov et al., 2013), deformations caused by subsurface mining (Wegmuller et al., 2000; Walter et al., 2009), pipeline monitoring (Werner Zirnig, 2004), deformations induced by oil extraction (Fuhrmann et al., 2016), and water vapor mapping (Alshawaf et al., 2012).

Different SAR sensors, especially European ERS-1/2 and Envisat, and German TerraSAR-X satellites acquired SAR data over Germany in the last two decades. After the launch of Sentinel-1 constellation with its 6-day repeat interval, however, the availability of regular SAR data acquisition over the country has been dramatically increased. In total, as illustrated in Figure 6.1, six ascending and six descending orbits of S-1 cover the whole country. Furthermore, there are some overlaps between data from neighboring orbits. Consequently, the coverage frequency of S-1 is as short as 1 to 2 days at any part of the country.

In the next sections of the paper, we first briefly describe InSAR processing of S-1 and InSAR time-series approaches. Then, we present an example of a large-scale interferogram with a short temporal baseline over Germany and evaluate it against tropospheric models provided by ERA-Interim and GNSS. In the following sections, two areas subject to localized displacements are investigated using S-1 InSAR time-series analysis.

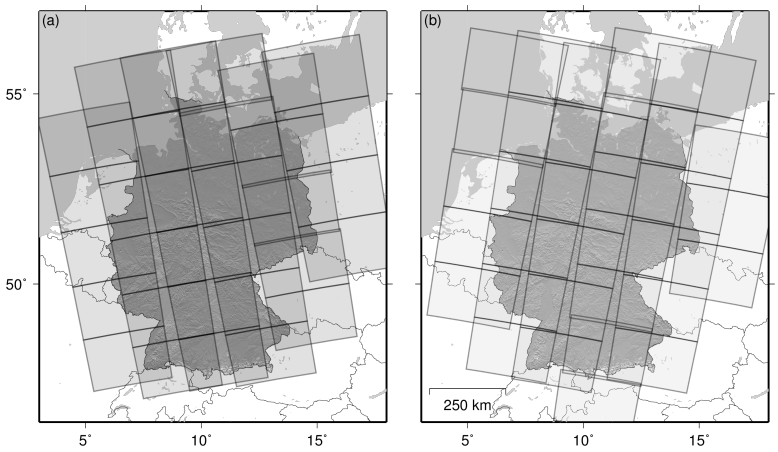


Figure 6.1.: Coverage of Sentinel-1 SAR images using the standard acquisition mode over Germany (highlighted by the shaded relief map) in (a) ascending and (b) descending tracks. Along each orbit, a few frames of SAR images are acquired which are represented by thick polygons.

6.3. Sentinel-1 InSAR Processing

S-1 can collect SAR images in four different modes. StripMap (SM) and Extra Wide-swath (EW) are two modes that are implemented for consistency of the SAR data with those acquired by ERS and Envisat. Over the open ocean, the data is acquired in Wave Mode (WM). Nonetheless, Interferometric Wide-swath (IW) is the standard acquisition mode of S-1 over land, which is suitable for interferometric applications. In this mode, the data covers a swath of 250 km with a spatial resolution of $\sim 5 \times 20$ m^2 in range and azimuth directions (Torres et al., 2012). To produce such a large coverage from a single acquisition in space, the SAR data in IW mode is acquired using the Terrain Observation with Progressive Scan (TOPS) operation (De Zan and Monti Guarnieri, 2006).

A TOPS SAR image consists of three sub-swaths with ∼2 km overlap, and each sub-swath is formed from several slightly overlapping subsets called bursts (see Figure 6.2). The sensor does not record each sub-swath continuously, but records one burst of a specific sub-swath while the antenna is moving along its orbit. Then the antenna is steered so it can record one burst of another sub-swath. As a result of steering the antenna, a Doppler variation is present in the azimuth direction. To prevent this from causing any phase jump between subsequent bursts, the accuracy of coregistration between image pairs should be in the order of 1/1000 of azimuth resolution which is equivalent to a few centimeters on the ground (Gonzáález et al., 2015).

Traditional coregistration approaches based on image matching cannot reach such a high level of accuracy needed for TOPS interferometry. However, together with orbital state vectors and terrain heights they can be used as a first order estimation of coregistration parameters (Yagüe-Martínez et al., 2016). Then, in an iterative approach, double difference interferograms in the overlapping areas between consecutive bursts are generated, and the coregistration parameters are refined by spectral diversity methods as described in Scheiber and Moreira (2000).

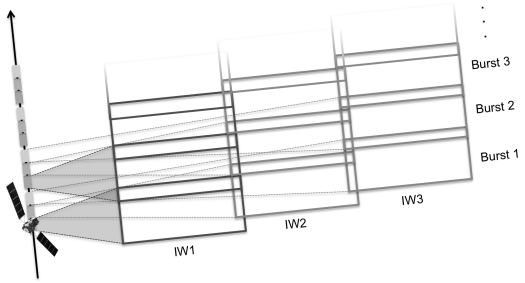


Figure 6.2.: Schematic illustration of Sentinel-1 TOPS mode imaging. The SAR image is acquired in three overlapping sub-swaths (IW1 to IW3) and each sub-swath consists of several overlapping bursts.

After precise coregistration of S-1 image pairs, they can be used, similar to other traditional SAR data in StripMap mode, to produce the interferometric phase, which can be expressed by the following equation:

$$\Delta\phi = \phi_{orb} + \phi_{topo} + \phi_{def} + \phi_{atm} + \phi_{noise} \tag{6.1}$$

The interferometric phase in Equation 6.1 is the sum of contributions from several factors including orbital status (ϕ_{orb}), topography (ϕ_{topo}), surface displacement (ϕ_{def}), atmospheric artifacts (ϕ_{atm}), and noise (ϕ_{noise}). When the interesting parameter is displacement, all other terms should be accounted for and removed from the interferometric phase.

The phase difference from orbital status is caused by the shift in the orbital path of two SAR acquisitions. Thanks to precise orbital state vector data of the Sentinel-1 satellites in the order of a few centimeters, this contribution can be compensated accurately (Yagüe-Martínez et al., 2016). The topographic phase contribution can be expressed as

$$\phi_{topo} = -\frac{4\pi}{\lambda}\frac{B_{perp}h}{R\sin\theta} \tag{6.2}$$

where λ, h, R, θ, and B_{perp} are wavelength (5.6 cm for S-1), elevation of the target pixel above reference ellipsoid, distance between sensor and ground target, incidence angle, and perpendicular baseline of the interferogram, respectively. The topographic phase contribution is proportional to the perpendicular baseline of the interferogram. Therefore, smaller perpendicular baselines are preferred for deformation monitoring because they reduce the residual effect that might remain in interferograms by not completely removed topographic contributions, e. g. due to errors in the reference DEM (h). Because S-1 is designed to be suitable for deformation analysis, its orbit is maintained in a way that the perpendicular baseline is kept small in the order of 150 m (Yagüe-Martínez et al., 2016) and as a result, the sensitivity of S-1 interferograms to inaccuracies of DEMs is low.

The interferometric phase is also affected by differences in propagation delays through troposphere or ionosphere in the time of SAR image acquisitions. C-band SAR images in mid-latitudes are less susceptible to ionospheric effects (Hanssen, 2001), and hence the major atmospheric contribution in S-1 interferograms in mid-latitudes comes from the troposphere. This effect is driven by the changes in refractivity of the troposphere at the time of two SAR acquisitions. The two-way slant range delay ϕ_{tropo} for a specific target at elevation h_1 in a SAR image can be expressed as:

$$\phi_{tropo} = \frac{-4\pi}{\lambda} \frac{10^{-6}}{\cos\theta} \int_{h_1}^{h_2} (N_{hydro} + N_{wet}) dh \tag{6.3}$$

where h_2 is the height of the effective tropospheric layer, and N_{hydro} and N_{wet} are refractivity corresponding to hydrostatic and wet delays. Two different categories of atmospheric corrections are typically applied on SAR interferograms. In the first category, the atmospheric effect is calculated and mitigated solely based on the phase information of the interferograms. For example, assuming the tropospheric effect behaves randomly in time, it is possible to average several interferograms from the same area to reduce the effect (Zebker et al., 1997). Furthermore, InSAR time-series approaches such as PSI or SBAS can also mitigate the tropospheric effects by filtering signals that are strongly correlated in space but not in time (Ferretti et al., 2001; Berardino et al., 2002).

The other category of atmospheric mitigation methods is based on external information, in which different sources, such as global atmospheric models, GNSS, or spectrometer data that provide information about the atmospheric condition at the time of SAR acquisition, are used for tropospheric correction of interferograms (Bekaert et al., 2015a).

The other undesired contributions to the interferometric phase, produced by error sources such as phase decorrelation and soil moisture, are summed up in ϕ_{noise}, which are usually assumed to be negligible for displacement applications. After removing the unwanted phase contributions from the interferogram, the remaining interferometric phase can be attributed to displacements by

$$\phi_{def} = \frac{-4\pi}{\lambda} \Delta r \tag{6.4}$$

where Δr is the displacement of the target pixel in the line-of-sight (LOS) direction that can be expressed in terms of a 3-dimensional displacement vector by

$$\Delta r = \begin{bmatrix} -\cos\alpha\sin\theta & \sin\alpha\sin\theta & \cos\theta \end{bmatrix} \begin{bmatrix} v_x & v_y & v_z \end{bmatrix}^T \tag{6.5}$$

where α is the heading of the satellite and v_x, v_y and v_z are displacements in east-west, south-north and vertical directions, respectively. The imaging geometry of the SAR sensor (heading and incidence angle) defines its sensitivity to surface movement of the target pixel in three dimensions. Because SAR

satellites, including S-1, move around the earth in polar orbits their heading angles are close either to 180 (for descending tracks) or 360 (for ascending tracks). Therefore, their measurements are more sensitive to displacements in vertical and east-west directions than to the north-south direction.

When S-1 interferograms are formed they can be adopted, similar to any other InSAR datasets, in time-series approaches. InSAR time-series approaches were initially developed to overcome the problem of phase decorrelation and atmospheric artifacts in conventional InSAR using long series of SAR data. In general, time-series methods produce a stack of interferograms, detect coherent pixels with high signal to noise ratio, estimate and reduce unwanted errors in the interferograms, and finally calculate the time-series and the average rate of displacement (Berardino et al., 2002; Ferretti et al., 2011; Hooper, 2008).

Two different kinds of coherent pixels can be found in interferograms based on surface scattering mechanisms: persistent scatterers (PS) and distributed scatterers (DS). A resolution cell containing a strong scatterer that dominates other scatterer elements inside the pixel is called a persistent scatterer pixel. For example, the phase of a building inside a resolution cell will remain stable through time and appears as a strong scatterer in a sequence of SAR images. Such scattering is the dominant scattering mechanism in urban areas (Osmanoğlu et al., 2011). On the other hand, a distributed scatterer refers to the case where some scatterers are distributed homogenously in a resolution cell. In non-urban areas and natural terrains without dense vegetation, most of the coherent pixels are DS rather than PS (Ferretti et al., 2011).

Depending on the type of coherent pixels, two broad categories of InSAR time-series analysis have been developed. The first one, called persistent scatterer interferometry (PSI), produces a stack of single-master interferograms by selecting one image as the supermaster and the rest of the images as slaves. Then, PS pixels are detected in the stack of single-master interferograms based on the behavior of amplitude or phase of the pixels in space and time (Ferretti et al., 2001; Hooper et al., 2004). In the second category, called Small Baseline Subset (SBAS), a network of multiple-master interferograms with short temporal and spatial baselines is produced. Then, DS pixels are selected based on interferometric coherence (Berardino et al., 2002) or phase statistics of the pixels (Hooper, 2008). In recent years, several other approaches have also been proposed for effectively combining PSI and SBAS methods (Ferretti et al., 2011) and increasing the number of detected scatterers for accurate deformation mapping (Bateson et al., 2015; Esmaeili and Motagh, 2016).

In this study, we use the PSI and SBAS methods implemented in StaMPS (Stanford Method for Persistent Scatterers) (Hooper et al., 2004; Hooper, 2008) for time-series analysis of S-1 data. Having produced a stack of single-master interferograms for PSI or multiple-master interferograms for SBAS, an initial set of coherent pixels is first selected in StaMPS based on the amplitude dispersion of the pixels. In the next step, by statistical analysis of the phase behavior, pixels with high signal to noise ratio are detected, for which the interferometric phase is unwrapped in both spatial and temporal dimensions. Finally, unwanted phase contributions are estimated and eliminated from the time-series of displacement.

6.4. Large-scale Sentinel-1 Processing

S-1 data in IW mode are provided by ESA as 250 km by 250 km Single Look Complex (SLC) images. While the sensor is capable of acquiring data up to 25 minutes in a specific orbit, corresponding to thousands of kilometers, S-1 products are segmented for the aim of simplicity into 250 km slices along a track. However, it is possible to concatenate consecutive frames of data and produce large-scale SLC images along the acquisition track.

ESA provides orbital data for S-1 with three different accuracies; the orbital data attached to the SLC products, the restituted orbit (accuracy of ∼10 cm in along and across track directions) which is available a few hours after data acquisition, and precise orbit data (3-D accuracy of ∼5 cm) which is available in about 20 days after the acquisition (Yagüe-Martínez et al., 2016). The orbital data attached to the SLC product is usually accurate enough when processing a subset or a full frame of Sentinel-1 data. However, when several frames along the same orbit are joined to form a large-scale SLC image, the precise orbit is needed to improve the accuracy of coregistration, removing the contribution from the orbital phase, and geocoding.

After merging consecutive frames of S-1 to produce a large-SLC image and applying the precise orbital data, it is possible to generate large-scale interferograms as described in the previous section. An example of such an interferogram across Germany is shown in Figure 6.3a. This 900-km-long interferogram, formed by joining four consecutive frames along orbit No. 44, covers a 250-kmwide band across the whole country in a 12-day time span between 7 and 19 January 2016. The orbital and topographic phases are removed by precise orbit data and SRTM 90-meter DEM (Farr and Kobrick, 2000).

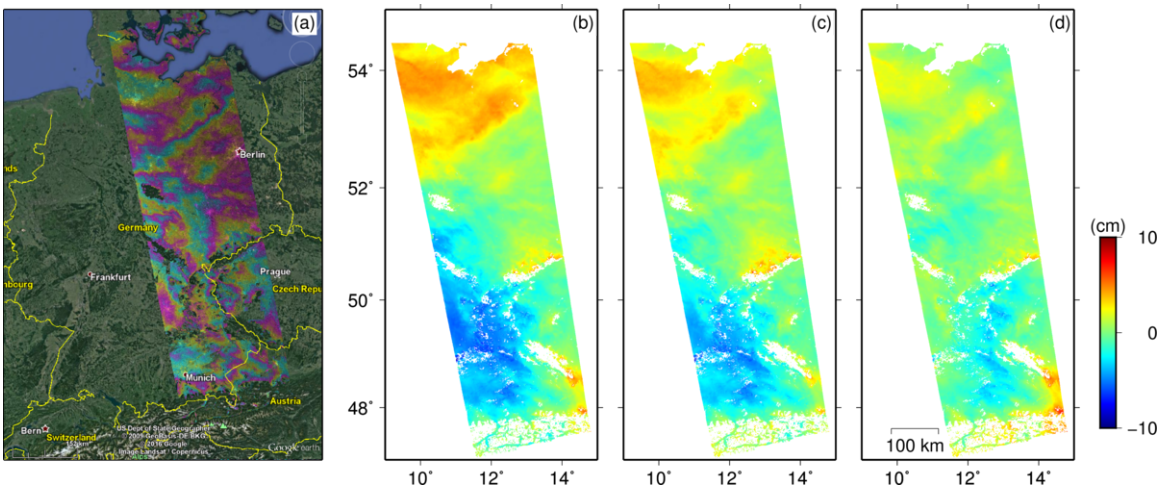


Figure 6.3.: (a) 900-km long Sentinel-1 interferogram between 7 and 19 January 2016 across Germany. Areas with coherence lower than 0.2 are masked. The background image (a) is from GoogleEarth™, (b) unwrapped phase of the interferogram, (c) and (d) unwrapped phase corrected for atmosphere with ERA-Interim and GNSS models.

Aside from some areas where the interferometric phase is decorrelated mainly because of dense vegetation, the quality of the interferometric phase shown in Figure 6.3a is high. The interferogram is mostly dominated by fringes in the order of one or more phase cycles over a distance of a few hundred

kilometers, which based on Equation 6.4 are equivalent to a few centimeters if they are caused by surface deformation (Figure 6.3b). Since we do not expect such a long-wavelength displacement in the order of centimeters in Germany, we attribute most of the signal to tropospheric phase delay. To examine this hypothesis, the interferometric phase is compared with the atmospheric phase delays derived from the ERA-Interim global meteorological model and GNSS.

The ERA-Interim is a global atmospheric model calculated by European Center for Medium-Range Weather Forecast (ECMWF) based on the assimilation of different input datasets. It provides several meteorological parameters, including pressure, temperature, and relative humidity at 6-hourly intervals at a grid of 70 km spatial resolution and 37 vertical intervals from sea level up to 50 km (Dee et al., 2011). Atmospheric parameters provided by ERA-Interim are interpolated using a vertical and horizontal spline interpolation and a linear interpolation in time to find the atmospheric phase delay from differences in water vapor (wet delay) and atmospheric pressure (hydrostatic delay) at each pixel of the interferogram. The estimated phase delay can then be used to correct the interferogram (Bekaert et al., 2015a).

Although positioning is the main aim of GNSS networks, because of redundancy of the recorded data, it is possible to estimate other parameters like the tropospheric phase delay from such networks. With around 350 GNSS stations in Germany, wet delay maps with a spatial resolution of 40 km and in 15 minutes temporal intervals can be estimated (Li et al. 2014). Tropospheric wet delay data derived from GNSS are successfully used to correct InSAR displacement maps (Li et al., 2005; Houlié et al., 2016).

We applied two atmospheric phase delay corrections estimated separately from ERA-Interim data and GNSS products to the S-1 unwrapped interferogram illustrated in Figure 6.3b. The results in Figure 6.3c-d show that the tropospheric correction based on GNSS data led to a better correction than ERA-Interim. Most of the variations from –10 cm to 10 cm in the unwrapped phase were removed after atmospheric correction using GNSS water vapor maps. ERA-Interim enhanced the RMS (Root Mean Square) of the interferometric phase from 2.7 cm in the original unwrapped interferogram to 2.1 cm in the corrected interferogram (21% reduction). On the other hand, GNSS-based correction significantly decreased the RMS of the interferometric phase to 1.3 cm in the corrected interferogram (52% reduction). This is mainly because of the dense network of GNSS permanent stations in Germany and the high temporal resolution of atmospheric products they provide.

It is worth noting that after the tropospheric correction, there are still some residuals left in the interferograms, which can be mainly attributed to turbulent troposphere. This is due to the spatial resolution of the atmospheric models by ERA-Interim or GNSS, which are coarser than the resolution of the S-1 interferograms. Therefore, they are not able to completely remove the turbulent tropospheric effect from the interferograms (Jolivet et al., 2011).

Another interesting point that can be inferred from our analysis in Figure 6.3, is the contribution that S-1 interferograms could have in estimating atmospheric parameters in the country scale. In recent years, a few studies have suggested methodologies to use SAR interferometry for atmospheric studies and assimilation into weather models (Alshawaf et al., 2015; Pichelli et al., 2015; Mateus et al., 2016). For atmospheric studies, high spatial resolution is the main power of InSAR, while low temporal

Table 6.1.: Sentinel-1 SAR dataset used to investigate displacements in Berlin. A/D indicates the orbit (Ascending or Descending) and # shows the number of SAR images. α and θ represent the heading, and incidence angle of the dataset in the study area.

No.	Orbit	Asc/Des	#	Time span	α (°)	θ (°)
1	44	A	61	2014.11.13 - 2017.01.01	351	44
2	95	D	64	2014.10.24 - 2017.01.05	189	43
3	146	A	68	2014.10.27 - 2017.01.02	349	36
4	168	D	63	2014.11.10 - 2017.01.16	191	34

resolution and small coverage area, compared to other meteorological inputs, have been described as the major disadvantages of previous SAR missions. In a recent study, Mateus et al. (2017) used S-1 images over the Iberian Peninsula to derive perceptible water vapor maps and suggested the results might be of interest for meteorologists to assimilate them into numerical weather models. Although its temporal resolution is not as high as atmospheric models, with its large coverage and moderate spatial resolution, S-1 InSAR can be assimilated to improve the spatial density of atmospheric models.

6.5. Anthropogenic Ground Motion in Berlin

In this section, the performance of S-1 InSAR time-series analysis for evaluating localized displacements in an urban area is presented. The study is done in an area of around $10 \times 10\ km^2$, northwest of Berlin. Since 1992, salt pillows in this area are used as natural underground gas storage for the city of Berlin. The storage is located north of Grunewald forest in densely populated districts of Spandau and Charlottenburg, which makes the monitoring of the reservoir important. Kampes (2005) and Kuehn and Hole (2009) used ERS-1/2 data and reported an uplift with a maximum amount of $\sim$5 mm/yr between 1992 and 2005 in the region. In this study, two frames of ascending and two frames of descending S-1 data (listed in table 6.1) are processed over the study area to investigate the dynamics of the reservoir in the past two years. The area of expected displacement is relatively small in comparison to the overall S-1 scene size. Therefore, only a small subset of each SAR frame that covers the study area is processed. As the study area is mainly urbanized, PSI was used to perform the S-1 InSAR time-series analysis.

Since the study area is small and almost flat, the long-wavelength atmospheric phase delay appears in the S-1 interferograms like a randomly directed ramp. Therefore, a simple linear ramp from each unwrapped interferogram is removed before calculating the average velocity and time-series of displacement. Because of different heading and incidence angles of the data listed in table 6.1, interferograms produced from each dataset have different sensitivities to horizontal and vertical surface displacement. Assuming the expected displacement is mainly in vertical direction, we neglect the contribution of horizontal displacement and transform the displacement from LOS to the vertical by $v = LOS/\cos\theta$. The vertical displacement rates derived from different datasets are shown in Figure 6.4.

As seen in Figure 6.4, most of the urban area is densely covered by PS pixels mainly because buildings act like artificial targets with persistent phase characteristics through time. In the areas with dense vegetation, however, the density of detected pixels is very low. Particularly no persistent

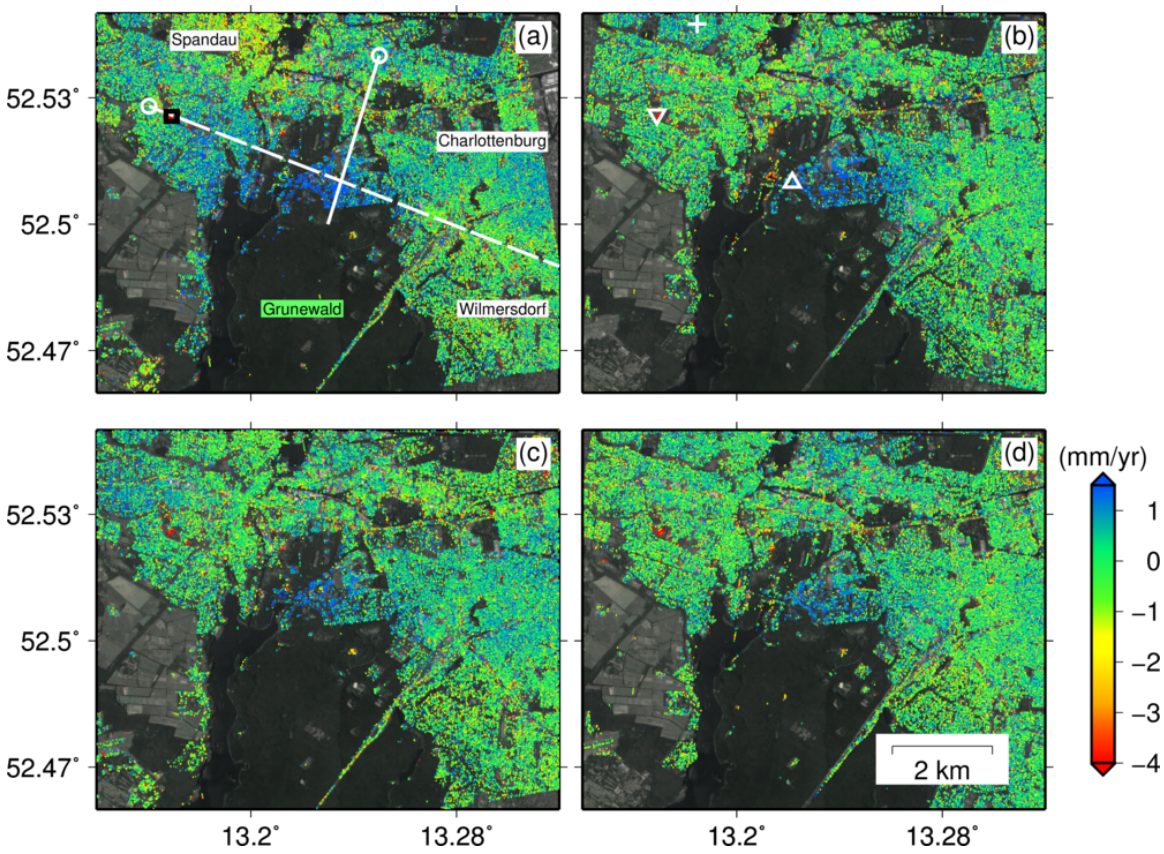


Figure 6.4.: (a)-(d) vertical displacement rates obtained by PSI method from Sentinel-1 orbits No. 44, 95, 146 and 168, respectively. The white dashed and thick lines represent the locations of profiles shown in Figure 6.5. White circles show the starting point of the profiles. The black square shows the location of a localized subsidence area shown in Figure 6.6. Triangles and plus sign show the locations of time-series plotted in Figure 6.7. Background image is from GoogleEarth™.

pixels are detected in the forested region of Grunewald, except for a line of pixels along the highway in the middle of the forest and a few isolated pixels at the places where some buildings are located.

The results from different datasets show an area of uplift that reaches 2 mm/yr at its peak. Comparing to the older results from ERS-1/2 (Kampes, 2005; Kuehn and Hole, 2009), we can infer that the rate of subsidence has decreased in recent years.

To better investigate the uplift signal, two 200-meter-wide profiles across the uplift area are extracted from the average rate maps (Figure 6.5). The first profile follows a 12-km line across the displacement area from northwest to southeast. The second profile is 5 km long from northeast to southwest. A moving average filter with a radius of 200 m was applied on the profiles to increase the signal to noise ratio. Profiles derived from different datasets are in general agreement. The peak of displacement is located at ∼4 to 6 km of the NW-SE profile and ∼4 km of the NE-SW profile showing about 2 mm/yr of uplift.

Our results also indicate a subsidence of ∼2 mm/yr at approximately 1 km in the NW-SE profile. To better illustrate this, a zoom in the area of subsidence from results obtained using S-1 orbit No. 44 is shown in Figure 6.6. The subsidence signal with maximum velocity of 8 mm/yr is related to a small

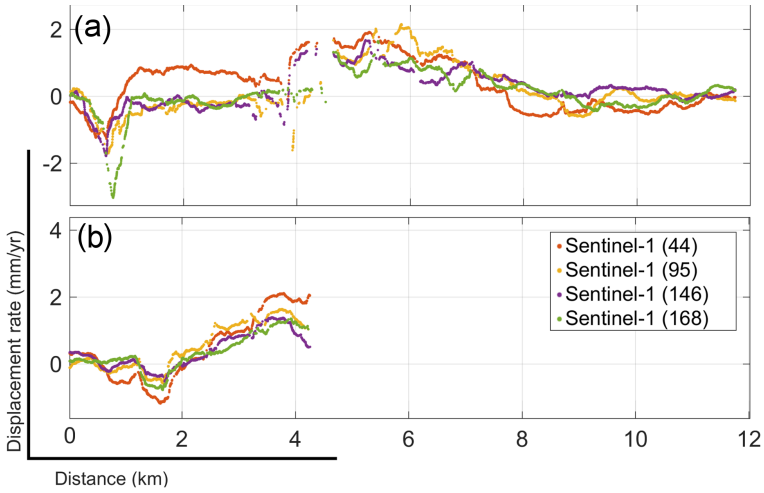


Figure 6.5.: (a) and (b) Profiles of average velocities along the white dashed and solid lines in Figure 6.4 derived from different Sentinel-1 datasets.

area of about 250 × 250 m^2, called Egelpfuhl; similar results are obtained in this region using other datasets (results not shown here). This area in Berlin was used as a landfill for demolishing waste as well as household waste after the Second World War. In the 2000s, the gas produced from demolishing waste in this landfill was extracted for safety reasons and some gardens where constructed in the area. As seen in Figure 6.6, the subsidence is localized in the former landfill area. Therefore, we assume it is most probably related to the settlement of the old demolishing landfill.

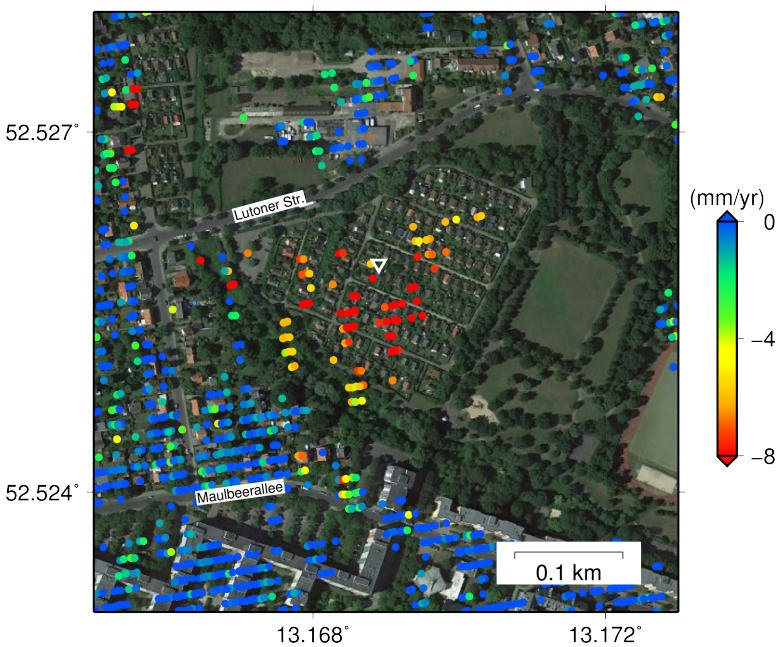


Figure 6.6.: Vertical displacement rates obtained by PSI method from Sentinel-1 orbit No. 44 in the Egelpfuhl area, west of Berlin. The triangle shows the location of the downward-pointing triangle in Figure 6.4b. Background image is from GoogleEarth™.

Some examples of displacement time-series at different locations (see Figure 6.4) are shown in Figure 6.7. The time-series (a, d, g, j) show the trend of the displacement in the uplift area. Interestingly,

with its dense temporal resolution, S-1 InSAR analysis reflects up to 2 cm of seasonal variations in displacement. The variations are likely to be related to charge and discharge of the storage; we observe uplift during summer time (the period of gas injection) and subsidence during winter time (the extraction period).

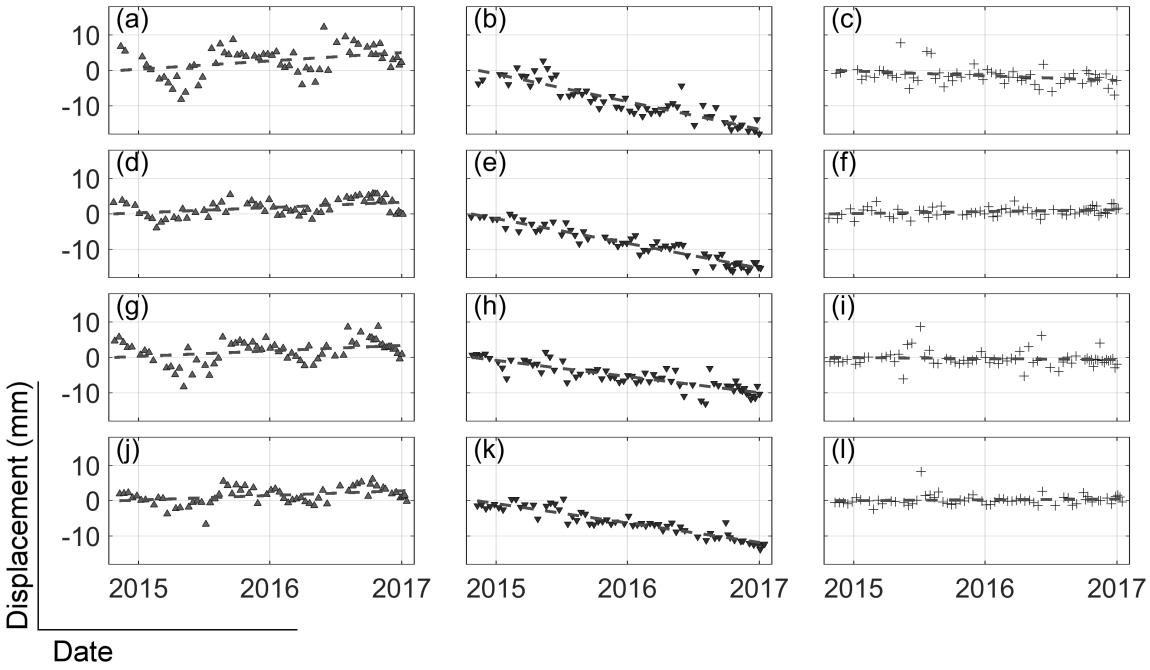


Figure 6.7.: The time-series of vertical displacements at three different locations for different orbits of the Sentinel-1 dataset: (a-c), (d-f), (g-i), and (j-l) show the results from S-1 orbits No. 44, 95, 146, and 168, respectively. Left, middle, and right panels correspond to the uplift area, the subsidence area, and a stable area away from deformation zones that are shown in Figure 6.4 with an upward-pointing triangle, downward-pointing triangle, and plus sign, respectively.

The time-series of displacement in the Egelpfuhl landfill area (b, e, h, k) show a clear trend of subsidence with less seasonal fluctuations. To assess the accuracy, the time-series of displacement for a stable point is also plotted (c, f, i, l). This point does not show any clear trend or meaningful variations, confirming that the trend and seasonal variation signals we observed in the displacement areas are not caused by spatially correlated artifacts. The low RMS of the time-series for this stable point (2.5, 1.3, 2.2, and 1.4 mm corresponding to orbit No. 44, 95, 146, and 168, respectively) indicates that the noise level in the time-series of the displacements is in the order of a few millimeters ($<$ 2.5 mm).

To evaluate the consistency of the results derived from different S-1 datasets (Figure 6.4), the discrepancy between them is estimated and the RMS of the differences is used as a measure of accuracy. Histograms of differences between average velocities estimated from orbits No. 95, 146, and 168 with respect to orbit No. 44 are illustrated in Figure 6.8. Small differences (RMS equal to 1.4, 1.3, and 1.3 mm/yr for orbit No. 95, 146, and 168) confirm that the results from different datasets are in good agreement.

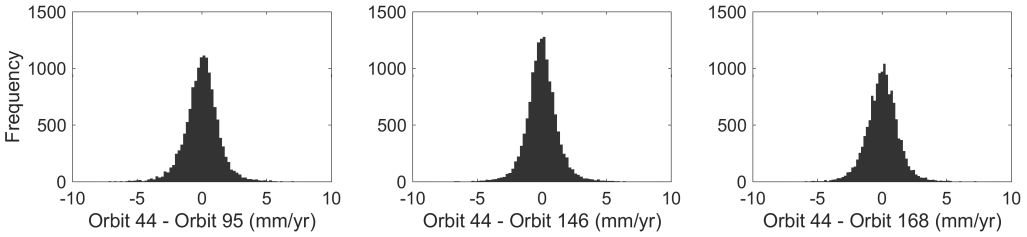


Figure 6.8.: Histogram of differences between average velocities in Berlin estimated from Sentinel-1 orbits No. 95, 146, and 168 with respect to orbit No. 44.

Table 6.2.: Sentinel-1 SAR dataset used to investigate displacements in the mining area south of Leipzig. A/D indicates the orbit (Ascending or Descending) and # shows the number of images. α and θ represent the heading and incidence angle of the SAR dataset, respectively.

No.	Orbit	A/D	#	Time span	α (°)	θ (°)
1	44	A	81	2014.10.20 - 2017.04.07	350	40
2	168	D	75	2014.10.17 - 2017.04.10	190	37

6.6. Mining-induced Deformation in Leipzig

Our second case study addresses an area subject to rapid displacement caused by open-pit mining activities near the city of Leipzig. A total area of 200 km^2 south of Leipzig has been a major reservoir providing brown coal for more than a century. Intense mining activities have dramatically changed the landscape, the geological and the hydrological situation of the region (Birkhölzer et al., 1998). During the mining activities, the groundwater level was lowered to below the mining level to make open-pit mining possible. After the reunification of Germany, several open-pit mines in the region were abandoned. Followed by rising of groundwater, some were filled with water and became lakes. There are still two major active mines in the region, which provide coal for power plants in the area. They were opened in the 1940s and expected to be running until the 2030s. In total they produce 20 million tons of brown coal each year. Land subsidence is an expected phenomenon in the mining areas south of Leipzig as a result of groundwater withdrawal (Wolkersdorfer and Thiem, 1999). Schäfer et al. (2007) used ERS2 and Envisat data in this region and reported displacements in the order of $\pm$1 cm over two years.

We used a collection of S-1 images between 2014.10.17 and 2017.04.10 in ascending and descending tracks to investigate the displacements in this area (see Table 6.2 for details). Because the area is not urbanized and most of coherent pixels are expected to be DS, the SBAS approach was used and a network of small baseline interferograms was produced for each track of data. In total, 205 and 270 small baseline interferograms were generated corresponding to Sentinel-1 orbit No. 44 and 168 respectively. The network was inverted using the least-squares approach and the average rate and time-series of displacement were estimated.

The 12-meter TanDEM-X DEM was used in the processing to remove the topographic phase from the interferograms. The resolution and accuracy of the TandDEM-X DEM used in the processing are high, but because the DEM was produced a few years before Sentinel-1 acquisitions, any changes

in topography, which is not unexpected in active mining areas, can cause unwanted phase residual in the interferograms. Based on Equation 6.2, for a Sentinel-1 interferogram in our study area with a perpendicular baseline of 85 m and an incidence angle of 40°, an error of ∼200 m in the DEM causes a complete phase cycle, which can be misinterpreted as 2.6 cm of displacement. To restrain the topographic residuals only interferograms with short perpendicular baselines (maximum 85 m) were used in the SBAS network. Furthermore, after interferograms are unwrapped, spatially-correlated DEM errors, that are proportional to perpendicular baselines, are estimated and removed from the unwrapped interferograms.

Figure 6.9a-b show the GoogleEarth™ image of the study area and its shaded relief map, respectively. Two active open-pit mining areas are indicated in this figure. Some older mines that were filled with water and became lakes are also visible in the eastern part of this figure. Figure 6.9c-d show the average LOS velocities from the S-1 time-series analysis. Although the vegetation cover in some areas caused low density of detected pixels, the density in the mining areas is high except for some regions that are most probably subject to rapid changes and thus loss of coherence due to mining activities. While the areas away from active mines do not show any significant displacement, the two active mining areas and their surroundings show some strong displacement signals.

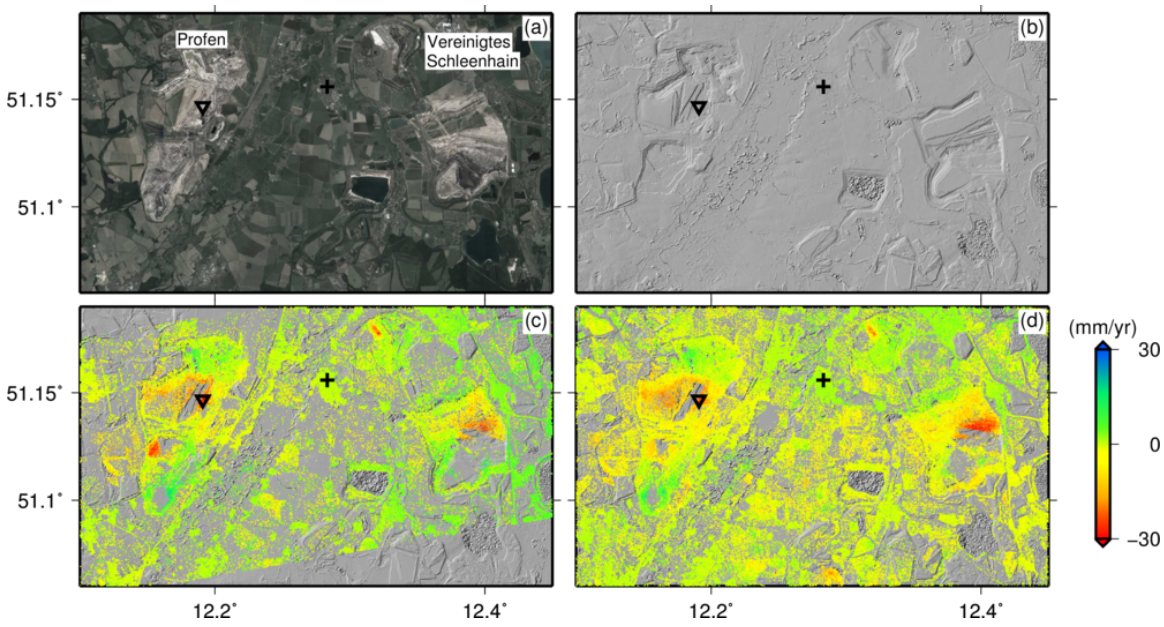


Figure 6.9.: (a) GoogleEarth™ view of the active mining area south of Leipzig, (b) shaded relief map of the study area derived from TanDEM-X 12-meter DEM, (c) and (d) average velocity maps in the LOS direction from the satellite to the ground, derived from the SBAS analysis of Sentinel-1 orbits No. 44 and 168, respectively. Downward-pointing triangles and plus signs show the location of the time-series plots in Figure 6.10.

The displacement rates in the mining area reach a maximum amount of 30 mm/yr away from the satellite at some locations. The time-series of displacement in the main deforming region is mostly dominated by a linear declining trend in time, as illustrated in Figure 6.10. Time-series of displacement in a non-deforming area does not show much variation (RMS equal to 2.7 mm and 1.7 mm for orbits No.

44 and 168, respectively), which confirms that the magnitude of unwanted signals in the time-series is low in comparison to cm-scale displacement signal that we observe in the mining area.

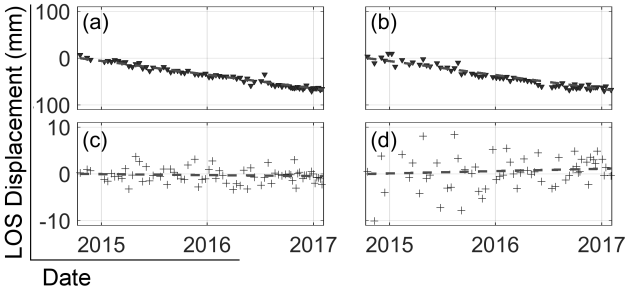


Figure 6.10.: Examples of LOS displacement time-series at: (a, b) a subsidence area (downward-pointing triangle in Figure 6.9) in the active mining region, and (c, d) a non-deforming area (plus sign in Figure 6.9). (a,c) and (b,d) correspond to results derived from S-1 orbits No. 44 and 168.

To estimate the consistency between the two datasets, the average velocities in Figure 6.9 are first transformed from LOS to vertical direction by neglecting the horizontal displacement, and then are compared with each other. Figure 6.11 illustrates the histogram of differences between the average vertical velocities. The RMS of differences between ascending and descending results is approximately 6 mm/yr that verifies their consistency. However, this RMS of the differences between datasets in Leipzig is higher than those in Berlin. We attribute this to neglecting the contribution of horizontal displacements. For example, based on Equation 6.5 and imaging geometries of the S-1 dataset in Table 6.2, 10 mm/yr of displacement in East-West direction will project on the line-of-sight as movements equal to 6 mm/yr towards the satellite for descending orbits and 6 mm/yr away from the satellite for ascending orbits in our study area. When horizontal movements are neglected, such a displacement can be misinterpreted as 7 mm/yr of subsidence and 8 mm/yr of uplift in descending and ascending orbits, respectively. As a result, the RMS of differences between average velocities of different datasets might increase by neglected horizontal displacements.

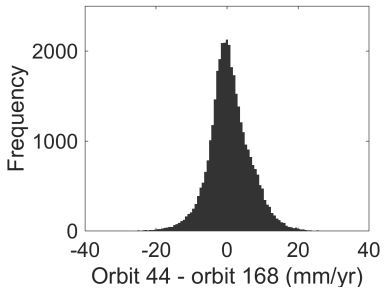


Figure 6.11.: Histogram of differences for vertical displacement rates in Leipzig derived from different Sentinel-1 datasets.

We take advantage of different imaging geometries of datasets to estimate the vertical and horizontal components of displacement. Based on Equation 6.5, the sensitivity of line-of-sight measurements in our study area to the south-north motions is only 11%, while it is about 60% and 80% for east-west and vertical motions. Therefore, we neglect the south-north component of motion and estimate east-west and vertical displacement rates from the two line-of-sight velocities. The results are shown in Figure

6.12. As seen in Figure 6.12, the maximum amount of vertical displacement rates reaches 40 mm/yr around active mining areas. As expected, horizontal motion increases in regions with high gradients of vertical movement and reaches maximum rates of 48 mm/yr at some locations.

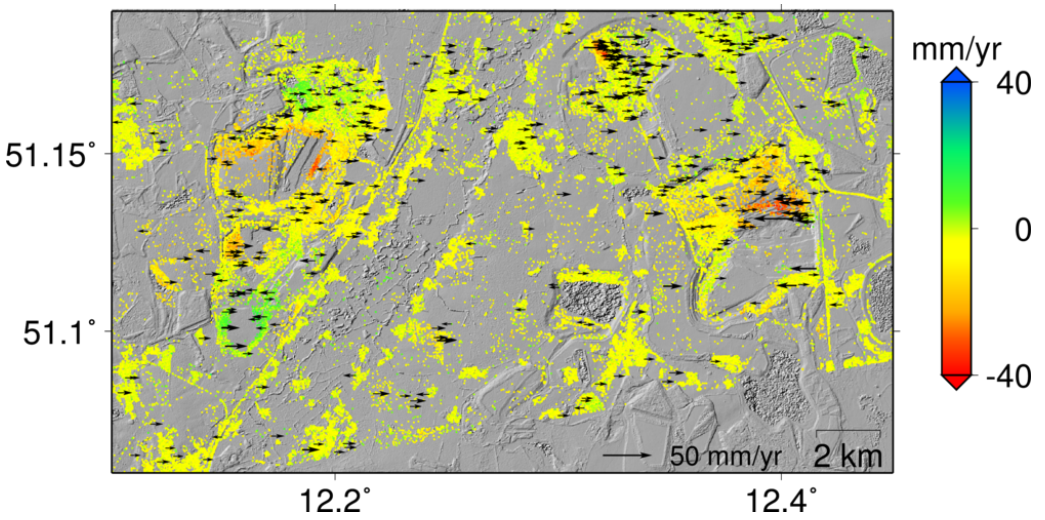


Figure 6.12.: Vertical and east-west displacement rates in active mining area south of Leipzig. The background colors are vertical displacement rates and arrows are horizontal motions. For a better visualization, only 90% of vectors with east-west displacement larger than 1 cm/yr are shown in this figure.

6.7. Conclusions and Prospect

In this paper, some highlights of Sentinel-1 SAR interferometry in Germany were presented to evaluate the potential and possibilities provided by this technique for deformation monitoring and atmospheric phase delay analysis. First, a 900-km-long Sentinel-1 interferogram across the country was presented. Atmospheric corrections revealed that most of ±10 cm phase change in this interferogram was caused by tropospheric wet delay. The atmospheric water vapor estimated from a dense network of GNSS measurements improved the quality of the interferogram by 52% while ERA-Interim could improve it by 21%. Although tropospheric phase delay is a disadvantage for displacement applications, with its large spatial coverage and high spatial density, Sentinel-1 provides great opportunities for atmospheric studies. Future research should focus on incorporating/assimilating InSAR measurements in atmospheric models. In particular, the major phase contribution in Sentinel-1 interferograms with short time intervals in mid-latitudes comes from changes in water vapor at the time of image pair acquisitions. Therefore, it can produce an estimate of relative water vapor conditions at the times of acquisitions that can be of interest for meteorologists.

Secondly, we demonstrated the capability of S-1 time-series analysis for monitoring small-magnitude displacements related to gas storage and landfill compaction in north-western part of Berlin and cm-scale displacements due to active mining in Leipzig. With its 6-day acquisition time interval, large coverage, and moderate spatial resolution, Sentinel-1 provides new emerging opportunities to investigate localized displacements in much more temporal details than currently possible with other satellite-based SAR systems. We have observed a maximum of ∼2 mm/yr uplift during October 2014

to January 2017, and up to 2 cm of variations due to seasonal charge and discharge of the gas storage. A localized subsidence signal of ∼8 mm/yr, due to the settlement of the old demolishing landfill and gas extraction in Egelpfuhl, northwest of Berlin, was also detected. For the mining area in Leipzig, subsidence rates as much as 4 cm/yr in active mining areas were found for the period between October 2014 and April 2017.

Although we did not have access to ground truth for validation and accuracy assessment of our InSAR time-series results, statistical analyses of the results enabled us to evaluate their consistency with each other and provided a measure of accuracy that we can achieve by S-1 InSAR time-series analyses. The RMS of differences between average velocities derived from different Sentinel-1 datasets was <1.4 mm/yr and 6 mm/yr for Berlin and Leipzig, respectively. The maximum RMS of the time-series of displacements at stable areas was approx. 3 mm that shows the power of Sentinel-1 InSAR time-series analyses to detect displacements with magnitudes of as small as a few millimeters.

With its free data policy and 20-year acquisition plan, Sentinel-1 provides great opportunities for InSAR geodesy to be widely applied by both scientific and commercial users to generate information for the purpose of hazard and risk management related to natural and manmade phenomena. In the future, developing new methodologies to automatically obtain the data, detecting areas prone to a specific process, and obtaining the results from appropriate InSAR time-series approaches can help us extract the maximum benefit from near real-time SAR data provided by Sentinel-1. At the same time, new challenges arise for handling of the massive datasets provided by the mission. Sentinel-1 provides 10 TB of products daily. With its large spatial coverage and medium resolution, each SLC data of this sensor is in the order of a few GB. Mosaicking these images along a specific orbit and interferometric processing multiply the need for disk space and dramatically increases the required processing loud that can be challenging to handle. Development of innovative processing chains using cloud-based systems like ESA's Geohazards Exploitation Platform GEP (De Luca et al., 2015) or CODE-DE (Copernicus Data and Exploitation Platform – Deutschland) (Reck et al., 2016) should be further explored in future to deal with the huge amounts of SAR data provided by the Sentinel-1 constellation.

6.8. Acknowledgements

We thank Fadwa Alshawaf and Galina Dick from GFZ for providing water vapor models from GNSS observations. We thank Dr. Wetzel from GFZ for translating the ab- stract in German. This work was supported by Initiative and Networking Fund of the Helmholtz Association in the frame of Helmholtz Alliance "Remote Sensing and Earth System Dynamics". TanDEM-X DEM data are provided by DLR under proposal number motagh_IDEM_GEOL0157. Some figures were generated using Generic Mapping Tools (Wessel et al., 2013). Sentinel-1 data were provided by ESA.

Chapter 7

Subsequent Work: Measurement of Localized Deformations over Extensive Areas

7.1. Introduction

In this chapter, the method proposed in chapter 3 is successfully applied on two individual stacks of Sentinel-1 data in Iran and Germany to identify localized displacements and estimate their time series. The performance of the proposed approach in mitigating tropospheric errors from the stack of interferograms is then investigated. In this regard, the results are compared with the results from interferograms corrected using a simple 2-D ramp removal and GACOS (Generic Atmospheric Correction Online Service for InSAR) model.

7.2. SAR Datasets

Two datasets of Sentinel-1 are used in this study. The first dataset is acquired along a descending track (track 35) of Sentinel-1 across Iran from the Caspian sea in the northeast to the Persian Gulf in the southwest. This dataset covers an area as long as 950 km and 250 km wide and includes 52 acquisition dates between 2014.10.08 and 2017.10.28. The second dataset is acquired along a descending track (track 139) of Sentinel-1 covering a 550-km long and 250-km wide area in the west of Germany. It includes 78 acquisition dates between 2014.10.15 and 2017.10.11.

7.3. Sentinel-1 Interferograms

The networks of interferograms are generated using image pairs with temporal baselines between 80 and 120 days. Then, the connections are checked to ensure each image is connected to at least one image forward and one image backward in time. Any image that does not meet this criterion is connected to the nearest image to the temporal baseline thresholds. In total 112 interferograms are generated for track 35, and 234 interferograms are generated for track 139. The topography component is removed from the interferograms in Iran using a 90-m SRTM DEM (Farr and Kobrick, 2000) and in Germany using a 90-m TanDEM-X DEM (Zink et al., 2014). A multilook of 25 by 5 in range and azimuth directions respectively, is applied to the interferograms that yield to approximately 100x100-m ground pixel sizes.

Figure 7.1 presents four examples of large-scale interferograms from track 35. The interferograms are obviously contaminated by tropospheric artifact; Along with topography-correlated fringes, there are long-wavelength and short-wavelength fringes visible. The former is attributed to lateral variations of the troposphere and the later to the turbulence in the troposphere.

Two close-up views of the interferograms are shown in Figure 7.2. The first one illustrates the subsidence area to the southwest of Tehran. The interferograms exhibit a consistent fringe pattern corresponding to land subsidence. In addition there are some temporally-variable and topography-correlated fringes that are attributed to the tropospheric phase delay. The second close-up view shows an area in the Zagros mountains in central Iran where the interferograms are dominated by topography-dependent phase from tropospheric phase delay.

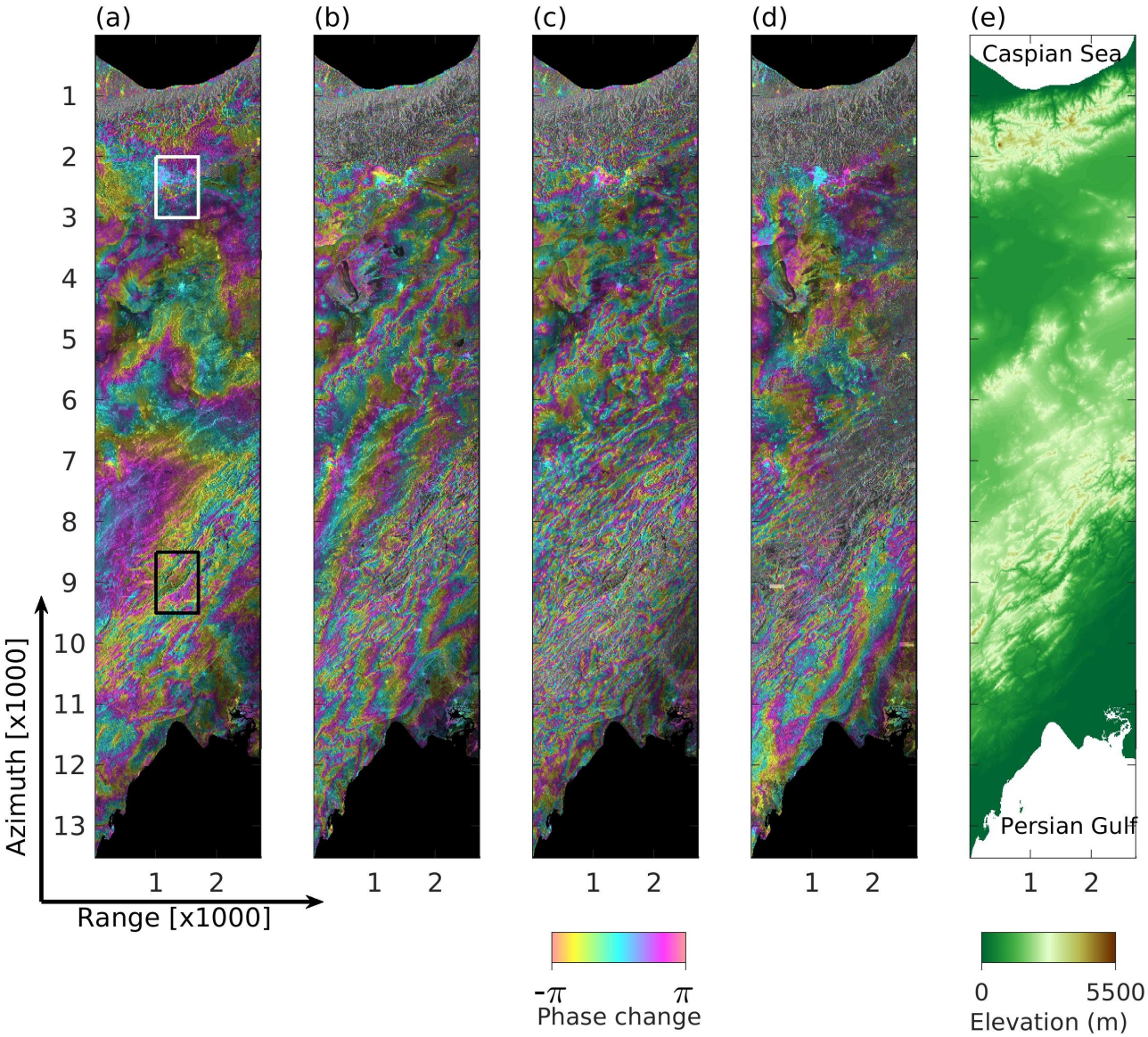


Figure 7.1.: Four examples of large-scale interferograms from track 35 of Sentinel-1 between (a) 2017.08.05-2017.10.28 (84 days), (b) 2017.04.07-2017.07.12 (96 days), (c) 2016.07.29-2016.11.02 (96 days), (d) 2017.02.18-2017.05.13 (84 days). (e) DEM in the SAR image coordinate. White and black boxes show two close-up views shown in Figure 7.2.

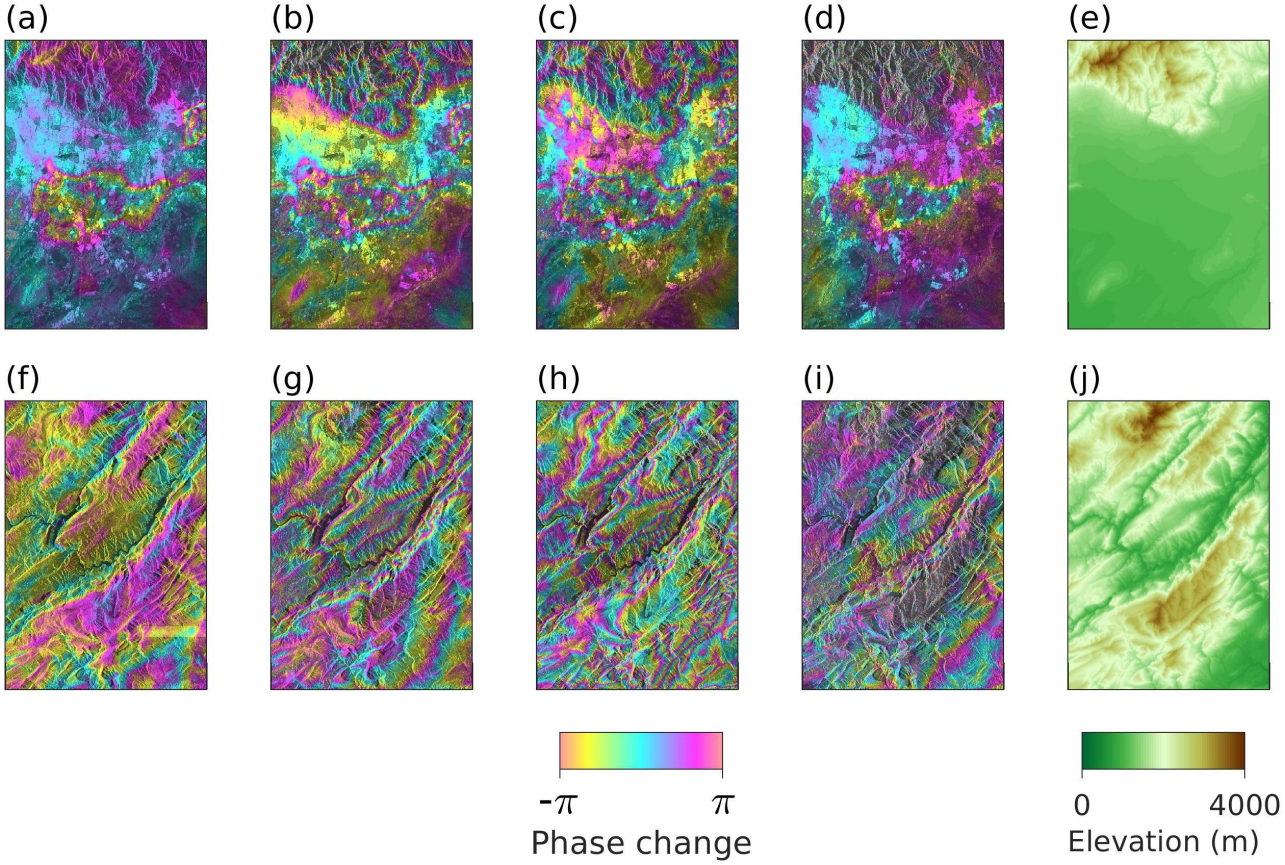


Figure 7.2.: Close-up view of interferograms in Figure 7.1. Top panel interferograms, corresponding to the white box, show the subsidence area to the southwest of Tehran where consistent subsidence fringes are observed. Bottom panel, corresponding to the black box, shows an area in Zagros mountains. Interferograms in both areas are contaminated by tropospheric phase delay.

7.4. Corrected Interferograms

Figure 7.3 shows an example interferogram from track 35 before and after correction using different approaches. A simple 2-D ramp reduced some of the long-wavelength errors but left the topography-dependent part intact. Tropospheric correction using GACOS model corrected some of the broad-scale as well as the topography-correlated artifact. The magnitude of remaining fringes in both approaches reaches several centimeters. In contrast, the adaptive correction outperformed the other two approaches and removed most parts of the broad-scale and topography-correlated signals. Although the corrected interferogram highlights the localized displacements, there are still some remaining phase delays, particularly evident near the Persian Gulf, most likely attributed to turbulence in the troposphere.

The close-up views of the corrected interferogram, presented in Figure 7.4, confirm the better performance of the adaptive correction. The top panel shows the subsidence area near Tehran which is distinguished better after the adaptive correction. The bottom panel shows the area in Zagros mountains that exhibits a highly topography-dependent phases. The adaptive correction reduced most parts of the phase delay. However, some small-scale residuals remained in the interferogram.

Figure 7.5 shows an example interferogram from track 139 before and after correction using different approaches. In contrast to the study area in Iran, in this region, the topography variations are significantly lower. Therefore, phase delay from stratified troposphere is limited, and the major error contribution is from broad-scale tropospheric variations. All correction methods reduced the tropospheric phase delay, but the adaptive approach appears to perform significantly better and remove most of the errors.

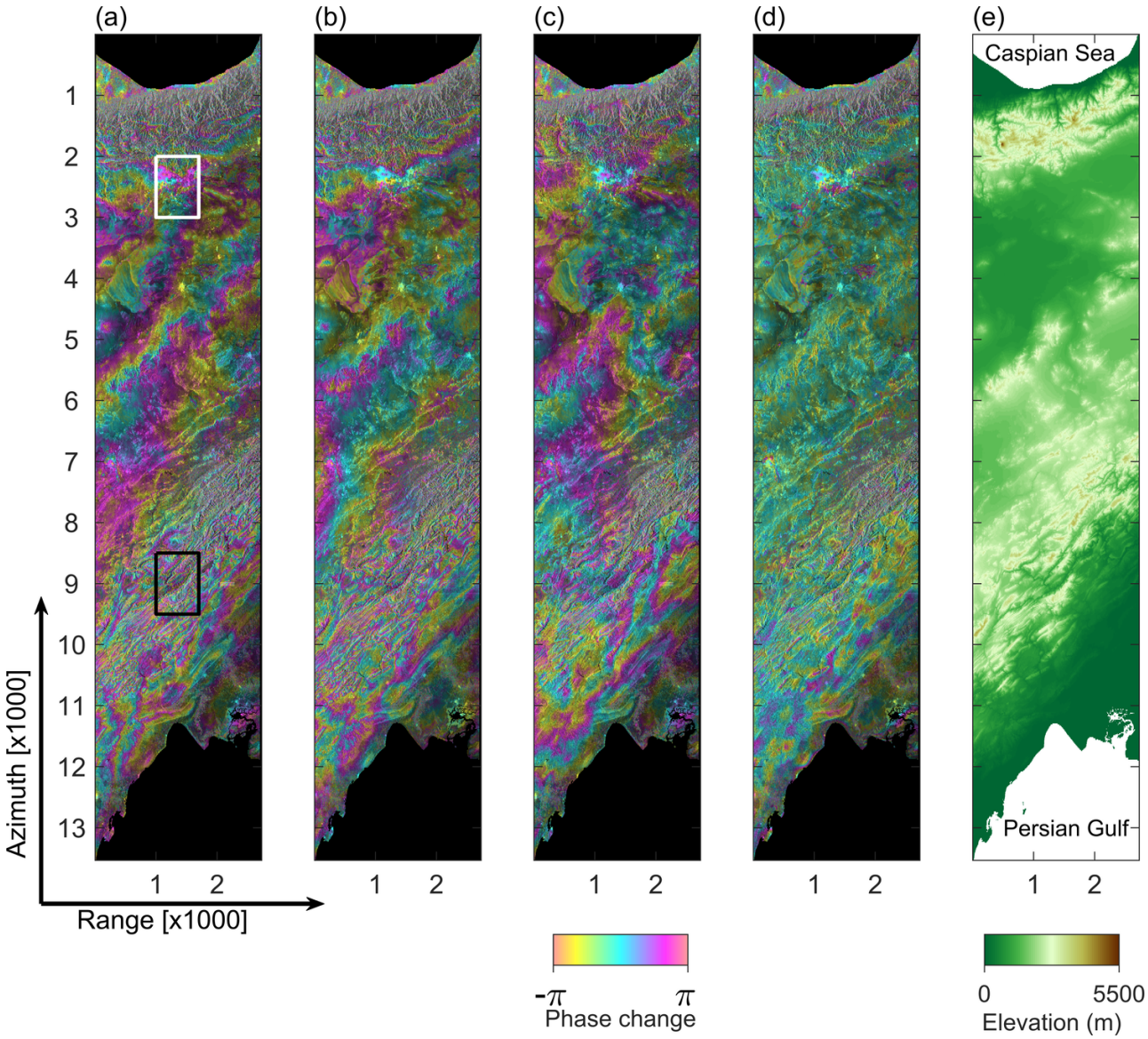


Figure 7.3.: Example of a re-wrapped interferogram from track 35 between 2014.10.08 and 2015.01.12 (96 days). (a) original interferogram. (b) interferogram after a 2-D ramp removal. (c) interferogram after GACOS tropospheric correction. (d) interferogram after adaptive correction. (e) DEM in the SAR image coordinates. The white and black boxes indicate the close-up views illustrated in Figure 7.4

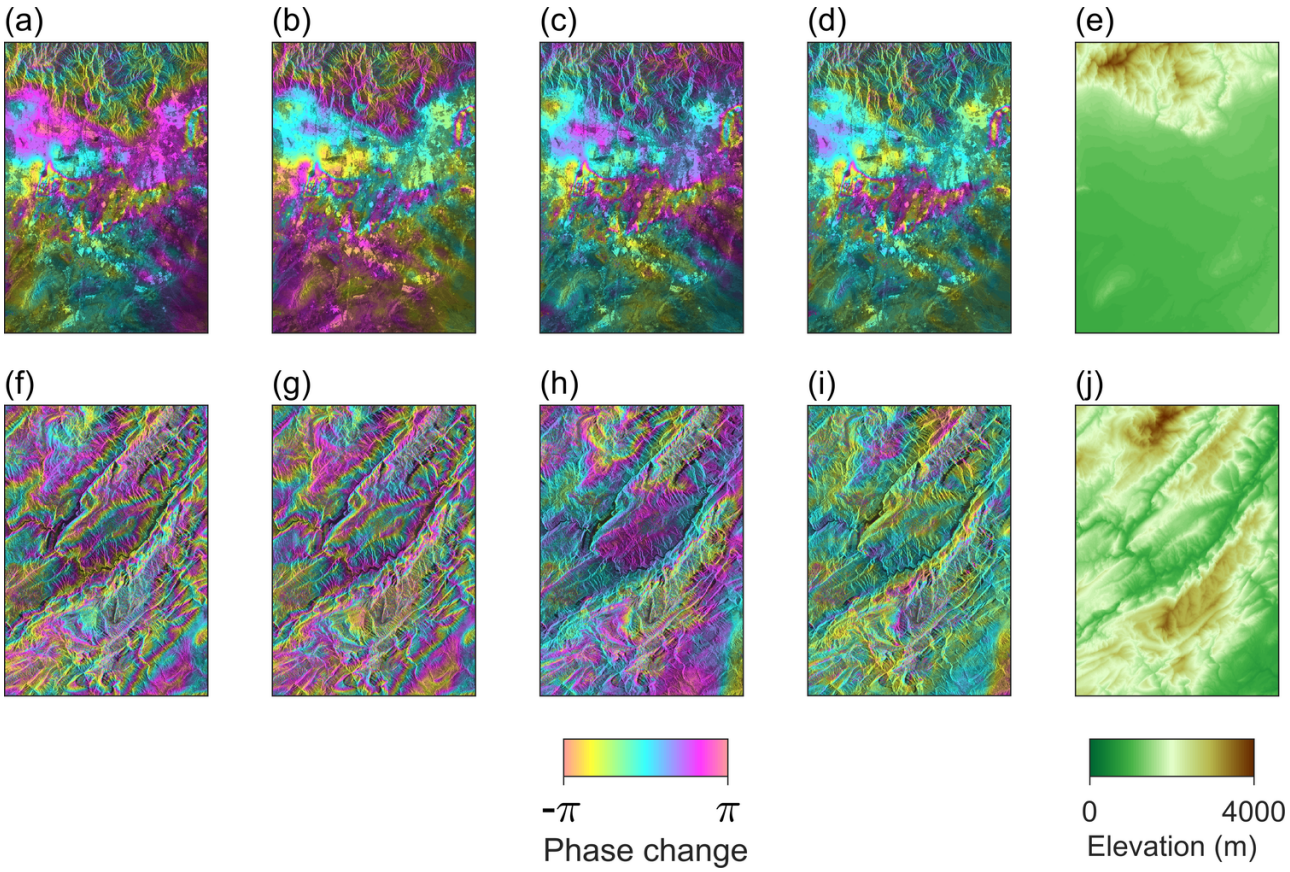


Figure 7.4.: Close-up view of the interferogram in Figure 7.3. Top panel, corresponding to the white box, shows the subsidence area to the southwest of Tehran. Bottom panel, corresponding to the black box, shows an area in Zagros mountains.

7.5. Displacement Maps and Time Series

The linear displacement rates in track 35 in Iran estimated from different approaches are shown in Figure 7.6. Although it is possible to visually distinguish the major displacement signals in the results obtained from original interferograms, after 2-D ramp removal, and after GACOS correction, they fail to separate many localized displacements from the background tropospheric noise. The stacking of original interferograms contains remaining of broad-scale and topography-dependent tropospheric delays. A 2-D ramp removal slightly improves the result by reducing some parts of the long-wavelength artifacts.

Stacking of the interferograms corrected using GACOS further improves the results but fails to entirely address the tropospheric effect. The remainings of the tropospheric phase are particularly visible in the north and south where troposphere is more variable due to proximity to the Caspian Sea and the Persian Gulf. Stacking of interferograms after adaptive correction considerably reduces the tropospheric artifacts and provides a clear picture of localized displacements across the country.

Approximately 20 subsidence areas are detected that appear to be attributed to over-extraction of groundwater as a widespread problem across Iran. Among them, two examples are shown in Figure 7.7; The first example indicates the land subsidence to the southwest of Tehran. The peak of subsidence

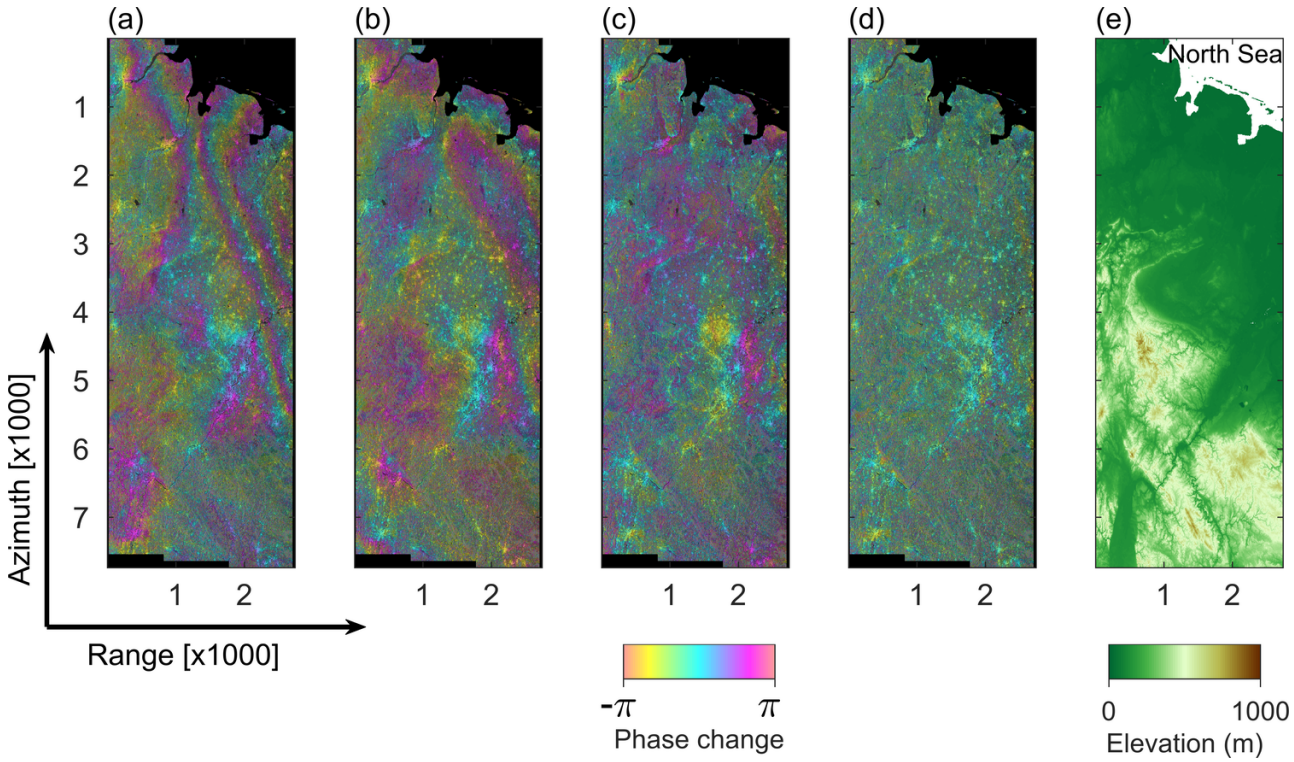


Figure 7.5.: Example of a re-wrapped interferogram from track 139 between 2016.01.14 and 2016.05.01 (108 days). (a) original interferogram. (b) interferogram after a 2-D ramp removal. (c) interferogram after GACOS correction. (d) interferogram after adaptive correction. (e) DEM in the SAR image coordinates.

in this region exceeds 20 cm/yr. The time series of displacement clearly shows the long-term trend of displacement superimposed on seasonal variations due to charge/discharge of aquifer in Tehran. The second example shows the displacement around Tehran's international airport with maximum subsidence of approximately 5 cm/yr. The results for both areas are in agreement with the previous results obtained from Small Baseline InSAR presented in chapter 5.

The linear displacement rates in track 139 in Germany, estimated from different approaches, are shown in Figure 7.8. The results confirm that the adaptive correction performs better in separating displacement from background tropospheric noise in this track, similar to the results in track 35. Approximately 10 localized displacement areas are detected in the average velocity map. Two examples of them are shown in Figure 7.9; The first area is the largest detected displacement zone in track 139 that is caused by open-pit mining in Tagebau Hambach near Cologne. Subsidence up to approximately 10 cm/yr are most likely occurred by lowering of groundwater. An example time series illustrated in this figure shows that a constant trend of subsidence is the primary component of displacement. The second example in Figure 7.9 illustrates the displacement in the Etzel gas storage facilities in Schleswig-Holstein in the north of Germany with a maximum of approximately 8 cm/yr of subsidence. Time series of displacement for an example point indicates a non-linear pattern of subsidence in this area. Although the declining pattern is evident in the time series, it also exhibits short term variations that show periods of acceleration and deceleration of displacement.

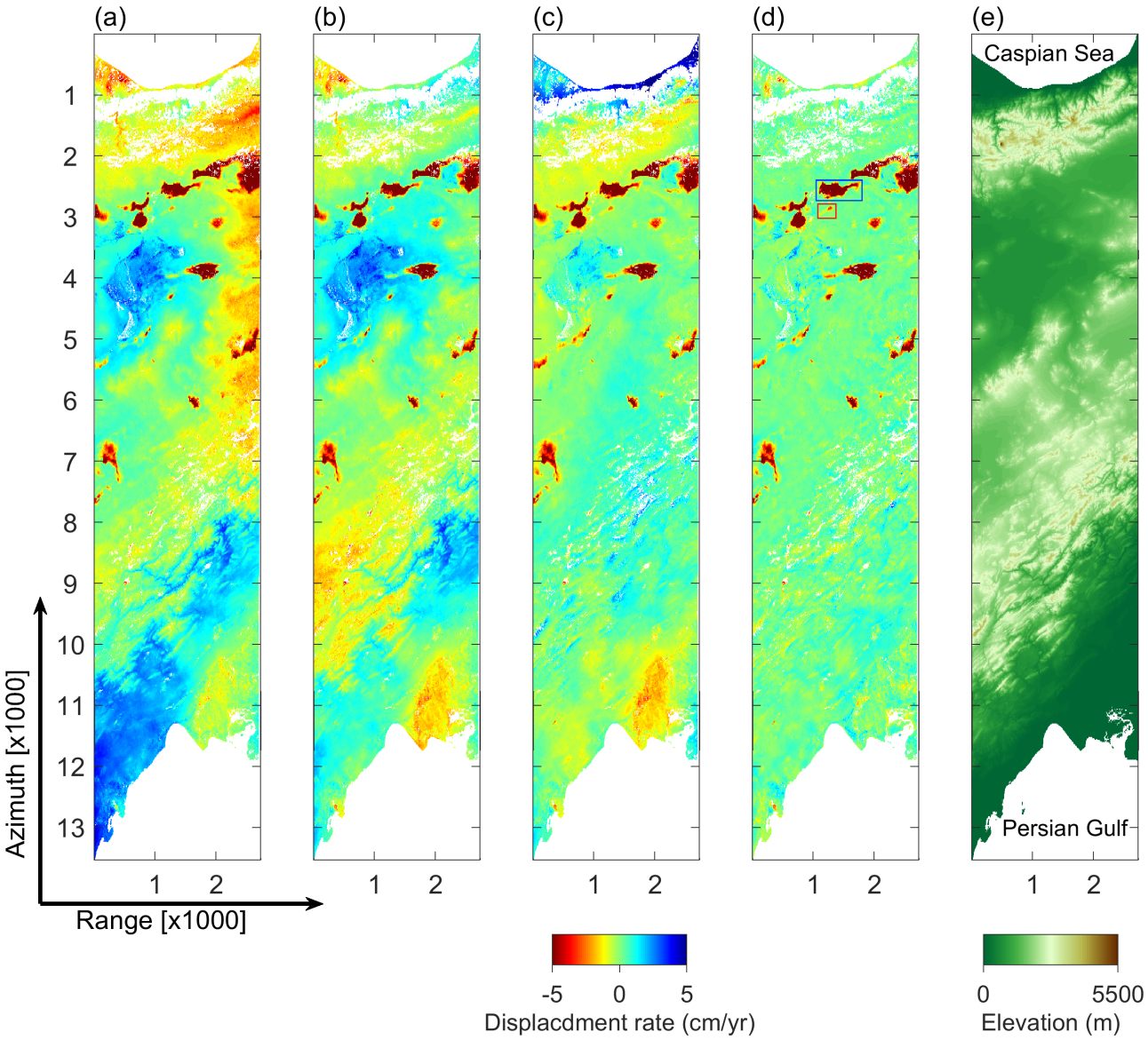


Figure 7.6.: Linear displacement rate in track 35 of Sentinel-1 in Iran using stacking of (a) original interferograms, (b) interferograms after a 2-D ramp removal, (c) interferograms after GACOS tropospheric correction, (d) interferograms after adaptive correction. The color scale is saturated to visualize the performance of tropospheric corrections better. The displacement rates are converted from the satellite line of sight to vertical. The blue and red boxes indicates areas for which the detailed InSAR results are presented in Figure 7.7. (e) DEM in the SAR image coordinates.

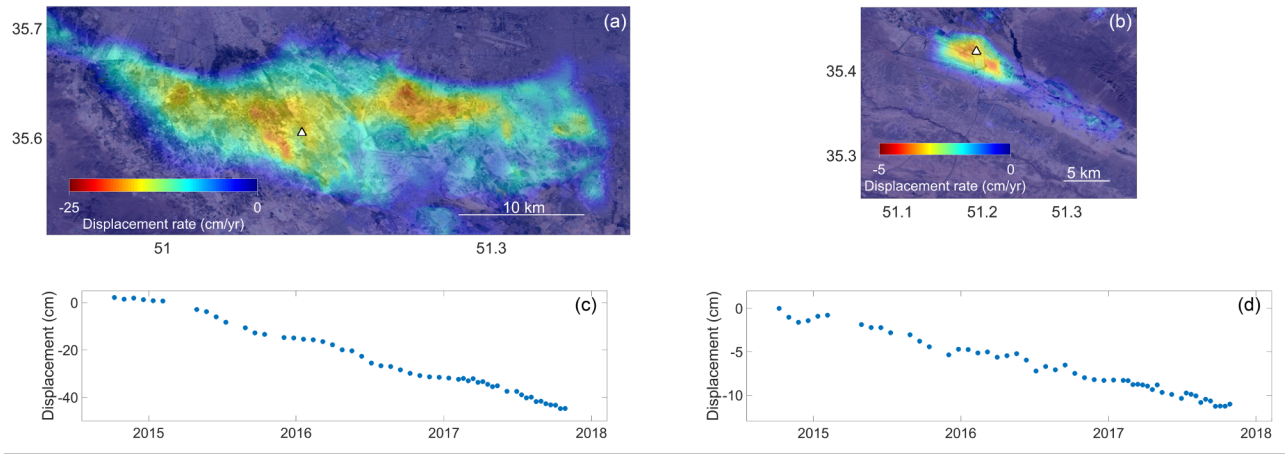


Figure 7.7.: Examples of localized displacement in Iran (a) Linear rate of subsidence to the southwest of Tehran. (b) Linear rate of subsidence around Tehran International airport. (c) and (d) examples of displacement time series for locations indicated by white triangles. The displacements are geocoded and converted from line of sight to vertical. Background images are from Google Earth™.

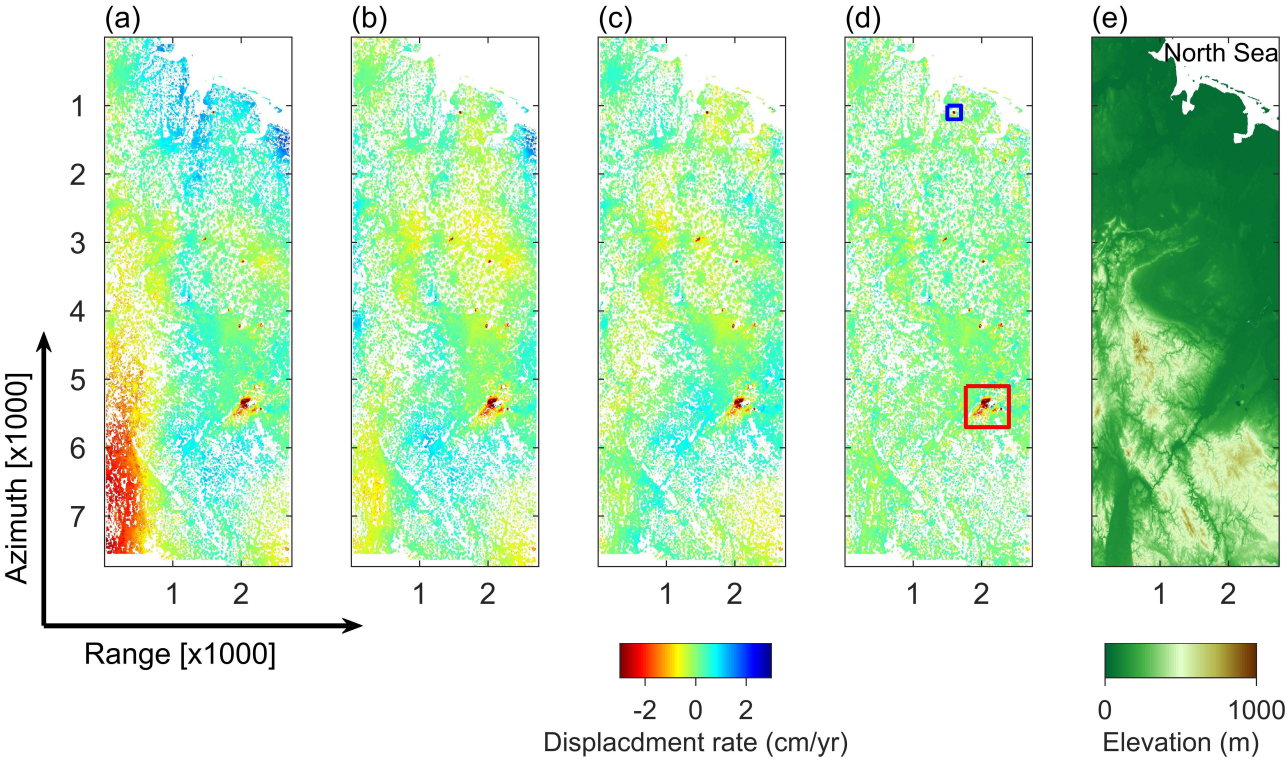


Figure 7.8.: Linear rate of displacement in track 139 of Sentinel-1 in Germany using stacking of (a) original interferograms, (b) interferograms after 2-D ramp removal, (c) interferograms after GACOS correction, (d) interferograms after adaptive correction. The color scale is saturated to better visualize the performance of tropospheric corrections. The displacement rates are converted from satellite line of sight to vertical. The red and blue boxes indicate areas for which detailed InSAR results are presented in Figure 7.9. (e) DEM in the SAR image coordinates.

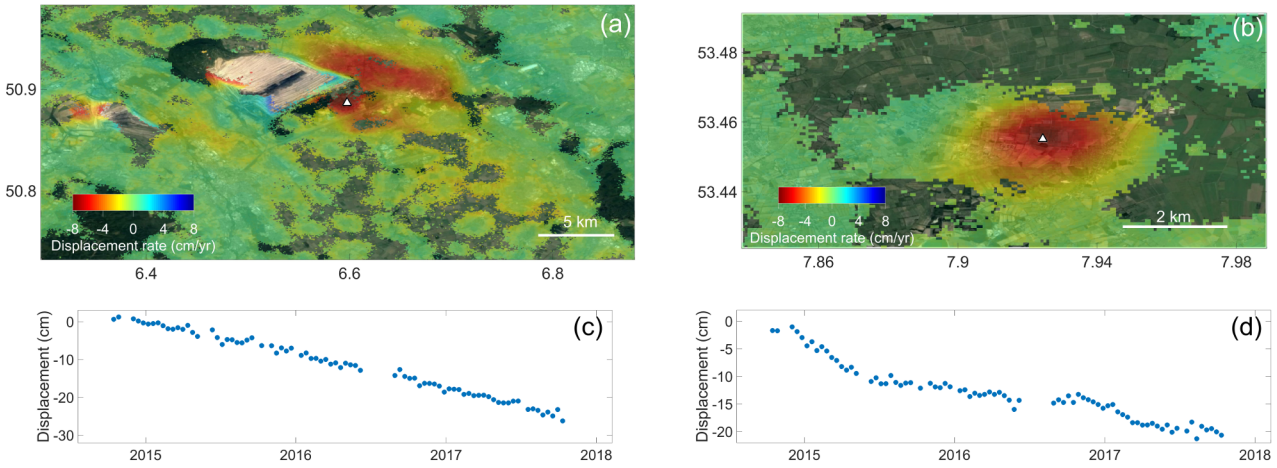


Figure 7.9.: Examples of localized displacement in Germany in (a) Tagebau hambach mining area in North Rhine-Westphalia and (b) Etzel gas storage facilities in Schlewig-Holstein. (c) and (d) examples of displacement time series for locations indicated by white triangles. The displacements are geocoded and converted from line of sight to vertical. Background images are from Google Earth™.

7.6. Discussion

A visual inspection of the interferograms and the estimated rates of displacement confirm that the adaptive approach proposed in this study improved the results and provided a reliable tool for the detection and monitoring of localized displacements. To further evaluate the performance of different correction approaches in reducing the errors, the Root Mean Square (RMS) of individual interferograms, the RMS of average rates of displacement, and the dependency of errors to relative distances are investigated. In order to perform an unbiased investigation, areas of displacement are excluded from the estimations. The displacement areas are identified based on the displacement rate map obtained from interferograms after adaptive correction.

As a measure of remaining errors in the interferograms, the RMS of individual interferograms are estimated. The RMS values for track 35, illustrated in Figure 7.10-a, confirm that all correction approaches reduce the tropospheric effect. While the RMS of the original interferograms reach 7 cm, the 2-D ramps and GACOS approaches decrease the standard deviation to a maximum of approximately 5 cm and 3 cm respectively. On the other hand, the adaptive correction significantly improves the RMS and decreases it to a maximum of approximately 1 cm.

The RMS of average velocity estimated from different numbers of interferograms in track 35 are illustrated in Figure 7.10-b. As expected, the estimated RMS decreases as the number of interferograms increases. For the number of interferograms more than 50, RMS of average velocity using adaptive correction converges towards 0.3 cm/yr. In the other three approaches, although the RMS generally decrease to approximately 2 cm/yr, it does not converge. This is caused by considerable remains of tropospheric artifact in the interferograms.

The RMS of individual interferograms and RMS of average velocities in track 139 are shown in Figure 7.11. The RMS of individual interferograms are improved from a maximum of approximately

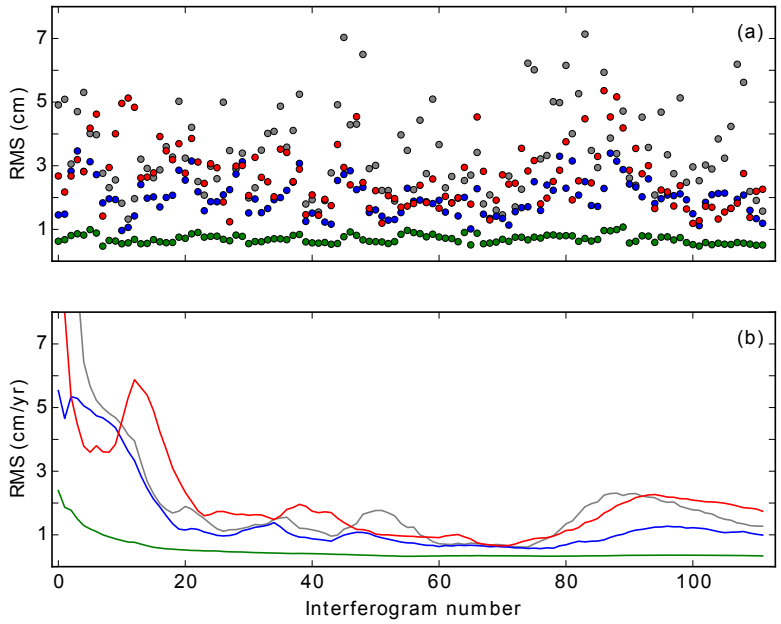


Figure 7.10.: (a) Standard deviation of individual interferograms corrected using different approaches in track 35. (b) RMS of average velocities estimated using different number of interferograms. Gray circles and line correspond to original interferograms. Blue, red, and green circles and lines correspond to interferograms corrected using a 2-D ramp removal, using GACOS model, and using the adaptive approach respectively.

6 cm in the original interferograms to 4 cm after 2-D ramp removal, 3 cm after GACOS correction, and 1 cm after adaptive correction of interferograms. Similar to the results in track 35, in this track, the RMS of the linear rate of displacement using adaptive correction converges towards approximately 0.3 cm/yr. Taking the estimated RMS of displacement rates as a measure of precision, in both study areas, displacement exceeding 1 cm/yr (3σ) can be detected reliably with 95% confidence interval.

To evaluate the dependency of remaining errors to the relative distance, at every 10-km intervals between 0 and 700 km, 1000 pairs of pixels are randomly sampled. The results for track 35, shown in Figure 7.12, indicates that when using the original interferograms, the average and standard deviation of velocity difference increase with distance. Although it flattens from a distance of approximately 200 km, it increases again after a distance of 500 km. The 2-D ramp removal and GACOS correction decrease the dependency to relative distance. The adaptive correction significantly improves the results and completely removes the dependency to distance.

The dependency of errors to the relative distance in track 139 is shown in Figure 7.13. Similar to the results in track 35, using original interferograms yield an apparent dependency of the error to the relative distance. Using the 2-D ramp and GACOS correction significantly decreases the dependency. The adaptive correction removes the dependency of the errors to relative distance entirely. As a result, there is no need to select a reference point close to the area of interest.

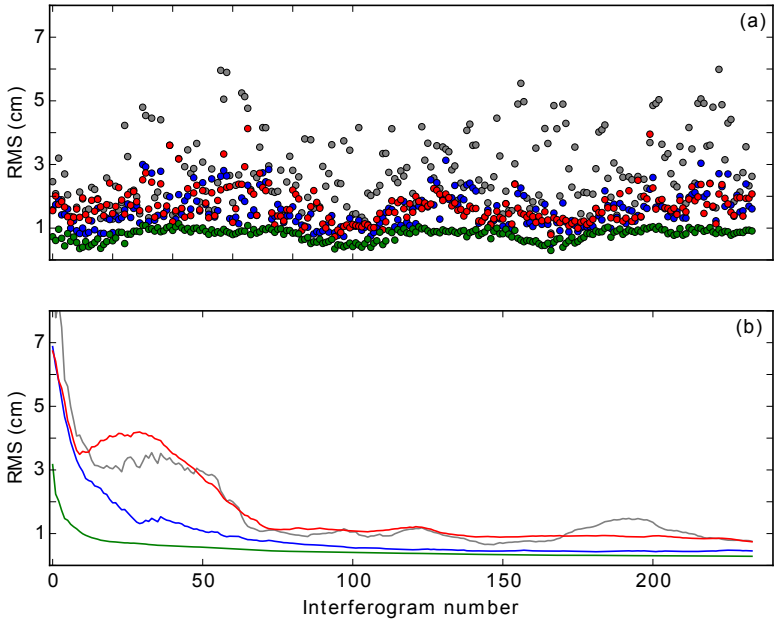


Figure 7.11.: (a) Standard deviation of individual interferograms corrected using different approaches in track 139. (b) RMS of average velocities estimated using different number of interferograms. Gray circles and line correspond to original interferograms. Blue, red, and green circles and lines correspond to interferograms corrected using a 2-D ramp, using GACOS model, and using the adaptive approach respectively.

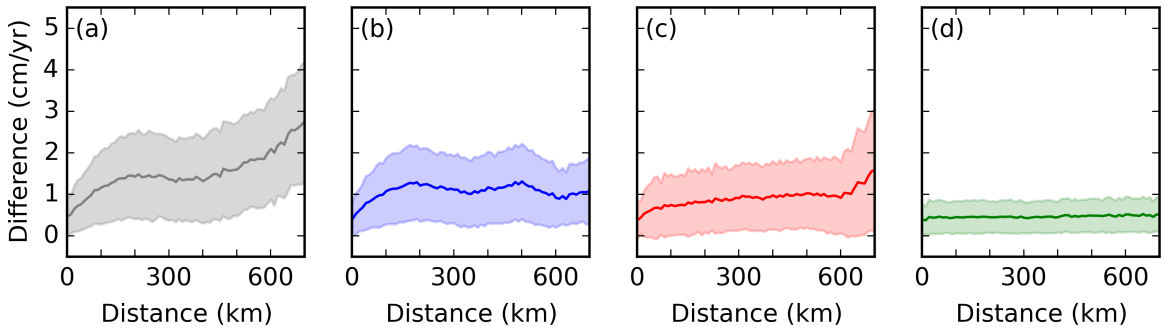


Figure 7.12.: Average and standard deviation of velocities as a function of relative distance. a-d correspond to the results in track 35 shown in Figure 7.6 a-d.

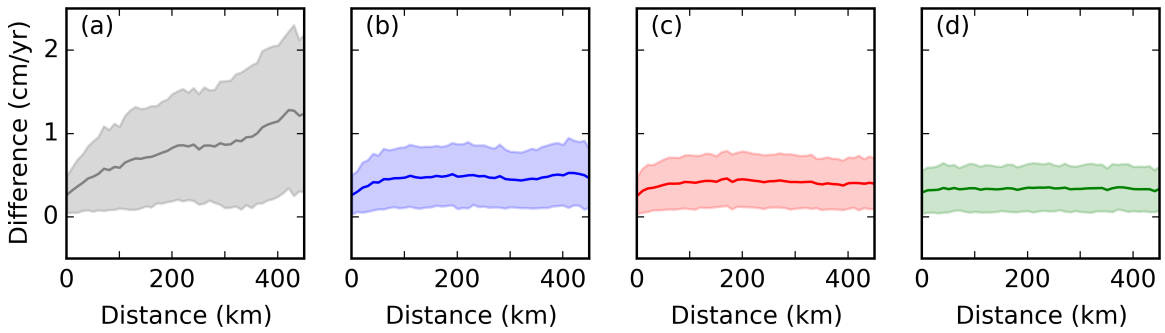


Figure 7.13.: Average and standard deviation of velocities as a function of relative distance. a-d correspond to the results in track 139 show in Figure 7.8 a-d.

7.7. Conclusion

In this chapter, a workflow was provided to process large stacks of interferograms in order to rapidly detect localized displacement areas on a country scale. An adaptive method was proposed to mitigate the broad-scale and stratified tropospheric errors from the interferograms using their own interferometric phase information. It also addressed the selection of reference area by removing the dependency of errors to relative distance. The proposed workflow detected several areas of localized displacement in Iran and Germany as well as their time series of displacement.

The results obtained after adaptive correction were compared with the results after a 2-D ramp removal and after GACOS tropospheric correction. The comparison confirms that the adaptive correction outperformed the other mentioned approaches. The adaptive correction significantly improved the results by separating the localized displacements from the background errors. it removed most parts of the broad-scale and topography-correlated errors from the individual interferograms and reduced the RMS of them to lower than 1 cm. Then, by stacking several interferograms, the remaining errors were mitigated and the RMS of average velocities reduced to approximately 0.3 cm/yr.

It should be noted that while the proposed approach removes the broad-scale phase changes from the interferograms, it is not able to distinguish displacement signals with similar long-wavelength behavior, e.g., tectonic interseismic or postseismic signals. Therefore, this approach cannot be used to detect such signals unless the window size is chosen large enough, so the desired displacement is not filtered out. However, increasing the window size decreases the ability of the method in mitigating the tropospheric phase delay. Another limitation of this approach is that it works with multilooked interferograms in order to reduce the processing load. Therefore, for spot displacements like sinkholes or very localized landslides, the signal might be obscured after multilooking.

The results of the proposed workflow highlighted non-tectonic displacement areas that can be further investigated in terms of geohazard or geophysical processes. Combining the large-scale displacement maps with other layers of geospatial data is particularly helpful to identify areas that need further deformation monitoring or rapid response by decision makers. For such areas, sophisticated InSAR time series techniques such as StaMPS (Hooper, 2008) or SqueeSAR (Ferretti et al., 2011) can also be performed at the local scale in order to analyze the data at the highest possible resolution and extract the maximum amount of information from the data.

Chapter 8

Cooperation Works

During the completion of this thesis, the author was involved in several other research projects that led to the publication of three peer-reviewed papers in line with the findings of this thesis. All those projects use InSAR measurements from different sensors to study surface deformation at local to regional scales. In the following, those works are briefly presented and the author contributions are described.

8.1. Quantifying Land Subsidence in the Rafsanjan Plain, Iran Using InSAR Measurements

published as:

Motagh, M., Shamshiri, R., **Haghshenas Haghighi, M.**, Wetzel, H.U., Akbari, B., Nahavandchi, H., Roessner, S., Arabi, S., 2017. *Quantifying groundwater exploitation induced subsidence in the Rafsanjan plain, southeastern Iran, using InSAR time-series and in situ measurements.* Engineering Geology 218, 134–151.

8.1.1. Abstract

Decades of groundwater overexploitation for agriculture and industrial development have resulted in substantial land subsidence in the Rafsanjan plain of southeastern Iran. This work presents the results of an InSAR time series analysis obtained by the exploitation of Envisat, ALOS and Sentinel-1 (S1) SAR data archives between June 2004, and May 2016, to investigate land subsidence in the plain. The InSAR analysis revealed an area of approximately 1000 km^2 within the study area showing subsidence of > 5 cm/year and locally exceeding 30 cm/yr in the last decade. This area of significant subsidence is limited in its spatial extent to the agricultural land and is partly influenced by Quaternary faults. The temporal and areal relationships of subsidence and groundwater level data suggest that a significant part of the observed subsidence in the Rafsanjan region is caused by intense groundwater extraction that has led to widespread compaction within the upper parts of the up to 300 m thick unconsolidated sediments, causing irreversible and inelastic deformation of the aquifer. The average volume storage loss of the aquifer system due to overexploitation is estimated to have been approximately 300 million cubic metre (mcm)/yr over the last decade.

8.1.2. Author Contribution

The author of the thesis contributed to this paper by providing InSAR time series analysis of ALOS data and decomposition of line-of-sight measurements to vertical and east-west components. The results, combined with Envisat and Sentinel-1 InSAR, helped to analyze the temporal behavior of subsidence and indicated that the rate of subsidence has slightly decreased in recent years, but the extent of affected areas remained the same. Comparing the InSAR results with groundwater level data confirmed that the decline of the groundwater level is responsible for the observed displacement. Decomposition of line-of-sight measurement to vertical and east-west components revealed that although the subsidence is the dominant part of observed displacement, horizontal displacement locating at the margins of subsidence area towards the peaks of subsidence reaches several centimeters (Figure 8.1).

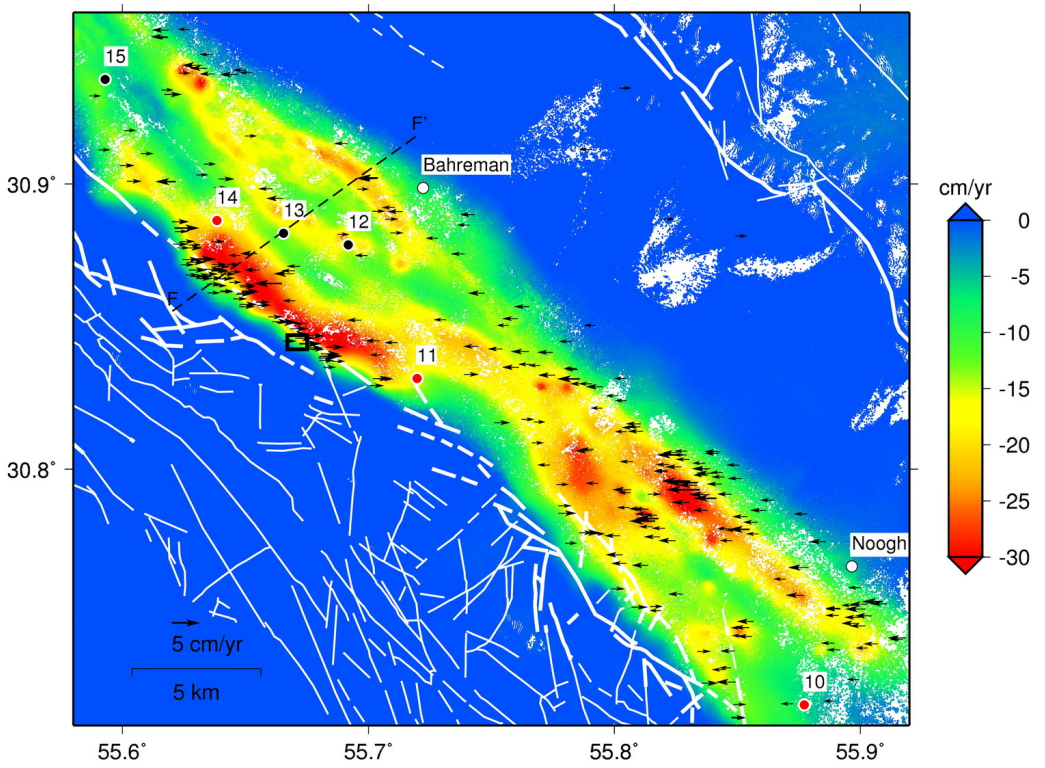


Figure 8.1.: Average 2015–2016 vertical and east-west displacement rates derived from the decomposition of the Sentinel-1 ascending and descending LOS velocities; the background color corresponds to vertical displacement rates and arrows to horizontal displacement rates. The black and red-filled circles correspond to the locations of piezometric wells in the area. The red-filled circles mark the locations of the wells with negative correlations between ground surface displacement and groundwater level. The white lines depict the faults and lineaments. The white-filled circles show the main townships and villages. Figure from (Motagh et al., 2017).

8.2. Characterizing Post-construction Settlement of Masjed-Soleyman Dam Using TerraSAR-X SpotLight InSAR

published as:

Emadali, L., Motagh, M., **Haghshenas Haghighi, M.**, 2017. *Characterizing post-construction settlement of the Masjed-Soleyman embankment dam, Southwest Iran, using TerraSAR-X SpotLight radar imagery.* Engineering Structures 218, 134–151.

8.2.1. Abstract

Geodetic monitoring of infrastructures is one of the key tasks in surveying and engineering geology. Systematic monitoring and assessment of the exterior deformation of embankment dams for safety analysis are often difficult when using classical surveying techniques due to time-consuming surveying procedures and high labour costs. Modern remote sensing techniques play an important role in efficiently assessing deformation: changes in the geometry, position and orientation of dams. In this study, we present the feasibility of effective post-construction deformation monitoring of the

Masjed-Soleyman dam in Iran using high-resolution (∼1 m) synthetic aperture radar (SAR) imagery in SpotLight (SL) mode from the X-band TerraSAR-X (TSX) satellite. This dam has been monitored over the last 15 years using classical surveying techniques, which provide horizontal and vertical deformation measurements of the structure. We show that high-resolution X-band SAR data provide a much more detailed identification of dam deformation in the crest and downstream that is not possible to infer from classical surveying techniques with few sparse geodetic monuments. High-resolution TSX data reveal that the dam is currently subject to two different deformation regimes: one is related to the crest and its adjacent area downstream, with a maximum rate of deformation of approximately 13 cm/yr in the radar line-of-sight (LOS). The other is related to the lower part of the downstream, with a maximum LOS velocity of 7 cm/yr. The effect of this centimetre displacement rate has been shown through several damage features on the dam body, including minor to large dislocation cracks on the crest and a significant deformation zone on the downstream slope.

8.2.2. Author Contribution

The author of the thesis contributed to this paper by performing time series analysis of SpotLight TerraSAR-X data (Figure 8.2) and assessing the effect of pixel size and multilooking on the ability of InSAR in detecting complex deformation regime of the dam. InSAR time series analysis at highest possible resolution provided spatially dense measurements of surface deformation, presenting a more complete picture of the deformation on the crest and downstream embankment of the dam that was difficult to obtain using sparse geodetic measurements. The analysis of interferograms with different multilooking factors highlighted the importance of high-resolution SAR imaging to map the deformation on the crest of the dam. Such a detailed mapping of deformation would not be possible using medium resolution SAR sensor like Sentinel-1.

8.3. InSAR Observation of the 18 August 2014 Mormori (Iran) Earthquake

published as:

Motagh, M., Bahroudi, A., **Haghshenas Haghighi, M.**, Samsonov, S., Fielding, E., Wetzel, H., 2015. *The 18 August 2014 Mw 6.2 Mormori, Iran, earthquake: A thin-skinned faulting in the Zagros mountain inferred from InSAR measurements.* Seismological Research Letters 86, 775–782.

8.3.1. Author Contribution

The author of the thesis performed the atmospheric correction of the interferograms used in this paper to infer the faulting mechanism of the 2014 Mw 6.2 Mormori, Iran, earthquake. Two RADARSAT-2 interferograms exhibit fringes strongly correlated with topography that indicates the contribution from stratified tropospheric phase delay (Figure 8.3-a and c). To mitigate this effect, together with any artifact fringes resulting from orbital errors or broad-scale tropospheric phase delay, a bilinear ramp combined with a linear height-dependent model is fitted to the unwrapped interferograms. The

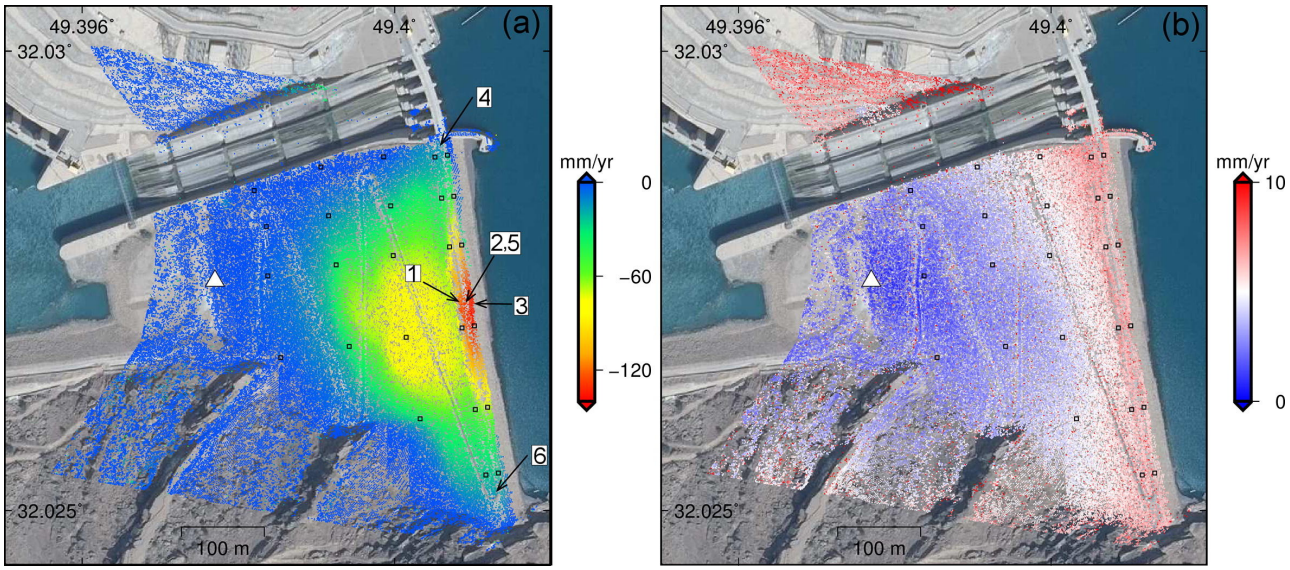


Figure 8.2.: (a) Average 2014–2015 displacement rate along the LOS direction derived from TerraSAR-X SpotLight data overlaid on a Google Earth™ image. The white triangle is the location of the InSAR measurement reference point. The black squares are locations of terrestrial geodetic measurement points. The numbers indicate locations where evidence of surface deformation of the dam were observed in the field. (b) Standard deviations of mean LOS velocity. Figure from (Emadali et al., 2017).

potential deformation area around the epicenter is masked out before estimating the model parameters. The corrected interferograms show significant improvement with most of the topography-correlated signals have been removed. Clear fringe lobes around the epicenter area are then observable (Figure 8.3-b and d), which are used in dislocation modeling and geological interpretation that suggest a seismogenic thin-skinned crustal shortening west of the Zagros mountain range.

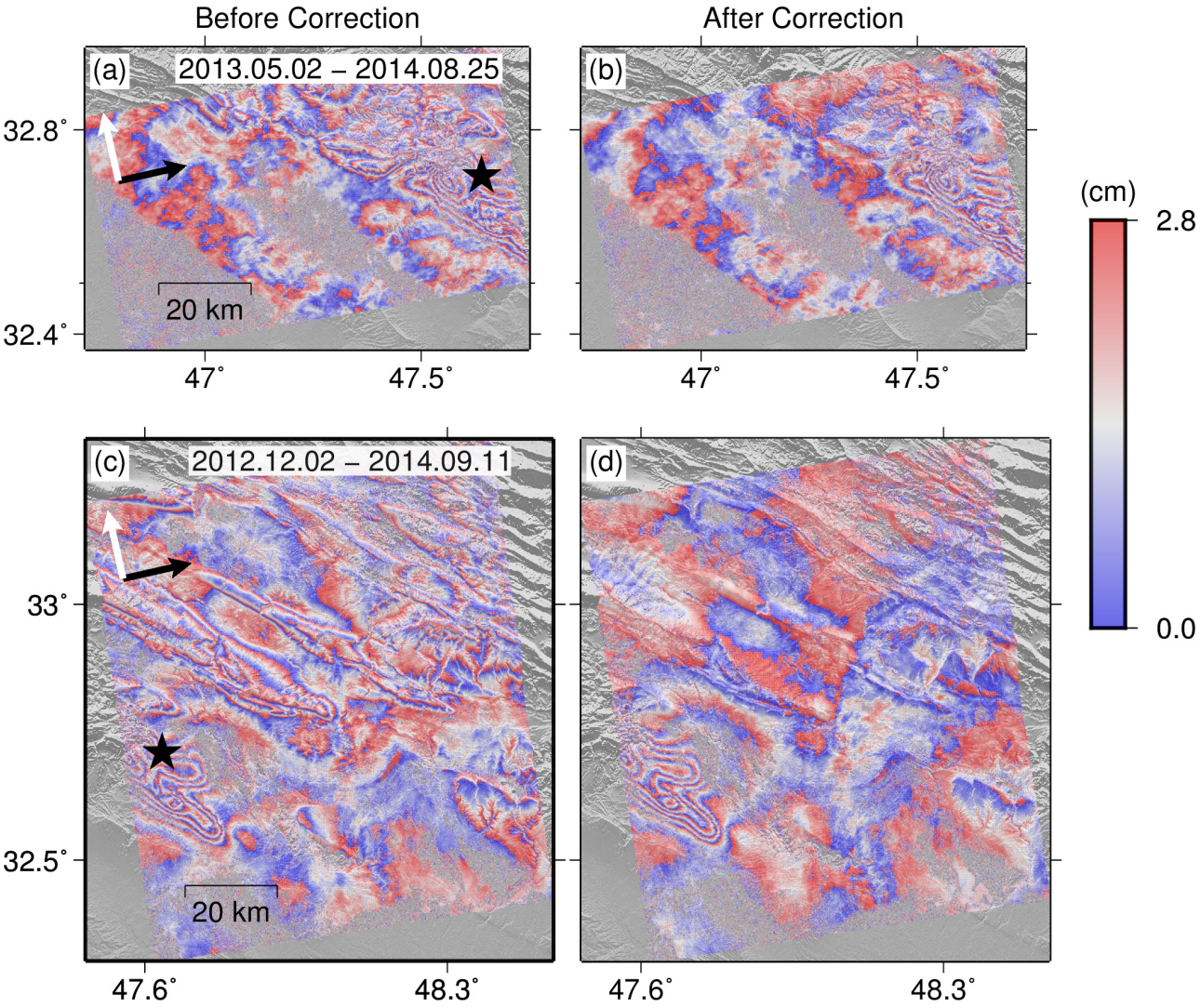


Figure 8.3.: The RADARSAT-2 interferograms used in this study before (left) and after (right) empirical atmospheric corrections. (a,b) The 2013.05.02–2014.08.25 interferogram. (c,d) The 2012.12.02–2014.09.11 interferogram. The interferograms have been unwrapped and rewrapped again with each fringe representing 2.8 cm of line-of-sight displacement from ground to satellite. Blue to red correspond to LOS uplift. Black star, earthquake epicenter from the Iranian Seismological Center catalog; white arrow, azimuth direction; black arrow, LOS direction. Figure from (Motagh et al., 2015).

Chapter 9

Summary and Future Work

In this thesis, local to regional displacements in the range of a few mm/yr to several cm/yr related to different earth surface processes in different regions were investigated. Using the archive of the old SAR sensors such as Envisat ASAR and ALOS PALSAR, made it possible to analyze the temporal behavior of displacement over long periods of time. On the other hand, the new generation of SAR sensors, such as TerraSAR-X and Sentinel-1, that are currently in orbit, helped to monitor the current status of the displacement.

In chapter 4, Small Baseline time series analysis was applied on SAR data from Envisat and TerraSAR-X satellites that revealed a very localized slope movement in the order of a few mm/yr in Taihape, New Zealand. It has been found that from 2003 to 2011, the landslide was active with a maximum detected displacement of $<$10 mm/yr. Then, the link between the surface displacement and the rainfall and groundwater variations was analyzed. It has been shown that better temporal and spatial resolution of TerraSAR-X significantly improved the ability to obtain information about the extremely slow landslide movement in the region. The results also showed that satellite imaging geometry plays an essential role in its ability to map slope displacements in specific directions.

In chapter 5, Small Baseline time series analysis was applied on a large stack of SAR data acquired by different satellites to investigate regional subsidence in Greater Tehran, Iran. Three major subsidence areas were detected in the region with the peaks of subsidence exceeding 25 cm/yr to the southwest of Tehran, 5 cm/yr near Tehran international airport and 20 cm/yr near Varamin. The analysis showed that from 2003 to 2017, the subsidence has been migrating towards the urban area of Tehran and its international airport. It has also been analyzed how the surface responded to the short and long-term variations of groundwater and found that a large portion of land subsidence in Tehran is likely to be irrecoverable. The findings have shown how the rich archive of older satellites can provide details on both the short- and long-term displacement regimes of the study area. It was also discussed that regular data acquisition provided by new sensors such as TerraSAR-X and Sentinel-1 made it possible to obtain reliable displacements using computationally faster and less sophisticated InSAR time series approaches.

In chapter 6, Sentinel-1 data was used to investigate localized displacements in the order of mm/yr to cm/yr in two study areas in Germany. The results have shown how high temporal resolution of Sentinel-1 helps to precisely monitor the temporal development of local to regional displacements. Using Persistent Scatterer InSAR, a localized uplift of approximately 2 mm/yr, as well as seasonal variations of up to 2 cm attributed to underground gas storage in Berlin was measured. Furthermore, localized subsidence of 8 mm/yr due to the settlement of an old demolishing landfill was observed. In an active mining area near Leipzig, Small Baseline InSAR measured subsidence as much as 4 cm/yr as well as the east-west movement of up to 5 cm/yr. Moreover, the presence of tropospheric artifact in large-scale interferograms across Germany was also analyzed in this chapter, and atmospheric corrections using phase delays from ERA-I model and GNSS measurements were compared.

In chapters 3 and 7, the limitations of external data from ERA-Interim in mitigating the tropospheric error in large-scale interferograms were discussed. A new workflow was proposed to analyze the massive stream of Sentinel-1 in order to reduce the tropospheric phase delay and detect localized displacements over extensive areas. The proposed method also removed the dependency of errors to relative distance

and therefore relaxed the need to select a reference point near the desired displacement area. The proposed workflow was applied on two long tracks of Sentinel-1 data across Iran and Germany and successfully mapped the displacement areas.

In summary, the results of this thesis have shown that dense temporal measurements are vital to the InSAR observations of the dynamics of earth surface deformation and finding their link to the driving mechanisms. From local to regional scales, InSAR time series analysis accurately mitigates the errors and provides reliable displacements in the order of a few mm/yr to cm/yr. However, as the size of the study area increases, tropospheric artifact becomes a major limiting factor for InSAR measurements. It has been shown that although using external atmospheric information from global weather models or GNSS measurements can significantly reduce the tropospheric error in InSAR measurements, the low temporal or spatial resolutions are the main limiting factor of such information. This thesis has shown that temporally dense and regular data provided by the Sentinel-1 mission is beneficial to mitigate the tropospheric artifact and map the localized displacements on a nation-wide scale.

Based on the findings of this thesis, the three research questions raised in chapter 1 can be answered as follows:

1. What is the performance of InSAR in monitoring local to regional geohazards caused by different earth surface processes and how Sentinel-1 SAR mission with dense and regular temporal resolution can improve it?

   Four different geohazards including landslide, land subsidence due to groundwater pumping, mining deformation, and land uplift due to gas storage has been investigated in this study. Although the nature of the studied issues and their environments were significantly different, InSAR successfully outlined the deforming areas and measured the long-term and temporal variations of surface displacement in all study areas. In the past, the lack of SAR data coverage by former sensors made InSAR inapplicable in many areas. However, even in areas where data were available, sporadic data acquisition plans limited the potential of InSAR in revealing temporal variations of deformation. Nevertheless, they offer a great insight into the history of displacement for areas where any SAR data is available in the archives of older sensors. Sentinel-1 mission solved the limitation on data availability by providing regular SAR data all over the world. The high temporal resolution of Sentinel-1 data allows a detailed temporal analysis of displacement and can precisely reveal both long and short term variations of surface displacement. Furthermore, coverage of an area by different tracks of Sentinel-1 allows a cross-comparison of the results and decomposition of measurements from the line of sight into other components.

2. To what extent atmospheric artifact is important in InSAR analysis at local, regional and national scales? How can it be addressed in order to highlight the displacement signals at different scales?

   Based on the findings of this thesis, although the effect of the atmospheric artifact can be significant in individual interferograms, in local to regional scales InSAR time series analysis is capable of significantly reducing it. Furthermore, selecting reference areas close enough to

the study area decreases the effect of atmospheric phase delay in the results. The results of the InSAR time series at local to regional scales can achieve an estimation of long-term displacement down to a mm/yr scale and seasonal variations as small as a few mm when regular SAR data with high temporal resolution are available. However, as the size of study area increases, the effect of atmospheric artifact rises dramatically. This limits the effectiveness of tropospheric correction using external information when their temporal and spatial resolution is not adequate. A new approach proposed in this thesis successfully reduced the atmospheric artifact and highlighted the localized displacement signals in broad areas. The proposed method benefited from temporally dense observations of Sentinel-1 and used the interferometric phase information to filter out topography-correlated and broad-scale parts of atmospheric artifact effectively. Then, averaging the interferograms reduced the turbulent part of the troposphere that is highly uncorrelated in time.

3. How localized deformations can be efficiently detected and measured over large areas in the scale of hundreds to thousands of kilometers using Sentinel-1 mission which provides temporally dense and regular data with extensive spatial coverage? What are the main challenges and how they can be tackled?

   Sentinel-1 is the first SAR mission specifically designed to acquire data for InSAR applications. Its narrow orbital tube gives great flexibility in designing the network of interferograms for time series analysis. On the other hand, dense temporal observations allow the generation of interferograms with high-quality phases. Atmospheric artifact is the main challenge in large-scale Sentinel-1 interferometry. On the one hand, the atmospheric phase delay obscures the displacement signals and makes it difficult to distinguish them. On the other hand, the propagation of errors with distance makes areas far from the reference point highly contaminated by errors. Therefore, a careful atmospheric correction is needed in order to achieve reliable displacement information at large scales. The findings of this thesis show that atmospheric correction using current atmospheric models is not successful mainly due to limited spatial or temporal resolution of them. Using the internal phase information, the proposed method successfully reduced the atmospheric artifact from individual interferograms and decreased the propagation of error with distance. Using such correction solves the main challenge of large-scale InSAR and highlights the displacement anomalies in the results.

9.1. Future works

The proposed workflow for large-scale displacement mapping successfully detected land subsidence areas across Iran as well as anthropogenic subsidence and uplifts attributed to mining and gas storage across Germany. The results provide an overall picture of the displacement situation in large areas and indicate areas for further investigations. In those areas, InSAR time series analysis can be performed at highest possible resolution using Sentinel-1 data or high-resolution SAR sensors like TerraSAR-X for detail mapping or near real time monitoring of geohazards. Furthermore, historical analysis can be performed in areas where SAR data are available in the archives of older SAR sensors such as ERS1/2, Envisat, and ALOS.

The proposed approach in this thesis was used to locate and measure subsidence/uplift in large scales. The applications of this approach can be extended to detection of landslide movements in large areas. In this regard, a detailed analysis of slopes would be needed for a correct interpretation of the displacement maps. Converting the line of sight displacements to slope movements might be helpful when interpreting the results. It should be noted that because of side looking geometry of SAR, InSAR measurement is not sensitive to certain slope movements. Using both ascending and descending SAR geometries increases the chance to obtain maximum relevant information on different slopes.

The proposed method in this thesis successfully detected hot spots of displacement from SAR data acquired in descending tracks of Sentinel-1. Then, the obtained displacements were converted from satellite line of sight to vertical component by neglecting the horizontal movements. However, our regional analysis showed that the horizontal movements, particularly in land subsidence and mining areas, may reach several centimeters. Large-scale displacement maps in ascending orbits can be combined with the descending results to distinguish horizontal and vertical movements.

In our study areas, tropospheric correction using the GACOS model was not successful in reliably removing tropospheric artifact from large-scale interferograms. It was mainly because of limited temporal and spatial resolutions of atmospheric models used to produce GACOS phase delays. GACOS estimates phase delays from high resolution ECMWF weather model at 0.125-degree spatial resolution and 6-hour intervals. The new generation of ECMWF ERA-5 reanalysis data with an hourly temporal resolution might significantly improve the tropospheric correction.

Although the proposed workflow successfully detected localized displacements over extensive areas in Iran and Germany, it should be noted that it has significant limitations in measuring broad-scale displacements like tectonic displacements. This approach is not able to separate such displacements from long-wavelength tropospheric artifact. In such cases, tropospheric correction based on external tropospheric data would be more relevant.

The tropospheric correction can be improved in areas like Germany where dense networks of GNSS stations are available. However, the findings of this thesis show that the spatial distribution of the stations highly affect the quality of the results. An unbiased interpolation of the tropospheric phase delay is a challenge when using sparse GNSS tropospheric measurements. On the other hand, Sentinel-1 mission provides temporally dense and regular SAR data acquisition. As shown in this thesis, while short term interferograms do not exhibit significant displacement signals, they are highly affected by atmospheric phase delays. Future work can focus on integrating data from GNSS or high-resolution atmospheric models with InSAR observations made from images with short-temporal baseline in approaches like machine learning to improve estimations of atmospheric artefacts in InSAR phase measurement.

Appendix A

Software and Tools

This chapter provides a brief overview of the software and their parameter configurations used in this study. The used software can be classified into three main groups: Interferometric tools to produce the interferograms, InSAR time series analysis tools, and mathematical tools to interpret the results. In the following, each group of is briefly described.

For Interferometric processing, three software were used. ROI_PAC (Rosen et al., 2004) was used to generate SLC images from raw SAR images acquired by ALOS and Envisat. DORIS software (Kampes and Usai, 1999) was used to coregister SLC data, resample them and generate the interferograms of ALOS, Envisat, and TerraSAR-X. For Sentinel-1 data, GAMMA software was used to coregister, resample and generate the interferograms. DORIS and ROI_PAC are free and open source software while GAMMA is commercial.

Time series analysis of data in chapters 4-6 were performed using StaMPS/MTI software (Hooper et al., 2013) version 3.3b1. The main parameters configuration used for each study area is listed in tables A.1-A.3.

Cross Wavelet and Wavelet Coherence Toolbox (Grinsted et al., 2004) was used in chapters 4 and 5 to analyze the time series of displacement and find their link to other field measurements.

Table A.1.: Parameters used in StaMPS/MTI software in chapter 4.

Parameter	Default value	Envisat	TerraSAR-X
filter_grid_size	50	50	10
merge_resample_size	100	0	0
unwrap_grid_size	200	50	20

Table A.2.: Parameters used in StaMPS/MTI software in chapter 5.

Parameter	Default value	Envisat	ALOS	TerraSAR-X Stripmap	TerraSAR-X Spotlight	Sentinel-1
unwrap_method	3D-Quick	3D	3D	3D	3D	3D
unwrap_grid_size	200	50	50	50	50	50
scla_deramp	'n'	'y'	'y'	'y'	'y'	'y'
merge_resample_size	100	50	50	-	-	-

Table A.3.: Parameters used in StaMPS/MTI software in chapter 6.

Parameter	Default value	Berlin	Leipzig
weed_neighbours	'y'	'n'	'y'
scla_deramp	'n'	'y'	'y'

Bibliography

Abbassi, M.R., Farbod, Y., 2009. Faulting and folding in quaternary deposits of Tehran's piedmont (Iran). Journal of Asian Earth Sciences 34, 522–531.

Adam, N., Gonzalez, F.R., Parizzi, A., Brcic, R., 2013. Wide area persistent scatterer interferometry: Current developments, algorithms and examples, in: 2013 IEEE International Geoscience and Remote Sensing Symposium - IGARSS, pp. 1857–1860.

Akbari, V., Motagh, M., 2012. Improved ground subsidence monitoring using small baseline SAR interferograms and a weighted least squares inversion algorithm. IEEE Geoscience and Remote Sensing Letters 9, 437–441.

Akbarimehr, M., Motagh, M., Haghshenas Haghighi, M., 2013. Slope stability assessment of the sarcheshmeh landslide, northeast iran, investigated using insar and gps observations. Remote Sensing 5, 3681–3700.

Alipour, S., Motgah, M., Sharifi, M.A., Walter, T.R., 2008. InSAR time series investigation of land subsidence due to groundwater overexploitation in Tehran, Iran, in: 2008 Second Workshop on Use of Remote Sensing Techniques for Monitoring Volcanoes and Seismogenic Areas, pp. 1–5.

Alshawaf, F., Fersch, B., Hinz, S., Kunstmann, H., Mayer, M., Thiele, A., Westerhaus, M., Meyer, F., 2012. Analysis of atmospheric signals in spaceborne insar - toward water vapor mapping based on multiple sources, in: 2012 IEEE International Geoscience and Remote Sensing Symposium, pp. 1960–1963.

Alshawaf, F., Hinz, S., Mayer, M., Meyer, F.J., 2015. Constructing accurate maps of atmospheric water vapor by combining interferometric synthetic aperture radar and gnss observations. Journal of Geophysical Research: Atmospheres 120, 1391–1403.

Amelung, F., Galloway, D.L., Bell, J.W., Zebker, H.A., Laczniak, R.J., 1999. Sensing the ups and downs of Las Vegas: InSAR reveals structural control of land subsidence and aquifer-system deformation. Geology 27, 483–486.

Amidi, S., Nogol-Sadat, A.A., Hushmandzadeh, A., Beruzzi, A., Lofti, M., Nazer, N.K., Mahdavi, M., Cailallat, C., Dehlavi, P., Martin-Jantin, B., 1984. Geological quadrangle map of Iran, Saveh sheet, scale 1:250,000. Report. Geological Survey of Iran (GSI), Tehran.

Arabi, S., Maleki, E., Talebi, A., 2008. Report of land subsidence in south-west of Tehran. Report. National Cartographic Center of Iran (NCC), Tehran.

Bachmanov, D., Trifonov, V., Hessami, K., Kozhurin, A., Ivanova, T., Rogozhin, E., Hademi, M., Jamali, F., 2004. Active faults in the Zagros and central Iran. Tectonophysics 380, 221 – 241. Active Faults of the Eastern Hemisphere.

Baldi, P., Cenni, N., Fabris, M., Zanutta, A., 2008. Kinematics of a landslide derived from archival photogrammetry and gps data. Geomorphology 102, 435 – 444.

Bamler, R., Hartl, P., 1998. Synthetic aperture radar interferometry. Inverse Problems 14, R1–R54.

Bateson, L., Cigna, F., Boon, D., Sowter, A., 2015. The application of the intermittent sbas (isbas) insar method to the south wales coalfield, uk. International Journal of Applied Earth Observation and Geoinformation 34, 249 – 257.

Baum, R.L., Galloway, D.L., Harp, E.L., 2008. Landslide and land subsidence hazards to pipelines. Report 2008-1164.

Bekaert, D., Walters, R., Wright, T., Hooper, A., Parker, D., 2015a. Statistical comparison of InSAR tropospheric correction techniques. Remote Sensing of Environment 170, 40 – 47.

Bekaert, D.P.S., Hooper, A., Wright, T.J., 2015b. A spatially variable power law tropospheric correction technique for insar data. Journal of Geophysical Research: Solid Earth 120, 1345–1356.

Bell, J.W., Amelung, F., Ferretti, A., Bianchi, M., Novali, F., 2008. Permanent scatterer InSAR reveals seasonal and long-term aquifer-system response to groundwater pumping and artificial recharge. Water Resources Research 44, W02407.

Berardino, P., Fornaro, G., Lanari, R., Sansosti, E., 2002. A new algorithm for surface deformation monitoring based on small baseline differential SAR interferograms. Geoscience and Remote Sensing, IEEE Transactions on 40, 2375–2383.

Birkhölzer, J., Opheys, S., Rouvé, G., 1998. A Conceptual Study on the Rehabilitation of the Lignite Mining Area South of Leipzig. Springer Netherlands, Dordrecht. pp. 99–110.

Bürgmann, R., Rosen, P.A., Fielding, E.J., 2000. Synthetic Aperture Radar Interferometry to measure Earth's surface topography and its deformation. Annual Review of Earth and Planetary Sciences 28, 169–209.

Cascini, L., Fornaro, G., Peduto, D., 2010. Advanced low- and full-resolution dinsar map generation for slow-moving landslide analysis at different scales. Engineering Geology 112, 29 – 42.

Castel, T., Martinez, J.M., Beaudoin, A., Wegmüller, U., Strozzi, T., 2000. Ers insar data for remote sensing hilly forested areas. Remote Sensing of Environment 73, 73 – 86.

Castellazzi, P., Garfias, J., Martel, R., Brouard, C., Rivera, A., 2017. InSAR to support sustainable urbanization over compacting aquifers: The case of Toluca Valley, Mexico. International Journal of Applied Earth Observation and Geoinformation 63, 33 – 44.

Castellazzi, P., Martel, R., Galloway, D.L., Longuevergne, L., Rivera, A., 2016. Assessing groundwater depletion and dynamics using GRACE and InSAR: Potential and limitations. Groundwater 54, 768–780.

Cavalié, O., Doin, M.P., Lasserre, C., Briole, P., 2007. Ground motion measurement in the lake mead area, nevada, by differential synthetic aperture radar interferometry time series analysis: Probing the lithosphere rheological structure. Journal of Geophysical Research: Solid Earth 112.

Chadwick, J., Dorsch, S., Glenn, N., Thackray, G., Shilling, K., 2005. Application of multi-temporal high-resolution imagery and gps in a study of the motion of a canyon rim landslide. ISPRS Journal of Photogrammetry and Remote Sensing 59, 212 – 221. Remote Sensing and Geospatial Information for Natural Hazards Characterization.

Chakraborty, A., Okaya, D., 1995. Frequency-time decomposition of seismic data using wavelet-based methods. Geophysics 60, 1906–1916.

Chaussard, E., Wdowinski, S., Cabral-Cano, E., Amelung, F., 2014. Land subsidence in central Mexico detected by ALOS InSAR time-series. Remote Sensing of Environment 140, 94–106.

Chen, C., Pei, S., Jiao, J., 2003. Land subsidence caused by groundwater exploitation in Suzhou City, China. Hydrogeology Journal 11, 275–287.

Cigna, F., Lasaponara, R., Masini, N., Milillo, P., Tapete, D., 2014. Persistent scatterer interferometry processing of cosmo-skymed stripmap himage time series to depict deformation of the historic centre of rome, italy. Remote Sensing 6, 12593–12618.

Cigna, F., Osmanoğlu, B., Cabral-Cano, E., Dixon, T.H., Ávila Olivera, J.A., Garduño-Monroy, V.H., DeMets, C., Wdowinski, S., 2012. Monitoring land subsidence and its induced geological hazard with Synthetic Aperture Radar Interferometry: A case study in Morelia, Mexico. Remote Sensing of Environment 117, 146–161.

Colesanti, C., Wasowski, J., 2006. Investigating landslides with space-borne synthetic aperture radar (sar) interferometry. Engineering Geology 88, 173 – 199.

Columbus, J., Sirguey, P., Tenzer, R., 2011. A free fully assessed 15 metre digital elevation model for new zealand. Survey Quarterly 300, 16.

Corapcioglu, M.Y., Bear, J., 1983. A mathematical model for regional land subsidence due to pumping: 3. Integrated equations for a phreatic aquifer. Water Resources Research 19, 895–908.

Cruden, D., Varnes, D., 1996. Landslides investigation and mitigation, transportation research board. Landslide types and process, National Research Council, National Academy Press, Special Report 247, 36–75.

De Luca, C., Cuccu, R., Elefante, S., Zinno, I., Manunta, M., Casola, V., Rivolta, G., Lanari, R., Casu, F., 2015. An on-demand web tool for the unsupervised retrieval of earth's surface deformation from sar data: The p-sbas service within the esa g-pod environment. Remote Sensing 7, 15630–15650.

De Zan, F., Monti Guarnieri, A., 2006. Topsar: Terrain observation by progressive scans. IEEE Transactions on Geoscience and Remote Sensing 44, 2352–2360.

Dee, D.P., Uppala, S.M., Simmons, A.J., Berrisford, P., Poli, P., Kobayashi, S., Andrae, U., Balmaseda, M.A., Balsamo, G., Bauer, P., Bechtold, P., Beljaars, A.C.M., van de Berg, L., Bidlot, J., Bormann, N., Delsol, C., Dragani, R., Fuentes, M., Geer, A.J., Haimberger, L., Healy, S.B., Hersbach, H., Hólm, E.V., Isaksen, L., Kållberg, P., Köhler, M., Matricardi, M., McNally, A.P., Monge-Sanz, B.M., Morcrette, J.J., Park, B.K., Peubey, C., de Rosnay, P., Tavolato, C., Thépaut, J.N., Vitart, F., 2011. The era-interim reanalysis: configuration and performance of the data assimilation system. Quarterly Journal of the Royal Meteorological Society 137, 553–597.

Dehghani, M., Valadan Zoej, M.J., Hooper, A., Hanssen, R.F., Entezam, I., Saatchi, S., 2013. Hybrid conventional and Persistent Scatterer SAR interferometry for land subsidence monitoring in the Tehran Basin, Iran. ISPRS Journal of Photogrammetry and Remote Sensing 79, 157–170.

Delacourt, C., Allemand, P., Casson, B., Vadon, H., 2004. Velocity field of the "la clapière" landslide measured by the correlation of aerial and quickbird satellite images. Geophysical Research Letters 31.

Delacourt, C., Briole, P., Achache, J.A., 1998. Tropospheric corrections of sar interferograms with strong topography. application to etna. Geophysical Research Letters 25, 2849–2852.

Doornbos, E., Scharroo, R., 2004. Improved ERS and Envisat precise orbit determination, in: Envisat & ERS Symposium, 6-10 Septermber 2004, Salzburg, Austria (ESA SP-572, April 2005).

Eineder, M., Adam, N., Bamler, R., Yague-Martinez, N., Breit, H., 2009. Spaceborne Spotlight SAR Interferometry With TerraSAR-X. IEEE Transactions on Geoscience and Remote Sensing 47, 1524–1535.

Ellen, S.D., Liu, L.S., Fleming, R.W., Reid, M.E., Johnsson, M.J., 1995. Relation of slow-moving landslides to earth materials and other factors in valleys of the Honolulu District of Oahu, Hawaii. Report 95-218.

Elliott, J.R., Biggs, J., Parsons, B., Wright, T.J., 2008. Insar slip rate determination on the altyn tagh fault, northern tibet, in the presence of topographically correlated atmospheric delays. Geophysical Research Letters 35.

Emadali, L., Motagh, M., Haghshenas Haghighi, M., 2017. Characterizing post-construction settlement of the Masjed-Soleyman embankment dam, Southwest Iran, using TerraSAR-X SpotLight radar imagery. Engineering Structures 143, 261 – 273.

Esmaeili, M., Motagh, M., 2016. Improved Persistent Scatterer analysis using Amplitude Dispersion Index optimization of dual polarimetry data. ISPRS Journal of Photogrammetry and Remote Sensing 117, 108 – 114.

Esmaeili, M., Motagh, M., Hooper, A., 2017. Application of dual-polarimetry SAR images in multitemporal InSAR processing. IEEE Geoscience and Remote Sensing Letters 14, 1489–1493.

Ezquerro, P., Herrera, G., Marchamalo, M., Tomás, R., Béjar-Pizarro, M., Martínez, R., 2014. A quasi-elastic aquifer deformational behavior: Madrid aquifer case study. Journal of Hydrology 519, 1192 – 1204.

F. Raspini, S. Bianchini, C.D.V.S.M.C.L.D.R.J.D.M.G., 2015. Subsidence mapping, characterization, and modeling: the esa-gmes terrafirma services, pp. 9535 – 9535 – 11.

Farr, T.G., Kobrick, M., 2000. Shuttle radar topography mission produces a wealth of data. Eos, Transactions American Geophysical Union 81, 583–585.

Fattahi, H., Amelung, F., 2013. Dem error correction in insar time series. IEEE Transactions on Geoscience and Remote Sensing 51, 4249–4259.

Fattahi, H., Amelung, F., 2014. Insar uncertainty due to orbital errors. Geophysical Journal International 199, 549–560.

Fattahi, H., Amelung, F., 2015. Insar bias and uncertainty due to the systematic and stochastic tropospheric delay. Journal of Geophysical Research: Solid Earth 120, 8758–8773.

Fattahi, H., Simons, M., Agram, P., 2017. Insar time-series estimation of the ionospheric phase delay: An extension of the split range-spectrum technique. IEEE Transactions on Geoscience and Remote Sensing 55, 5984–5996.

Ferretti, A., Fumagalli, A., Novali, F., Prati, C., Rocca, F., Rucci, A., 2011. A new algorithm for processing interferometric data-stacks: Squeesar. IEEE Transactions on Geoscience and Remote Sensing 49, 3460–3470.

Ferretti, A., Prati, C., Rocca, F., 2001. Permanent scatterers in SAR interferometry. IEEE Transactions on Geoscience and Remote Sensing 39, 8–20.

Fornaro, G., Reale, D., Verde, S., 2013. Bridge thermal dilation monitoring with millimeter sensitivity via multidimensional sar imaging. IEEE Geoscience and Remote Sensing Letters 10, 677–681.

Foufoula-Georgiou, E., Kumar, P., Chui, C., 1994. Wavelets in Geophysics. volume 4. Academic Press.

Francesca, C., Luke, B., Colm, J., Claire, D., 2013. Nationwide monitoring of geohazards in great britain with insar: Feasibility mapping based on ers-1/2 and envisat imagery, in: 2013 IEEE International Geoscience and Remote Sensing Symposium - IGARSS, pp. 672–675.

Froese CR, Van der Kooij M, K.K., 2004. Advances in the application of InSAR to complex, slowly moving landslides in dry and vegetated terrain, in: Landslides: evaluation and stabilization. Proceedings of the Ninth International Symposium on Landslides. Rio de Janeiro, p. 1255–1264.

Froude, M.J., Petley, D.N., 2018. Global fatal landslide occurrence from 2004 to 2016. Natural Hazards and Earth System Sciences 18, 2161–2181.

Fuhrmann, T., Knöpfler, A., Mayer, M., Schenk, A., Westerhaus, M., Zippelt, K., Heck, B., 2016. An inventory of surface movements in the upper rhine graben area, southwest germany, from sar-interferometry, gnss and precise levelling, in: Rizos, C., Willis, P. (Eds.), IAG 150 Years, Springer International Publishing, Cham. pp. 419–425.

Gabriel, A.K., Goldstein, R.M., Zebker, H.A., 1989. Mapping small elevation changes over large areas: Differential radar interferometry. Journal of Geophysical Research: Solid Earth 94, 9183–9191.

Galloway, D., Burbey, T., 2011. Review: Regional land subsidence accompanying groundwater extraction. Hydrogeology Journal 19, 1459–1486.

Galloway, D.L., Hudnut, K., Ingebritsen, S., Phillips, S., Peltzer, G., Rogez, F., Rosen, P., 1998. Detection of aquifer system compaction and land subsidence using interferometric synthetic aperture radar, Antelope Valley, Mojave Desert, California. Water Resources Research 34, 2573–2585.

Gili, J.A., Corominas, J., Rius, J., 2000. Using global positioning system techniques in landslide monitoring. Engineering Geology 55, 167 – 192.

Gleeson, T., Wada, Y., Bierkens, M.F.P., van Beek, L.P.H., 2012. Water balance of global aquifers revealed by groundwater footprint. Nature 488, 197–200.

Goldstein, R.M., Werner, C.L., 1998. Radar interferogram filtering for geophysical applications. Geophysical Research Letters 25, 4035–4038.

Goldstein, R.M., Zebker, H.A., Werner, C.L., 1988. Satellite radar interferometry: Two-dimensional phase unwrapping. Radio Science 23, 713–720.

Gomba, G., Parizzi, A., Zan, F.D., Eineder, M., Bamler, R., 2016. Toward operational compensation of ionospheric effects in SAR interferograms: The split-spectrum method. IEEE Transactions on Geoscience and Remote Sensing 54, 1446–1461.

Gonzáález, P.J., Bagnardi, M., Hooper, A.J., Larsen, Y., Marinkovic, P., Samsonov, S.V., Wright, T.J., 2015. The 2014–2015 eruption of fogo volcano: Geodetic modeling of sentinel-1 tops interferometry. Geophysical Research Letters 42, 9239–9246.

Gourmelen, N., Amelung, F., Lanari, R., 2010. Interferometric synthetic aperture radar–gps integration: Interseismic strain accumulation across the hunter mountain fault in the eastern california shear zone. Journal of Geophysical Research: Solid Earth 115.

Greif, V., Vlcko, J., 2012. Monitoring of post-failure landslide deformation by the ps-insar technique at lubietova in central slovakia. Environmental Earth Sciences 66, 1585–1595.

Grinsted, A., Moore, J.C., Jevrejeva, S., 2004. Application of the cross wavelet transform and wavelet coherence to geophysical time series. Nonlinear Processes in Geophysics 11, 561–566.

Haghipour, A., Taraz, H., Daneshmand, F.V., 1987. Geological quadrangle map of Iran, Tehran sheet, scale 1: 250,000. Report. Geological Survey of Iran (GSI), Tehran.

Haghshenas Haghighi, M., Motagh, M., 2016. Assessment of ground surface displacement in Taihape landslide, New Zealand, with C- and X-band SAR interferometry. New Zealand Journal of Geology and Geophysics 59, 136–146.

Haghshenas Haghighi, M., Motagh, M., 2017. Sentinel-1 insar over germany: Large-scale interferometry, atmospheric effects, and ground deformation mapping. zfv – Zeitschrift für Geodäsie, Geoinformation und Landmanagement 4, 245 – 256.

Haghshenas Haghighi, M., Motagh, M., 2019. Ground surface response to continuous compaction of aquifer system in tehran, iran: Results from a long-term multi-sensor insar analysis. Remote Sensing of Environment 221, 534 – 550.

Haghshenas Haghighi, M., Motagh, M., Esmaeili, M., 2013. Continuous compaction of aquifer system in Tehran, Iran, as evidenced by C-band, L-band and X-band radar measurements, in: The 5th TerraSAR-X Science Team Meeting, Oberpfaffenhofen, Germany.

Hancox, G., Wright, K., 2005. Analysis of landsliding caused by the 15-17 February 2004 rainstorm in the Wanganui-Manawatu hill country, southern North Island, New Zealand. science report. Institute of Geological & Nuclear Sciences.

Handwerger, A.L., Roering, J.J., Schmidt, D.A., 2013. Controls on the seasonal deformation of slow-moving landslides. Earth and Planetary Science Letters 377-378, 239 – 247.

Hanssen, R.F., 2001. Radar interferometry: data interpretation and error analysis. volume 2. Springer Science & Business Media.

Heimlich, C., Gourmelen, N., Masson, F., Schmittbuhl, J., Kim, S.W., Azzola, J., 2015. Uplift around the geothermal power plant of landau (germany) as observed by insar monitoring. Geothermal Energy 3, 2.

Helm, D.C., 1975. One-dimensional simulation of aquifer system compaction near Pixley, California: 1. Constant parameters. Water Resources Research 11, 465–478.

Helm, D.C., 1976. One-dimensional simulation of aquifer system compaction near Pixley, California: 2. Stress-Dependent Parameters. Water Resources Research 12, 375–391.

Hetland, E.A., Musé, P., Simons, M., Lin, Y.N., Agram, P.S., DiCaprio, C.J., 2012. Multiscale insar time series (mints) analysis of surface deformation. Journal of Geophysical Research: Solid Earth 117.

Hoffmann, J., Galloway, D.L., Zebker, H.A., 2003. Inverse modeling of interbed storage parameters using land subsidence observations, Antelope Valley, California. Water Resources Research 39.

Hoffmann, J., Zebker, H.A., Galloway, D.L., Amelung, F., 2001. Seasonal subsidence and rebound in Las Vegas Valley, Nevada, observed by Synthetic Aperture Radar Interferometry. Water Resources Research 37, 1551–1566.

Hole, J., Bromley, C., Stevens, N., Wadge, G., 2007. Subsidence in the geothermal fields of the taupo volcanic zone, new zealand from 1996 to 2005 measured by insar. Journal of Volcanology and Geothermal Research 166, 125 – 146.

Hooper, A., 2008. A multi-temporal InSAR method incorporating both persistent scatterer and small baseline approaches. Geophysical Research Letters 35, L16302.

Hooper, A., 2009. A statistical-cost approach to unwrapping the phase of InSAR time series, in: Proc. Fringe 2009 Workshop, Frascati, Italy, (30 November - 4 December 2009 (ESA SP-677, March 2010)), pp. 1–6.

Hooper, A., Bekaert, D., Spaans, K., 2013. Stamps/MTI Manual Version 3.3 b1.

Hooper, A., Bekaert, D., Spaans, K., Arıkan, M., 2012. Recent advances in SAR interferometry time series analysis for measuring crustal deformation. Tectonophysics 514–517, 1–13.

Hooper, A., Zebker, H., Segall, P., Kampes, B., 2004. A new method for measuring deformation on volcanoes and other natural terrains using InSAR persistent scatterers. Geophysical Research Letters 31, L23611.

Hooper, A., Zebker, H.A., 2007. Phase unwrapping in three dimensions with application to InSAR time series. Journal of the Optical Society of America A 24, 2737–2747.

Houlié, N., Funning, G.J., Bürgmann, R., 2016. Use of a gps-derived troposphere model to improve insar deformation estimates in the san gabriel valley, california. IEEE Transactions on Geoscience and Remote Sensing 54, 5365–5374.

Jolivet, R., Grandin, R., Lasserre, C., Doin, M.P., Peltzer, G., 2011. Systematic insar tropospheric phase delay corrections from global meteorological reanalysis data. Geophysical Research Letters 38.

Jung, H.S., Lee, D.T., Lu, Z., Won, J.S., 2013. Ionospheric correction of SAR interferograms by multiple-aperture interferometry. IEEE Transactions on Geoscience and Remote Sensing 51, 3191–3199.

Kampes, B., Usai, S., 1999. Doris: The delft object-oriented radar interferometric software, in: 2nd international symposium on operationalization of remote sensing, enschede, the netherlands, Citeseer. p. 20.

Kampes, B.M., 2005. Displacement parameter estimation using permanent scatterer interferometry. Ph.D. thesis. TU Delft, Delft University of Technology.

Kampes, B.M., Hanssen, R.F., Perski, Z., 2003. Radar interferometry with public domain tools, in: Proceedings of FRINGE.

Keys, R., 1981. Cubic convolution interpolation for digital image processing. IEEE Transactions on Acoustics, Speech, and Signal Processing 29, 1153–1160.

Kimura, H., Yamaguchi, Y., et al., 2000. Detection of landslide areas using satellite radar interferometry. Photogrammetric Engineering and Remote Sensing 66, 337–344.

Kircher, M., Roth, A., Adam, N., Kampes, B., Neugebauer, H.J., 2003. Remote sensing observation of mining induced subsidence by means of differential sar-interferometry, in: IGARSS 2003. 2003 IEEE International Geoscience and Remote Sensing Symposium., pp. 209–211 vol.1.

Knill, J.L., Jones, K.S., 1968. Ground-water conditions in Greater Tehran. Quarterly Journal of Engineering Geology and Hydrogeology 1, 181–194.

Kuehn, Friedrich, H.P.S.M.B.R., Hole, J., 2009. Experience with satellite radar for gas storage monitoring. Erdoel Erdgas Kohle 125.

Kumar, V., Venkataraman, G., Rao, Y.S., and, G.S., 2008. Spaceborne insar technique for study of himalayan glaciers using envisat asar and ers data, in: IGARSS 2008 - 2008 IEEE International Geoscience and Remote Sensing Symposium, pp. IV – 1085–IV – 1088.

Lanari, R., Zoffoli, S., Sansosti, E., Fornaro, G., Serafino, F., 2001. New approach for hybrid strip-map/spotlight SAR data focusing. IEE Proceedings - Radar, Sonar and Navigation 148, 363–372.

Li, Z., Fielding, E.J., Cross, P., Muller, J.P., 2006. Interferometric synthetic aperture radar atmospheric correction: Gps topography-dependent turbulence model. Journal of Geophysical Research: Solid Earth 111.

Li, Z., Muller, J.P., Cross, P., Fielding, E.J., 2005. Interferometric synthetic aperture radar (insar) atmospheric correction: Gps, moderate resolution imaging spectroradiometer (modis), and insar integration. Journal of Geophysical Research: Solid Earth 110, B03410.

Liu, D., Sowter, A., Niemeier, W., 2014. Process-related deformation monitoring by psi using high resolution space-based sar data: a case study in düsseldorf, germany. Natural Hazards and Earth System Sciences Discussions 2, 4813–4830.

Lu, Z., Danskin, W.R., 2001. InSAR analysis of natural recharge to define structure of a ground-water basin, San Bernardino, California. Geophysical Research Letters 28, 2661–2664.

Lu, Z., Kwoun, O., 2008. Radarsat-1 and ers insar analysis over southeastern coastal louisiana: Implications for mapping water-level changes beneath swamp forests. IEEE Transactions on Geoscience and Remote Sensing 46, 2167–2184.

Lubitz, C., Motagh, M., Wetzel, H.U., Kaufmann, H., 2013. Remarkable urban uplift in staufen im breisgau, germany: Observations from terrasar-x insar and leveling from 2008 to 2011. Remote Sensing 5, 3082–3100.

Luca, C.D., Zinno, I., Manunta, M., Lanari, R., Casu, F., 2017. Large areas surface deformation analysis through a cloud computing p-sbas approach for massive processing of dinsar time series. Remote Sensing of Environment 202, 3 – 17. Big Remotely Sensed Data: tools, applications and experiences.

Mahmoudpour, M., Khamehchiyan, M., Nikudel, M.R., Ghassemi, M.R., 2016. Numerical simulation and prediction of regional land subsidence caused by groundwater exploitation in the southwest plain of Tehran, Iran. Engineering Geology 201, 6 – 28.

Maraun, D., Kurths, J., 2004. Cross wavelet analysis: significance testing and pitfalls. Nonlinear Processes in Geophysics 11, 505–514.

Martelet, G., Sailhac, P., Moreau, F., Diament, M., 2001. Characterization of geological boundaries using 1-d wavelet transform on gravity data: Theory and application to the himalayas. GEOPHYSICS 66, 1116–1129.

Massey, C., 2010. The dynamics of reactivated landslides: Utiku and Taihape, North Island, New Zealand. Ph.d. thesis. Durham University.

Massey, C., Petley, D., McSaveney, M., 2013. Patterns of movement in reactivated landslides. Engineering Geology 159, 1 – 19.

Massonnet, D., Feigl, K.L., 1998. Radar interferometry and its application to changes in the earth's surface. Reviews of Geophysics 36, 441–500.

Mateus, P., Catalão, J., Nico, G., 2017. Sentinel-1 interferometric sar mapping of precipitable water vapor over a country-spanning area. IEEE Transactions on Geoscience and Remote Sensing 55, 2993–2999.

Mateus, P., Tomé, R., Nico, G., Catalão, J., 2016. Three-dimensional variational assimilation of insar pwv using the wrfda model. IEEE Transactions on Geoscience and Remote Sensing 54, 7323–7330.

Meyer, F., 2010. A review of ionospheric effects in low-frequency sar — signals, correction methods, and performance requirements, in: 2010 IEEE International Geoscience and Remote Sensing Symposium, pp. 29–32.

Milillo, P., Bürgmann, R., Lundgren, P., Salzer, J., Perissin, D., Fielding, E., Biondi, F., Milillo, G., 2016. Space geodetic monitoring of engineered structures: The ongoing destabilization of the mosul dam, iraq. Scientific Reports 6, 37408.

Millin-Chalabi, G., McMorrow, J., Agnew, C., 2014. Detecting a moorland wildfire scar in the peak district, uk, using synthetic aperture radar from ers-2 and envisat asar. International Journal of Remote Sensing 35, 54–69.

Motagh, M., Bahroudi, A., Haghighi, M.H., Samsonov, S., Fielding, E., Wetzel, H., 2015. The 18 august 2014 mw 6.2 mormori, iran, earthquake: A thin-skinned faulting in the zagros mountain inferred from insar measurements. Seismological Research Letters 86, 775–782.

Motagh, M., Djamour, Y., Walter, T.R., Wetzel, H.U., Zschau, J., Arabi, S., 2007. Land subsidence in Mashhad Valley, northeast Iran: Results from InSAR, levelling and GPS. Geophysical Journal International 168, 518–526.

Motagh, M., Schurr, B., Anderssohn, J., Cailleau, B., Walter, T.R., Wang, R., Villotte, J.P., 2010. Subduction earthquake deformation associated with 14 november 2007, mw 7.8 tocopilla earthquake in chile: Results from insar and aftershocks. Tectonophysics 490, 60 – 68.

Motagh, M., Shamshiri, R., Haghshenas Haghighi, M., Wetzel, H.U., Akbari, B., Nahavandchi, H., Roessner, S., Arabi, S., 2017. Quantifying groundwater exploitation induced subsidence in the Rafsanjan plain, southeastern Iran, using InSAR time-series and in situ measurements. Engineering Geology 218, 134–151.

Motagh, M., Walter, T.R., Sharifi, M.A., Fielding, E., Schenk, A., Anderssohn, J., Zschau, J., 2008a. Land subsidence in Iran caused by widespread water reservoir overexploitation. Geophysical Research Letters 35, L16403.

Motagh, M., Wang, R., Walter, T.R., Bürgmann, R., Fielding, E., Anderssohn, J., Zschau, J., 2008b. Coseismic slip model of the 2007 August Pisco earthquake (Peru) as constrained by Wide Swath radar observations. Geophysical Journal International 174, 842–848.

Motagh, M., Wetzel, H.U., Roessner, S., Kaufmann, H., 2013. A terrasar-x insar study of landslides in southern kyrgyzstan, central asia. Remote Sensing Letters 4, 657–666.

Nitti, D.O., Hanssen, R.F., Refice, A., Bovenga, F., Nutricato, R., 2011. Impact of dem-assisted coregistration on high-resolution sar interferometry. IEEE Transactions on Geoscience and Remote Sensing 49, 1127–1143.

Notti, D., Mateos, R.M., Monserrat, O., Devanthéry, N., Peinado, T., Roldán, F.J., Fernández-Chacón, F., Galve, J.P., Lamas, F., Azañón, J.M., 2016. Lithological control of land subsidence induced by groundwater withdrawal in new urban AREAS (Granada Basin, SE Spain). Multiband DInSAR monitoring. Hydrological Processes 30, 2317–2331.

NZGS, 2005. Field description of soils and rock: guideline for the field classification and description of soil and rock for engineering purposes. Report. New Zealand Geotechnical Society.

Osmanoğlu, B., Dixon, T.H., Wdowinski, S., Cabral-Cano, E., Jiang, Y., 2011. Mexico city subsidence observed with persistent scatterer insar. International Journal of Applied Earth Observation and Geoinformation 13, 1 – 12.

Parizzi, A., Brcic, R., 2011. Adaptive insar stack multilooking exploiting amplitude statistics: A comparison between different techniques and practical results. IEEE Geoscience and Remote Sensing Letters 8, 441–445.

Pavelko, M.T., 2004. Estimates of hydraulic properties from a one-dimensional numerical model of vertical aquifer-system deformation, Lorenzi Site, Las Vegas, Nevada. US Department of the Interior, US Geological Survey.

Perissin, D., Wang, Z., Lin, H., 2012. Shanghai subway tunnels and highways monitoring through cosmo-skymed persistent scatterers. ISPRS Journal of Photogrammetry and Remote Sensing 73, 58 – 67. Innovative Applications of SAR Interferometry from modern Satellite Sensors.

Petley, D., 2012. Global patterns of loss of life from landslides. Geology 40, 927–930.

Phien-wej, N., Giao, P.H., Nutalaya, P., 2006. Land subsidence in Bangkok, Thailand. Engineering Geology 82, 187–201.

Pichelli, E., Ferretti, R., Cimini, D., Panegrossi, G., Perissin, D., Pierdicca, N., Rocca, F., Rommen, B., 2015. Insar water vapor data assimilation into mesoscale model mm5: Technique and pilot study. IEEE Journal of Selected Topics in Applied Earth Observations and Remote Sensing 8, 3859–3875.

Poland, J.F., 1984. Guidebook to studies of land subsidence due to ground-water withdrawal.

Pritchard, M.E., Fielding, E.J., 2008. A study of the 2006 and 2007 earthquake sequence of pisco, peru, with insar and teleseismic data. Geophysical Research Letters 35, L09308.

Qu, F., Lu, Z., Zhang, Q., Bawden, G.W., Kim, J.W., Zhao, C., Qu, W., 2015. Mapping ground deformation over Houston–Galveston, Texas using multi-temporal InSAR. Remote Sensing of Environment 169, 290 – 306.

Reck, C., Campuzano, G., Dengler, K., Heinen, T., Winkler, M., 2016. German copernicus data access and exploitation platform, in: Proceedings of 2016 Conference on Big Data from Space, Auditorio de Tenerife, pp. 1–4.

Rosen, P.A., Hensley, S., Joughin, I.R., Li, F.K., Madsen, S.N., Rodriguez, E., Goldstein, R.M., 2000. Synthetic aperture radar interferometry. Proceedings of the IEEE 88, 333–382.

Rosen, P.A., Hensley, S., Peltzer, G., Simons, M., 2004. Updated repeat orbit interferometry package released. Eos, Transactions American Geophysical Union 85, 47–47.

Rossi, C., Gonzalez, F.R., Fritz, T., Yague-Martinez, N., Eineder, M., 2012. Tandem-x calibrated raw dem generation. ISPRS Journal of Photogrammetry and Remote Sensing 73, 12 – 20. Innovative Applications of SAR Interferometry from modern Satellite Sensors.

Rott, H., Nagler, T., 2006. The contribution of radar interferometry to the assessment of landslide hazards. Advances in Space Research 37, 710 – 719. Natural Hazards and Oceanographic Processes from Satellite Data.

Rott, H., Scheuchl, B., Siegel, A., Grasemann, B., 1999. Monitoring very slow slope movements by means of sar interferometry: A case study from a mass waste above a reservoir in the Ötztal alps, austria. Geophysical Research Letters 26, 1629–1632.

Rufino, G., Moccia, A., Esposito, S., 1998. Dem generation by means of ers tandem data. IEEE Transactions on Geoscience and Remote Sensing 36, 1905–1912.

Salvi, S., Stramondo, S., Funning, G., Ferretti, A., Sarti, F., Mouratidis, A., 2012. The sentinel-1 mission for the improvement of the scientific understanding and the operational monitoring of the seismic cycle. Remote Sensing of Environment 120, 164 – 174. The Sentinel Missions - New Opportunities for Science.

Samsonov, S., d'Oreye, N., Smets, B., 2013. Ground deformation associated with post-mining activity at the french–german border revealed by novel insar time series method. International Journal of Applied Earth Observation and Geoinformation 23, 142 – 154.

Samsonov, S.V., d'Oreye, N., González, P.J., Tiampo, K.F., Ertolahti, L., Clague, J.J., 2014. Rapidly accelerating subsidence in the Greater Vancouver region from two decades of ERS-ENVISAT-RADARSAT-2 DInSAR measurements. Remote Sensing of Environment 143, 180 – 191.

Samsonov, S.V., Tiampo, K.F., Feng, W., 2016. Fast subsidence in downtown of Seattle observed with satellite radar. Remote Sensing Applications: Society and Environment 4, 179 – 187.

Santoro, M., Askne, J.I.H., Wegmuller, U., Werner, C.L., 2007. Observations, modeling, and applications of ers-envisat coherence over land surfaces. IEEE Transactions on Geoscience and Remote Sensing 45, 2600–2611.

Schäfer, M., Walter, D., Busch, W., 2007. Dinsar ground movement monitoring in the rural environment of an open pit mining area, in: Proc. Envisat Symposium, Montreux, Switzerland.

Scheiber, R., Moreira, A., 2000. Coregistration of interferometric SAR images using spectral diversity. IEEE Transactions on Geoscience and Remote Sensing 38, 2179–2191.

Schmidt, D.A., Bürgmann, R., 2003. Time-dependent land uplift and subsidence in the Santa Clara valley, California, from a large interferometric synthetic aperture radar data set. Journal of Geophysical Research: Solid Earth 108, 2416.

Schumann, H., Poland, J., 1969. Land subsidence, earth fissures and groundwater withdrawal in south-central Arizona, USA, in: International Symposium on Subsidence, Tokyo.

Scifoni, S., Bonano, M., Marsella, M., Sonnessa, A., Tagliafierro, V., Manunta, M., Lanari, R., Ojha, C., Sciotti, M., 2016. On the joint exploitation of long-term DInSAR time series and geological information for the investigation of ground settlements in the town of Roma (Italy). Remote Sensing of Environment 182, 113 – 127.

Shamshiri, R., Motagh, M., Baes, M., Sharifi, M.A., 2014. Deformation analysis of the Lake Urmia causeway (LUC) embankments in northwest Iran: insights from multi-sensor interferometry synthetic aperture radar (InSAR) data and finite element modeling (FEM). Journal of Geodesy 88, 1171–1185.

Shemshaki, A., Bolourchi, M., Ansari, F., 2005. investigating land surface subsidence in Tehran Plain and Shahriar (First report, in persian). Report. Geological Survey of Iran (GSI).

Singleton, A., Li, Z., Hoey, T., Muller, J.P., 2014. Evaluating sub-pixel offset techniques as an alternative to d-insar for monitoring episodic landslide movements in vegetated terrain. Remote Sensing of Environment 147, 133 – 144.

Sowter, A., Bateson, L., Strange, P., Ambrose, K., Syafiudin, M.F., 2013. Dinsar estimation of land motion using intermittent coherence with application to the south derbyshire and leicestershire coalfields. Remote Sensing Letters 4, 979–987.

Strozzi, T., Farina, P., Corsini, A., Ambrosi, C., Thüring, M., Zilger, J., Wiesmann, A., Wegmüller, U., Werner, C., 2005. Survey and monitoring of landslide displacements by means of l-band satellite sar interferometry. Landslides 2, 193–201.

Sun, H., Grandstaff, D., Shagam, R., 1999. Land subsidence due to groundwater withdrawal: potential damage of subsidence and sea level rise in southern New Jersey, USA. Environmental Geology 37, 290–296.

Teatini, P., Ferronato, M., Gambolati, G., Gonella, M., 2006. Groundwater pumping and land subsidence in the Emilia-Romagna coastland, Italy: Modeling the past occurrence and the future trend. Water Resources Research 42, W01406.

Thompson, R.C., 1982. Relationship of Geology to Slope Failures in Soft Rocks of the Taihape-Mangaweka Area, Central North Island, New Zealand. Ph.D. thesis. University of Auckland.

Tomás, R., Li, Z., Lopez-Sanchez, J.M., Liu, P., Singleton, A., 2015. Using wavelet tools to analyse seasonal variations from InSAR time-series data: a case study of the Huangtupo landslide. Landslides , 1–14.

Torrence, C., Compo, G.P., 1998. A practical guide to wavelet analysis. Bulletin of the American Meteorological Society 79, 61–78.

Torres, R., Snoeij, P., Geudtner, D., Bibby, D., Davidson, M., Attema, E., Potin, P., Rommen, B., Floury, N., Brown, M., Traver, I.N., Deghaye, P., Duesmann, B., Rosich, B., Miranda, N., Bruno, C., L'Abbate, M., Croci, R., Pietropaolo, A., Huchler, M., Rostan, F., 2012. GMES Sentinel-1 mission. Remote Sensing of Environment 120, 9 – 24.

Vernant, P., Nilforoushan, F., Chéry, J., Bayer, R., Djamour, Y., Masson, F., Nankali, H., Ritz, J.F., Sedighi, M., Tavakoli, F., 2004. Deciphering oblique shortening of central Alborz in Iran using geodetic data. Earth and Planetary Science Letters 223, 177 – 185.

Walter, D., Wegmüller, U., Spreckels, V., Hannemann, W., Busch, W., 2009. Interferometric monitoring of an active underground mining field with high-resolution sar sensors, in: Proceedings of ISPRS Hannover Workshop, Hannover, Germany.

Wang, H., Wright, T.J., Biggs, J., 2009. Interseismic slip rate of the northwestern xianshuihe fault from insar data. Geophysical Research Letters 36.

Wasowski, J., Bovenga, F., 2014. Investigating landslides and unstable slopes with satellite multi temporal interferometry: Current issues and future perspectives. Engineering Geology 174, 103 – 138.

Wegmuller, U., Strozzi, T., Werner, C., Wiesmann, A., Benecke, N., Spreckels, V., 2000. Monitoring of mining-induced surface deformation in the ruhrgebiet (germany) with sar interferometry, in: IGARSS 2000. IEEE 2000 International Geoscience and Remote Sensing Symposium., pp. 2771–2773.

Wegmuller, U., Werner, C., Strozzi, T., Wiesmann, A., 2004. Monitoring mining induced surface deformation, in: IGARSS 2004. 2004 IEEE International Geoscience and Remote Sensing Symposium, pp. 1933–1935 vol.3.

Werner, C., Wegmüller, U., Strozzi, T., Wiesmann, A., 2000. Gamma SAR and interferometric processing software, in: Proceedings of the Ers-Envisat symposium, Gothenburg, Sweden, p. 1620.

Werner Zirnig, Russ Pride, I.L.R.C.i.D.H., 2004. The presense and pipemon projects–defining the ways of using space-borne earth observation services for pipeline monitoring, in: Proceedings of the International Gas Research Conference (IGRC), Vancouver, Canada.

Wessel, P., Smith, W.H.F., Scharroo, R., Luis, J., Wobbe, F., 2013. Generic mapping tools: Improved version released. Eos, Transactions American Geophysical Union 94, 409–410.

Wolkersdorfer, C., Thiem, G., 1999. Ground water withdrawal and land subsidence in northeastern saxony (germany). Mine Water and the Environment 18, 81–92.

Wright, T., Parsons, B., Fielding, E., 2001. Measurement of interseismic strain accumulation across the north anatolian fault by satellite radar interferometry. Geophysical Research Letters 28, 2117–2120.

Xiuming, J., Chao, M., Anyuan, Z., 2008. Environmental investigation and evaluation of land subsidence in the datong coalfield based on insar technology. Acta Geologica Sinica - English Edition 82, 1035–1044.

Yagüe-Martínez, N., Prats-Iraola, P., González, F.R., Brcic, R., Shau, R., Geudtner, D., Eineder, M., Bamler, R., 2016. Interferometric processing of Sentinel-1 TOPS data. IEEE Transactions on Geoscience and Remote Sensing 54, 2220–2234.

Zebker, H.A., Chen, K., 2005. Accurate estimation of correlation in insar observations. IEEE Geoscience and Remote Sensing Letters 2, 124–127.

Zebker, H.A., Goldstein, R.M., 1986. Topographic mapping from interferometric synthetic aperture radar observations. Journal of Geophysical Research: Solid Earth 91, 4993–4999.

Zebker, H.A., Rosen, P.A., Hensley, S., 1997. Atmospheric effects in interferometric synthetic aperture radar surface deformation and topographic maps. Journal of Geophysical Research: Solid Earth 102, 7547–7563.

Zebker, H.A., Villasenor, J., 1992. Decorrelation in interferometric radar echoes. IEEE Transactions on Geoscience and Remote Sensing 30, 950–959.

Zink, M., Bachmann, M., Brautigam, B., Fritz, T., Hajnsek, I., Moreira, A., Wessel, B., Krieger, G., 2014. Tandem-x: The new global dem takes shape. IEEE Geoscience and Remote Sensing Magazine 2, 8–23.

Zinno, I., Bonano, M., Buonanno, S., Casu, F., De Luca, C., Manunta, M., Manzo, M., Lanari, R., 2018. National scale surface deformation time series generation through advanced dinsar processing of sentinel-1 data within a cloud computing environment. IEEE Transactions on Big Data , 1–1.

Acknowledgement

First and foremost, I would like to thank my supervisor, Prof. Dr. Mahdi Motagh, for his generous support, constructive guidance, and warm encouragements throughout my PhD journey. I am sincerely grateful to the head of the Institute of Photogrammetry and GeoInformation (IPI), Prof. Dr. Christian Heipke, for his constant support, great patience, and thoughtful advice. I would like to express my sincere appreciation to Prof. Dr. Luis Guanter, the former head of section 1.4 Remote Sensing of GFZ, for supporting my research, being always cheerful, and for making the working environment at our section friendly and comfortable. I am grateful to Sylvia Magnussen, the system administrator of section 1.4 Remote Sensing, who worked tirelessly behind the scenes to provide technical support without which I could not stay focused on my research. I am deeply thankful to Dr. Hans-Ulrich Wetzel who has helped on geological interpretations of my research with his extensive knowledge and also for his warm welcome and supports during the first days of my stay in Potsdam. I would like to thank the members of radar working group of Section 1.4 especially Dr. Julia Neelmeijer who gave me helpful advice that made the PhD writing and submission process going smoothly. Last but not least, I owe a deep gratitude to my family for their constant support and encouragement and a especial thanks to Shadi for everything she has done for me. This work was supported by Initiative and Networking Fund of the Helmholtz Association in the frame of Helmholtz Alliance 'Remote Sensing and Earth System Dynamics'.

Curriculum Vitae

Personal Information

Mahmud Haghshenas Haghighi
Born on 03.04.1986 in Estahban, Iran

Study

2009–2012 M.Sc. Civil Engineering - Remote Sensing
University of Tehran, Tehran, Iran

2004–2009 B.Sc. Civil Engineering - Surveying
University of Tabriz, Tabriz, Iran

Work Experience

2014-2019 Doctoral Researcher
GFZ German Research Centre for Geosciences, Potsdam, Germany

2009 Surveying Engineer
Peymayesh Gostar Pakan Co., Shiraz, Iran

Peer-Reviewed Publications

2019 **M Haghshenas Haghighi**, M Motagh, *Ground surface response to continuous compaction of aquifer system in Tehran, Iran: Results from a long-term multi-sensor InSAR analysis*, Remote Sensing of Environment.

2017 **M Haghshenas Haghighi**, M Motagh, *Sentinel-1 InSAR over Germany: Large-Scale Interferometry, Atmospheric Effects, and Ground Deformation Mapping*, ZFV – Zeitschrift für Geodäsie, Geoinformation und Landmanagement.

2017 L Emadali, M Motagh, **M Haghshenas Haghighi**, *Characterizing post-construction settlement of the Masjed-Soleyman embankment dam, Southwest Iran, using TerraSAR-X SpotLight radar imagery*, Engineering Structures.

2017 M Motagh, R Shamshiri, **M Haghshenas Haghighi**, H-U Wetzel, B Akbari, H Nahavandchi, S Rossner, S Arabi , *Quantifying groundwater exploitation induced subsidence*

in the Rafsanjan plain, southeastern Iran, using InSAR time-series and in situ measurements, Engineering Geology.

2016 **M Haghshenas Haghighi** , M Motagh, *Assessment of ground surface displacement in Taihape landslide, New Zealand, with C-and X-band SAR interferometry*, New Zealand Journal of Geology and Geophysics.

2015 M Motagh, A Bahroudi, **M Haghshenas Haghighi**, S Samsonov, E Fielding , HU Wetzel, *The 18 August 2014 Mw 6.2 Mormori, Iran, Earthquake: A Thin-Skinned Faulting in the Zagros Mountain Inferred from InSAR Measurements*, Seismological Research Letters.

2014 N Abdolmaleki, M Motagh, A Bahroudi, MA Sharifi , **M Haghshenas Haghighi**, *Using Envisat InSAR time-series to investigate the surface kinematics of an active salt extrusion near Qum, Iran*, Journal of Geodynamics.

2013 M Akbarimehr, M Motagh , **M Haghshenas Haghighi**, *Slope Stability Assessment of the Sarcheshmeh Landslide, Northeast Iran, Investigated Using InSAR and GPS Observations*, Remote Sensing.

2013 M Motagh, J Beavan, EJ Fielding , **M Haghshenas**, *Postseismic Ground Deformation Following the September 2010 Darfield, New Zealand, Earthquake From TerraSAR-X, COSMO-SkyMed, and ALOS InSAR*, Geoscience and Remote Sensing Letters.

Wissenschaftliche Arbeiten der Fachrichtung Geodäsie und Geoinformatik der Leibniz Universität Hannover

(Eine vollständige Liste der Wiss. Arb. ist beim Geodätischen Institut, Nienburger Str. 1, 30167 Hannover erhältlich.)

Nr. 327	SCHACK, Lukas:	Object-based matching of Persistent Scatterers to Optical Oblique Images (Diss. 2016)
Nr. 328	REICH, Martin:	Global Image Orientation from Pairwise Relative Orientations (Diss. 2016)
Nr. 329	KLINGER, Tobias:	Probabilistic multi-person localisation and tracking (Diss. 2016)
Nr. 330	SCHMIDT, Alena:	Markierte Punktprozesse für die automatische Extraktion von Liniennetzen in Rasterdaten (Diss. 2016)
Nr. 331	HOFMANN, Franz:	Lunar Laser Ranging - verbesserte Modellierung der Monddynamik und Schätzung relativistischer Parameter (Diss. 2017)
Nr. 332	BRIEDEN, Phillip:	Validierung von GOCE-Gravitationsgradienten in Kreuzungspunkten und Zukunftsperspektiven der Satellitengradiometrie (Diss. 2017)
Nr. 333	VON GÖSSELN, Ilka:	Simulationsbasierte Effizienzoptimierung von Messprozessen am Beispiel der tachymetrischen Netzmessung (Diss. 2017)
Nr. 334	HOFMANN, Sabine:	Potential von LiDAR Mobile Mapping für hochgenaue Karten (Diss. 2017)
Nr. 335	ALBERT, Lena:	Simultane Klassifikation der Bodenbedeckung und Landnutzung unter Verwendung von Conditional Random Fields (Diss. 2017)
Nr. 336	NIEMEYER, Joachim:	Verwendung von Kontext zur Klassifikation luftgestützter Laserdaten urbaner Gebiete (Diss. 2017)
Nr. 337	EGGERT, Daniel:	Effiziente Verarbeitung und Visualisierung von Mobile Mapping Daten (Diss. 2017)
Nr. 338	FITZNER, Daniel:	Estimation of Spatio-Temporal Moving Fields at High Resolution (Diss. 2017)
Nr. 339	CZIOSKA, Paul:	Meeting point locations for shared rides (Diss. 2018)
Nr. 340	FEUERHAKE, Udo:	Erfassung von Trajektorien und Erkennung von Bewegungsmustern (Diss. 2018)
Nr. 341	HUANG, Hai :	Bayesian Models for Pattern Recognition in Spatial Data (Habil. 2018) . (Nicht im Layout unserer Schriftenreihe erschienen, sondern als Heft DGK Reihe C, Heft 751)
Nr. 342	BOCK, Urs Fabian:	Dynamic Parking Maps from Vehicular Crowdsensing (Diss. 2018)
Nr. 343	KRAWINKEL, Thomas:	Improved GNSS Navigation with Chip-scale Atomic Clocks (Diss. 2018)
Nr. 344	GOSWAMI, Sujata:	Understanding the sensor noise in the GRACE range-rate observations by analyzing their residuals (Diss. 2018)
Nr. 345	ZHANG, Yin:	Expected Utilities for Decision Making and Steering of Measurement Processes (Diss. 2018)
Nr. 346	SCHLICHTING, Alexander:	Fahrzeuglokalisierung durch Automotive Laserscanner unter Verwendung statischer Merkmale (Diss. 2018)
Nr. 347	RÖTH, Oliver	Extraktion von hochgenauer Fahrspurgeometrie und -topologie auf der Basis von Fahrzeugtrajektorien und Umgebungsinformationen (Diss. 2018)
Nr. 348	NEELMEIJER, Julia:	Observing Inter- and Intra-Annual Glacier Changes and Lake Loading Effects from Synthetic Aperture Radar Remote Sensing (Diss. 2018)
Nr. 349	HOBERG, Thorsten:	Conditional Random Fields zur Klassifikation multitemporaler Fernerkundungs daten unterschiedlicher Auflösung (Diss. 2018)
Nr. 350	SCHILLING, Manuel:	Kombination von klassischen Gravimetern mit Quantensensoren (Diss. 2019)
Nr. 351	MILLER, Dominik:	Seismic noise analysis and isolation concepts for the ALPS II experiment at DESY (Diss. 2019)
Nr. 352	ALI, Bashar:	Optimierte Verteilung von Standorten der Schulen unter dem Einfluss des demografischen Wandels am Beispiel Grundschulen (Diss. 2019)
Nr. 353	ZHAO, Xin:	Terrestrial Laser Scanning Data Analysis for Deformation Monitoring (Diss. 2019)
Nr. 354	HAGHIGHI, Mahmud Haghshenas:	Local and Large Scale InSAR Measurement of Ground Surface Deformation (Diss. 2019)

Die Arbeiten werden im Rahmen des wissenschaftlichen Schriftenaustausches verteilt und sind nicht im Buchhandel erhältlich. Der Erwerb ist zu einem Stückpreis von € 25,00 bei den herausgebenden Instituten möglich.